Development and Application of Data Assimilation Methods in Reactor Physics

Thèse N° 7525

Daniel Jerôme SIEFMAN

2019

EPFL
ÉCOLE POLYTECHNIQUE
FÉDÉRALE DE LAUSANNE

In dedication to Alice and Rollo,

I could never have imagined a happier family for myself.

Acknowledgements

My favorite quote attributed to Sir Isaac Newton is, "If I have seen further than others, it is by standing upon the shoulders of giants." The work I have done during my thesis surely stands on the shoulders of decades of inspired research. But importantly, I stood on other giant shoulders during my life and during my foray into independent research.

In the workplace, I must thank Prof. Andreas Pautz and Dr. Mathieu Hursin, who directed and supervised my research. Dr. Hursin has been my scientific advisor since the summer of 2013. My career has been inextricably influenced by him, and I will be forever thankful for his patience and guidance. I am eternally in debt to Prof. Pautz who helped to sponsor my stay in Switzerland for the past six years. It has been an indelible experience to live in Lausanne and work at EPFL. In my later years, I will surely reflect upon this as my *Bildungsroman.*

I would also like to thank my colleagues at LRS: Oskari Pakari, Vincent Lamirand, Carlo Fiorina, Stefan Radman, Pavel Frajtag, Adolfo Rais, and Axel Laureau. I must give a special shout out to my office mates in room PH D3 445,[1] Alessandro Scolaro and Fanny Vitullo. Thank you all for coloring my workday and always bringing positive energy into a room that would otherwise be fetid with the stress and negativity that a difficult day of research brings.

My family deserves important consideration as they have shouldered the burden of me being so far from home for so long. My mother deserves important recognition for getting me here. As a pre-teen, I detested math and refused to put any effort into the subject. She bought me a desk, forced to me sit down and do my algebra homework, and one thing lead to another and now I do math every day. My father taught me the lessons about life: how to work, what are life's priorities, how to build relationships, and how to handle pressure. I use these lessons every day of my life and I would not be the same without them. To my first friends, and my forever friends, Melanie and Amanda. I read a study that said that strong and happy sibling relationships are the foundations of a good life into adulthood, and I think we have that. I love you both tremendously and I cannot wait to see how our fates unwind.

Finally, I must thank Alice who has been with me from the start to the end of my thesis. We have been so lucky to work only 100 m apart for three years. I have cherished all the last minute coffee and lunch breaks, and all the huddled sessions to overcome obstacles in our research. This era together is the base for a bright future, wherever we will be together. You mean more to me than even I can understand, and please never forget that.

Lausanne, Switzerland
June 28th, 2019
D. S.

---

[1] https://www.youtube.com/watch?v=OFr74zI1LBM

Abstract

Simulations of nuclear reactor physics can disagree significantly from experimental evidence, even when the most accurate models are used. An important part of this bias from experiment is caused by nuclear data. The nuclear data have inherent uncertainties due to the way they are evaluated, which then propagate to nuclear reactor simulations. This creates a bias and an uncertainty in a predicted reactor parameter like k_{eff} or the composition of spent fuel. This thesis focuses on data assimilation techniques to ameliorate the effects of nuclear data. Data assimilation takes integral experiments and assimilates them in a Bayesian way to improve simulations. It can also be used to find trends and areas needing improvement in evaluated nuclear data. The research focuses on advancing the data assimilation theory and knowledge used in reactor physics, especially on techniques that require stochastic sampling of the nuclear data. Furthermore, the research takes advantage of rich experimental data available from the Proteus research reactor at the Paul Scherrer Institute.

The thesis showed, for the first time, that two methods based on stochastic sampling (called MOCABA and BMC) gave equivalent results to each other and to the traditional method called GLLS. This was corroborated with two independent studies that used different experiments, neutron transport codes, nuclear data, and processing codes. The first study used the JEZEBEL-Pu239 benchmark, the Serpent2 neutron transport code, and NUSS. The second study used reactivity experiments from the LWR-Phase II experiments at Proteus, CASMO-5 for neutron transport, and SHARK-X. While using Serpent2, several questions pertaining to the stochastic uncertainty of its sensitivity coefficients arose. To address these, a new method called eXtended GLLS, or xGLLS, was proposed and tested in the thesis. xGLLS showed that the uncertainties associated with sensitivity coefficients have a negligible effect on the data assimilation as long as the calculated integral parameters themselves were converged. The final study focused on adjusting the fission yields and covariances made by the GEF code with post-irradiation examination experiments from Proteus. The adjustment improved the accuracy of predicted nuclide concentrations in spent fuel and improved the agreement between the GEF fission yields and those of ENDF/B-VIII.0 and JEFF3.3.

Key words: Data Assimilation, Nuclear Data, Reactor Physics, Neutronics, Bayes' Theory

Résumé

Les simulations en physique des réacteurs nucléaires pourraient être en désaccord avec les expériences, même avec des modèles plus sophistiqués. L'un des principaux biais entre les simulations et les expériences provient des données nucléaires. L'incertitude inhérente à l'évaluation de données nucléaires se propage aux simulations de réacteurs nucléaires. Ces données d'entrée introduisent un biais et créent une incertitude sur les paramètres calculés d'un réacteur, comme la criticité ou la composition des combustibles usés. Cette thèse se concentre sur l'assimilation de données afin d'améliorer l'impact des données nucléaires. L'assimilation de données utilise les résultats des expériences intégrales et les intègre de façon Bayésienne pour améliorer les simulations. Son application permet aussi de mettre en évidence des tendances dans les données nucléaires évaluées et de rechercher des données qui ont besoin d'amélioration. Les travaux de recherche menés durant cette thèse se focalisent sur l'amélioration de la théorie et de la compréhension de l'assimilation de données pour la neutronique, en particulier avec les techniques utilisant l'échantillonnage stochastique des données nucléaires. De plus, ces travaux profitent fortement de données expérimentales provenant du réacteur nucléaire de recherche Proteus à l'Institut Paul Scherrer.

Cette thèse démontre pour la première fois que les deux méthodes basées sur l'échantillonnage stochastique (appelées MOCABA et BMC) produisent des résultats équivalents entre elles, ainsi qu'avec la méthode traditionnelle basée sur les sensibilités (appelée GLLS). La conclusion est corroborée dans ce travail par deux études indépendantes utilisant des expériences, des codes de transport neutronique, des données nucléaires, et des codes d'analyse, tous différents entre les études. La première étude est basée sur l'expérience de référence JEZEBEL-Pu239, le code de transport des neutrons Serpent2, et le code d'échantillonnage stochastique NUSS. La seconde étude utilise les expériences de réactivité provenant de la campagne « LWR-Phase II » du réacteur Proteus, le code CASMO-5 pour la neutronique, et SHARK-X. En utilisant Serpent2, plusieurs questions ont été posées concernant les incertitudes statistiques des coefficients de sensibilité. Afin de répondre à ces questions durant cette thèse, une nouvelle méthode intitulée « eXtended GLLS » ou xGLLS a été proposée et testée. Cette méthode a démontré que les incertitudes associées aux coefficients de sensibilité avaient un effet négligeable sur l'assimilation de données pourvu que les paramètres intégraux calculés soient suffisamment précis. L'étude finale s'est concentrée sur les rendements de fission et les matrices de covariance générés avec le code GEF, ainsi que l'assimilation des expériences de post-irradiation de Proteus. Les ajustements des rendements de fission ont amélioré la précision des concentrations de nucléides simulées dans les combustibles usés

ainsi que l'accord entre les rendements de fission produits par GEF et ceux des bases de données ENDF-B/VIII.0 et de JEFF3.3.

Mots Clés : assimilation de données, données nucléaires, physique de réacteurs, neutronique, théorie de Bayes

Contents

Contents

List of Figures

List of Tables

1 **Introduction**

> The best model of a cat is another, or
> preferably the same, cat.
>
> <div align="right">NORBERT WEINER – 1945</div>

1.1 Background and Context

Computational science is the business of making predictions. We describe a system with mathematical formulae, or *models*,[1] in order to predict its behavior. Through models, we seek to further understand systems like weather patterns, biochemistry, or nuclear reactors. Then we can design new technologies, or analyze and improve existing systems. When we compare a model prediction to reality, there is invariably a *bias* or a difference between prediction and reality.[2] The never-ending battle in computational science is to minimize the bias of a model while concurrently minimizing the resources spent on solving it. Resources are things like time, human effort, computational power, or space on a hard drive. More simply, we strive to make our predictions as accurate and efficient as possible.

The bias exists, in part, because of the need to economize resources. We often must simplify the physics of a system so that not only can the models be solved, but also solved in a reasonable amount of time with available computer power. The bias may also arise because we simply do not yet know how to fully model a system or how to solve its model. We must then resort to approximating the physics to have a model that is predictive and solvable. With the advancement of science, we can make fewer approximations in our models which, in

---

[1] For clarity, we can give a more formal definition of a model. In modelling, there is generally a system (it can be natural or artificial) that is governed by a set of rules. A model is created to describe this system and to predict its behavior. A model could be a set of differential equations that can be solved using the rules of mathematical calculus. While the model may follow a set of immutable physical laws, many models may exist to describe the same system and can be compatible with data or evidence.

[2] The bias of a model is a metric used in validation. The bias is the degree to which the model is a good representation. A small bias indicates a good degree of representation and a large bias a poor degree of representation.

turn, lead to reduced biases. Advancements in technology increase computational power permitting more complex and accurate models that were previously unfeasible. Although these modern and more sophisticated models have greatly reduced biases, biases still, and will *forever*, exist.

If we imagine a world where the physics of a system are perfectly known and modeled, and we have infinite computational power, we still could not eliminate the bias. An insurmountable asymptote blocks the way. Fortunately, we know the culprit: the inputs into our models. Models need starting conditions to make a prediction, which are often called *input parameters* or *independent variables*. If these input parameters are inaccurate, this will have a knock-on effect in the model's *output parameters* or the *dependent variables*. As we reduce the parts of the bias caused by approximations and simplifications, the bias will become more and more dominated by a single source: the input parameters.

To illustrate this idea, take for example a computational model that predicts the strength and trajectory of a hurricane. The results of the model have high stakes because they are used to make decisions about where and when people need to be evacuated. If the bias is too large, the wrong people may be evacuated and many lives may be in danger. The model needs many input parameters, one of which is the ocean temperature. To measure the temperature, a buoy with a thermometer is dropped from an airplane and it then communicates the temperature with a radiowave. In the hurricane model, the location of the buoy's measurement and the temperature itself are input variables.

Unfortunately, inputs such as these are based on measurements and are, therefore, uncertain. These are *aleatoric uncertainties* that come from the randomness of the measurement.[3] Any measured value will always have a range of other values that could also be the true value; when it is repeated ten times, it will have ten different values. Consider the buoy sensor from earlier, it has aleatoric variations in its measured temperature that are caused by experimental errors and imperfect instruments. It also has *epistemic uncertainties* or systematic uncertainties that could, in theory, be eliminated but in practice cannot. An epistemic uncertainty would exist in the buoy's location: how much did it glide in the air before splashing down? How much did it drift in the tempest's raging current? How does an imperfection calibration of the buoy's equipment affect the reported location?

Depending on which buoy location and which temperature is used as the model input, the model will give a different output. When considering that a hurricane model may need many thousands of input temperatures, atmospheric pressures, or wind velocities and that all of these measurements have uncertain behavior, it is easy to imagine that these input uncertainties can have an important effect on the model's prediction. Because we cannot use the true input parameters in the model, the model will inevitably have a bias.

This thinking lead to the development of two fields in statistics: *uncertainty quantification* and

---

[3]Aleatoric uncertainty comes from the Latin word *alea*, or dice.
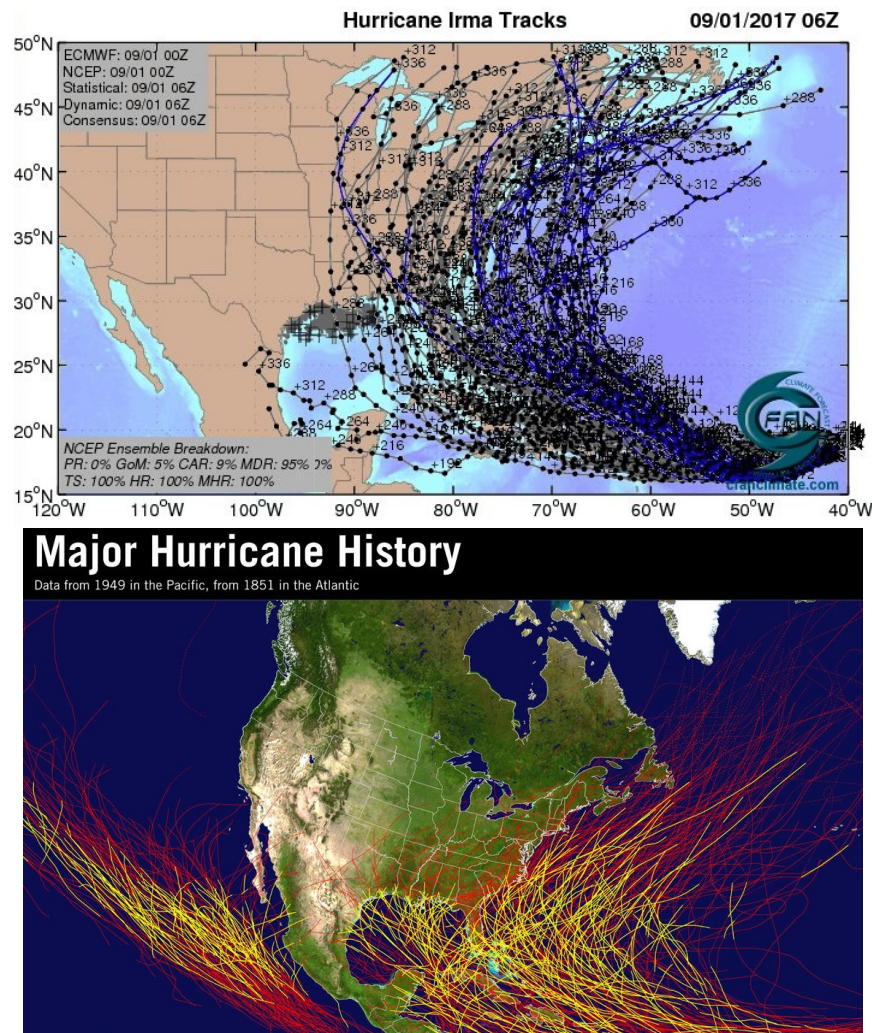
Figure 1.1 – Predicted trajectories of Hurricane Irma in 2017 using UQ (top) and historical hurricane data that can be used in DA (bottom).

sensitivity analysis [1]. Uncertainty quantification (UQ) refers to the techniques and processes that allow us to estimate the uncertainty in a model's output caused by uncertain inputs. When the hurricane model predicts the eye's location in 24 hours to be 25° 28' 7.3956" N and 80° 28' 39.1944" W, UQ would say that because of input uncertainties the location is 25° 28' 7.3956" ± 1' N and 80° 28' 39.1944" ± 2' W. Authorities may then decide to evacuate everyone within the uncertainty range, not only those directly in line with the prediction.

Sensitivity Analysis (SA) goes one step further. It is the study of how uncertainty in the output of a model can be apportioned to different sources of uncertainty in the model's input.[4] It allows the breakdown of the uncertainty in a hurricane's predicted location to the different input measurements. SA might say that 40% of the uncertainty comes from the ocean temperature

---

[4]When we use our best-estimate models and do UQ and SA, this approach is called BEPU (best-estimate plus uncertainties), which is becoming the new standard in nuclear science and engineering.

input, 20% from the atmospheric pressure input, 10% from satellite imagery, *etc.* Knowing this, we could then intelligently invest resources to improve our model predictions. For example, if the temperature measurements have the largest uncertainty contribution, we could choose to invest in improving the buoy thermometer and adding a GPS tracker to better know its location.

While there is always room for improvement in a model's input uncertainties, the uncertainties will nevertheless always exist. Furthermore, while we can hope for improvement in the future, we must ask ourselves what can we do **now** so that our models have less uncertainty and smaller biases? Another statistical method called *data assimilation* addresses this question. Data assimilation (DA) integrates, or assimilates, how the computational model performed in past applications to improve how it performs in the current application. By assimilating this previous experience, we can improve the bias and reduce the uncertainty of our predictions.[5] DA requires no re-evaluation of the model inputs nor changes to the complexity of the model; it can be used **now** to have more accurate and more precise predictions.

DA was pioneered in the field of meteorology and used extensively to predict meteorological phenomena like hurricanes [2]. When DA is applied to hurricane modeling, we assimilate how the model performs when applied to historical hurricanes in order to improve how it predicts the current hurricane. The historical record of hurricanes is used to train, or *calibrate*, the model so that the bias between the true hurricanes' trajectories and what the model predicts them to be is minimized. The uncertainty of the model predictions is also reduced. By assimilating previous experience, the model predictions become more accurate and precise.

1.2   Data Assimilation in Neutronics

The physics of nuclear reactors is extensively modeled with complex computer codes, just like hurricanes. The outputs of their models are essential to design new reactors, to maximize the efficiency of existing reactors, to ensure reactor safety, and to manage radioactive waste. The modern form of these analyses uses *best-estimate* codes with uncertainty quantification. This framework is often called *Best-Estimate Plus Uncertainties*, or BEPU [3, 4, 5]. BEPU allows to reduce conservatism in safety margins and to improve the quality of safety analysis.

BEPU requires *validation*, which can be defined as follows [6, 7]:

- **Validation**: The process of determining the degree to which a model is an accurate representation of the real world considering the intended uses of the model.

Validation is typically done by comparing the output of a code to experimental observations. The comparison is traditionally metrized with the *bias*. Quantifying the bias is so important

---

[5]DA is sometimes called *inverse uncertainty quantification* and UQ is called *forward uncertainty quantification*. UQ moves forward through the model, starting with the uncertain inputs and ending with a quantification of the uncertainty on the outputs. DA moves inversely through the model, starting with the outputs and working backwards through the model to calibrate the inputs.

that international standards were created for it (*e.g.* ANSI/ANS-8.24-2007 for criticality safety [8]). The bias, b_c, between a model's calculated value, C, and an experimental value, E, is formally defined as Eq. (1.1). An unbiased result (*i.e.* the model perfectly predicts E) would have $b_c = 0$.

$$b_c = \frac{C}{E} - 1 \tag{1.1}$$

BEPU seeks to avoid conservatism and expert judgment by using probability theory: the outputs of models have their uncertainty quantified. Rather than arbitrarily imposing a conservative margin on the model's predictions, a model output is said *to satisfy a design or safety constraint within uncertainties*. Likewise, the bias is said to be *within the model's and experiment's uncertainties*. These uncertainties, or $C \pm \Delta_C$ and $E \pm \Delta_E$, are used to quantify the bias' uncertainty, Δ_{b_c}.

$$\Delta_{b_c} \approx \sqrt{\left(\frac{\Delta_C}{E}\right)^2 + \left(\frac{C\Delta_E}{E^2}\right)^2} \tag{1.2}$$

Δ_C can arise from a number of sources. There are uncertainties in the technical inputs into the model: fuel enrichment, cladding thickness, *etc*. There are also uncertainties in the input physical constants, which in neutronics, are primarily nuclear data. Nuclear data describe the probability of certain reactions occurring in nuclear physics. They include the probability of a neutron scattering off a nucleus or causing the nucleus to fission, how many neutrons are released per fission, and which daughter nuclei are produced after fission. The nuclear data have epistemic and aleatoric uncertainties because they are evaluated by combining approximated nuclear physics and experimental evidence. These uncertainties propagate through a neutronics model to create a bias and an uncertainty [9]. That means that all states of interest in the reactor predicted by the model are biased and uncertain as a result of the nuclear data, including the reactor power, the reactivity coefficients, and k_{eff}.

When Δ_{b_c} is quantified, a validation criterion can be defined:

1. *Success*: b_c is explained by its uncertainty,

   $$|b_c| \leq |\Delta_{b_c}|$$

2. *Failure*: b_c is not explained by its uncertainty

   $$|b_c| > |\Delta_{b_c}|$$

In the case of failure, several options could be pursued. Assuming that E and Δ_E are correct and the model is truly best-estimate (it has no model inaccuracy or user error), the failed validation

occurred because of inaccurate model inputs. Often in nuclear engineering, especially for criticality benchmarks and reactor physics benchmarks,[6] the technical input uncertainties are negligible. This means that only the nuclear data made the validation fail. Thus to improve the bias, the nuclear data must be improved.

During the course of the validation, the bias may appear to be satisfactory, but Δ_{b_c} may be determined to be unsatisfactorily large. If $b_c = 0.01$ but $\Delta_{b_c} = 0.50$, the validation is technically successful, but not highly meaningful. The uncertainties are so large as to make qualifications of the model unsatisfactory. In this case, usually $\Delta_C >> \Delta_E$ meaning that the input uncertainties are very large.

This problem is often encountered with fast reactors. The nuclear data important for their physics have large uncertainties and, therefore, model predictions for them have large Δ_C. For instance, in Ref. [10] the uncertainties of key core parameters of sodium cooled fast reactors are given. k_{eff} had an uncertainty of 1.66%, the sodium void coefficient of 23.4%, and the power peak of 0.5%. Especially for safety related parameters like the sodium void coefficient, the Δ_C is at an unacceptable level, despite the fact that the validation would have been successful by the criterion $|b_c| \leq |\Delta_{b_c}|$. Here again, the nuclear data, particularly their covariances, must be changed in order to reduce Δ_C.

The first, and best, option is to proceed to re-evaluate the nuclear data so that they create a better b_c with a smaller Δ_C. Ideally this is done, but there are hindrances. First is the large complexity of the nuclear data evaluation process. Each evaluated nuclear data library, like ENDF/B-VIII.0 [11], requires thousands of man-hours from collaborators all across the world to complete. Changes must follow quality assurance processes and be scientifically corroborated. This is a very good idea, but is slow and makes the nuclear evaluation process long. For example, the last two major releases of the USA's Evaluated Nuclear Data File (ENDF), ENDF/B-VII.1 and ENDF/B-VIII.0, were seven years apart (in 2011 and 2018, respectively).

Another hindrance is that a re-evaluation likely requires new and expensive experimental data. A measurement of a nuclear datum includes the operating cost of experimental facilities, the labor of scientific and technical support personnel, the materials for the measurement (target, detectors), and computer resources to analyze and store the data. One estimate put the cost of a single new measurement at 400,000 USD [12]. If smaller biases and reduced uncertainties are urgently needed, like for a start-up company designing a new fast reactor, any improvement through nuclear data re-evaluation is likely unattainable. The process is either too long and/or too costly.

The question is then what can be done **now** to improve b_c and reduce Δ_C? The answer is data assimilation! DA provides a statistically founded way to incorporate experimental evidence into the nuclear data in order to improve b_c and reduce Δ_C by means of adjusting

---

[6]There is an important difference between a benchmark and a regular experiment. Benchmarks are experiments that have been peer reviewed. They are described in detail and can be repeatedly and consistently modeled by qualified specialists. All benchmarks are experiments, but not all experiments are benchmarks.

the nuclear data. Importantly, DA is data-driven and based on probability theory. This means that it requires much less expert judgment and is thus less prone to human errors. In the previous section, historical hurricanes were used in the DA to improve predictions about incoming hurricanes. In neutronics, integral parameters from benchmarks are used. They are parameters like k_{eff}, reaction rate ratios, reactivity coefficients, or nuclide concentrations after burnup. They are "integral" because they depend on the integrated effect of all model inputs, including the nuclear data.

Besides just reducing uncertainties and modifying the bias, DA can be used in validation studies of *application* systems. An application system is under investigation (*i.e.* being modeled) and has no associated experimental data. Without an E, Eq. (1.1) cannot be used, *i.e.* there is no direct way to validate the model to know how trustworthy its predictions are. Without trust in model predictions, it then becomes difficult to project economic and safety analyses, and subsequently to make confident engineering decisions.

Ideally, *mockup experiments* are used to validate an application. These experiments are designed to be similar to the application but scaled down and modified to be technically feasible to produce. In the mockup approach, first b_c of the mockup is calculated for a given neutronics model and then it is reinterpreted and translated to the application [13, 14, 15, 16]. The mockup approach has limitations in practice. For example, in the very early stages of design, there may be no funding available to develop a mockup experiment, often a complicated and expensive task. Or, there may be no facilities or expertise to conduct mockup experiments. In these cases of insufficient experimental evidence, how can reactor physicists reliably estimate the bias of the simulations of their designs? DA of course!

DA can be used with benchmarks that are "similar enough" to the application. These benchmarks were not necessarily designed to replicate the application's characteristics, but behave similarly to input nuclear data thanks to their physical similarities. This is analogous to using the historical record of hurricanes to evaluate the potential bias of the current hurricane. DA then leads to increased confidence in model predictions of an application despite being unable to explicitly validate said model. This idea is often called *bias correction* in the literature. Such analyses were traditionally done in neutronics to design fast reactors [17, 18, 19, 20, 21, 22]. At that time, and still to some extent today, the nuclear data related to fast reactors were poorly known. The bias correction feature of DA was used for the design of the fast reactors PHENIX and SUPERPHENIX in France [9]. They predicted the critical mass of SUPERPHENIX within ~300 pcm, despite the large uncertainties arising from the nuclear data and model inaccuracies.

In recent years, research has focused on the adjusted nuclear data created by DA. They can be used by nuclear data evaluators to target where and how nuclear data can be improved. This is possible because DA changes the mean value and uncertainties of nuclear data. This is the main advantage of DA over SA: SA only identifies which nuclear data drive Δ_C, while DA details how the nuclear data affect both b_C and Δ_C.

After applying DA, individual adjustments can be examined step-by-step, noting which are larger than others. The most consistent nuclear data tend to have marginal adjustments, while the least consistent undergo larger adjustments and, therefore require further study. At $400,000 an experiment and requiring years of work, any tool that helps the re-evaluation process proceed more quickly and efficiently should be employed. DA can be one of these tools by highlighting the "problem" nuclear data. DA can also be used to efficiently design experiments to validate nuclear data [23]. Importantly it should be stated that DA is not used to create new nuclear data, just to more intelligently understand the current nuclear data. The adjustments can also be used to create cross correlations between nuclear data and between nuclides which are not traditionally available [24, 25, 26, 27].

The OECD/NEA's Working Party on International Nuclear Data Evaluation Co-operation established numerous subgroups that focused on DA for nuclear data evaluation. The subgroups' central objectives were and are to provide a DA framework for adjusting nuclear data and to recommend adjustments to evaluators when they seek to improve nuclear data files. Subgroups 26 [10], 33 [28], 39, and 46 all focused on DA in neutronics problems. They also sought to establish guidelines to enlarge the experimental databases used in DA. Additionally, they defined criteria to extrapolate the results of an adjustment to different applications.

A general critique of adjusting nuclear data with integral experiments is that, by using a small set of integral data to fit potentially thousands of nuclear data, the physics behind the nuclear data evaluation are lost. However, if the nuclear data are probabilistic, is it wrong to change the probability distribution as long as the changes respect the prior? From a Bayesian view point, any value covered by the prior is the possible "true" value and should be considered as a possible adjustment. If these posteriors improve the performance of the nuclear data, then that does not violate what was originally known about the nuclear data. Another issue is that a few integral parameters are being fit to many thousands of nuclear data (given the multi-group format). This means that the adjusted nuclear data can really only be considered as "application specific." If they are applied to other integral data that are dissimilar to those used in the fitting, which can be quantified with a correlation coefficient, then it is very likely that a degradation in the bias of these new integral benchmarks occurs. In a sense, there is a "price" that is paid to improve the bias and reduce the uncertainties: generality is lost for the improvement of a select set of integral data.

1.3   Aim and Structure of Thesis

DA is primarily used in neutronics for three purposes:

1. Predicting the bias of critical systems in criticality safety [29].

2. Reducing the uncertainties of advanced reactor designs [13].

3. Searching for trends and areas of improvement in nuclear data [9].

These goals can all be accomplished with different mathematical formulations. Each formulation has certain advantages and disadvantages that might merit its use in specific scenarios. The start of this thesis in 2015 coincided with several advancements in the mathematical formulations of DA for use in neutronics. New methods based on the stochastic sampling (SS) of input parameters were beginning to be used. The stochastic methods work by randomly sampling the input nuclear data with the uncertainty information contained in the data's library. The SS approach is typically applied with the assumption that the nuclear data have multi-variate normal distributions. Alternatively, the stochastic methods could be used with Total Monte Carlo (TMC) [30]. TMC preserves the true distribution of the nuclear data by sampling the model parameters used to evaluate said nuclear data [31].

Two of these methods, MOCABA [32, 33, 34] and BMC [35], were the particular focus of this thesis. These new methods, and their performance relative to the traditional technique called Generalized Linear Least Squares (GLLS), became a central point of the research. GLLS uses first-order perturbation theory, *i.e.* it assumes that C is a linear function of nuclear data, given that only small changes to the nuclear data are made. Both stochastic methods have the desirable trait that they can be applied without assuming that first-order perturbation theory is valid. This is important because non-linear relationships between C and nuclear data can occur for certain integral parameters [36] and for burnup problems [37]. Additionally, GLLS requires sensitivity coefficients for which calculation routines can be difficult to implement in neutron transport codes. SS can be easily used in any neutron transport code and thereby reduce the development time needed to perform DA. BMC can also be used in TMC-like applications where nuclear data or integral parameters are non-Gaussian.

Concurrently to the thesis, international interest formulated around the idea of the consistency between the C and E values of integral benchmarks. In this work, the two are considered inconsistent if $b_c >> \Delta_{b_C}$, *i.e.* the E uncertainties and the uncertainties in C caused by nuclear data do not explain the observed bias. This represents a danger to applying DA because a central assumption in its formulation is that b_c and Δ_C are caused by input uncertainties. If somehow they are not, perhaps the E or Δ_E are not of high quality or input correlations are missing, DA might induce spurious and unreliable adjustments. How to quantify and account for these inconsistencies also became a topic of research.

The thesis was also conceived to use integral data from the Proteus research reactor in DA, *i.e.* use them in someway to validate critical safety cases, to reduce uncertainties in advance reactor designs, or to find trends in nuclear data. Proteus was a zero-power (maximum 1 kW and flux of 5×10^9 n/s-cm^2) nuclear research reactor that operated from 1968 to 2011 at the Paul Scherrer Institue (PSI). During its operation history, it was used for several experimental campaigns that investigated reactors like the gas-cooled fast reactor, the high-conversion light water reactor, the high temperature reactor, and the light water reactor (LWR).

The thesis project was established with four main goals:

1. Review, analyze, improve, and (if possible) propose new DA theory for use in neutronics,

2. Use DA in new ways in the field of neutronics,

3. Develop tools to apply DA with the codes used at PSI,

4. Apply DA methods to experimental data sets from the Proteus research reactor.

These four goals were integrated into the research of the thesis and into the structure of this document. A chapter-wise summary of the thesis is given below. It details the work and advancements made during the thesis and how these addressed the stated goals.

Chapter 2 – Overview of Data Assimilation Theory

The start of the thesis coincided with the development of stochastic DA methods in neutronics. How these methods were theoretically related to each other and to GLLS had not yet been presented. This chapter presents the first unified description of GLLS, MOCABA, and BMC from the same principles, *i.e.* Bayes' theory. Additionally, it presents in more detail the idea of inconsistent integral data and the mathematical techniques used to address them, especially the Marginal Likelihood Optimization technique. In this way, the first goal of the thesis was accomplished, to review and analyze DA theory in neutronics. The main scientific value of this section is the unification under a single umbrella of the DA theory.

Chapter 3 – Comparison of Data Assimilation Methods

With the DA theory reviewed and analyzed, it was necessary to analyze the methods' performance in case studies. This was important from a research aspect to test if all mathematical formulations perform equivalently given identical conditions. It provided practical experience with the DA methods, especially in how they behave as algorithms. Chp. 3 is devoted to studying the DA methods. To effect a case study required developing the tools necessary to do DA, which was another central goal of the thesis. First, a toy problem was used to study the DA methods in a simplified way. Then, the criticality benchmark JEZEBEL-Pu239 was used to test all the DA methods. The benchmark was simulated with Serpent2 to maximize model accuracy and with the ENDF/B-VII.1 nuclear data. This case study with JEZEBEL-Pu239 was the first to ever compare the different DA methods. The adjustments of nuclear data, nuclear data covariance matrices, and calculated integral parameters are all presented. Additionally, specific focus is given to the convergence behavior of the stochastic DA methods.

Chapter 4 – Data Assimilation of the LWR-Proteus Phase II Reactivity Experiments

The Proteus research campaigns are a rich and valuable source of information that can be used in DA. A specific experimental campaign of Proteus, LWR-Phase II, was chosen for DA in this thesis. In Chp. 4, DA is applied to this campaign using CASMO-5 and the UQ/SA tool SHARK-X. In this way, tools also needed to be developed, satisfying the thesis' goal. The study served to first independently confirm the comparison of Chp. 3 with a different experiment,

nuclear data library, and neutron transport code. Secondly, the study's scientific purpose was to focus on the inconsistency of the experiment's integral data. Finally, it gave insights into the bias behavior of CASMO-5 and ENDF/B-VII.1 nuclear data for this Proteus experiment. Because the integral data are reactivities, the insights are important for criticality safety and fuel cycle management, especially of spent fuel pools.

Chapter 5 – Data Assimilation of Post-Irradiation Examination Experiments

Chp. 5 presents a study that extended DA beyond its normal application range and took full advantage of the stochastic DA methods. Post-irradiation examination experiments were used as integral data to adjust the fission yields produced by a code called GEF [38]. The DA focused on the bias and uncertainty of the calculated concentrations of fission products in spent fuel. Accurate simulations of the inventory of fission products are important for criticality safety, decay heat, fuel cycle optimization, and nuclear waste management analysis. The fission products in this study had biases of up to 50% and, therefore, proved to be interesting targets for DA. Additionally, the GEF model to create fission yields is non-linear and produced non-Gaussian integral parameters, which proved to be an interesting behavior to test the BMC and MOCABA methods. Furthermore, the post-irradiation examination data have a large degree of inconsistency making them an interesting application of the Marginal Likelihood Optimization technique.

This chapter presents the adjustments of GEF's model parameters, of the fission yields and covariances between fission yields, and of the calculated fission product concentrations. The adjustments are compared between BMC and MOCABA, and between applying and not applying Marginal Likelihood Optimization. This study is, to our knowledge, the first to use stochastic DA with post-irradiation examination data and the first to perform DA of integral data for fission yields. This chapter addresses the thesis goals: it uses Proteus data, it explores DA theories in new ways, and it builds tools for PSI/EPFL modeling schemes.

Chapter 6 – eXtended Generalized Linear Least Squares

A stated goal of the thesis was to propose new theories. An opportunity for theoretical advancements arose through the coincidental development of sensitivity features in Monte Carlo neutron transport codes. Such codes are part of the tool suite used at PSI and EPFL and, therefore, these new features were of very high interest. The sensitivity coefficients that are calculated by these codes, and subsequently used in GLLS, have their own uncertainties due to the nature of Monte Carlo neutron transport. These uncertainties had never been accounted for or extensively studied in the GLLS theory. In collaboration with Manuele Aufiero and Adrien Bidaud at the University of California Berkeley, a new DA theory called xGLLS was developed during this thesis. xGLLS is an extended form of the GLLS equations that takes into account the sensitivity uncertainties in the theory. Its principal is that if the sensitivities are highly uncertain, xGLLS should constrain the assimilation and create smaller adjustments of

the nuclear data and integral parameters.

Chp. 6 serves to both present and analyze xGLLS. xGLLS was tested using the sensitivity co-efficients produced by Serpent2. The integral data from an NEA benchmark were used for the assimilation. The study compared the effect that different levels of sensitivity uncertainty had on the adjustments, both with xGLLS and with the classic GLLS method that does not account for the uncertainties. A convergence criterion for optimizing sensitivity calculations with continuous-energy Monte Carlo neutron transport codes was also proposed and sup-ported with evidence. Because these simulations require so many computational resources, the convergence criterion can be extremely useful for future studies with continuous-energy Monte Carlo neutron transport codes, both for DA and for simpler uncertainty quantification studies.

2 Overview of Data Assimilation Theory

> Bayes's theorem is nominally a mathematical formula. But it is really much much more than that. It implies that we must think differently about our ideas – and how to test them.
>
> –N. SILVER, *The Signal and the Noise* [39]

To understand data assimilation first requires us to think in a probabilistic way. The traditional way to interpret probability is called the *frequentist approach*. For frequentists, the probability of some event is the relative frequency that it occurs. To find the probability of a coin landing heads up, it must be flipped a sufficient number of times while recording the frequency of the number of heads to tails. Unfortunately, calculating a relative frequency for very rare phenomena, like a nuclear core meltdown or the sun's supernova, is difficult. The frequentist approach is also problematic for making a prediction. If we want to find the probability that a hurricane will hit Miami, we would need a number of hurricanes with identical conditions and then we would need to count the frequency of them striking the city.

In such cases, it is useful to take the *Bayesian*, or subjective, approach to probability. For Bayesians, probability is a mental construct indicating a degree of belief that an event, or hypothesis, is true. When probability is interpreted in such a way, the sample space corresponds to a hypothesis, proposition, or prediction that can be either true or false. The probability associated with the hypothesis A, or $p(A)$, is the *a priori* quantification of how correct we believe A is. We can assign a probability to a model's prediction, or to the hypothesis that what the model predicts is correct. Input parameters can also have probabilities, which relate to our degree of belief that an input's true value lies within a specified interval. The probability that a hurricane hits Miami is then a mathematical description of how confident we are in that hypothesis (*i.e.* the hurricane model and its input parameters).

2.1 Bayes' Theory

The foundation of DA is *Bayesian inference, i.e.* something is inferred through the application of Bayes' theory. Bayesian inference updates a hypothesis as new evidence is acquired. The hypothesis can be the prediction of a model, whether it is the path of a hurricane or a reactor simulation with certain nuclear data. Both the model itself and the inputs are also hypotheses. The physics of the system are hypothesized to be represented by the model and the inputs are hypothesized to have the given values. In reality, neither the model nor the inputs are exactly known but rather approximated (hypothesized) with the available knowledge. The goal of Bayesian inference is to update the hypothesis by incorporating new evidence. From the updated hypothesis, new model predictions and inputs are obtained.

The original hypothesis is called the *prior*; it is what is hypothesized to be true "prior" to assimilating evidence. The prior represents our best knowledge about the model and its inputs. The second term in Bayesian inference is called the *likelihood* and it measures how likely the evidence would exist given our hypothesis. In other words, it measures the compatibility of the evidence with the prior. The likelihood is not a probability as it does not adhere to the rules of probabilities (*e.g.* belonging between 0 and 1). In nuclear applications, the prior is the nuclear data and neutron transport code. The likelihood is the compatibility of a parameter's value from an integral experiment with our initial hypothesis. The hypotheses are therefore the nuclear data, the neutron transport code, and the model of the integral experiment.

Bayes' formula can be written as Eq. (2.1). Here, we are interested in the value of a given parameter, θ, for which there is a probability density function (PDF). The PDF used to describe θ is the prior, $p(\theta)$. We also have a set of evidence, or data. This data is fixed no matter what the value of θ is. The likelihood is $\mathscr{L}(\text{data}|\theta)$: the likelihood of having this data given our hypothesis for θ. The denominator has no dependence on θ, *i.e.* it has been marginalized with respect to θ. It is the probability of obtaining the data given all possible values of θ. Bayes' formula gives the *posterior* or $p(\theta|\text{data})$. It is θ's updated PDF posterior to assimilating the experimental evidence.

$$p(\theta|\text{data}) = \frac{\mathscr{L}(\text{data}|\theta)\, p(\theta)}{p(\text{data})} \tag{2.1}$$

Bayes' theorem is often shown as Eq. (2.2) where the posterior is proportional to $\mathscr{L}(\text{data}|\theta)\, p(\theta)$, *i.e.* without the denominator $p(\text{data})$. With this proportionality, the calculation of $p(\text{data})$ is avoided, which is often a difficult integral. One reason it is possible to define Bayes' theorem with this proportionality is that $p(\text{data})$ is a marginal probability distribution with no dependency on θ, or, in other words, it is a constant. Additionally, it is possible to choose $p(\theta)$ and $\mathscr{L}(\text{data}|\theta)$ such that $p(\theta|\text{data})$ is proportional to their product.[1] When the prior's distribution

---

[1] This is the case for the GLLS and MOCABA methods presented in the following sections.

is chosen in such a way, it is called a *conjugate prior*.

$$p(\theta|\text{data}) \propto \mathcal{L}(\text{data}|\theta)\, p(\theta) \tag{2.2}$$

The *maximum likelihood estimate* method (MLE) is commonly used in statistics to incorporate experimental evidence in the estimate of a model's parameters. The likelihood function is defined, and then its maximum is found with respect to θ, as shown in Eq. (2.3).

$$\hat{\theta}_{\text{MLE}}(\text{data}) = \underset{\theta}{\arg\max}\left[\mathcal{L}(\text{data}\,|\,\theta)\right] \tag{2.3}$$

In contrast to MLE, with Bayesian statistics we have the prior distribution, $p(\theta)$. It allows us to treat θ as a random variable and to calculate the posterior. The posterior distribution of θ can then be estimated with the *maximum a posteriori* method (MAP), or Eq. (2.4). MAP estimates θ as the mode[2] of the posterior distribution of this random variable. The MAP and MLE estimates are very similar. The only difference between their equations is that the MAP estimate includes more information by taking into account the prior. In this way, MAP weights the likelihood with the prior. When a uniform distribution, *i.e.* a constant, is used as the prior, the MAP estimate coincides with the MLE estimate.

$$\begin{aligned} \hat{\theta}_{\text{MAP}}(\text{data}) &= \underset{\theta}{\arg\max}\left[p(\theta|\text{data})\right] \\ &= \underset{\theta}{\arg\max}\left[\mathcal{L}(\text{data}|\theta)\, p(\theta)\right] \end{aligned} \tag{2.4}$$

Performing a Bayesian update, or doing DA, then requires techniques to find the MAP estimate of $\hat{\theta}_{\text{MAP}}(\text{data})$. Sometimes, the modes of the posterior distribution can be analytically solved for in the case where conjugate priors are used. It is also possible to do the maximization with numerical optimization or with the Monte Carlo method. The various ways that MAP modes are estimated in neutronics problems are discussed in the next section.

2.2 Data Assimilation in Neutronics

DA for neutronics begins with Bayes' theorem in Eq. (2.5). The prior is the nuclear data, $\boldsymbol{\sigma}$, which has the PDF $p(\boldsymbol{\sigma})$. It is represented as a vector, $\boldsymbol{\sigma} = \{\sigma_i | i = 1, \cdots, N_\sigma\}$, where N_σ is the number of nuclear data. The evidence used to update the prior are benchmark integral parameters, $\mathbf{E}$, which are represented as the vector, $\mathbf{E} = \{E_i | i = 1, \cdots, N_E\}$, where N_E is the number of integral parameters. The prior and the data together lead to the likelihood function,

---

[2]For a continuous PDF, it is common to refer to its local maxima as *modes*. If there is only one maximum, the PDF is unimodal, which is the case when assuming Gaussian distributions.

$\mathscr{L}(\mathbf{E}|\boldsymbol{\sigma},\text{model})$. It conceptually describes the likelihood of obtaining $\mathbf{E}$ given $\boldsymbol{\sigma}$ and the neutron transport code (the model). Finally, the posterior is the PDF $p(\boldsymbol{\sigma}'|\mathbf{E},\text{model})$.

$$p(\boldsymbol{\sigma}'|\mathbf{E},\text{model}) \propto \mathscr{L}(\mathbf{E}|\boldsymbol{\sigma},\text{model})\,p(\boldsymbol{\sigma},\text{model}) \tag{2.5}$$

The GLLS, MOCABA, and BMC DA methods all apply MAP estimation to find the posterior parameters, *i.e.* they maximize Eq. (2.5). However, how the MAP modes are estimated varies between each method because of the approximations they employ and the tools they use. MAP is done instead of MLE in order to take into account the prior information about $\boldsymbol{\sigma}$. This prior information is the whole nuclear data evaluation process (differential data, physics models). If MLE was used instead, it would simply maximize the likelihood with an arbitrary $\boldsymbol{\sigma}$, giving no weight to the prior and our confidence in the nuclear data evaluation process.

From this point onward, GLLS and MOCABA will be treated separately from BMC because of a key assumption that these two methods make. BMC will be treated later in Section 2.2.3. GLLS and MOCABA assume that the prior and likelihood functions are multivariate normal PDFs. The assumption is made, in part, to make the mathematics of Bayes' theorem easier to handle. It is also statistically well founded as it is based on the principle of *maximum entropy* [40]. According to this principle, a chosen PDF would not create any spurious information or hide any assumptions if it maximized the information entropy. Usually only two moments of the PDF are known, which are typically the mean and the variance. In neutronics problems this is often the case for the experimental integral data and the nuclear data.[3] When this happens, the most objective PDF following the maximum entropy principle is a Gaussian distribution.

The nuclear data are assumed to follow the PDF shown in Eq. (2.6). $p(\boldsymbol{\sigma})$ has mean values given by the vector $\boldsymbol{\sigma}_0$ and an uncertainty distribution described by the covariance matrix $\mathbf{M}_\sigma$, whose size is $N_\sigma \times N_\sigma$. The matrix $\mathbf{M}_\sigma$ has diagonal terms that are variances of each nuclear datum and off-diagonal terms that are covariances between nuclear data.

$$p(\boldsymbol{\sigma}|\boldsymbol{\sigma}_0,\mathbf{M}_\sigma) = (2\pi)^{-N_\sigma/2}\det(\mathbf{M}_\sigma)^{-1/2}\cdot\exp\left[-\frac{1}{2}(\boldsymbol{\sigma}-\boldsymbol{\sigma}_0)^T\mathbf{M}_\sigma^{-1}(\boldsymbol{\sigma}-\boldsymbol{\sigma}_0)\right] \tag{2.6}$$

$\mathscr{L}(\mathbf{E}|\boldsymbol{\sigma},\text{model})$ is also assumed to have a multivariate normal distribution, as seen in Eq. (2.7). Here, the term $\mathbf{C}(\boldsymbol{\sigma}_0)$ is the vector of integral parameters calculated using the neutronics model and $\boldsymbol{\sigma}_0$. Implicitly, $\mathbf{C}(\boldsymbol{\sigma}_0)$ and $\mathbf{E}$ are assumed to follow multivariate normal distributions, with covariance matrices $\mathbf{M_M}$ and $\mathbf{M_E}$, respectively, which are added together in this notation to form $\mathbf{M_{EM}}$ ($\mathbf{M_{EM}} = \mathbf{M_E} + \mathbf{M_M}$) in Eq. (2.7). $\mathbf{M_M}$ contains the uncertainty in $\mathbf{C}(\boldsymbol{\sigma}_0)$ created by the neutronics model. This may include the stochastic uncertainty of Monte Carlo neutron transport, or the estimated uncertainty caused by approximations and discretization in deter-

---

[3]Using TMC or sampling GEF model parameters to create samples of the nuclear data would be an exception. There, the full distribution would be preserved and there would be no need to assume normality.

ministic neutron transport. How the covariance matrices are chosen and created are essential to the quality of the DA, and will be discussed in depth later in this thesis.

$$\mathscr{L}(\mathbf{E}|\boldsymbol{\sigma}, \text{model}) = (2\pi)^{-N_E/2} \det(\mathbf{M_{EM}})^{-1/2} \cdot \exp\left[-\frac{1}{2}\big(\mathbf{E} - \mathbf{C}(\boldsymbol{\sigma}_0)\big)^T \mathbf{M_{EM}}^{-1}\big(\mathbf{E} - \mathbf{C}(\boldsymbol{\sigma}_0)\big) \right] \quad (2.7)$$

Using these prior and likelihood normal PDFs, the posterior distribution can be written as Eq. (2.8). Here, Eqs. (2.6) and (2.7) are multiplied together and the constant terms are absorbed into the proportionality. Because the prior and likelihood are both normal, the posterior will also be normal, meaning it will also be an exponential function. It is then possible to reduce Eq. (2.8) further by taking the negative logarithm of each side, giving Eq. (2.9). In this equation, the posterior distribution is expanded and its mean and covariance matrix, $\boldsymbol{\sigma}'$ and $\mathbf{M}'_\sigma$ respectively, have the same dimensions as the prior mean and covariance matrix.

$$p(\boldsymbol{\sigma}'|\mathbf{E}, \text{model}) \propto \exp\left[-\frac{1}{2}\big(\mathbf{E} - \mathbf{C}(\boldsymbol{\sigma}_0)\big)^T \mathbf{M_{EM}}^{-1}\big(\mathbf{E} - \mathbf{C}(\boldsymbol{\sigma}_0)\big) \right] \cdot \exp\left[-\frac{1}{2}(\boldsymbol{\sigma} - \boldsymbol{\sigma}_0)^T \mathbf{M}_\sigma^{-1}(\boldsymbol{\sigma} - \boldsymbol{\sigma}_0) \right]$$
$$(2.8)$$

$$(\boldsymbol{\sigma}' - \boldsymbol{\sigma}_0')^T \mathbf{M}_\sigma'^{-1}(\boldsymbol{\sigma}' - \boldsymbol{\sigma}_0') \propto \big(\mathbf{E} - \mathbf{C}(\boldsymbol{\sigma}_0)\big)^T \mathbf{M_{EM}}^{-1}\big(\mathbf{E} - \mathbf{C}(\boldsymbol{\sigma}_0)\big) + (\boldsymbol{\sigma} - \boldsymbol{\sigma}_0)^T \mathbf{M}_\sigma^{-1}(\boldsymbol{\sigma} - \boldsymbol{\sigma}_0) \quad (2.9)$$

To find the moments of the posterior distribution, one must maximize $p(\boldsymbol{\sigma}'|\mathbf{E}, \text{model})$, which is equivalent to minimizing Eq. (2.9) [17, 18]. An extensive derivation using Lagrangian multipliers can be found in Appendix A.1 for GLLS, but can equally be used to derive the MOCABA equations. The general form of the equations for the posteriors is given below. The posterior mean of the calculated values, $\mathbf{C}'$, is shown to be Eq. (2.10) and its covariance matrix, $\mathbf{M}'_\mathbf{C}$, to be Eq. (2.11). $\boldsymbol{\sigma}'$ and $\mathbf{M}'_\sigma$ are derived as Eq. (2.12) and Eq. (2.13), respectively. Here, $\mathbf{M}_{\sigma,\mathbf{C}}$ is the covariance matrix of $\boldsymbol{\sigma}$ and $\mathbf{C}$ whose dimensions are $N_\sigma \times N_E$.

$$\mathbf{C}' = \mathbf{C}(\boldsymbol{\sigma}_0) + \mathbf{M_C}\big[\mathbf{M_C} + \mathbf{M_{EM}}\big]^{-1}\big[\mathbf{E} - \mathbf{C}(\boldsymbol{\sigma}_0)\big] \qquad (2.10)$$

$$\mathbf{M}'_\mathbf{C} = \mathbf{M_C} - \mathbf{M_C}\big[\mathbf{M_C} + \mathbf{M_{EM}}\big]^{-1}\mathbf{M_C} \qquad (2.11)$$

$$\boldsymbol{\sigma}' = \boldsymbol{\sigma}_0 + \mathbf{M}_{\sigma,\mathbf{C}}\big[\mathbf{M_C} + \mathbf{M_{EM}}\big]^{-1}\big[\mathbf{E} - \mathbf{C}(\boldsymbol{\sigma}_0)\big] \qquad (2.12)$$

$$\mathbf{M}'_\sigma = \mathbf{M}_\sigma - \mathbf{M}_{\sigma,\mathbf{C}}\big[\mathbf{M_C} + \mathbf{M_{EM}}\big]^{-1}\mathbf{M}_{\sigma,\mathbf{C}}{}^T \qquad (2.13)$$

A few interesting details can be found in Eqs. (2.10)–(2.13). First, the posterior covariance matrices $\mathbf{M}'_\mathbf{C}$ and $\mathbf{M}'_\sigma$ have no dependence on the mean values of $\boldsymbol{\sigma}$, $\mathbf{E}$, or $\mathbf{C}$. The uncertainties are, therefore, reduced solely through the incorporation of $\mathbf{M_E}$ in the case of $\mathbf{M}'_\mathbf{C}$ and through the assimilation of $\mathbf{M_E}$ and $\mathbf{M}_{\sigma,\mathbf{C}}$ in the case of $\mathbf{M}'_\sigma$. Secondly, the magnitude of the $\boldsymbol{\sigma}'$ adjustment and the reduction in uncertainty in $\mathbf{M}'_\sigma$ is proportional to the magnitude of the terms in $\mathbf{M}_{\sigma,\mathbf{C}}$. In other words, for there to be a significant adjustment of $\boldsymbol{\sigma}$, there must be a significant degree of correlation between $\mathbf{C}$ and $\boldsymbol{\sigma}$, *i.e.* $\mathbf{C}$ must be sensitive to $\boldsymbol{\sigma}$. Finally, the size of the adjustment of $\mathbf{C}$ and $\boldsymbol{\sigma}$ using Eqs. (2.10) and (2.12) is proportional to the difference between $\mathbf{C}$ and $\mathbf{E}$. If $\mathbf{C} - \mathbf{E} = \mathbf{0}$, the data agree perfectly and there is no room to adjust.

Importantly, through the assimilation of $\mathbf{E}$ into $\boldsymbol{\sigma}'$, these two data sets become correlated. The covariances between $\mathbf{E}$ and $\boldsymbol{\sigma}'$ are given by the matrix $\mathbf{M}'_{\sigma,\mathbf{E}}$ in Eq. (2.14). These correlations are often ignored in the DA literature, but they can be important in some applications. For instance, if the adjustments are done in an iterative manner [41], after the first iteration $\boldsymbol{\sigma}'$ is correlated to $\mathbf{E}$ and this can be taken into account in the equations.[4]

$$\mathbf{M}'_{\sigma,\mathbf{E}} = -\mathbf{M}_{\sigma,\mathbf{C}}\big[\mathbf{M_C} + \mathbf{M_{EM}}\big]^{-1}\mathbf{M_{EM}} \tag{2.14}$$

In theory, $\boldsymbol{\sigma}$ and $\mathbf{E}$ can also be correlated in the prior, before DA. This may arise if the integral benchmarks were used in an *ad hoc* fashion to tune the performance of an evaluated nuclear data library. Correlations may arise inversely, where the nuclear data were used in the experimental process, maybe as a normalization constant. In this case, these correlations can also be taken into account in the adjustment equations, as outlined in Appendix A.1. In practice, these correlations either do not exist or are unknown and extremely hard to account for. Because of this, they are most often ignored and the DA equations are usually used as presented in this section.

$\mathbf{M_C}$ and $\mathbf{M}_{\sigma,\mathbf{C}}$ are the only parameters in Eqs. (2.10)–(2.13) that need to be calculated, all others are inputs. The primary difference between GLLS and MOCABA is the assumptions and techniques that each make to approximate $\mathbf{M_C}$ and $\mathbf{M}_{\sigma,\mathbf{C}}$. GLLS, summarized in Section 2.2.1, assumes first-order perturbation theory and uses sensitivity coefficients to estimate $\mathbf{M_C}$ and $\mathbf{M}_{\sigma,\mathbf{C}}$. MOCABA uses the Monte Carlo method, as described in Section 2.2.2.

2.2.1   Generalized Linear Least Squares

GLLS is widely used by many institutions (*e.g.* PSI, JAEA, ORNL, INL [9]) for DA. In some applications, it is called BLUE or Best Linear Unbiased Estimator. While GLLS has been derived here with Bayes' theory, it is also possible to derive it from a linear least-squares regression analysis. In GLLS, a generalized linear model approximates $\mathbf{C}(\boldsymbol{\sigma})$ with Eq. (2.15), which is a first-order Taylor series expansion of $\mathbf{C}(\boldsymbol{\sigma})$. The sensitivity coefficients, $\mathbf{S}$, are the first

---

[4]These correlations are not included in the study summarized in Ref. [41].

derivatives of $\mathbf{C}(\boldsymbol{\sigma})$, $\frac{\partial \mathbf{C}}{\partial \boldsymbol{\sigma}}$, evaluated at $\boldsymbol{\sigma}_0$ or the nominal nuclear data means. The term $\mathbf{H}$ is the Hessian matrix of second-order derivatives, or $\frac{\partial^2 \mathbf{C}}{\partial \boldsymbol{\sigma}^2}$. $\mathbf{S}$ is a matrix of dimensions $N_E \times N_\sigma$. The sensitivity coefficient for integral parameter $C^{(i)}$ to nuclear datum $\sigma^{(j)}$ is given in Eq. (2.16).

$$
\begin{aligned}
\mathbf{C}(\boldsymbol{\sigma}) &= \mathbf{C}(\boldsymbol{\sigma}_0) + \frac{\partial \mathbf{C}}{\partial \boldsymbol{\sigma}}\bigg|_{\boldsymbol{\sigma}=\boldsymbol{\sigma}_0} (\boldsymbol{\sigma} - \boldsymbol{\sigma}_0) + \frac{1}{2}(\boldsymbol{\sigma} - \boldsymbol{\sigma}_0)^T \mathbf{H}(\boldsymbol{\sigma} - \boldsymbol{\sigma}_0) + \cdots \\
&\approx \mathbf{C}(\boldsymbol{\sigma}_0) + \mathbf{S}(\boldsymbol{\sigma} - \boldsymbol{\sigma}_0)
\end{aligned}
\tag{2.15}
$$

$$
\mathbf{S}^{(i,j)} = \frac{\partial C^{(i)}}{\partial \sigma^{(j)}}\bigg|_{\sigma^{(j)}=\sigma_0^{(j)}}
\tag{2.16}
$$

The posterior moments are derived using the prior and likelihood of Eqs. (2.6) and (2.7) and the linear approximation of Eq. (2.15) [17, 18]. The posterior nuclear data's mean values, $\boldsymbol{\sigma}'$, and their covariance matrix $\mathbf{M}'_\sigma$ are given in Eqs. (2.17) and (2.18), respectively.

$$
\boldsymbol{\sigma}' = \boldsymbol{\sigma}_0 + \mathbf{M}_\sigma \mathbf{S}^T \left[\mathbf{S} \mathbf{M}_\sigma \mathbf{S}^T + \mathbf{M_{EM}} \right]^{-1} \left[\mathbf{E} - \mathbf{C}(\boldsymbol{\sigma_0}) \right]
\tag{2.17}
$$

$$
\mathbf{M}'_\sigma = \mathbf{M}_\sigma - \mathbf{M}_\sigma \mathbf{S}^T \left[\mathbf{S} \mathbf{M}_\sigma \mathbf{S}^T + \mathbf{M_{EM}} \right]^{-1} \mathbf{S} \mathbf{M}_\sigma
\tag{2.18}
$$

The posterior calculated values, $\mathbf{C}'$, can be simplified from Eq. (2.10) to Eq. (2.19) with the use of $\mathbf{S}$. The posterior covariance matrix of $\mathbf{C}$, $\mathbf{M}'_\mathbf{C}$, can be simplified from Eq. (2.11) to Eq. (2.20).

$$
\mathbf{C}'(\boldsymbol{\sigma}') = \mathbf{C}(\boldsymbol{\sigma}_0) + \mathbf{S}(\boldsymbol{\sigma}' - \boldsymbol{\sigma}_0)
\tag{2.19}
$$

$$
\mathbf{M}'_\mathbf{C} = \mathbf{S} \mathbf{M}'_\sigma \mathbf{S}^T
\tag{2.20}
$$

The risk of using the linear approximation can be illustrated with Fig. 2.1. Where the derivative is evaluated around σ_0, the linearity assumption is a good approximation of $C(\sigma)$. Farther from σ_0 the assumption is less accurate and will result in larger and larger errors. When using GLLS in neutronics, the linear approximation is accurate for the traditional integral parameters like k_{eff}, reaction rate ratios, or reactivity coefficients. It can become inaccurate when there is a large uncertainty associated with σ_0 [42]. When this uncertainty is large, a large adjustment can occur far from σ_0, and therefore into the non-linear regions of $C(\sigma)$. Another problem can be that $C(\sigma)$ is just strongly non-linear and no first-order approximation could accurately capture the important higher-order terms.
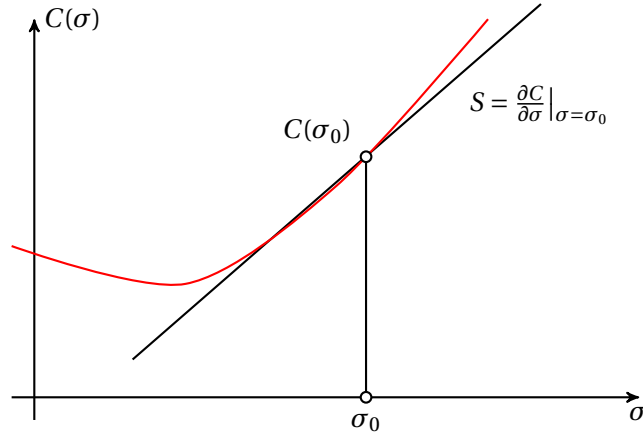
Figure 2.1 – Linear approximation of the relationship between a calculated integral parameter C and a nuclear datum σ used in GLLS.

2.2.2 Monte Carlo Bayesian Analysis (MOCABA)

MOCABA is an alternative to GLLS that avoids a linearity assumption, but at the same time keeps the Gaussian assumption. GLLS employs this assumption to approximate the matrices $\mathbf{M}_{\sigma,\mathbf{C}}$ and $\mathbf{M}_{\mathbf{C}}$. These approximations make the posterior distributions analytically calculable (*i.e.* with sensitivity coefficients) using the terms $\mathbf{M}_\sigma \mathbf{S}^T$ and $\mathbf{S}\mathbf{M}_\sigma \mathbf{S}^T$, which are $\mathbf{M}_{\sigma,\mathbf{C}}$ and $\mathbf{M}_{\mathbf{C}}$, respectively. Refs. [33, 43] show that the GLLS equations are first-order perturbation theory estimates of the MOCABA equations. Appendix A.2 provides a derivation of the MOCABA equations. MOCABA is similar to the UMC-G method used in nuclear data evaluation [44], but does not used a Markov Chain Monte Carlo algorithm.

To calculate $\mathbf{M}_{\mathbf{C}}$ and $\mathbf{M}_{\sigma,\mathbf{C}}$, MOCABA uses the Monte Carlo method to randomly sample nuclear data with the uncertainty information found in the nuclear-data covariance files. For every randomly sampled nuclear data file, $\boldsymbol{\sigma}_i$, a neutron transport simulation is done with it to create a calculated value for the integral parameters $\mathbf{C}(\boldsymbol{\sigma}_i)$, or $\mathbf{C}_i$. When N samples of $\boldsymbol{\sigma}$ are performed, the integral parameters are simulated N times to create a population of calculated values: $\mathbf{C}_1, \mathbf{C}_2, \dots, \mathbf{C}_N$. This population set is then used to estimate $\mathbf{M}_{\mathbf{C}}$ and $\mathbf{M}_{\sigma,\mathbf{C}}$ with Eqs. (2.21) and (2.22), where $\bar{\mathbf{C}}$ and $\bar{\boldsymbol{\sigma}}$ are the population means of $\mathbf{C}$ and $\boldsymbol{\sigma}$. Finally, $\hat{\mathbf{M}}_{\mathbf{C}}$ and $\hat{\mathbf{M}}_{\sigma,\mathbf{C}}$ are used in Eqs. (2.10)–(2.13) to calculate the posteriors.

$$\hat{\mathbf{M}}_{\mathbf{C}} = \frac{1}{N-1} \sum_{i=1}^{N} (\mathbf{C}_i - \bar{\mathbf{C}})(\mathbf{C}_i - \bar{\mathbf{C}})^T \tag{2.21}$$

$$\hat{\mathbf{M}}_{\sigma,\mathbf{C}} = \frac{1}{N-1} \sum_{i=1}^{N} (\boldsymbol{\sigma}_i - \bar{\boldsymbol{\sigma}})(\mathbf{C}_i - \bar{\mathbf{C}})^T \tag{2.22}$$

MOCABA, as described, assumes that $\mathbf{C}$, $\mathbf{E}$, and $\boldsymbol{\sigma}$ obey normal distributions. Ref. [33] details

how it can be modified to account for non-normal PDFs. It would require mapping **C** onto an approximately normally distributed vector by means of an invertible variable transformation. Its PDF could then be chosen from a more general class of PDFs to better model the behavior. The MOCABA equations are then applied to the transformed **C**. The true $\mathbf{C}'$ is then obtained by applying the inverse transformation to the transformed $\mathbf{C}'$.

A clear drawback of MOCABA is that N is limited to finite sizes in Eqs. (2.21) and (2.22). Because of this, the accuracy of the calculated posteriors will be limited by the statistical accuracy of $\hat{\mathbf{M}}_{\mathbf{C}}$ and $\hat{\mathbf{M}}_{\sigma,\mathbf{C}}$. When applying MOCABA, the posteriors need to be carefully monitored for statistical convergence.

2.2.3 Bayesian Monte Carlo (BMC)

BMC stochastically searches for the MAP moments to calculate $\mathbf{C}'$, $\mathbf{M}_{\mathbf{C}}'$, σ', and $\mathbf{M}_{\sigma}'$.[5] It makes no assumptions about the prior distribution [35, 45]; the nuclear data can be sampled from any PDF. This feature is the primary advantage of BMC in comparison to MOCABA and GLLS. When using BMC, a random sample σ_i is first drawn from $p(\sigma)$. It is then used in the neutron transport code to get a random sample of the calculated integral data, $\mathbf{C}_i$. Each $\mathbf{C}_i$ is compared to **E** to see how σ_i changed the agreement between **C** and **E**. A cost function metrizes $\mathbf{C}_i$ and **E** agreement and is defined as Eq. (2.23). Here, χ_i^2 is the squared distance between $\mathbf{C}_i$ and **E**, normalized by the covariance matrix $\mathbf{M}_{\mathbf{EM}}$.

$$\chi_i^2 = \left(\mathbf{E} - \mathbf{C}_i\right)^T \mathbf{M}_{\mathbf{EM}}^{-1}\left(\mathbf{E} - \mathbf{C}_i\right) \tag{2.23}$$

Each χ_i^2 is used to calculate a weight, w_i, for that nuclear data sample as seen in Eq. (2.24). Smaller χ_i^2 values indicate better agreement between **E** and $\mathbf{C}_i$ and, consequently, create larger weights. Nuclear data samples with higher w_i contribute more to adjustments, whereas those with smaller w_i contribute less. In cases where **C**, **E**, and σ are normally distributed, this definition of w_i is equivalent to the likelihood function of Eq. (2.7).

$$w_i = \exp\left(-\frac{\chi_i^2}{2}\right) \tag{2.24}$$

The weights are then used to calculate weighted averages that are the posterior means and covariances for **C** and σ: Eqs. (2.25) and (2.26) for $\mathbf{C}'$ and $\mathbf{M}_{\mathbf{C}}'$ and Eqs. (2.27) and (2.28) for σ' and $\mathbf{M}_{\sigma}'$. It is in this way that BMC searches for the MAP distribution: it explores the prior to

---

[5]BMC has been used for differential data in nuclear data evaluations as well and is often known as UMC-B (Unified Monte Carlo Breakfast) [44]

find which combination of $\boldsymbol{\sigma}_i$ maximize the agreement between $\mathbf{C}$ and $\mathbf{E}$.

$$\mathbf{C}' = \frac{\sum_{i=1}^N w_i \mathbf{C}_i}{\sum_{i=1}^N w_i} \tag{2.25}$$

$$\mathbf{M}'_{\mathbf{C}} = \frac{\sum_{i=1}^N w_i (\mathbf{C}_i - \bar{\mathbf{C}})(\mathbf{C}_i - \bar{\mathbf{C}})^T}{\sum_{i=1}^N w_i} \tag{2.26}$$

$$\boldsymbol{\sigma}' = \frac{\sum_{i=1}^N w_i \boldsymbol{\sigma}_i}{\sum_{i=1}^N w_i} \tag{2.27}$$

$$\mathbf{M}'_{\sigma} = \frac{\sum_{i=1}^N w_i (\boldsymbol{\sigma}_i - \bar{\boldsymbol{\sigma}})(\boldsymbol{\sigma}_i - \bar{\boldsymbol{\sigma}})^T}{\sum_{i=1}^N w_i} \tag{2.28}$$

Under certain circumstances, weight degeneracy can occur when applying BMC. The majority of the weights are zero or near zero-valued and only a few samples contribute to the posterior. This can be particularly prevalent when the χ^2 values are large, which may happen for large disagreement between $\mathbf{C}$ and $\mathbf{E}$, large covariances in $\mathbf{M_C}$ or $\mathbf{M_E}$, or when there are many integral parameters (degrees of freedom). To counter this behavior, another approach called Backward-Forward Monte Carlo (BFMC) [46] has been proposed in the literature. BFMC calculates the weights with Eq. (2.29), where the χ^2 of a random sample is normalized with the minimum χ^2 of the sample set. BFMC was shown in one case study to improve the weight distribution and the convergence rate of the posteriors [45].

$$w_i = \exp\left(-\frac{\chi_i^2}{\chi_{\min}^2}\right) \tag{2.29}$$

The weight proposed in Ref. [46] actually has the weight defined as $w_i = \exp\left(-(\chi_i^2/\chi_{\min}^2)^2\right)$. However the most common weight correction that we have encountered in the literature is the one that is presented here, and it is for that reason that it is presented and is the subject of the thesis. This weight correction was labeled BFMC in the literature, despite the contradiction with the definition and proposed name in Ref. [46]. For consistency with the international community, the definition of Eq. (2.29) was retained along with name BFMC.

2.2.4 Summary

There are four principal DA methods in neutronics: GLLS, MOCABA, BMC, and BFMC. GLLS uses first-order perturbation theory to compute the posterior moments. This requires as-

suming that all random variables are normally distributed. It also requires evaluating the sensitivity coefficients of the calculated integral parameters to the nuclear data. MOCABA, BMC, and BFMC all use stochastic sampling of the nuclear data to estimate the MAP modes. MOCABA also assumes that all random variables have normal distributions. BMC and BFMC do not assume anything about the distributions of the random variables. Therefore, MOCABA is not limited to linear applications like GLLS but may give biased MAP modes for non-normal applications. BMC and BFMC are more flexible in this sense. They could be used with nuclear data whose PDFs are non-normal, like those that can be found in TENDL [47] or that exist for fission yields created by GEF [38].
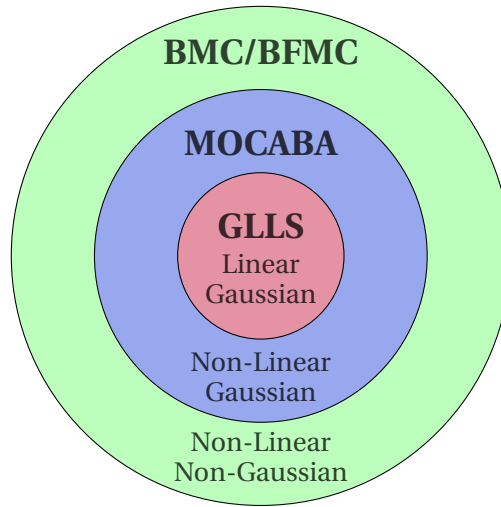
Figure 2.2 – Areas of applicability for BMC/BFMC, MOCABA, and GLLS.

It should be noted that the methods presented here are often known by different names in the DA literature. DA is often applied in a time-dependent or sequential manner, like the tracking of a hurricane. The neutronics problems focused on in this thesis have DA applied to them in a time-independent, or stationary manner.[6] In time-dependent applications, the DA methods are often referred to as Kalman Filters. GLLS would be called an extended Kalman Filter [48], MOCABA an Ensemble Kalman Filter [2], and BMC a Particle Filter [49]. While the history of DA in the field of neutronics is not totally clear, it is certainly possible that the methods discussed herein are adapted from or inspired by the Kalman Filter literature.

2.3 Consistency Checks

When DA is applied to adjust nuclear data, it is important to consider the consistency between the prior (*i.e.* σ and the neutronics model) and **E**. This is because, it is assumed that **C** and **E**

---

[6]In Chp. 5, DA is done for burnup simulations that have time dependence. From the point of view of DA, there is no time-dependence because there is only one experimental value being used over the whole irradiation history, *i.e.* the measured fission product concentration at end of life. It would be time-dependent if the concentrations were available at every stage of the burnup simulation.

would be equal if not for their uncertainties. In other words, $\boldsymbol{\sigma}$ is tacitly assumed to be correct, but just not sufficiently accurate for $\mathbf{C}(\boldsymbol{\sigma})$ to equal $\mathbf{E}$. When we assimilate $\mathbf{E}$ and $\mathbf{M_E}$ into $\boldsymbol{\sigma}$ and $\mathbf{M}_{\sigma}$, the adjusted nuclear data are expected to remain consistent with their prior nominal values and within the range of their prior uncertainties.

When $\mathbf{C}$ and $\mathbf{E}$ deviate significantly, the integral parameters are considered to be *inconsistent*. If we indiscriminately include all $\mathbf{E}$, even those that are inconsistent, the posterior nuclear data may be overfit, *i.e.* adjusted to an unreasonable or unphysical extent. Unphysical here means that the adjustments do not respect the underlying nuclear physics and differential experimental data that were used in the nuclear data evaluation process. Spurious adjustments may cause the assumption of linearity to be violated in the case of GLLS or maybe even create negative-valued nuclear data. Moreover, with inconsistent integral parameters DA may even fail to improve the posterior calculated integral parameters!

The integral data can be inconsistent simply if $\mathbf{E}$ is poorly known in terms of its means or in terms of the variances and covariances in $\mathbf{M_E}$. It is very common for covariance data to be unavailable in databases like ICSBEP [50] or IRPhE [51]. With very old and poorly characterized experiments, it also possible for variances to be over/under-estimated. DA can also be poor if there are significant biases in the neutronics model of the integral parameter. This may be due to approximations in the physics (multigroup energy structure, 2D representation, reflective boundary conditions) or limited/inaccurate modeling, which may occur when the system's geometry, composition, or state conditions over time (temperature, density, burnup) are poorly known. There may also be issues with $\mathbf{M}_{\sigma}$, usually due to too low uncertainties or missing covariances [24].

Finally, there is an important, but often over-looked danger in DA: the double counting of integral benchmarks [52]. Certain keystone benchmarks like JEZEBEL and FLATTOP have already been used to a certain extent in the construction of nuclear data libraries. Because of this, these experiments are correlated to the nuclear data libraries. This is the "first-counting" of the integral data. The "second-counting" is using the integral benchmarks again in DA. If the correlation between the integral benchmarks and the nuclear data library ($\mathbf{M}_{\sigma,\mathbf{E}}$) is not taken account, the possibility of making dangerous and unphysical adjustments increases. In this case, the χ^2 of the integral data set is likely to be too low, indicating that a degree of fitting has already occurred. This type of integral parameter is considered to be "over-consistent;" the agreement between $\mathbf{C}$ and $\mathbf{E}$ is over-consistent with what would be expected by statistical theory. In contrast, in the more classical case where there are large biases and low uncertainties, this integral datum is labeled as "under-consistent."

Foundational literature in the field of DA has treated model inaccuracies in different ways. For instance, the inaccuracy introduced by a deterministic code was previously quantified as an additional uncertainty that was determined through a parametric analysis of model parameters (energy group structure, angular discretization) and the use of expert judgment. Criteria were also defined to remove, or filter out, integral data that were inconsistent. For

instance, in Subgroup 33 of the NEA's WPEC, the Adjustment Margin (AM) criterion was proposed. In the TSURFER module of SCALE [53] and in other DA literature [40], χ^2-filtering metrics are proposed. The drawback of these approaches is primarily the loss of experimental data. An integral datum is binarily removed from the adjustment if a threshold is reached. In theory, all the experimental data are valuable for DA (and a significant amount of resources has been invested in them) but they just need to be weighted in the appropriate way. By removing integral data, we lose valuable resources.

Another approach is to treat inconsistent data in a more data-driven and statistically founded way. Here, integral data are weighted in a continuous manner by increasing or decreasing an extra uncertainty term. If an integral datum is under-inconsistent, the extra uncertainty is increased thereby signifying a decreased confidence in that datum. With larger uncertainty, the datum influences the adjustment to a lesser extent and thereby decreases any potential non-physically-based adjustments it may introduce to the nuclear data. Contrarily, for over-consistent integral data, a negative uncertainty term is added. One such way to estimate this extra uncertainty in neutronics is Marginal Likelihood Optimization (MLO) [54, 55, 56].

2.3.1 χ^2 Parameter

A measure that is often used in the literature to quantify the consistency of an integral data set is the χ^2 parameter. It can be calculated before and after the adjustment to evaluate the improvement between **C** and **E**, *i.e.* the improvement of $\boldsymbol{\sigma}$. On the most basic level, it is just the squared Mahalanobis distance, or the squared distance between two vectors, $(\mathbf{E} - \mathbf{C})$, normalized by the covariance matrices of the vectors, $\mathbf{M_C} + \mathbf{M_{EM}}$, as given by Eq. (2.30).

$$\chi^2 = \left(\mathbf{E} - \mathbf{C}\right)^T (\mathbf{M_C} + \mathbf{M_{EM}})^{-1} \left(\mathbf{E} - \mathbf{C}\right) \tag{2.30}$$

In probability and statistics, χ^2 is defined to have its own distribution. The χ^2 distribution with N degrees of freedom is given in Eq. (2.31), where $\Gamma(N/2)$ denotes the gamma function. The number of degrees of freedom is equal to the number of integral parameters, or N_E. As Pearon's χ^2 test, it measures the deviation of a true distribution from a hypothetical one, the likelihood that an observed difference between data sets arose by chance.

$$p(x < \chi^2 < x + dx) = \frac{1}{2^{N/2}\Gamma(N/2)} x^{N/2-1} \exp(-x/2) dx, \quad x > 0, \quad (n = 1, 2, \cdots) \tag{2.31}$$

The following asymptotic properties of the χ^2 distribution should be noted: χ^2 is normal with a mean N_E and a variance $2N_E$. If $\chi^2/N_E \approx 1$, the experimental data and prior are very likely to be free of errors and to be consistent with their assumptions. When $\chi^2/N_E >> 1$ or $\chi^2/N_E << 1$, there is very likely an inconsistency. To reject a hypothesis, χ^2 is calculated for a significance level α and for the number of degrees of freedom N_E. If χ^2 exceeds the critical

fractile value[7] $\chi^2_\alpha(N_E)$, then the hypothesis is rejected. A general criterion for evaluating an integral parameter data set is Eq. (2.32), with the value of α being subject to personal judgment.

$$\alpha < p_{N_E}(\chi^2) < 1 - \alpha \tag{2.32}$$

In Section 2.2 the possibility that $\mathbf{E}$ and $\boldsymbol{\sigma}$ are correlated was discussed. This would then create a correlation between $\mathbf{C}$ and $\mathbf{E}$. The most complete χ^2 metric would take this into account. To illustrate this, take a discrepancy vector $\mathbf{d}$ as shown in Eq. (2.33).

$$\mathbf{d} = \mathbf{C}(\boldsymbol{\sigma}) - \mathbf{E} \tag{2.33}$$

The covariance matrix of $\mathbf{d}$ would then be defined as Eq. (2.34).[8]

$$\begin{aligned} \mathbf{M_d} &= \left\langle \Delta(\mathbf{C} - \mathbf{E}) - \Delta(\mathbf{C} - \mathbf{E})^T \right\rangle \\ &= \left\langle \Delta\mathbf{C}\Delta\mathbf{C}^T \right\rangle + \left\langle \Delta\mathbf{E}\Delta\mathbf{E}^T \right\rangle - \left\langle \Delta\mathbf{C}\Delta\mathbf{E}^T \right\rangle - \left\langle \Delta\mathbf{E}\Delta\mathbf{C}^T \right\rangle \\ &= \mathbf{M_C} + \mathbf{M_E} - \mathbf{M_{C,E}} - \mathbf{M_{E,C}} \end{aligned} \tag{2.34}$$

The χ^2 could then be given by Eq. (2.35). The difficulty here is to calculate the matrix $\mathbf{M_{C,E}}$. As $\mathbf{C}$ is a function of $\boldsymbol{\sigma}$, a relationship exists between $\mathbf{M}_{\sigma,\mathbf{E}}$ and $\mathbf{M_{C,E}}$. It is shown through linear perturbation theory in Appendix A.1 that this relationship is $\mathbf{M_{C,E}} = \mathbf{SM}_{\sigma,\mathbf{E}}$. Again, the difficulty here is knowing $\mathbf{M}_{\sigma,\mathbf{E}}$ in the prior. After the assimilation, posterior covariances exist in the form of $\mathbf{M}'_{\sigma,\mathbf{E}}$ which then manifest in the form of $\mathbf{M}'_{\mathbf{C,E}}$. These could be taken into account in the calculation of χ^2, although in practice they are not.

$$\chi^2 = \mathbf{d}^T \mathbf{M_d}^{-1} \mathbf{d} \tag{2.35}$$

2.3.2 Adjustment Margin Filtering

The adjustment margin (AM) quantifies if the uncertainties of C and E of a single integral datum can explain its bias. AM can also be considered as a quantification of how much room or margin an integral datum has to accommodate an adjustment to decrease its bias. If AM values are negative, the total uncertainty of C and E in the one-standard-deviation range is not sufficient to account for the bias. For this case, an over-fitting of the nuclear data to the integral parameters would likely occur. In contrast, positive AM values indicate inclusion of

---

[7]These can usually be found in published tables as $\chi^2_{1-\alpha}(N_E)$

[8]The symbol $\langle \cdot \rangle$ denotes the expected value of some random variable. The mean of random variable x would be $\langle x \rangle = \int_\infty p(x)x\,dx$, where $p(x)$ is the PDF of x. The symbol Δ represents possible deviations from the mean value, or $x - \langle x \rangle$. Therefore, $\langle \Delta x \Delta x \rangle = \int_\infty (x - \langle x \rangle)(x - \langle x \rangle)p(x)\,dx$.

the bias in the uncertainty and the viability of a benchmark for DA.

AM is calculated with Eq. (2.36), where Δ_C is relative the standard deviation of a calculated integral parameter C caused by nuclear data and Δ_{EM} is the quadratic combination of experimental and modeling/methodological uncertainty (Eqs. (2.37) and (2.38)) providing a combined relative standard deviation.

$$AM = \Delta_C + \Delta_{EM} - \left| \frac{E - C}{C} \right| \qquad (2.36)$$

$$\Delta_{ND} = \sqrt{[\mathbf{M_C}]_{(i,i)}} \qquad (2.37)$$

$$\Delta_{EM} = \sqrt{[\mathbf{M_E}]_{(i,i)} + [\mathbf{M_M}]_{(i,i)}} \qquad (2.38)$$

2.3.3 $\Delta\chi^2$-filtering

The AM metric takes only the variances in $\mathbf{M_C}$, $\mathbf{M_E}$, and $\mathbf{M_M}$ into account. This omits valuable covariance information from the total χ^2 that can be used to determine the consistency of an integral data set. A recommended method from Ref. [53], called $\Delta\chi^2$-filtering, takes into account all covariances between integral data. It calculates the change in χ^2 when a particular response is omitted from its evaluation. That is, calculating χ^2 with the ith response omitted from the $\mathbf{C}$ and $\mathbf{E}$ vectors and from the corresponding rows and columns in $\mathbf{M_C}$ and $\mathbf{M_E}$. The equations for calculating χ^2 and $\Delta\chi^2$ are given in Eqs. (2.30) and (2.39).

$$\Delta\chi^2 = \chi^2 - \chi^2_{\neq i} \qquad (2.39)$$

The criterion for filtering out a parameter is then specified with a maximum allowable $\Delta\chi^2$. The maximum $\Delta\chi^2$ allowed can be thought of as the degree to which biases in $\mathbf{C}$ and $\mathbf{E}$ are accepted into the adjustment results. In this study, we define the threshold, ϵ, to be equal to a number of standard deviation of the χ^2 distribution per degree of freedom, as calculated with Eq. (2.40) and discussed in Refs. [40, 54]. Here, α is the number of standard deviations and N_E is the number of integral parameters or degrees of freedom. If the $\Delta\chi^2$ of an integral parameter calculated with Eq. (2.39) exceeds ϵ, this parameter is removed from actively influencing the adjustment.

$$\epsilon = 1 + \frac{\alpha\sqrt{2N_E}}{N_E} \qquad (2.40)$$

2.3.4 Marginal Likelihood Optimization

AM or $\Delta\chi^2$-filtering simply remove integral parameters that are inconsistent. The primary disadvantage of filtering is that information is lost when a benchmark is removed from the DA. If significant time was spent in analyzing and modeling the benchmark only for it to be rejected, this would be a waste. Additionally, it is rather coarse and binary where experiments are categorically classified as good or bad. If one integral parameter has an AM of -0.001 and another of -4, both would be removed from the adjustment despite one clearly being much more inconsistent than the other. It is preferable to address the consistency of the calculation and experiment in a continuous and statistically rigorous way. In this section, we summarize the Marginal Likelihood Optimization (MLO) approach to address inconsistent integral data [54, 55, 56]. MLO is a Bayesian procedure that generates a factor to re-scale the uncertainty of an integral parameter so that it is then consistent.

The principle behind MLO is that there are numerous causes of inconsistency between **C** and **E**. It may be caused by an underestimation of nuclear data uncertainties, unaccounted for experimental uncertainty or covariance, or errors in neutronics modeling. These unknown sources of bias are accounted for with extra uncertainty that makes **C** and **E** consistent. By accounting for the uncertainty, we decrease the χ^2, *i.e.* we improve the consistency. The extra uncertainty is then put into a covariance matrix, $\mathbf{M_{extra}}$, that is used in DA. If the inconsistency is primarily caused by errors in neutronics modeling, MLO can be considered to be a data-driven way to estimate $\mathbf{M_M}$ without extensively using expert judgment.

To estimate the extra uncertainty requires redefining χ^2 as Eq. (2.41) and the likelihood function as Eq. (2.42). To estimate the extra variance terms requires maximizing Eq. (2.42), or minimizing its negative logarithm, with numerical methods.

$$\chi^2 = \left(\mathbf{E} - \mathbf{C}\right)^T \left(\mathbf{M_E} + \mathbf{M_M} + \mathbf{M_C} + \mathbf{M_{extra}}\right)^{-1} \left(\mathbf{E} - \mathbf{C}\right) \tag{2.41}$$

$$\mathcal{L}(\mathbf{E}|\boldsymbol{\sigma}, \text{model}) = \frac{e^{-\chi^2/2}}{\sqrt{(2\pi)^N \det\left(\mathbf{M_E} + \mathbf{M_M} + \mathbf{M_C} + \mathbf{M_{extra}}\right)}} \tag{2.42}$$

$$\underset{\mathbf{M_{extra}}}{\arg\max} \left[\frac{1}{2}\left(N * \log(2\pi) + \log\left(\det\left(\mathbf{M_E} + \mathbf{M_M} + \mathbf{M_C} + \mathbf{M_{extra}}\right)\right) + \chi^2\right)\right] \tag{2.43}$$

Ref. [54] alternatively defines $\mathcal{L}(\mathbf{E}|\boldsymbol{\sigma}, \text{model})$ as Eq. (2.44) so it can be used with the random samples of $\boldsymbol{\sigma}$ and **C** in TMC/BMC. Instead of the **C** distribution being accounted for in $\mathbf{M_C}$, it appears in the summation term $\sum e^{-\chi_i^2/2}$, where χ_i^2 is calculated in Eq. (2.23). The negative logarithm of this likelihood is also then minimized to estimate $\mathbf{M_{extra}}$. Ref. [54] also provides ways to estimate a common covariance term in $\mathbf{M_{extra}}$, which was not investigated as part of

this thesis.

$$\mathscr{L}(\mathbf{E}|\boldsymbol{\sigma}, \text{model}) = \frac{\sum e^{-\chi_i^2/2}}{\sqrt{(2\pi)^N \det(\mathbf{M_E} + \mathbf{M_M} + \mathbf{M_{extra}})}} \tag{2.44}$$

2.4 Nuclear Data

Nuclear data have been much discussed in this document and deserve a deeper examination. Nuclear data are numerical representations of nuclear phenomena. They include interactions between neutrons and nuclides, the decay constants for nuclides, the energy spectra of neutrons emitted in fission, and many more phenomena. The nuclear data concerning neutrons are very important in neutronics, and are the primary focus of this thesis.

One type of nuclear data is a *cross section*. A cross section represents the probability that a particle, *e.g.* a neutron, interacts with a nuclide. When a neutron interacts with a nucleus, usually two things happen. First, the neutron and nucleus coalesce to form a compound nucleus that then decays. The decay may consist of emitting an elastic or inelastic neutron, a γ-ray, or two neutrons. The compound nucleus may also fission. Cross sections can be thought of as the probability of the compound nucleus formation and of a certain decay pathway being followed. The cross section only quantifies the probability of a certain kind of interaction. It does not describe the PDF of the recoil particle's angle or energy. These angular and energy distributions are a different kind of nuclear data.

Neutron cross sections are dependent on the energy of incident neutrons and the properties of the interacting nucleus. In fact, by the nature of the compound nucleus formation, the cross sections have maxima at certain incident neutron energies. These maxima are called *resonances*. They arise because nuclei have excited states that correspond to different configurations of the nucleons in the nucleus. The compound nucleus is more likely to form when it is produced in one of these excited states. If the incident neutron and target nucleus have the right combination of properties and energy, the probability of interaction spikes, or there is a resonance. The resonances are described by another kind of nuclear data, *resonance parameters*. They are used to describe the resonance behavior instead of storing the cross sections in a very fine energy grid at the resonances.

Along with cross sections, angular and energy distributions, and resonance parameters there are still further nuclear data of interest in neutronics. Some of these are listed below,

- **Fission yields**: the probability of obtaining different fission products after the fission of a particular nuclide at a given incoming neutron energy.

- **Fission multiplicities**: the average number of neutrons released per fission, which can be prompt neutrons (emitted at the moment of fission), delayed neutrons (emitted in

the decay chain of fission products), or prompt and delayed neutrons combined.

- **Prompt fission neutron spectra**: a PDF that describes the energy of prompt neutrons emitted after fission.

- **Half-lives and branching ratios**: descriptions of the decay pathways of radionuclides.

Fission yields (FY) are important nuclear data for this thesis and are the focus of Chp. 5. They are key to calculating the nuclide inventory of spent fuel. Knowing this inventory is the basis for many types of nuclear engineering analyses, such as reactor and fuel cycle safety, the storage of spent nuclear fuel and its transportation, radiation shielding, the geological disposal of nuclear waste, nuclear safeguards, non-proliferation, nuclear forensic analysis, and the measurement of reactor anti-neutrinos.

FYs define the distribution of fission products following fission. They depend on which nuclide undergoes fission and on the energy of the neutron causing fission. The FYs can be described by isotope, atomic number, or mass number. Describing the FYs by mass number is particularly useful because it aids in tracking the decay chain of fission products, which usually decay through the emission of a β^- particle. The isotope and atomic number yields change while β^- decay occurs, while the mass number yields do not.

An *independent yield* describes the fraction of a nuclide produced directly from fission after emission of prompt neutrons but prior to any radioactive decay (including delayed neutron emission). Importantly, it is defined as **before** decay because fission fragments are born neutron-rich and may quickly decay to other nuclides. Another type of FY data is the *cumulative yield*. It extends beyond the independent FY and includes decay of the fission products at a time scale of $T_{1/2} > 1$ms, such as by β^-, α, or delayed-neutron decay pathways. In other words, it describes the amount of a fission product produced over all time after fission. A *chain yield* is also defined, which is equal to the sum of all stable/long–lived cumulative yields for a given mass chain, *i.e.* for a given mass number.

A classic way to measure a cross section is by using time-of-flight experiments. A beam of neutrons is focused on a target sample that contains a nuclide of interest. From the length between the neutron source and the target (L) and the time that it takes the neutron to travel from source to target (t), the neutron energy (E) can be calculated as in Eq. (2.45), where m is the neutron mass and v is the neutron velocity.

$$E = \frac{mv^2}{2} = \frac{mL^2}{2t^2} \tag{2.45}$$

The neutron flux, ϕ, after passing through the target of thickness d, is experimentally calculated and compared to Eq. (2.46). Here, N is the target's number density, and σ_t is the total cross section of the nuclides in the target. The σ_t includes all possible reactions between the

target's nuclides and the incident neutrons (*e.g.* elastic scattering, fission, capture, etc).

$$\phi = \phi_0 e^{dN\sigma_t} \qquad (2.46)$$

The σ_t can then be extracted with the uncollided and collided neutron flux, as in Eq. (2.47).

$$\sigma_{tot} = -\frac{\ln(\phi/\phi_0)}{dN} \qquad (2.47)$$

The EXFOR (EXchange FORmat) database contains a large collection of the experimental data that were obtained in experiments like time-of-flight [57].[9] These data are considered as *differential experimental data*. They are measured in clean experiments for a particular nuclide and at a particular energy. For certain cross sections, the energy ranges are so dense with experimental information that a direct fit and linear interpolation between data points is possible. These cross sections can be found in *Neutron Cross Section Standards* [58].

Other data are not as well known, as there are invariably missing regions of experimental evidence. It is then necessary to fill in the gaps between experimental data points in order to have cross sections as a continuous function of incident neutron energy. Additionally, consistency rules may need to be enforced, such as cross sections summing up to another cross section, or PDFs summing to unity. To fill in the gaps and force consistency, models and extrapolation are used. The combination of modeling and experiment evidence create *evaluated nuclear data*. To create evaluated nuclear data, some degree of fitting between the nuclear models and the experimental data is required. Codes like SAMMY [59] and REFIT [60] use least squares to fit resonance parameters. These statistical analyses are also used when multiple experimental measurements are available for the same quantity of interest.

All the nuclear data of interest for technical applications are evaluated, compiled, and stored in *evaluated nuclear data libraries*. They differ in which differential experimental data they use, which nuclear models are employed, and how the fitting analyses are done. Some of the libraries include ENDF/B, JEFF, JENDL, CENDL, BROND, and TENDL [47]. Most of the evaluated nuclear data are stored in the ENDF format (Evaluated Nuclear Data Format) [61]. The data are enumerated with strict conventions to standardize the process and make them easily machine readable. The data are available for neutron energies of 1×10^{-5} eV to 20 MeV, and sometimes up to 200 MeV. Processing codes such as NJOY [62] and PREPRO [63] exist to create ENDF files and to process the data. They can perform Doppler broadening of resonances or collapse the cross sections into energy bins. NJOY can also create a file format called ACE (**A C**ompact **E**NDF) that is used in continuous-energy Monte Carlo transport codes.

Because the nuclear data are often, in part, derived from experimental data, they have un-

---

[9]For neutron cross sections, there are 20,000 data sets which contain more then 3.6 million data points [55].

certainties. The experiments are subject to stochastic processes, like counting statistics or neutron flux instabilities, that mean that the differential data have uncertainties. Additionally, the differential data may have systematic uncertainties that create correlations. For example, if the same target material is used to measure several different energies, any error caused by the target material would be systematic to all the different energy measurements. Furthermore, often reference cross sections are used in cross section experiments; this can introduce another form of correlation. The covariances are also taken into account when the experimental data are fitted with the theoretical models.

The evaluated nuclear data provide estimates for the uncertainties of the nuclear data. These take the form of covariance matrices. It is common practice to use these covariance matrices to perform uncertainty quantification of parameters in neutronics, *i.e.* to propagate the uncertainty that arises from the nuclear data. This can be done through linear error propagation or with stochastic sampling [64].

2.5 Chapter's Key Points

- DA is based on Bayes' theory

- The four principal DA methods in neutronics are GLLS, MOCABA, BMC, and BFMC

- GLLS assumes that all random variables are normally distributed and that the calculated integral parameters are linear functions of nuclear data

- MOCABA, BMC, and BFMC all use stochastic sampling and do not make a linearity assumption

- MOCABA assumes that all random variables are normally distributed

- BMC and BFMC make no assumptions about any parameter's distribution

- It is important to account for the consistency between the calculated and experimental integral data

- DA with inconsistent integral data sets may produce spurious adjustments

- There are two approaches to account for inconsistency: remove inconsistent integral data or give them extra uncertainty

- The two principal methods proposed to remove inconsistent integral data are Adjustment Margin and $\Delta\chi^2$-filtering

- Marginal Likelihood Optimization can be used to add extra uncertainties, with the advantage being that no integral data are lost

- Nuclear data are evaluated from physics models and experiments. This is why they have inherent biases and uncertainties

3 Comparison of Data Assimilation Methods

> If one has really technically penetrated a subject, things that previously seemed in complete contrast might be purely mathematical transformations of each other.
>
> – John von Neumann

In this chapter, GLLS, MOCABA, BMC, and BFMC are compared and analyzed. This thesis is the first time that all the DA methods are compared for neutronics in one study. A comparison tests and characterizes the theoretical bases of the methods and deepens the understanding of their limitations and areas of applicability. Agreement between their posteriors given identical starting conditions (*e.g.* input nuclear data, neutron transport code, and benchmark model) would be scientifically beneficial. Firstly, good agreement would support the pervasive use of GLLS for traditional DA problems. Secondly, it would be auspicious for stochastic DA applications, especially non-linear or non-normal problems, by increasing the confidence in their results.

In Section 3.1, the DA methods are applied to simple toy problems. The toy models include normal and log-normal input variables that test the effects that non-normality may have on the DA. Additionally, varying degrees of inconsistency are studied. In Section 3.2, the DA methods are applied to a real application case: the JEZEBEL-Pu239 critical experiment. In this section, the actual adjustments are not of interest. They are not intended to validate the nuclear data or to serve as recommendations to nuclear data evaluators. Rather, the adjustments are examined to see how well the results from the DA methods agree when applied to the same benchmark system, neutron transport code, and input nuclear data.

3.1 Toy Problems

The following section presents an exercise to deepen our understanding of the DA methods. It uses a linear model and its independent variables are assigned normal and log-normal distributions. A linear model with Gaussian inputs tests the DA methods when all of the underlying assumptions are correct. In this case, GLLS gives the true moments of the posterior. It is then compared to MOCABA, BMC, and BFMC to determine if they are unbiased estimates of the MAP distribution.[1] A non-normal model tests how GLLS and MOCABA react when their normality assumption is invalid. Importantly, one should note that these examples are highly simplified and serve as pedagogical tools. They do not definitively describe and qualify the methods for real applications and for all scenarios.

The chosen linear model is Eq. (3.1). The variables σ_1 and σ_2 are implemented as multivariate normal and log-normal random variables. The coefficients a and b can be thought of as the physical properties of the systems, like the geometry or composition of a reactor. Two dependent variables are used, which are the integral parameters in neutronics. Eq. (3.1) can then be written as a linear system of equations as Eq. (3.2), where the coefficients a and b are recognized to be the slopes of C with respect to σ_1 and σ_2, or the sensitivity coefficients $\mathbf{S}$.

$$C(\sigma_1, \sigma_2) = a\sigma_1 + b\sigma_2 \tag{3.1}$$

$$\begin{bmatrix} C_1 \\ C_2 \end{bmatrix} = \begin{bmatrix} a_1 & b_1 \\ a_2 & b_2 \end{bmatrix} \times \begin{bmatrix} \sigma_1 \\ \sigma_2 \end{bmatrix} \tag{3.2}$$
$$\mathbf{C} = \mathbf{S}\boldsymbol{\sigma}$$

3.1.1 Linear and Normal Example

In this section, we present the posteriors from the four DA methods for an ideal case: a linear model with normal distributions. Here, the GLLS posteriors are the reference solution to which the other DA methods are compared. First, the posteriors are shown for a nominal case where the input parameters were chosen so that the integral parameters were consistent, *i.e.* the prior χ^2 was close 1.0 and within the standard deviation of the χ^2 distribution for two degrees of freedom (DoF). This nominal case represents a DA problem without, or minor, model inaccuracy. Then, the toy problem is re-done with larger and larger χ^2 values to induce

---

[1] Here, the idea of being a "biased" and "unbiased" estimate can be clarified with respect to the definition of bias in Eq. (1.1). A bias, in general, refers to the difference between the true value of a parameter and the expected value of its estimation. In Eq. (1.1), the true value is E and the expected value of the estimate is C. For DA, there is the true estimate of the MAP moments and the estimated MAP moments from the DA methods. If a DA method is unbiased, it will give the true estimate; if it is biased it will not. For a linear and normal toy problem, GLLS gives, for example, the true value of the posterior expected value of a parameter. This true value can then be compared to the estimated expected value from MOCABA, BMC, and BFMC to see if those methods are biased estimates.

larger inconsistencies and test how the methods perform.

Inputs

This example uses Eq. (3.1). The input parameters for a_1/a_2 and b_1/b_2, σ_1 and σ_2, the experimental integral parameters E_1 and E_2, and the covariance matrices for $\mathbf{E}$ and $\boldsymbol{\sigma}$ or $\mathbf{M_E}$ and $\mathbf{M}_\sigma$, are given below. They were arbitrarily chosen to have a reasonable prior χ^2 for the toy problem. Here, the prior χ^2 is 1.86 per DoF, and at two DoFs the standard deviation of the χ^2-distribution is 2.0 (calculated as $\sqrt{2*2}$).

$$a_1 = 2.0000, \quad a_2 = 0.5000, \quad b_1 = 0.2500, \quad b_2 = 1.0000$$

$$\boldsymbol{\sigma} = \begin{bmatrix} \sigma_1 \\ \sigma_2 \end{bmatrix} = \begin{bmatrix} 5 \\ 3 \end{bmatrix}, \quad \mathbf{M}_\sigma = \begin{bmatrix} \Delta^2_{\sigma_1} & \Delta_{\sigma_1,\sigma_2} \\ \Delta_{\sigma_1,\sigma_2} & \Delta^2_{\sigma_2} \end{bmatrix} = \begin{bmatrix} 0.5000 & 0.0200 \\ 0.0200 & 0.1000 \end{bmatrix}$$

$$\mathbf{E} = \begin{bmatrix} E_1 \\ E_2 \end{bmatrix} = \begin{bmatrix} 12.90 \\ 4.950 \end{bmatrix}, \quad \mathbf{M_E} = \begin{bmatrix} \Delta^2_{E_1} & \Delta_{E_1,E_2} \\ \Delta_{E_1,E_2} & \Delta^2_{E_2} \end{bmatrix} = \begin{bmatrix} 0.6450 & 0.3995 \\ 0.3995 & 0.9900 \end{bmatrix}$$

Applying GLLS requires finding the derivatives of C with respect to $\boldsymbol{\sigma}$, as shown below,

$$\mathbf{S} = \begin{bmatrix} \frac{\delta C_1}{\delta \sigma_1}\Big|_{\bar{\sigma}_1,\bar{\sigma}_2} & \frac{\delta C_1}{\delta \sigma_2}\Big|_{\bar{\sigma}_1,\bar{\sigma}_2} \\ \frac{\delta C_2}{\delta \sigma_1}\Big|_{\bar{\sigma}_1,\bar{\sigma}_2} & \frac{\delta C_2}{\delta \sigma_2}\Big|_{\bar{\sigma}_1,\bar{\sigma}_2} \end{bmatrix} = \begin{bmatrix} a_1 & b_1 \\ a_2 & b_2 \end{bmatrix}$$

Nominal Case Results

The results for the nominal case are presented in Table 3.1. They were calculated with one million samples of $\boldsymbol{\sigma}$ for the stochastic DA methods. We observe near perfect agreement between GLLS, MOCABA, and BMC for all posteriors, as is expected for a linear and normal application. This indicates that MOCABA and BMC are unbiased estimates of the MAP distribution. BFMC, however, shows more significant disagreement, and its adjustments were larger than those of the other methods. The differences are larger for the posterior variances and covariances, which can be three orders of magnitude lower than the other methods. The posterior χ^2 values (calculated with Eq. (2.30)) per DoF of GLLS, MOCABA, BMC, and BFMC are 0.72, 0.73, 0.74. and 0.24 respectively. For these specific input conditions, BFMC was not an unbiased estimate of the MAP. In the next section, the DA methods are applied with varying input conditions to further characterize their behavior, especially for BFMC.

Table 3.1 – Posteriors for the linear, normal toy problem. The i index indicates the index in the vectors and matrices. If $i = 1$, then $j = 2$. If $i = 2$, $j = 1$.

Parameter	$i = 1$				$i = 2$			
	GLLS	MOCABA	BMC	BFMC	GLLS	MOCABA	BMC	BFMC
C_i	12.63	12.63	12.63	12.93	5.897	5.898	5.897	4.979
$\mathrm{var}(C_i)$	0.4581	0.4583	0.4586	0.0024	0.1227	0.1227	0.1227	0.0008
$\mathrm{cov}(C_i, C_j)$	0.1445	0.1445	0.1444	0.0007	0.1445	0.1445	0.1444	0.0007
σ_i	5.950	5.950	5.950	6.230	2.923	2.923	2.922	1.864
$\mathrm{var}(\sigma_i)$	0.1119	0.1114	0.1121	0.0006	0.0900	0.0900	0.0901	0.0006
$\mathrm{cov}(\sigma_i, \sigma_j)$	0.0047	0.0046	0.0046	-0.0000	0.0047	0.0046	0.0046	-0.0000

Varying χ^2

The nominal case had a prior χ^2 per DoF of 1.86. Here, the prior χ^2 is systematically changed by altering **E** while keeping all other inputs constant. When **E** is close to **C**, the χ^2 is smaller, when **E** is farther from **C** it is larger. This is done to simulate an inconsistency between **C** and **E**, as might be encountered in real DA problems. From a mathematical point of view, the DA methods are ignorant of the inconsistency: they are just equations that receive inputs and give outputs. If the DA methods are all equivalent mathematically, they should give the same outputs no matter the supplied input. However from a theoretical point of view, it would be unwise to do DA with data sets that are significantly inconsistent, as this would produce non-physically-founded adjustments. The posterior **C** would be pushed towards **E**, perhaps past the limit of what is explained by theory, which would mean that the nuclear data are being adjusted unreasonably with respect to nuclear physics and differential data.

Fig. 3.1 shows the prior and posterior **C** mean values. Here, 1,000 samples of $\boldsymbol{\sigma}$ were done for the stochastic DA methods. Several interesting behaviors appear:

- At $\chi^2 = 0$, no adjustment occurs as **E** and **C** perfectly agree.

- As χ^2 increases, there is more **E**/**C** discrepancy and the adjustments are larger.

- GLLS, MOCABA, BMC, and BFMC agree well, up to a χ^2 value of around 10. An exception is C_2 with BFMC at very low χ^2.

- At large χ^2, the change to **C** becomes much greater than three standard deviations of the prior. This demonstrates the danger of doing DA with highly inconsistent data sets: the equations will do an adjustment no matter the inputs given to them. The user must ensure that the adjustments are based on sound statistics and are physically sensible.

- Above $\chi^2 = 10$, the BMC and BFMC posteriors begin to diverge from GLLS and MOCABA.

- At very large χ^2, the BFMC posteriors trend back towards the prior.

- For C_2, the posterior moves away from E_2. This is caused by the high correlation C_2 has with C_1 (correlation coefficient of 0.78), and C_1 driving the adjustment because its experimental uncertainty is smaller than C_2 and its calculation uncertainty is larger.
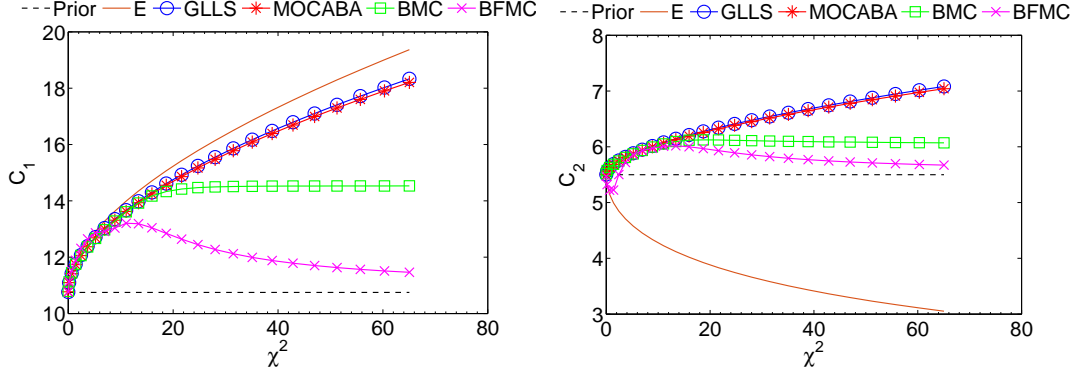
Figure 3.1 – Prior and posterior **C** means vs. χ^2 for the linear, normal toy problem.
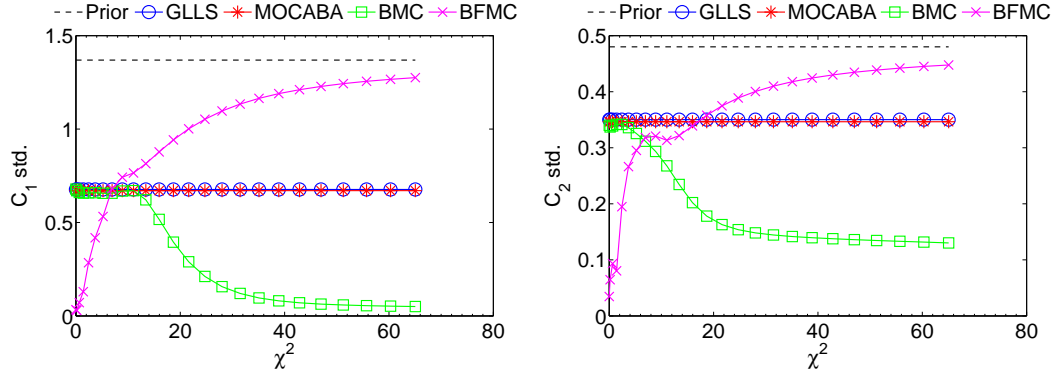
Figure 3.2 – Prior and posterior **C** standard deviations vs. χ^2 for the linear, normal toy problem.

Fig. 3.2 shows the prior and posterior **C** standard deviations. The following behaviors are interesting to summarize:

- The GLLS and MOCABA posteriors, and BMC's up to $\chi^2 \approx 10$ for C_1 and $\chi^2 \approx 5$ for C_2, are invariant with changing χ^2. This is a side-effect of how the χ^2 changes were induced, *i.e.* by changing **E**. Eq. (2.11) shows that $\mathbf{M_C}$ has no dependence on **E** and cannot be affected by changing **E**. If $\mathbf{M_E}$ or $\mathbf{M_\sigma}$ were modified to change χ^2, the uncertainties would have then varied.

- BFMC shows large disagreements with other methods. At very low χ^2, its posterior uncertainties are small. This region corresponds to the nominal case of the previous section. At higher χ^2, the posterior trends back towards the prior.

- At $\chi^2 \approx 5 - 15$, where the BMC posteriors begin to diverge from GLLS and MOCABA, the BFMC posteriors are closest to the other three DA methods.
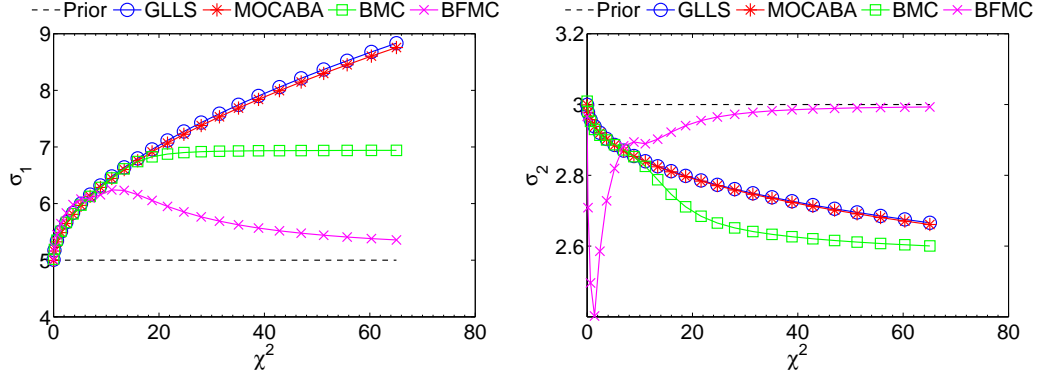
Figure 3.3 – Posterior $\boldsymbol{\sigma}$ vs. χ^2 for the linear, normal toy problem.
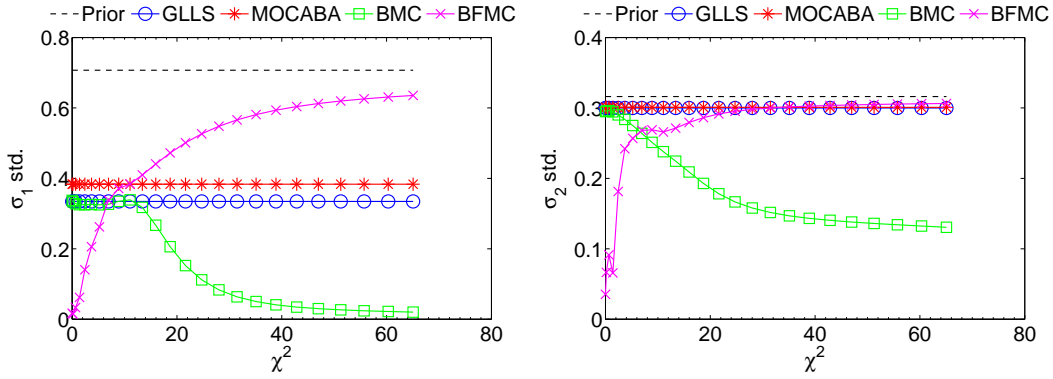
Figure 3.4 – Posterior $\boldsymbol{\sigma}$ standard deviations vs. χ^2 for the linear, normal toy problem.

Figs. 3.3 and 3.4 show the prior and posterior $\boldsymbol{\sigma}$ means and standard deviations. The behavior is similar to that observed for **C**:

- GLLS and MOCABA give near identical results.

- BMC results begin to diverge from GLLS and MOCABA at around $\chi^2 = 15$.

- As **C** and **E** become very inconsistent (as χ^2 gets large) the adjustments continue blindly and are much larger than the prior standard deviations.

- As the degree of inconsistency gets larger, BFMC trends back towards the prior.

- At low χ^2 values, BFMC gives very small posterior standard deviations, which was seen for the nominal case.

- BMC and BFMC perform more poorly for σ_2 and its standard deviation. This is linked to the low sensitivity of C_1 to σ_2; its sensitivity coefficient to σ_1 is 2 and to σ_2 is 0.25. Because σ_2 affects to a small degree the dependent variable that drives the adjustment, it becomes harder for BMC and BFMC to converge.

- The posterior σ_1 standard deviations of GLLS and MOCABA have small differences.

The prior and posterior χ^2 values are presented in Fig. 3.5. The GLLS and MOCABA χ^2 values agree no matter the prior χ^2. Again this is important to note: it does not matter if the DA is being done in a sensible way, *i.e.* to a consistent data set, the adjustments will be performed anyway. The DA must be applied with discretion if it is to be used in real world applications. BMC χ^2 values begin to diverge from MOCABA and GLLS at a prior $\chi^2 \approx 15$, and for BMC the posterior χ^2 is eventually larger than the prior.
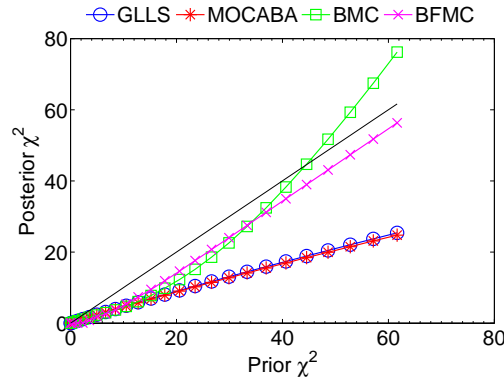
Figure 3.5 – Prior vs. posterior χ^2 values for the linear, toy problem.

These results lead to several questions:

- Why does BMC diverge from GLLS and MOCABA as χ^2 increases?

- Why does this divergence consistently occur at a certain point ($\chi^2 \approx 15$)?

- Why does BFMC give very small uncertainties for low χ^2?

- Why does BFMC converge to the prior as χ^2 becomes larger?

- Why did MOCABA and GLLS disagree only for the standard deviation of σ_1?

Why does BMC diverge from GLLS and MOCABA as χ^2 increases?

The answer to this question is connected to the sample size. As χ^2 increases, the BMC weights trend towards zero. This link between the weights and χ^2 can be seen in Eqs. (2.23) and (2.24): χ_i^2 is multiplied by -1/2 and then put into an exponential to calculate the weight, or

$\exp(-\chi_i^2/2)$. A large χ_i^2 creates a large negative value in an exponential, subsequently creating a small weight. If χ^2 is very large, its associated χ_i^2 are large and many weights are near zero. When the posteriors are calculated as weighted averages, large χ_i^2 values lead to very few samples that have significant weight. With a small sample size, there are too few rare weights with significant values to contribute to an accurate posterior. As the sample size increases, there are more of these rare weights leading to a more accurate or converged posterior.

The solution to this problem is to increase the sample size. With more samples, there are more rare and significant weights that can then contribute to a more accurate average. Fig. 3.6 shows the posterior mean and standard deviation of σ_2, both of which previously showed large disagreement between BMC and GLLS/MOCABA for large χ^2. The GLLS posterior is plotted as the reference value. With an increased sample size, the χ^2 value at which BMC diverges from GLLS increases. This result implies that for large χ^2 values, BMC will need to be applied with larger sample sizes in order to have accurate results.[2]
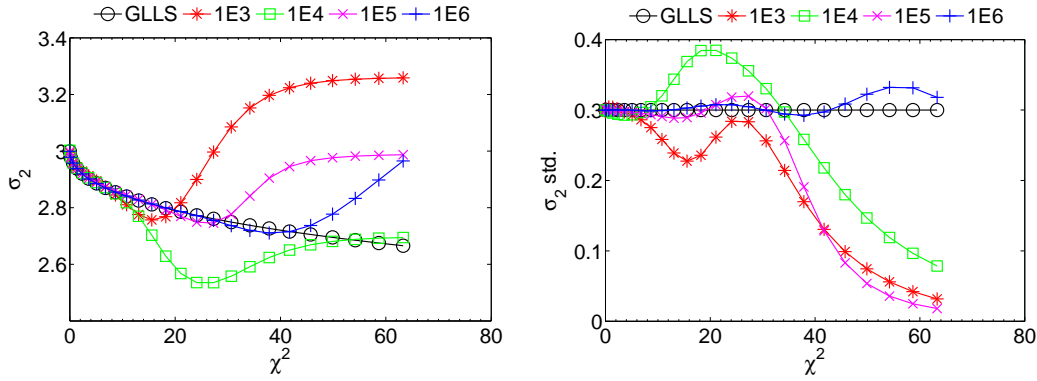
Figure 3.6 – BMC posteriors vs. χ^2 for different sample sizes.
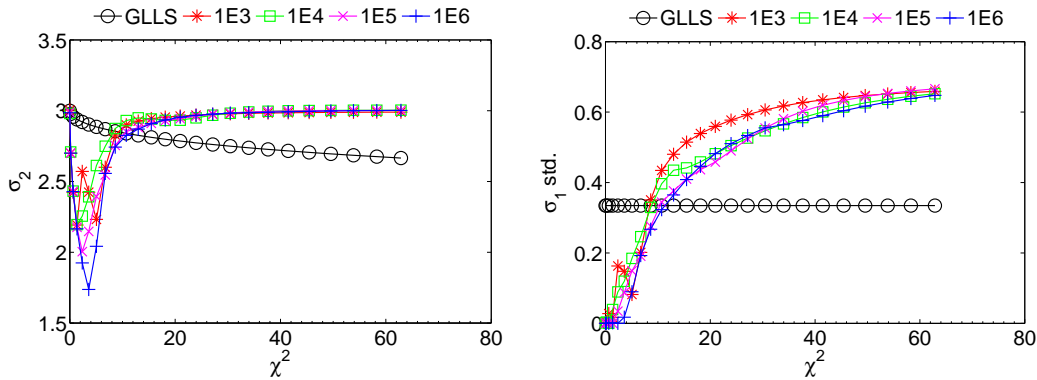
Figure 3.7 – BFMC posteriors vs. χ^2 for different sample sizes.

Increasing the sample size does not improve the BFMC posterior results. Fig. 3.7 gives the

---

[2]The line for 1,000 samples is different from that seen in previous plots. The difference is caused by a different set of 1,000 samples being used here.

BFMC posterior σ_2 and the σ_1 standard deviation, two parameters where BFMC disagreed greatly from the other methods. We observe that with increased sample sizes, there is no improved agreement between BFMC and GLLS. Therefore, the observed behaviors are not linked to the limited sample sizes, but rather to the BFMC formulation itself.

Why does BMC diverge consistently from GLLS at a certain point ($\chi^2 \approx 15$)?

What was so important about $\chi^2 \approx 15$ to create a consistent behavior in BMC? To understand further, please examine Fig. 3.8 which provides the standard deviation of the weight sample set vs. χ^2. For BMC, as χ^2 trends larger the spread of the weight distribution (quantified by the standard deviation) becomes smaller. At $\chi^2 = 15$, the standard deviation is approximately zero for BMC and its posteriors diverge from GLLS and MOCABA's when the sample size is 1,000.
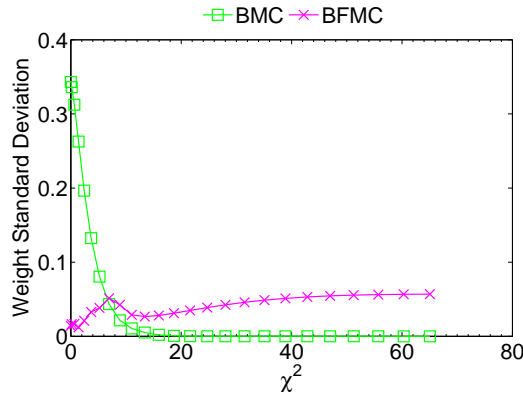
Figure 3.8 – Standard deviation of the BMC and BFMC weight distribution vs. χ^2.

BMC's behavior, where the spread in the weight distributions crashes towards zero with increasing χ^2, is often called *weight degeneracy*, or particle degeneracy, in the literature [65]. With very few significant weights, degeneracy causes slow convergence of the posteriors, *i.e.* more samples are needed for high accuracy. The extreme effect of weight degeneracy is that all the weights are zero and BMC no longer functions as an algorithm. In particle filtering, weight degeneracy is commonly tackled by re-sampling from the weight distributions [66]. While this is an interesting avenue for future work, it is outside the scope of the presented study and not discussed further.

Why does BFMC give very small uncertainties for low χ^2?

When the χ^2 is small, there is a strong chance that one $\chi^2_{\min}$ is very small, particularly much smaller than 1. When this is used in $\chi^2_i / \chi^2_{\min}$, it makes every evaluation of this expression much larger than the regular χ^2_i used in BMC, through division by a number much smaller than 1. Now, when the expression $\exp(-\chi^2_i / \chi^2_{\min})$ is evaluated to calculate the weights, all the weights have very small values due to the pronounced effect of $\chi^2_{\min}$. Finally, when the

posterior weighted averages are calculated, there are few weights with significant value to have accurate posteriors. For the covariance matrices $\mathbf{M}'_{\mathbf{C}}$ and $\mathbf{M}'_{\sigma}$, the posterior averages are calculated with the squared difference between numbers, see Eqs. (2.26) and (2.28), meaning that these small weights are applied to small numbers. This makes them crash towards to zero to larger extent than the means calculated with Eqs. (2.25) and (2.27).

Why does BFMC converge to the prior as χ^2 becomes larger?

This question is best answered with figures that illustrate how the prior χ^2 affects the χ_i^2 distributions and the weight distributions. These figures also help demonstrate the behavior described in the previous questions. Please examine Figs. 3.9, 3.10, and 3.11. On the left side of the figures is a histogram of χ_i^2 values calculated with Eq. (2.23) for 1,000 samples of $\boldsymbol{\sigma}$. It also shows χ_i^2 normalized by $\chi_{\min}^2$, as is done in BFMC. On the figures' right side are cumulative density functions (CDFs) of the weights calculated with BMC or BFMC. The CDFs characterize the distribution of the weights, particularly if most are near zero or if they are evenly spread, *i.e.* they have a flatter distribution. The difference vertically among plots is when $\mathbf{E}$ was varied to increase the prior χ^2. Each plot shows the average χ^2 calculated with the χ_i^2 sample set.

Begin with Fig. 3.9 which shows small χ_i^2 values. In BMC when χ_i^2 is small, small negative χ_i^2 are given to an exponential and produce large weights. As χ_i^2 trend towards 0, the weights trend towards 1. The CDFs show that the majority of the samples have a weight greater than zero. Furthermore, the weight distribution is fairly flat (*i.e.* the CDF is closer to a diagonal as it would be for a uniform distribution). With a flat distribution of weights, all samples are weighted evenly and the posterior returns to the prior. It is for this reason that BMC does not change the posterior from the prior when the χ^2 is small, *i.e.* when $\mathbf{C}$ and $\mathbf{E}$ already agree well.

For low χ_i^2, BFMC shows the opposite weight behavior to BMC. The normalization by $\chi_{\min}^2$ makes all $\chi_i^2/\chi_{\min}^2$ very large, so large as to make the normal χ_i^2 not visible on certain x-axes scales. Then, the weights all become very small with $\exp(-\chi_i^2/\chi_{\min}^2)$. The CDFs show that nearly 100% of the weights have zero values. This is a form of weight degeneracy and is why BFMC does not perform well for small χ^2.

Descending through the figures shows that as χ^2 becomes bigger, BMC and BFMC move in opposite directions. Bigger χ_i^2 push the BMC weights closer to zero. For BFMC, bigger χ_i^2 mean a larger $\chi_{\min}^2$, helping to make the weights larger. In the limit of $\chi_{\min}^2 \to 2$, the distributions of χ_i^2 and $\chi_i^2/\chi_{\min}^2$ are identical and BMC and BFMC will produce identical posteriors. This point is seen in Fig. 3.8 when the standard deviations of the BFMC and BMC weight distributions have the same value. The top of Fig. 3.10 shows a point close to this limit, where $\chi_{\min}^2 = 1.61$.

As χ^2 becomes even larger, the distributions of χ_i^2 and the weights for BMC and BFMC have their behaviors reversed. With very large χ_i^2, the BMC weights are all near zero and this eventually leads to weight degeneracy as seen in Fig. 3.11. To some extent, the weight degeneracy can be counter-acted with a larger sample size, as previously discussed. Oppositely with BFMC,
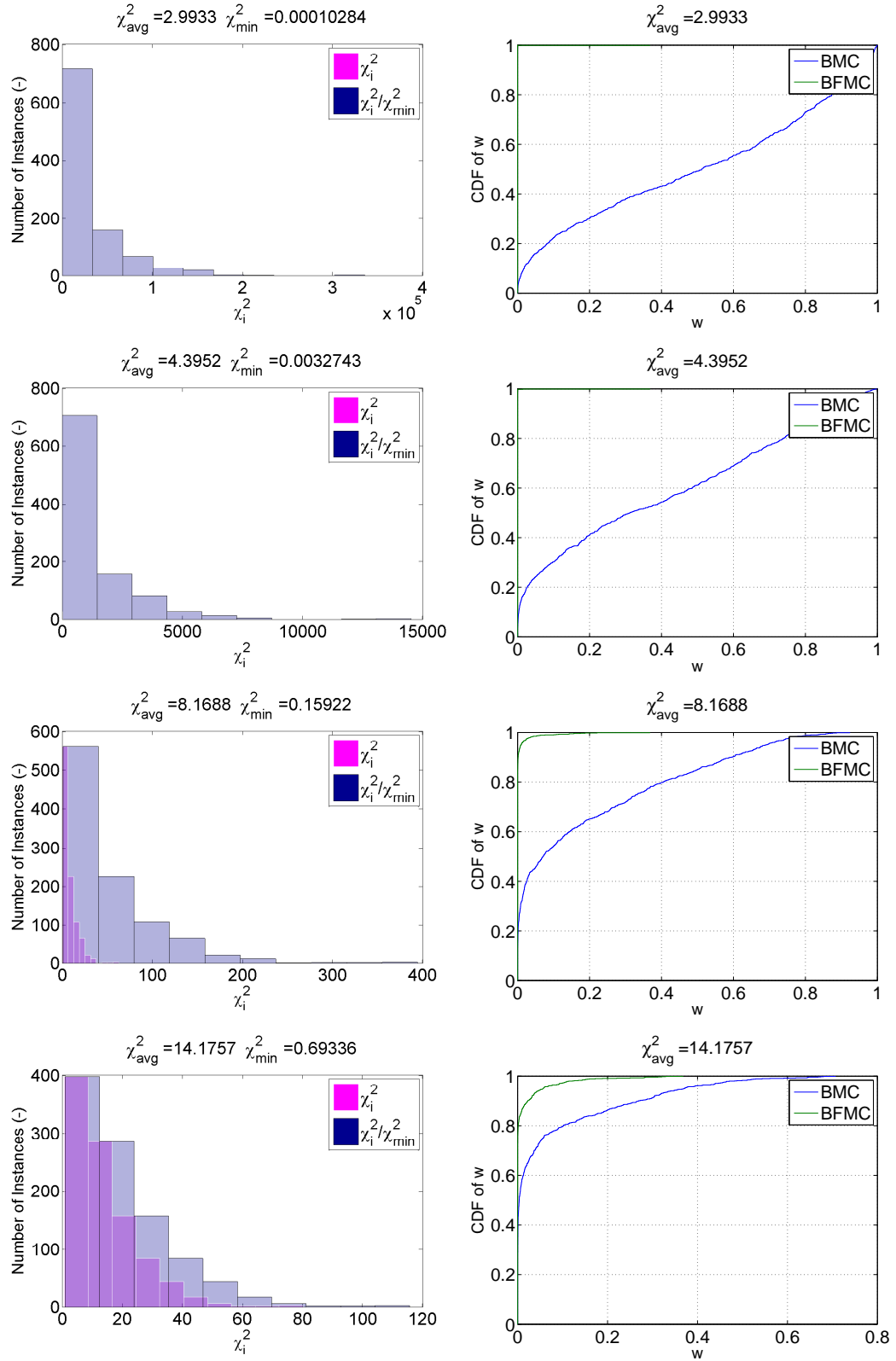
Figure 3.9 – Low prior χ_0^2 and its effect on the χ_i^2 distributions and CDF of weights.
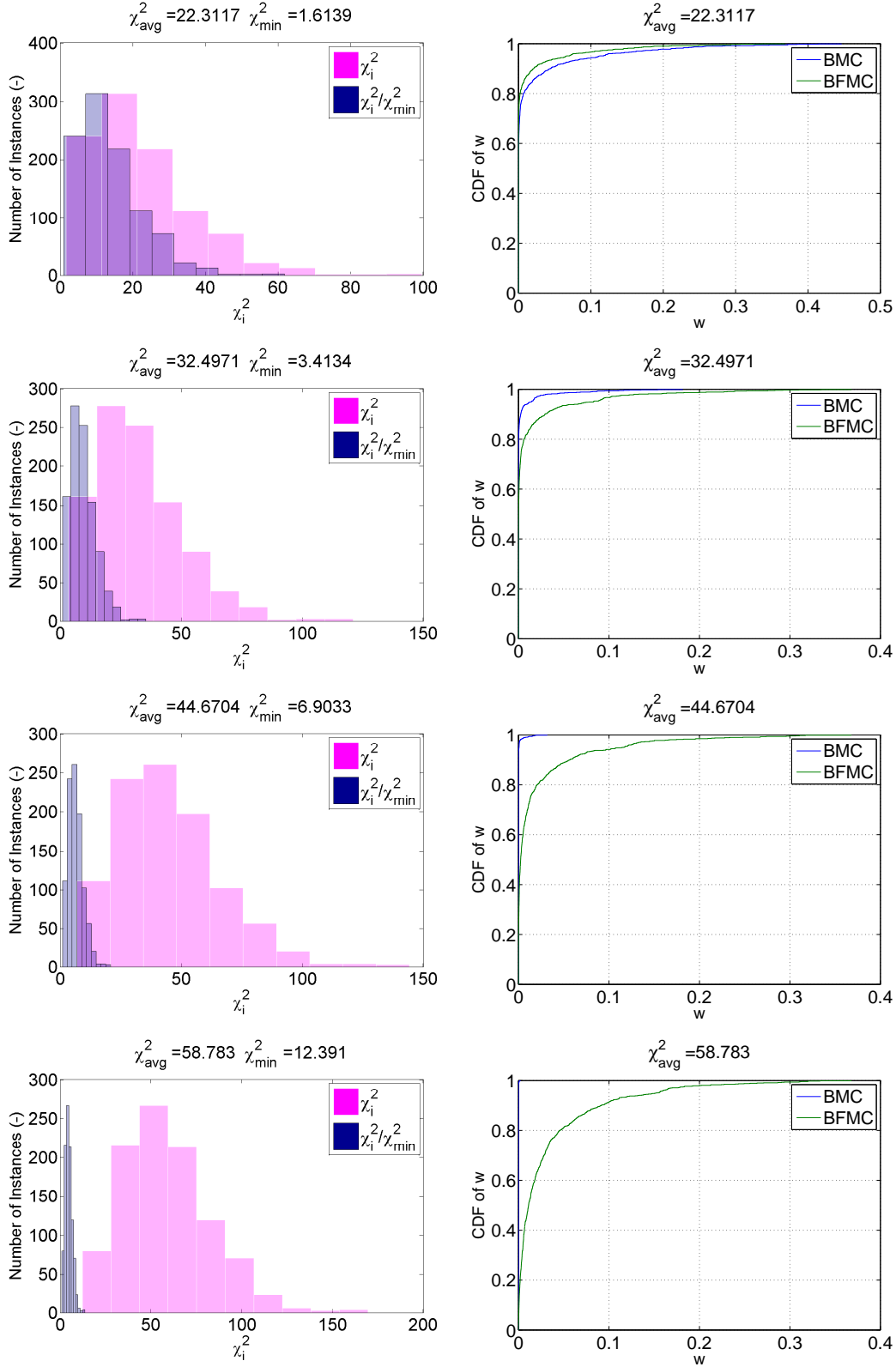
Figure 3.10 – Intermediate prior χ_0^2 and its effect on the χ_i^2 distributions and CDF of weights.
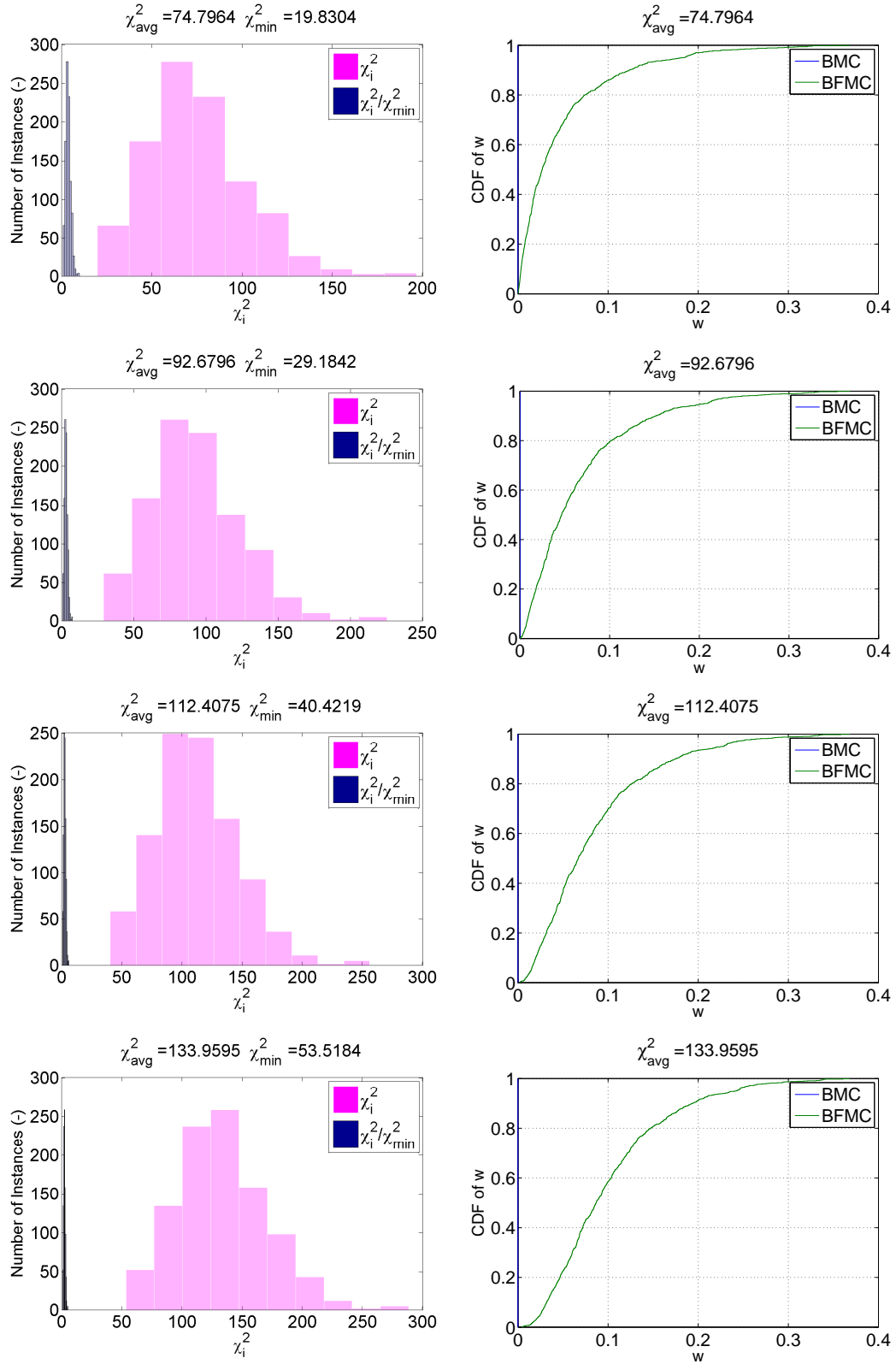
Figure 3.11 – High prior χ_0^2 and its effect on the χ_i^2 distributions and CDF of weights.

large χ_i^2 mean that $\chi_{\min}^2$ becomes larger and $\chi_i^2/\chi_{\min}^2$ becomes smaller. This makes the weights larger and flatter by the same effect previously described for BMC. Then with a flatter weight distribution all samples are equally weighted and the posterior returns toward the prior.

A certain χ^2 will push the weight calculation to the limit of double-precision floating point numbers in 64 bits of computer memory. The smallest number that can be represented in double precision is $2.225{\times}10^{-308}$,[3] meaning that the largest χ_i^2 before a weight reaches numerical zero is ~745.12. Practically speaking, the weights are effectively zero at smaller χ_i^2.

Importantly, BMC and BFMC are using the total χ^2 in their formulations, not the χ^2 per DoF. When there are many DoF, χ^2 becomes large, no matter the consistency of the data set. For example, highly consistent data with 50 DoF would have a χ^2 per DoF of 1.0 but a total χ^2 of 50. Despite the data set being consistent, BMC would begin to have weight degeneracy and BFMC would not create much adjustment, *i.e.* the prior would be near the posterior.

Why did MOCABA and GLLS disagree only for the standard deviation of σ_1?

Why are there slight differences between GLLS and MOCABA, *e.g.* the σ_1 standard deviation in Fig. 3.4? The differences are also related to the sample size. These increasing χ^2 were done each with 1,000 samples. With more samples, these differences disappear. This also shows the importance of considering the sample size when applying MOCABA.

Concluding Remarks

This toy problem provides evidence that indicates that BFMC is not an unbiased estimate of the MAP distribution. In other words, the normalization by $\chi_{\min}^2$ in Eq. (2.29) biases the MAP estimate from the true value shown by GLLS. Interestingly, the biased estimate of BFMC may be an advantageous behavior if we think of each DA method as an algorithm. We saw that applying GLLS, MOCABA, or BMC to inconsistent data sets will give posteriors that are ignorant of physics. BFMC has an auto-correcting behavior. For under-consistent data sets (too high prior χ^2) it will dampen the adjustment and keep it closer to the prior, which does not occur for GLLS, MOCABA, or BMC.

In general, the χ^2 needs to be carefully considered when applying all of the DA methods. On one hand, there is the issue of the consistency of the integral data set and if the adjustments are realistic. On the other hand, there is the performance of BMC and BFMC as algorithms. BMC will give an unbiased estimate of the MAP distribution, but only if enough samples are used. All BMC estimates should, therefore, be checked for proper statistical accuracy. BFMC gives a biased estimate of the MAP distribution. However this biasing can be considered a benediction as it helps to restrain the adjustments in the presence of inconsistent integral data sets. That BFMC is a biased method must balance with the fact that it compensates for

---

[3]According to the IEEE Standard for Floating-Point Arithmetic (IEEE 754).

the integral data set's inconsistency.

3.1.2 Linear and Log-Normal Example

The previous exercise provided evidence that GLLS, MOCABA, and BMC are all unbiased estimates of the MAP distribution. BMC's advantage over MOCABA and GLLS is that it preserves the true PDFs of $\boldsymbol{\sigma}$, $\mathbf{C}$, and $\mathbf{E}$. MOCABA and GLLS assume that the PDFs are a normal distributions. With the evidence from the previous exercise that supported BMC being an unbiased estimate of the posterior, we can use logical deduction: if the toy problem shows discrepancies between the BMC posterior and that from GLLS and MOCABA, it would show that GLLS and MOCABA are biased estimates of the MAP distribution in a non-normal case. In this case, BMC is now the mathematical reference solution.

BMC could be very useful in neutronics problems where there are non-normal PDFs, like for the fission yields produced by GEF that are discussed in Chp. 5. The fission yields induce a right-skewed distribution in the fission products which is similar to a log-normal distribution. Because of this, a log-normal distribution was chosen for the PDF of $\boldsymbol{\sigma}$ in this toy problem. It will also induce a log-normal distribution in $\mathbf{C}$. For $\mathbf{E}$, only the mean and covariance matrix $\mathbf{M_E}$ are needed still. There is no need to specify the higher moments with BMC, and GLLS and MOCABA use these two moments in normal distributions. First, a nominal case is presented and then the posteriors are presented with varying χ^2 values, identical to the previous section.

Inputs

The input parameters are shown below. These are slightly different than the previous case in order to be compatible with a log-normal distribution. The parameters of the log-normal distribution have been manipulated in order to generate a skewness and kurtosis similar to that observed in the fission products in Chp. 5. Here, the skewness of C_1 and C_2 is 0.91 and 1.35, respectively, and their kurtosis is 4.5 and 7.1, respectively.

$$a_1 = 2, \quad a_2 = 0.5, \quad b_1 = 0.25, \quad b_2 = 1$$

$$\boldsymbol{\sigma} = \begin{bmatrix} \sigma_1 \\ \sigma_2 \end{bmatrix} = \begin{bmatrix} 3 \\ 1 \end{bmatrix}, \quad \mathbf{M}_\sigma = \begin{bmatrix} \Delta_{\sigma_1}^2 & \Delta_{\sigma_1,\sigma_2} \\ \Delta_{\sigma_1,\sigma_2} & \Delta_{\sigma_2}^2 \end{bmatrix} = \begin{bmatrix} 0.8 & 0.06 \\ 0.06 & 0.4 \end{bmatrix}$$

$$\mathbf{E} = \begin{bmatrix} E_1 \\ E_2 \end{bmatrix} = \begin{bmatrix} 5 \\ 3 \end{bmatrix}, \quad \mathbf{M_E} = \begin{bmatrix} \Delta_{E_1}^2 & \Delta_{E_1,E_2} \\ \Delta_{E_1,E_2} & \Delta_{E_2}^2 \end{bmatrix} = \begin{bmatrix} 0.5 & 0.02 \\ 0.02 & 0.1 \end{bmatrix}$$

Table 3.2 – Posterior parameters for log-normal toy problem. The i index indicates the index in the vectors and matrices. If $i = 1$, then $j = 2$. If $i = 2$, $j = 1$.

Parameter	$i = 1$				$i = 2$			
	GLLS	MOCABA	BMC	BFMC	GLLS	MOCABA	BMC	BFMC
C_i	8.035	8.035	8.081	8.176	2.467	2.469	2.611	2.213
$\mathrm{var}(C_i)$	0.3543	0.3543	0.3673	0.0085	0.2185	0.2177	0.0965	0.0032
$\mathrm{cov}(C_i, C_j)$	0.1445	0.1443	0.1137	0.0030	0.1445	0.1443	0.1137	0.0030
σ_i	3.956	3.957	3.962	4.065	0.4892	0.4916	0.6303	0.1802
$\mathrm{var}(\sigma_i)$	0.0841	0.0836	0.0900	0.0020	0.1916	0.1939	0.0900	0.0025
$\mathrm{cov}(\sigma_i, \sigma_j)$	0.0059	0.0061	0.0028	0.0002	0.0059	0.0061	0.0028	0.0002

$$\mathbf{S} = \begin{bmatrix} \frac{\delta C_1}{\delta \sigma_1}\Big|_{\bar{\sigma}_1, \bar{\sigma}_2} & \frac{\delta C_1}{\delta \sigma_2}\Big|_{\bar{\sigma}_1, \bar{\sigma}_2} \\ \frac{\delta C_2}{\delta \sigma_1}\Big|_{\bar{\sigma}_1, \bar{\sigma}_2} & \frac{\delta C_2}{\delta \sigma_2}\Big|_{\bar{\sigma}_1, \bar{\sigma}_2} \end{bmatrix} = \begin{bmatrix} a_1 & b_1 \\ a_2 & b_2 \end{bmatrix}$$

Nominal Case Results

The results for the nominal case are presented in Table 3.2. We expect from theory that GLLS and MOCABA will agree, but they will disagree with BMC and BFMC. This is because GLLS and MOCABA cannot account for the non-normality of $\boldsymbol{\sigma}$ and $\mathbf{C}$. Building off the previous example, we know that the accuracy of the BMC posterior is highly dependent on the quality of the weight distribution and that we can measure the degree of degeneracy with the standard deviation of the weight distribution. Fig. 3.8 showed how the standard deviation of the weight distribution can be used to monitor weight degeneracy. A zero-valued or near zero-valued standard deviation would indicate weight degeneracy occurred. For this nominal case, the standard deviation of the normalized weights was 0.125, indicating that there was not a weight degeneracy and that the BMC posteriors were trustworthy. Additionally, one million samples were used for the stochastic methods to ensure statistical accuracy of the posteriors.

Table 3.2 shows that GLLS and MOCABA agreed well, but disagreed with BMC. The differences were particularly prominent for the variances, and the C_2 and σ_2 mean values. This result indicates that the log-normal distribution had an effect that only BMC can account for. Finally, BFMC disagreed with all other methods, similar to the previous example. It produced small posterior variances, caused by the low prior χ^2 value (calculated with Eq. (2.30)) of 2.86. The posterior χ^2 values of GLLS, MOCABA, BMC, and BFMC were 0.57, 0.57, 1.07, and 0.12, respectively.

Varying χ^2

Fig. 3.12 shows $\mathbf{C}'$ and Fig. 3.13 gives the $\mathbf{C}'$ standard deviations. For C_1, no significant differences appeared between BMC and GLLS/MOCABA, not for the mean or the standard deviation.

C_2, however, did show significant differences from GLLS/MOCABA. Importantly, these differences appeared without the existence of weight degeneracy. Furthermore, these simulations were done with 1 million samples of σ, and therefore were more accurate for this range of χ^2. The discrepancies seen for C_2 were linked to the fact that its distribution deviated larger from normality, exhibited by its kurtosis of 7.1.[4]
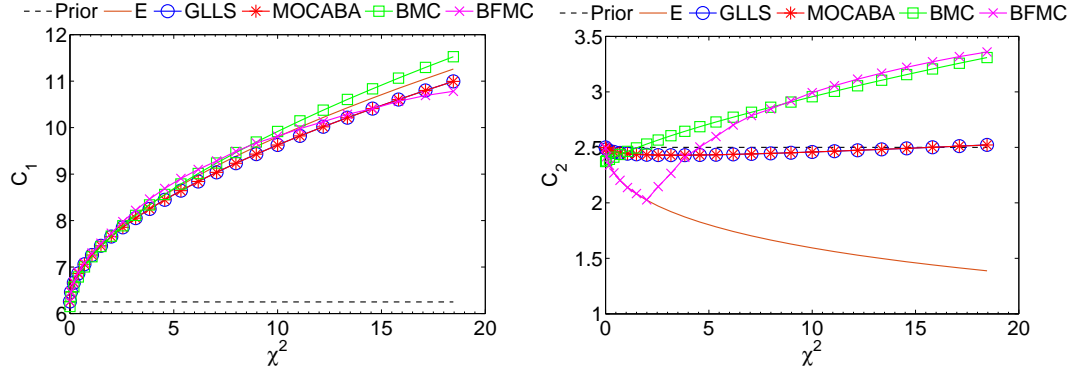
Figure 3.12 – $\mathbf{C}'$ vs. χ^2 for linear, log-normal toy problem.
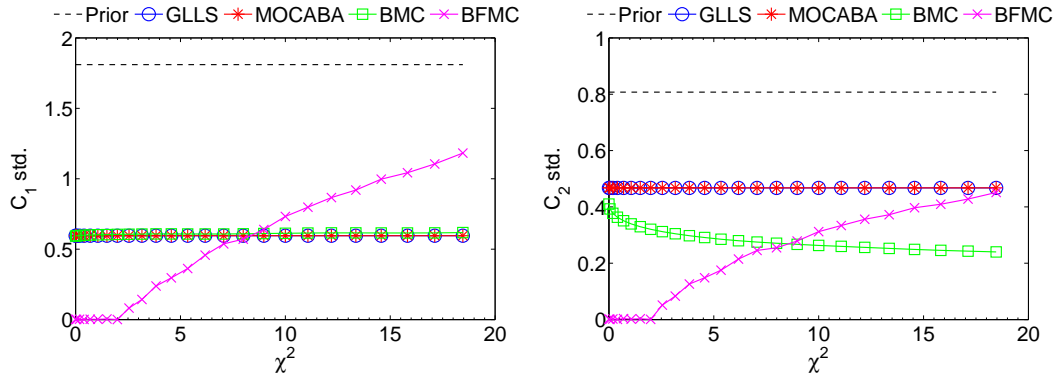
Figure 3.13 – $\mathbf{C}'$ standard deviations vs. χ^2 for linear, log-normal toy problem.

Fig. 3.14 shows the posterior σ values and Fig. 3.15 gives the posterior σ standard deviations. Similar to the $\mathbf{C}$ posterior, σ_2 and its standard deviation exhibit large differences between GLLS/MOCABA and BMC. σ_2 is the more highly non-normal parameter, with a kurtosis of 11.9 and a skewness of 2.1.

3.1.3 Toy Problem Summary

- For a linear, normal application, GLLS, MOCABA, and BMC all agreed well supporting that they are unbiased estimates of the MAP distribution.

---

[4] Kurtosis values greater than 3 indicate non-normality.
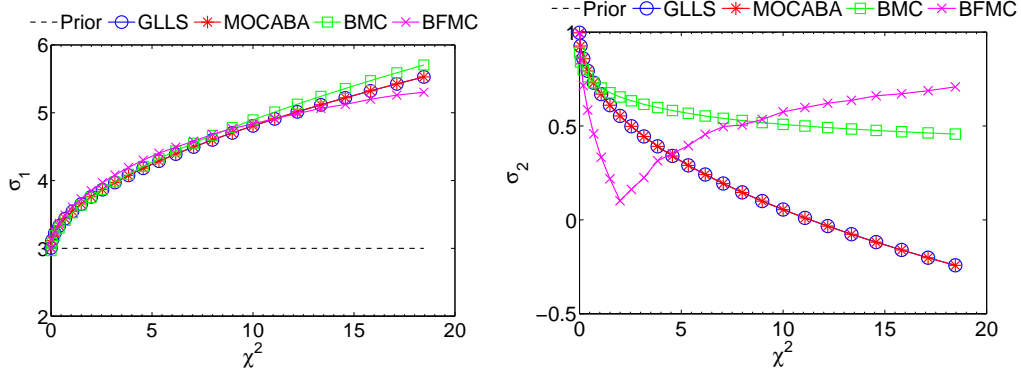
Figure 3.14 – Posterior σ means for linear, log-normal toy problem.
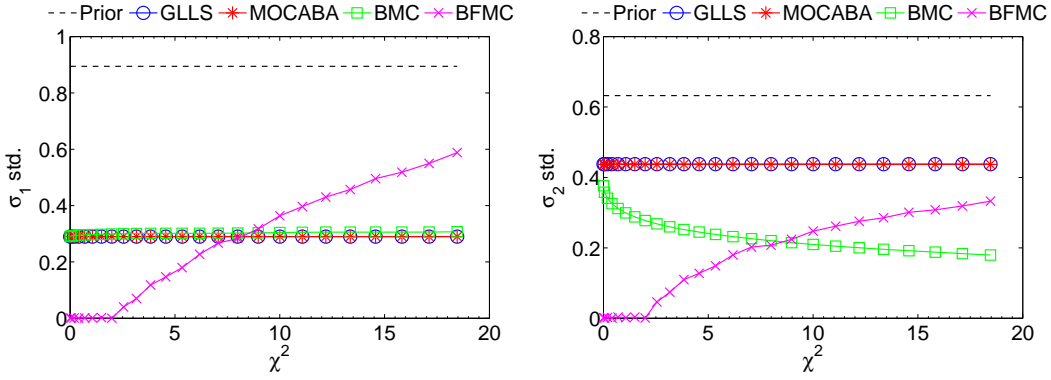
Figure 3.15 – Posterior σ standard deviations for linear, log-normal toy problem.

- BFMC gave inconsistent results compared to the other methods, supporting that it is a biased estimate of the MAP distributions for the toy problem.

- At low prior χ^2 values, BFMC exhibits weight degeneracy. At high χ^2 values, it creates posteriors that are close to the prior.

- BMC is sensitive to the prior χ^2: large χ^2 values cause weight degeneracy.

- There is an upper limit to the prior χ^2 value where total degeneracy occurs (*i.e.* all weights are zero) and BMC fails as an algorithm.

- The standard deviation and CDF of the weight distribution in BMC applications can be used to monitor weight degeneracy.

- Some degree of weight degeneracy can be accounted for with larger sample sizes.

- GLLS, MOCABA, and BMC are ignorant of the degree of consistency between the experimental and calculated data. Large and nonphysical adjustments would occur with these methods when large inconsistencies are present.

- BMC has weight degeneracy in the presence of large inconsistency, *i.e.* large χ^2.

- BFMC can be considered to counter-balance the inconsistency by keeping the posterior close to the prior when χ^2 is large.

- BMC was shown with a linear, log-normal toy problem to account for non-normality of the prior parameters' distributions.

3.2 Application to JEZEBEL-Pu239

The previous section showed how the DA methods behaved for idealized and extremely simplified application cases. It is important to apply the methods to a realistic neutronics problem. We then test their performance and see if the behaviors and issues previously outlined are significant for a real and complex scenario. The following section presents GLLS, MOCABA, BMC, and BFMC applied to a realistic case study: JEZEBEL-Pu239 [50].[5]

The benchmark's integral responses include k_{eff} and the spectral indices F28/F25, F49/F25, and F37/F25. Spectral indices are referred to as Fij which is the fission rate per atom of isotope 23j or 24j of element 9i (*i.e.* i = 2,3,4 for U, Np, and Pu). F37, for example, is the Np-237 fission rate. The nuclear data for Pu-239, Pu-240, Pu-240, U-235, U-238, and Np-237 were included. This means that their nuclear data were perturbed, that sensitivities were calculated for them, and that they were adjusted.

The following nuclear data from ENDF/B-VII.1 [68] were considered: Elastic scattering (MF3/ MT2), inelastic scattering (MF3/MT4), capture (MF3/MT102), fission (MF3/MT18), and the average prompt fission neutron multiplicity (MF1/MT456). The normalized prompt fission neutron spectrum (MF5/ MT18) for an incident neutron energy of 500 keV was considered only for Pu-239 and not the other nuclides. Those nuclides either did not influence the adjustment, like for Np-237, or the data was not available like with Pu-240.

Serpent version 2.1.29 [69] was used for neutron transport. It has Generalized Perturbation Theory (GPT) functions [70] to calculate the sensitivity coefficients for GLLS. The Serpent sensitivity calculations were done with 20 billion neutron histories and 15 latent generations, and followed the criterion proposed in Ref. [71] to have sufficiently accurate sensitivity coefficients.

To perform stochastic sampling, the tool NUSS [72] was used. It assumes multivariate Gaussian distributions as the nuclear data's prior. NUSS currently only supports Gaussian distributions for perturbing nuclear data. It creates multigroup perturbations from nuclear data covariances and applies them to the point-wise ACE-format nuclear data used in Serpent. The perturbations were then used to calculate the posterior nuclear data with MOCABA, BMC, and BFMC.

NUSS generated 10,000 samples of all of the aforementioned isotopes' nuclear data. For each

---

[5]These results were published in Ref. [67].

Figure 3.16 – The JEZEBEL-Pu239 experimental setup [50].

NUSS sample, a corresponding Serpent simulation with 200 million neutrons was done. In comparison to the sensitivity calculations, the 10,000 Serpent calculations for stochastic DA needed approximately four times more CPU time when running on equivalent hardware. The sensitivity coefficients and nuclear data were processed into a 187-energy-group structure suitable for fast reactors [62]. Importantly, it should be noted that a significant amount of work was done during this thesis to maintain and make more efficient the NUSS code system.

For NUSS perturbations, two important things should be stated. Firstly, the inelastic scattering cross section's covariance data are given for the total reaction, or MT4, instead of for the discrete level excitation cross sections from MT51 to MT91. When inelastic scattering is perturbed, the perturbation factors from MT4 are applied to all available MTs from 51-91. Secondly, for the normalized fission spectrum, the ACE-format data are given for incident neutron energies. Only one set of covariance data (at 500 keV) is used to modify all ACE fission spectrum data, regardless of the incident neutron energy. This is considered to be a reasonable assumption because of the neutron energy distribution in JEZEBEL-Pu239 and due to the limited availability of fission spectrum covariances. Additionally, the spectrum of fission neutrons is weakly dependent on initial energy, except for high neutron energies [62].

When NUSS creates perturbations, a Cholesky decomposition is performed on the nuclear data covariance matrix to ensure that it is semi-positive definite. NUSS fixes, in an *ad hoc* way, a negative definite matrix when negative eigenvalues exist. To have agreement between GLLS and the stochastic methods, it is important that this corrected matrix is used in GLLS and not the original, uncorrected matrix. In fact, when we used this uncorrected matrix in GLLS, the posterior nuclear data covariance matrix had irrational results, like negative variances.

The experimental covariances were taken from Ref. [9]. For the methodology and modeling

variance component in $\mathbf{M_{EM}}$, the statistical uncertainties of the calculated values from the Serpent simulation are used and are assumed to be uncorrelated. Ref. [9] recommends caution when adopting statistical errors of Monte Carlo codes because they do not use the correlation between fission sources from successive cycles to calculate the error. Because the correlation is not used, the real statistical error is underestimated by a factor of 1.4-3.1. Following their recommendations, the $\mathbf{C}$ values' statistical errors were multiplied by a factor of 2 in this study and then used in $\mathbf{M_{EM}}$.

A code system was developed during the thesis to perform DA. It is called DAN for **D**ata **A**ssimilation**N**. DAN reads multigroup nuclear data and covariance data, reads integral parameter input data in the form of a user input file, performs all necessary pre-processing of the inputs, does the actual DA calculations for GLLS, MOCABA, and BMC/BFMC, writes numerous output files, and plots sensitivity profiles and posterior nuclear data. DAN is specialized for Serpent and NUSS, but could easily be modified for other code systems.

3.2.1 Bootstrapping

Only a limited sample size N can be used in stochastic DA. That means that for independent and identical DA applications, *i.e.* with two different sample sets, different posteriors will be obtained. With smaller N, the posteriors will be less converged and there will be more variation between independent DA applications. In this study, the uncertainty associated with the posteriors from stochastic DA were estimated with a bootstrapping approach [73].

The bootstrap method estimates the standard error of the posterior values, *i.e.* the posterior calculated values and their uncertainty as well as the posterior nuclear data and their uncertainty. The bootstrap was performed by sampling with replacement n times from the 10,000 random samples of nuclear data and calculated values. This led to n sample sets of 10,000 samples. With each random sample of the sample set, MOCABA, BMC, and BFMC posteriors were calculated, leading to n sets of posteriors. The statistics of the posterior parameter of interest, θ, were then calculated with the n bootstrap samples. The posterior's bootstrap mean, $\bar{\theta}$, was calculated as well as the standard error of the mean, $SE_{\bar{\theta}}$, using Eqs. (3.3) and (3.4).

$$\bar{\theta} = \frac{\sum_{i=1}^{N} \theta_i}{n} \tag{3.3}$$

$$SE_{\bar{\theta}} = \left(\frac{\sum_{i=1}^{n} (\theta_i - \bar{\theta})^2}{n-1} \right)^{1/2} \tag{3.4}$$

In this study, 500 bootstrap samples were taken, leading to a 3% standard error in $\bar{\theta}$ and $SE_{\bar{\theta}}$ [74], which was considered to be sufficiently accurate four our purposes. Assuming that the bootstrap samples obey a normal distribution, 95%-confidence intervals are presented on the

results. They were calculated with Eq. (3.5), where $z^\alpha = 1.96$ for a 95%-confidence interval.

$$\theta \in \bar{\theta} \pm z^\alpha SE_{\bar{\theta}} \tag{3.5}$$

3.2.2 Posterior Calculated Values

The prior calculated-to-experimental ratios (**C**/**E**) and the prior uncertainties are presented in Table 3.3. The table presents the experimental standard deviation, $\Delta_\mathbf{E}$, the modeling standard deviation in **C** from Monte Carlo transport, $\Delta_\mathbf{M}$, and, the standard deviation of **C** caused by the prior nuclear data uncertainty, $\Delta_\mathbf{C}$. $\Delta_\mathbf{C}$ was calculated with two different approaches. The first, referred to as GPT in Table 3.3, evaluated the uncertainty with first-order error propagation using the GPT-calculated sensitivity coefficients and $\mathbf{M}_\sigma$, or $\mathbf{SM}_\sigma\mathbf{S}^T$.[6] The second, referred to as NUSS, is the population standard deviation of the 10,000 Serpent simulations done with the 10,000 NUSS-perturbed nuclear data. For these relative standard deviations, we see good agreement between the NUSS and GPT priors.

Table 3.3 – Prior input parameters into the DA methods. $\Delta_\mathbf{E}$, $\Delta_\mathbf{M}$, and $\Delta_\mathbf{C}$ are given as relative standard deviations.

	$\Delta_\mathbf{E}$(%)	$\Delta_\mathbf{M}$(%)	$\Delta_\mathbf{C}$ (%)		**C/E**
			GPT	NUSS	
F28/F25	1.1	0.2	3.5	3.5	0.978
F49/F25	0.9	0.2	0.8	0.8	0.975
F37/F25	1.4	0.1	3.5	3.5	0.988
k_{eff}	0.200	0.007	0.749	0.777	0.99971

Table 3.4 presents the **C** adjustments as posterior calculated-to-experimental ratios (**C'**/**E**) and posterior calculated-value uncertainties from nuclear data ($\Delta_{\mathbf{C'}}$). First comparing **C'**/**E** for the reaction rate ratios, only F28/F25 shows any difference at 0.001 between BMC and GLLS/MOCABA. BFMC shows slightly larger differences from the other three DA methods, at +0.002 for F28/F25 and F49/F25, and +0.001 for F37/F25. For k_{eff}, differences of 14-39 pcm are present. The $\Delta_{\mathbf{C'}}$ values show very small differences between GLLS, MOCABA, and BMC. BFMC, however, shows larger disagreement for F28/F25, F37/F25, and k_{eff}, where it predicts smaller $\Delta_{\mathbf{C'}}$ than the other methods. Smaller $\Delta_{\mathbf{C'}}$ values with BFMC were observed in Section 3.1 where the methods were analyzed with toy problems.

The observed differences in Table 3.4 are not significant from an engineering and application perspective. From a theoretical standpoint, they do warrant further examination. The simplest explanation is that they were caused by the limited sample size used in the stochastic DA methods. If an infinitely large sample size was used and there were still differences between the methods, then the differences could be attributed to other sources. These include the

---

[6]Often called the "Sandwich Rule" in nuclear engineering

Table 3.4 – Posterior calculated-to-experimental ratios ($\mathbf{C'}/\mathbf{E}$) and posterior relative standard deviations from nuclear data ($\Delta_{\mathbf{C'}}$).

	$\mathbf{C'}/\mathbf{E}$				$\Delta_{\mathbf{C'}}$ (%)			
	GLLS	MOCABA	BMC	BFMC	GLLS	MOCABA	BMC	BFMC
F28/F25	0.996	0.996	0.997	0.998	1.0	1.0	1.0	0.8
F49/F25	0.984	0.984	0.984	0.986	0.5	0.5	0.5	0.5
F37/F25	0.994	0.994	0.994	0.995	1.3	1.3	1.2	1.0
k_{eff}	0.99982	0.99996	1.00009	1.00021	0.192	0.192	0.193	0.160

methods themselves, the properties of the integral parameters (*e.g.* non-linearity or non-normality), or to problems in the analysis scheme such as the approximations made in NUSS or the statistical uncertainty of the Serpent-calculated sensitivities. Ideally, an infinitely large sample size could be used and this source of uncertainty could be eliminated. While this is impossible, it is possible to estimate a confidence interval for each of the posteriors. If the differences are larger than the confidence interval, we can more confidently attribute them to the DA methods or to other sources, rather than to simply the limited sample size.

Table 3.5 shows the 95%-confidence intervals of the posteriors as estimated with the bootstrap analysis detailed in Section 3.2.1. For $\mathbf{C'}/\mathbf{E}$ and $\Delta_{\mathbf{C'}}$ of the reaction rate ratios, the confidence intervals were larger than or equal to the differences between the DA methods. This indicates that the results agreed within the statistical behavior of stochastic DA methods. The $\mathbf{C'}/\mathbf{E}$ of k_{eff} showed significant differences only between GLLS and MOCABA. Here, the difference was 18 pcm, where the 95%-confidence interval of MOCABA was 1 pcm. Given that k_{eff} is highly linear and normal, it is unlikely that this was caused by the methods themselves, but rather by other sources like the NUSS perturbation scheme. Because this difference is so small from an application standpoint, it was not investigated further in this work.

The $\Delta_{\mathbf{C'}}$ of k_{eff} shows statistically significant differences between BFMC and the other DA methods. Its 95%-confidence interval of 0.012% is smaller than the differences with the other DA methods, which are 0.032% and 0.033%. Of course, this is also related to the fact that more significant digits are shown for k_{eff} than for the reaction rate ratios. This significant difference supports observations of the toy problem analysis of Section 3.1. There, BFMC was shown to be a biased estimate of the MAP distribution.

Table 3.5 – Bootstrap-estimated standard errors of the posterior calculated-to-experimental ratios ($\mathbf{C'}/\mathbf{E}$) and posterior relative standard deviations from nuclear data ($\Delta_{\mathbf{C'}}$).

	$\mathbf{C'}/\mathbf{E}$			$\Delta_{\mathbf{C'}}$ (%)		
	MOCABA	BMC	BFMC	MOCABA	BMC	BFMC
k_{eff}	0.00001	0.00017	0.00024	0.000	0.009	0.012
F28/F25	0.000	0.000	0.000	0.0	0.1	0.2
F49/F25	0.000	0.001	0.002	0.0	0.1	0.1
F37/F25	0.000	0.001	0.002	0.0	0.1	0.2
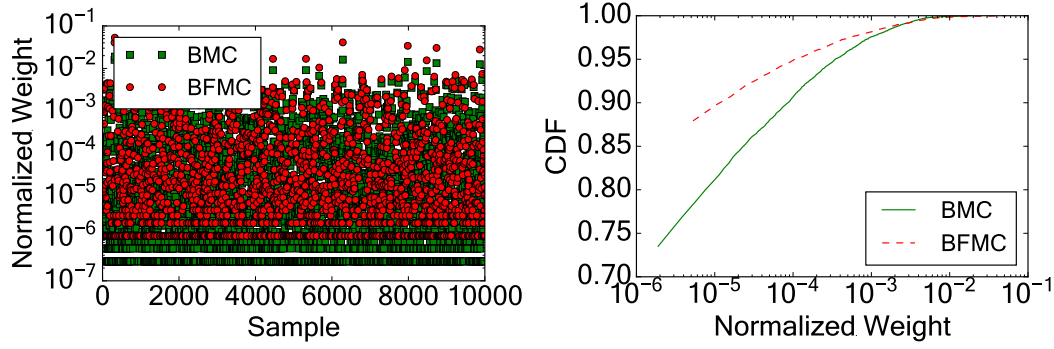
Figure 3.17 – Weight of each nuclear data sample set in BMC.

To assess the degree of weight degeneracy, we previously used the standard deviations of the weight distributions. We saw that BMC results became highly sensitive to sample size when its weight distribution's standard deviation was small. If this standard deviation approached 0, *i.e.* weight degeneracy occurred, the BMC posteriors became unreliable. When the BMC and BFMC weight distribution standard deviations were approximately equal, their posteriors showed reasonable agreement. For JEZEBEL-Pu239, the standard deviations of the BMC and BFMC normalized weight distributions[7] were 0.0006 and 0.0011, respectively. Their approximately equal values show how BMC and BFMC can agree well for this application case.

Figure 3.17 gives the normalized weights created by BMC and BFMC and the CDF of their weight distributions. Several interesting phenomena appear in this figure. Firstly, a lower weight bound can be observed in BMC and BFMC. In the weight distribution at left, this appears as horizontal lines where many samples have identical weight, *e.g.* at a weight of 9×10^{-6}. This is a round-off error in Eq. (2.24). A high χ^2 would mean that the given random sample had worse agreement between **C** and **E**. From the CDF, we see that approximately 75% of the BMC weights have this low value of 9×10^{-6}. Practically speaking, 75% of simulations did not serve to calculate the posterior because the weights were so small. Additionally from Fig. 3.17, what BFMC does to the weight distribution is more apparent. Effectively, it pushes the very low-valued weights up, as can be observed by where the horizontal, low weight lines are in the figure at left. The line shifts from 9×10^{-6} to 2×10^{-6}.

We noted that for BMC's weight-distribution standard deviation, we would expect that the method's accuracy might be dependent on the sample size. Obviously, from Table 3.4 there were enough samples to have accurate results. Nevertheless, it is interesting to examine the posteriors when fewer samples are used to see how this may affect a real application case. This is important because 10,000 samples can be impractical for some applications, especially if many benchmarks are used. Additionally, the bootstrap 95%-confidence intervals can be examined to see how they vary with different sample sizes.

Fig. 3.18 shows **C**$'$/**E** and $\Delta_{\mathbf{C}'}$ calculated with MOCABA, BMC, and BFMC at increasing popu-

---

[7]Normalized to the sum of all weights.

56
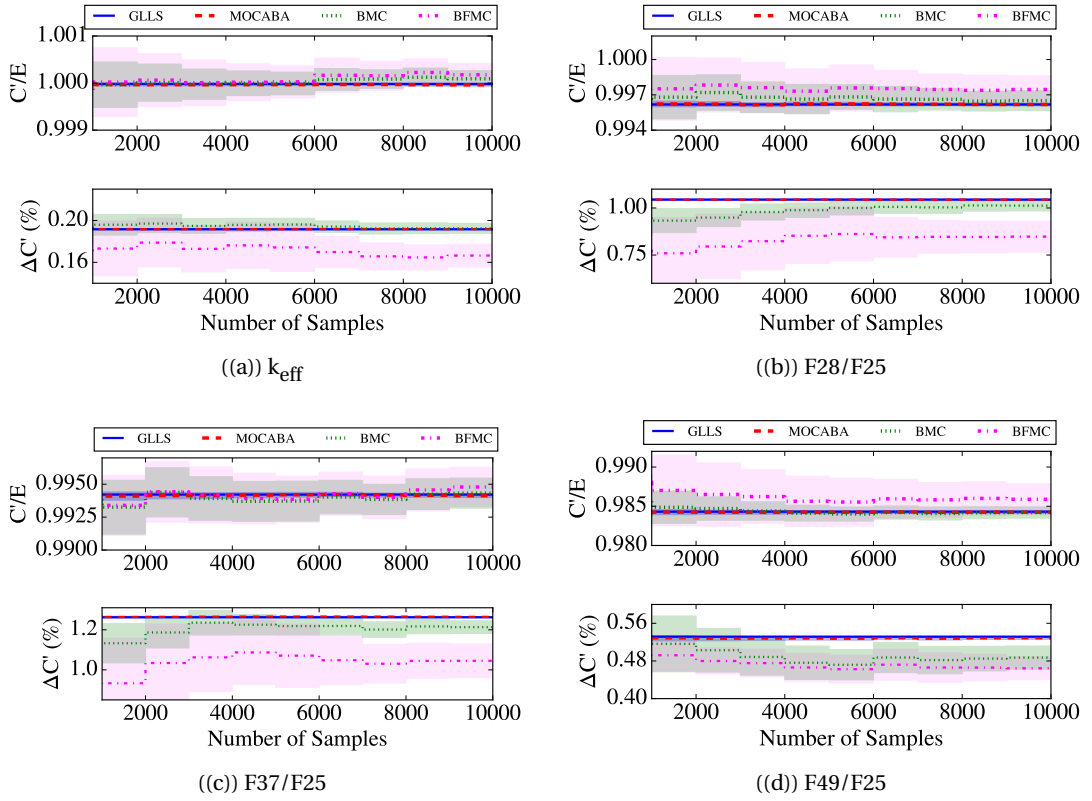
Figure 3.18 – $\mathbf{C'}/\mathbf{E}$ and $\Delta_{\mathbf{C'}}$ at every 1,000 additional samples to the population. Shaded regions are bootstrap-estimated 95%-confidence intervals (MOCABA's red region is difficult to discern with these axes).

lation sizes. At every 1,000 samples, the bootstrap-estimated 95%-confidence interval (see Eq. (3.5)) was calculated with 500 bootstrap samples and plotted. In general, BMC and BFMC showed larger fluctuations with sample size than MOCABA. Additionally, the bootstrap confidence intervals were larger for BMC and BFMC than for MOCABA. Both of these effects were more prominent for $\Delta_{\mathbf{C'}}$ than $\mathbf{C'}/\mathbf{E}$. BMC and BFMC did not have comparable convergence properties to MOCABA with an increasing number of samples. The BFMC $\Delta_{\mathbf{C'}}$ could be quite different from the other methods, even at 10,000 samples. Considering also their 95%-confidence intervals, it is unlikely that these differences were caused by the limited sample size.

We can examine BMC on a smaller sample-size interval to show how weight degeneracy affects convergence. Fig. 3.19 shows the convergence behavior of the BMC-calculated $\mathbf{C'}$ for F49/F25 vs. the sample number. Additionally, it shows the weight of each sample. In the figure, the posterior shows significant fluctuations of several tenths of a percent up to ~2,000 samples. Recall that when weight degeneracy occurs only a few very rare weights contribute to calculate the posterior. The large fluctuations correspond to rare samples that have an extremely large weight. For example at the 40th sample, a rare weight appears that significantly changes
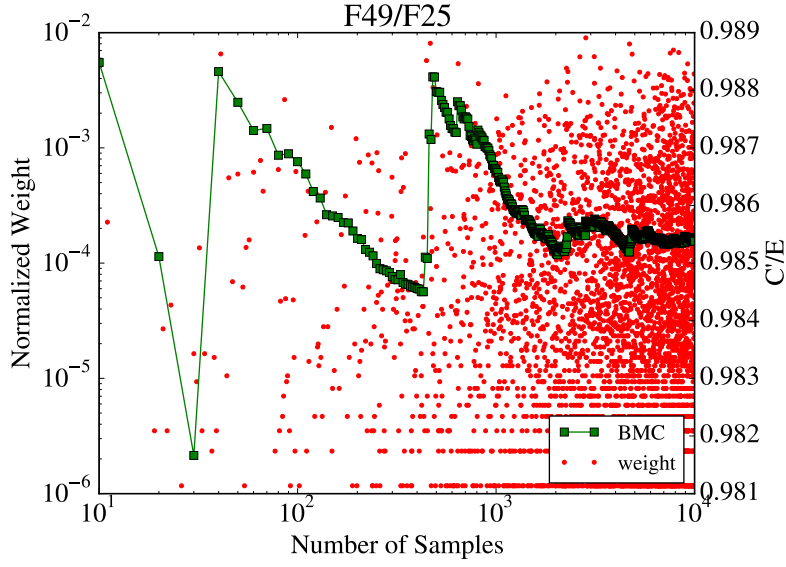
Figure 3.19 – Effect of rare weights on BMC's F49/F25 $\mathbf{C}'$.

the posterior. This occurs again at the 600th sample and several times again, albeit to a less significant extent at more than 1,000 samples. These outliers significantly change the posterior weighted average and lead to slower convergence behavior. With more weight degeneracy, there are more significant outliers. Their rarity then slows down the convergence of BMC.

The posterior χ^2 per DoF (N_E), calculated with Eq. (3.6), using each DA method is useful to globally assess the adjustment. The prior χ^2 per DoF was 1.21, showing that the prior already had good agreement between $\mathbf{C}$ and $\mathbf{E}$. GLLS, MOCABA, BMC, and BFMC created posterior χ^2 values per DoF of 0.58, 0.59, 0.62, and 0.47, respectively. BFMC's smaller posterior χ^2 was caused by its $\mathbf{C}'/\mathbf{E}$ values being slightly closer to 1.0.

$$\frac{\chi^2}{N_E} = \left(\mathbf{E} - \mathbf{C}'\right)^T (\mathbf{M}'_{\mathbf{C}} + \mathbf{M_{EM}})^{-1} \left(\mathbf{E} - \mathbf{C}'\right)/N_E \tag{3.6}$$

The small prior χ^2 per DoF also helps to explain why BFMC returned smaller posterior uncertainties than the other three DA methods. In the previous section, it was shown that for small prior χ^2 values, the bias in BFMC creates underestimated uncertainties for the MAP distribution. Here, the prior χ^2 was in the region where this behavior occurs.

Figure 3.20 displays the relative differences between the prior and posterior $\mathbf{M_C}$. The relative difference was calculated as Eq. (3.7), where $\mathrm{cov}(C_i, C_j)$ is the covariance between the calculated value of integral parameter i and j. In general, the posterior covariances agreed well between the methods. For GLLS, its most noticeable discrepancy with the other methods is that it reduced the covariance between k_{eff} and F49/F25 to a larger extent. BFMC shows larger reductions for all covariances and variances than the other methods (except for the GLLS
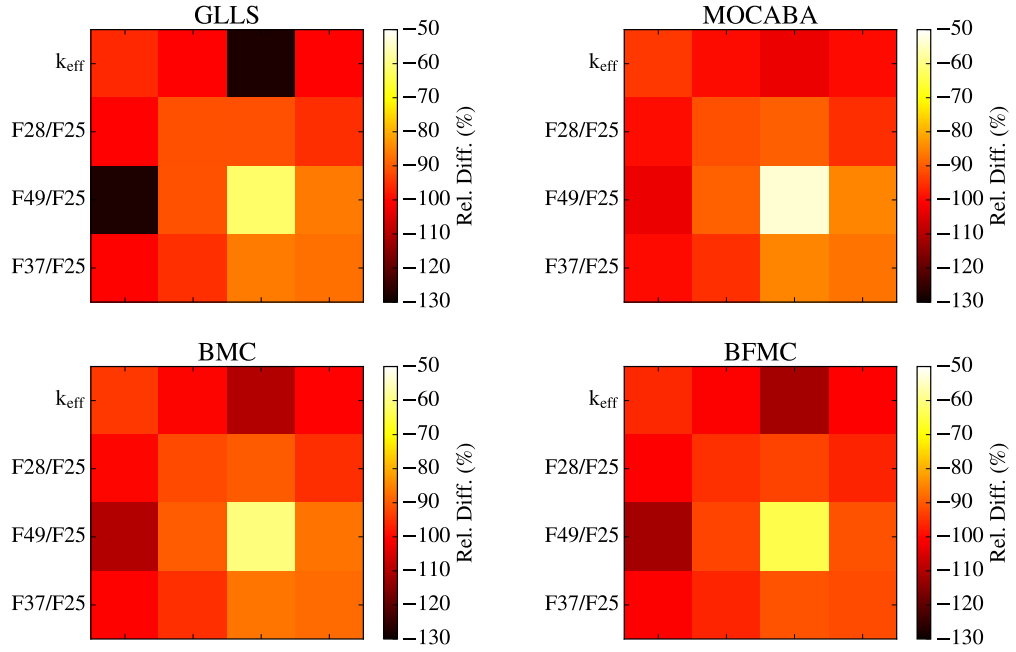
Figure 3.20 – Relative differences between prior and posterior $\mathbf{M_C}$.

covariance between k_{eff} and F49/F25).

$$\frac{\text{cov}(C_i', C_j') - \text{cov}(C_i, C_j)}{\text{cov}(C_i, C_j)} \tag{3.7}$$

3.2.3   Posterior Nuclear Data

In this section, the adjustments of nuclear data with each DA method are presented and analyzed. The analysis focuses on Pu-239 and its elastic, inelastic, fission, and capture (n,γ) cross sections and on its fission multiplicity ($\bar{\nu}$) and fission spectrum (χ). The adjustments of these six nuclear data are presented in Fig. 3.21. Beginning at the top left:

- **Elastic Scattering, Fig. 3.21(a)**: GLLS, MOCABA, BMC, and BFMC show agreement (within the estimated confidence intervals) across all energy ranges for relative adjustments and for the posterior standard deviations. BMC and BFMC have larger bootstrap-estimated standard errors than MOCABA, with BFMC being the largest.

- **Inelastic Scattering, Fig. 3.21(b)**: GLLS and MOCABA adjustments agree within the 95%-confidence interval. BMC and BFMC's adjustments again show more disagreement, but have larger standard errors. At ~0.1 MeV, the disagreements are slightly outside of the 95%-confidence interval, but would be included in a 99% interval.

((a)) Elastic Scattering, (n,e)

((b)) Inelastic Scattering, (n,i)

((c)) Fission, (n,f)

((d)) Capture, (n,γ)

((e)) Fission Multiplicity, $\bar{\nu}$

((f)) Fission Spectrum, χ
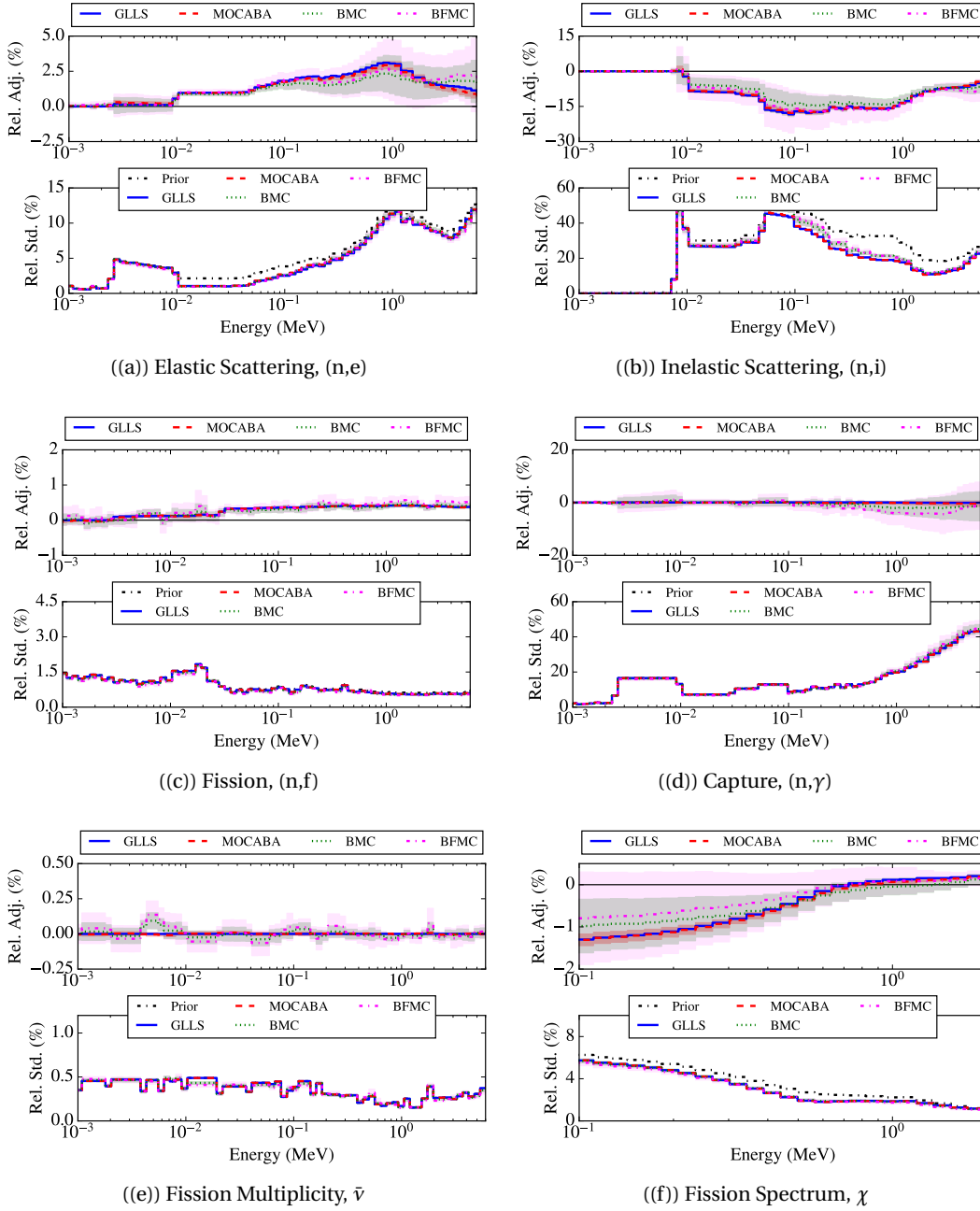
Figure 3.21 – Nuclear data adjustments for Pu-239. Shaded regions are 95%-confidence intervals estimated with bootstrapping. Each subfigure has the relative adjustment from prior to posterior, $(\boldsymbol{\sigma}' - \boldsymbol{\sigma}_0)/\boldsymbol{\sigma}_0$, above and the prior and posterior relative standard deviations below.

- **Fission, Fig. 3.21(c)**: MOCABA, GLLS, BMC, and BFMC show similar adjustments, with BFMC showing the largest disagreement, but also the largest bootstrap uncertainty.

- **Capture, Fig. 3.21(d)**: MOCABA and GLLS show consistent low-valued adjustments except for above 0.1 MeV. BMC and BFMC create larger adjustments (up to -2%), but are
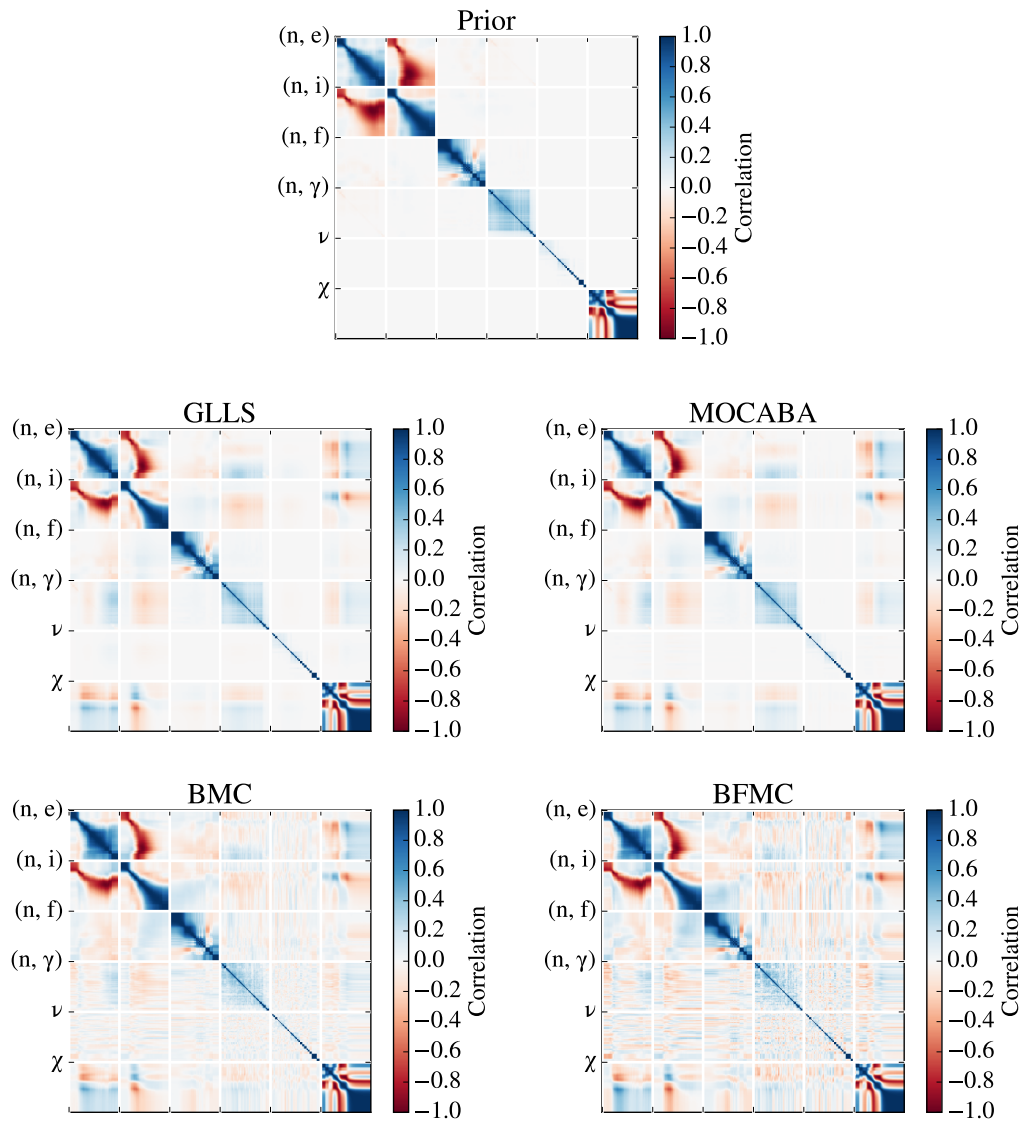
Figure 3.22 – Prior and posterior nuclear data correlation matrices plotted from high to low energy for each nuclear datum on the range of 20 MeV to 1 keV.

likely not statistically significant as shown by the large bootstrap uncertainty.

- **Fission Multiplicity, Fig. 3.21(e)**: GLLS shows small and indistinguishable adjustments. The stochastic methods exhibit non-zero adjustments, with BFMC's being as large as 0.10%. They are not likely statistically significant, as the confidence intervals cover 0%.

- **Prompt Fission Neutron Spectrum, Fig. 3.21(f)**: Good agreement between MOCABA and GLLS. Larger, but statistically insignificant, disagreement for BMC and BFMC especially below 0.5 MeV.

The general trend is that the adjustments with all four methods agree within their bootstrap confidence intervals. Potential biases from non-linearities or from other sources (*e.g.* NUSS sampling, sensitivity uncertainties) were not significant enough to show a difference for the considered sample size. We have demonstrated that the stochastic methods can effectively reproduce the GLLS adjustments. They could be used to either verify GLLS adjustments or for non-linear/non-normal problems. This is important for Chp. 5 where a GLLS reference solution is not available when adjusting fission yield data.

Another general trend is that the stochastic methods' uncertainty is higher at energy ranges with greater nuclear data uncertainties. For instance, the bootstrap uncertainties are large above 1 MeV for capture and elastic scattering, and between 0.1 and 0.5 MeV for the fission spectrum. These are energy regions where there is low sensitivity of the integral data to the nuclear data. These nuclear data received large perturbations because of their large uncertainties, but the perturbations create no physical effect in the integral parameters. This then creates random oscillations that take many samples to converge back to the nominal value in the posterior.

The Pu-239 nuclear data's correlation matrices for the prior and each of the posteriors are plotted in Fig. 3.22. Comparing the change from prior to posterior, we see that all four DA methods create correlations that did not previously exist, for example between elastic scattering, (n, e), and fission spectrum (χ), or between inelastic scattering, (n, i), and capture, (n, γ). These correlations between nuclear data that did not exist in the prior are often a large source of the uncertainty reduction in the posterior calculated values [24]. The correlations that did exist in the prior, for instance between (n, e) and (n, i) or within the energy groups of (n, i), were also reduced by all four DA methods.

The GLLS and MOCABA correlation matrices agree well. The BMC matrix shows the same trends as MOCABA and GLLS but has a large number of weak correlations (between ±0.2) in areas where MOCABA and GLLS produce zero-valued correlations. BFMC also shows the same trends and creates to an even larger extent these weak correlations. As evidenced before by the bootstrapping analysis, these two methods have larger uncertainties and these weak correlations are likely just statistical noise caused by using a limited sample size. Correlations between the nuclear data of different nuclides (*e.g.* between Pu-239 and Pu-241), which are not plotted here, are also created by the DA methods. These correlations do not exist in the prior covariance matrix and can also be an important source of uncertainty reduction in the posterior calculated values.

3.3 Conclusions

Three data assimilation methods have been compared: Generalized Linear Least Squares, Monte Carlo Bayesian Analysis, and Bayesian Monte Carlo (or GLLS, MOCABA, and BMC, respectively). Additionally, a subset of the BMC method, called BFMC, was also analyzed. The comparison was done using toy problems and realistic case study. The case study consisted of

Serpent version 2.1.29, ENDF/B-VII.1 nuclear data, and the JEZEBEL-Pu239 benchmark. For GLLS, sensitivity coefficients were calculated with Serpent. For MOCABA and BMC, random sampling was performed on the ACE data files using the NUSS code.

We concluded that MOCABA and BMC can effectively reproduce the posterior results from GLLS if they are employed with sufficiently large sample sizes. The toy problem showed that BMC can indeed account for non-normality. Importantly, it should be noted that non-linearity and non-normality often go hand in hand. If MOCABA were applied to a non-linear problem, its normality assumption may hurt its accuracy because the non-linearity may cause a non-normality. These findings are important for future applications where MOCABA and BMC could be used for integral parameters with non-normal responses to nuclear data perturbations, such as in burnup simulations.

BMC should be applied while carefully observing its weight distribution and the convergence of its posteriors. If there is sufficient weight degeneracy, many samples may be needed to have converged results. BFMC showed inconsistent results in comparison to the other methods, sometimes agreeing and disagreeing. For the JEZEBEL-Pu239 application, the disagreements were not as drastic as observed in the toy problem. Importantly however, BFMC still achieves the goal of improvement from prior to posterior. BFMC also tends to show even larger bootstrap-estimated uncertainties than BMC, while MOCABA showed the smallest.

From a mathematical view-point, the results of this chapter provide evidence that BFMC does not provide the true mathematical posterior. In fact for low χ^2 values, BFMC can provide dangerous posteriors that have very small uncertainties compared to the prior. The user of BFMC must be aware that it is not an ideal method for low χ^2 values. Luckily, this is rarely the case for complex scenarios because if there is a low χ^2 there would be no motivation to do DA in the first place.

Similarly, the user must be aware that for high χ^2 values GLLS, MOCABA, and BMC are also not ideal methods because they will result in over-fitting of the nuclear data and possibly spurious adjustments. Here, the fact that BFMC is biased can be considered "advantageous" because it helps to prevent an over-fitting of the nuclear data. A user of data assimilation has to then balance these considerations when working. Ideally, the integral data being used has a low-range of χ^2 values and BFMC can be avoided as a method and there is no danger of over-fitting.

3.4 Chapter's Key Points

- A toy problem showed that GLLS, MOCABA, and BMC are all unbiased estimates of the maximum *a posteriori* (MAP) distribution. BFMC is a biased estimate of the MAP distribution

- A real application with JEZEBEL-Pu239 confirmed this conclusion and also showed that BFMC, for this case, gave agreeing results with the other methods

- The consistency of the integral data set, or the size of χ^2, is important to consider in the adjustment

- If DA is done using GLLS, MOCABA, or BMC with an inconsistent data set, large adjustments can occur that may not respect the physics of the system being studied

- Large χ^2 values will cause weight degeneracy with BMC. In such as case, either many samples are needed to have a converged posterior, or all weights will be zero and no posterior can be calculated

- Inconsistency of the integral data is auto-compensated for by BFMC. As χ^2 gets bigger, BFMC will give posteriors that converge to the prior

- All of this highlights the importance of accounting for inconsistencies, either with a filtering technique or MLO

4 Data Assimilation of LWR-PROTEUS Phase II

> With four parameters I can fit an elephant, and with five I can make him wiggle his trunk.
>
> – John von Neumann

A primary goal of this thesis was to implement DA methods in the sensitivity analysis and uncertainty quantification tool SHARK-X and to perform DA with Proteus experimental data. This chapter presents how these two goals were approached with one study. The sensitivity coefficients and randomly-sampled nuclear data produced by SHARK-X were used to assimilate integral parameters from the LWR-PROTEUS Phase II experiment. The chapter is organized to first motivate the DA in Section 4.1, then to describe the LWR-PII experiment, SHARK-X, and the CASMO-5M models in Section 4.2, and finally to present the results in Section 4.3.

4.1 Introduction

The LWR Phase II (LWR-PII) experimental campaign was designed to investigate nuclear fuel with high burnups [75]. It took highly exposed fuel rods from Swiss nuclear power plants and measured their reactivity worth in the Proteus research reactor. The campaign was used at the PSI to validate simulated reactivity losses in high-burnup fuel [76, 77]. These simulations are vital for core design (both for fuel management and safety analysis) and for burnup credit, which is important for the criticality safety of the storage and transportation of spent fuel.

The experiment was used to validate CASMO-5M simulations with help from the tool SHARK-X for UQ and SA. SHARK-X [78, 79, 80, 81, 82, 83, 84] estimates the uncertainty of CASMO-5M calculations from nuclear data. Biases between the CASMO-5M calculations and the experiments were calculated to be as large as 7% and uncertainties from nuclear data were as high as 9% [85]. To reduce these biases and the calculation uncertainty, as well as to try to understand from where they originate, the DA methods discussed in this thesis were applied.

Because SHARK-X can perform uncertainty quantification with sensitivity coefficients or with stochastic sampling, DA methods using both of these techniques were implemented. GLLS was developed around SHARK-X's sensitivity features. For the stochastic sampling tools in SHARK-X, the methods of BMC, BFMC, and MOCABA were developed. The implementation of the DA methods is analyzed in terms of how they adjust the calculated values of integral parameters and reduce their associated uncertainty as well as how they adjust input nuclear data and their uncertainties. The ultimate goal is to gain insights into the bias behavior of the CASMO-5M simulations of LWR-PII and more generally into the bias and uncertainty of the modeled reactivity effects of high-burnup fuel with CASMO-5M. Does the bias originate from nuclear data, and if so, which nuclear data are the leading culprits?

4.2 Material and Methods

4.2.1 LWR-PROTEUS Phase II Experimental Campaign

The LWR-PII measured the effect of burnup on fuel reactivity. Proteus in this campaign was configured to represent an LWR. Irradiated fuel samples were inserted into and removed from the center of the reactor to evaluate the reactivity loss of fuel due to exposure. Eleven of these fuel samples (shown in Table 4.1) were used in this study.

Table 4.1 – Description of the fuel samples [75].

ID	Type	# of Cycles	Burnup (MWd/kg)
U1	UO_2	3	~38
U2	UO_2	3	~54
U3	UO_2	5	~71
U4	UO_2	5	~75
U5	UO_2	3	~91
U6	UO_2	7	~92
U7	UO_2	10	~121
M1	MOX	1	~21
M2	MOX	2	~44
M3	MOX	3	~64
M4	MOX	4	~72

The fuel samples were inserted into a centrally located stainless steel tank, see Fig. 4.1, filled with different moderators. The moderators were full-density H_2O, a mixture of H_2O and D_2O (37.0 w.% D_2O), and borated H_2O (2,023 ± 46 ppm of boric acid). In this chapter, the borated H_2O moderator is referred to as BHO and the D_2O/H_2O moderator as DHO. The reactivity was measured for each moderator, leading to 32 reactivities being available for DA.[1]

---

[1]The reactivity for the U4 sample in the BHO moderator was not measured, which is why there are 32 and not 33 reactivities.
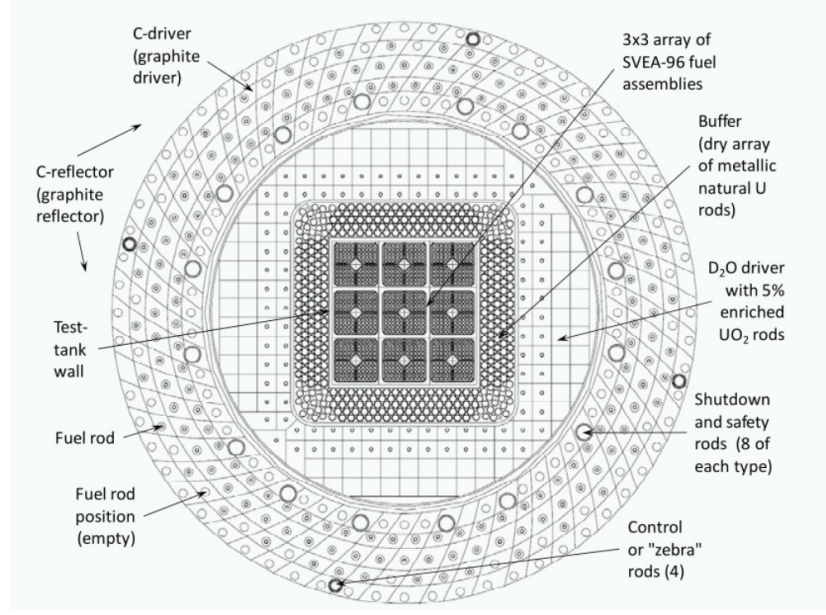
Figure 4.1 – Configuration of the center of Proteus during LWR-PII [86].

The absolute reactivity worth of a fuel sample, $\Delta\rho$, was measured by replacing a reference sample (U_{ref}) of fresh, 3.5 w.% enriched UO_2 with the given burned fuel sample, U_i. The reactivity worth is calculated with Eq. (4.1), where k_{ref} is k_{eff} with U_{ref} inserted into the core, and k_i the k_{eff} with U_i inserted. The $\Delta\rho$ of a natural uranium sample (U_{nat}) was also evaluated and used to create a *relative reactivity worth*, or $\Delta\rho_{rel}$, as seen in Eq. (4.2). This $\Delta\rho_{rel}$ is the integral parameter used for DA in this study.

$$\Delta\rho = \frac{1}{k_{ref}} - \frac{1}{k_i} \tag{4.1}$$

$$\Delta\rho_{rel} = \frac{\Delta\rho(U_{ref} \rightarrow U_i)}{\Delta\rho(U_{ref} \rightarrow U_{nat})} \tag{4.2}$$

In order to accurately perform a DA, the covariances between the experimental $\Delta\rho_{rel}$ needed to be estimated. Because each $\Delta\rho_{rel}$ used a normalization to a U_{nat} sample, $\Delta\rho_{rel}$ sharing the same moderating condition have an inherent correlation. The analysis to estimate these experimental correlations is provided in Appendix A.3.1. It describes other possible sources of correlation, besides only the normalization.

The standard deviations of the $\Delta\rho_{rel}$ are ~0.7% and the off-diagonal correlation coefficients are ~0.5. Compared to other DA problems, like the NEA benchmark in Chp. 6 where the relative standard deviations are as high as 3.0%, the experimental uncertainties are fairly low. With lower experimental uncertainties, we can expect greater reductions in the calculated value uncertainties from applying DA. In contrast with the NEA benchmark, there are many

more and higher experimental correlations for LWR-PII. Both of these factors together (*i.e.* low experimental uncertainty and large correlations) led to big χ^2 values with Eq. (2.23). This is important to keep in mind for later when the BMC and BFMC methods are discussed.

4.2.2 CASMO-5M Models

LWR-PII was simulated with the CASMO-5M fuel assembly code (version 1.07.01) [87] and the E7R0 125, 586-group nuclear data library based on ENDF/B-VII.1 [68]. The neutron transport calculations were done with the 19-energy-group structure of CASMO-5M. The models, shown in Fig. 4.2, simulated only the core's central assembly and had reflective boundary conditions on their outer surfaces. Criticality was achieved for U_{ref} by searching for the critical axial buckling. This critical buckling was then fixed for the rest of the models where the various U_i and U_{nat} were simulated as inside the core. The buckling was also fixed when SHARK-X perturbed the CASMO-5M inputs parameters. Seven significant digits were used in the post-processing, which accounted for rounding at the pcm level of k_{eff}. Such a convergence level can be hard to reach with CASMO-5M. Care must be taken to ensure that the eigenvalues are well converged and numerically precise. Therefore, a fixed number of 50 outer iterations was requested in the 2D transport calculations in order to obtain a tight convergence.
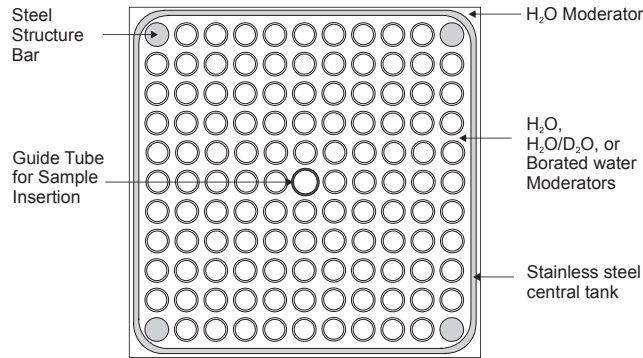
Figure 4.2 – 2D, reflected assembly model in CASMO-5 [76].

4.2.3 SHARK-X

The nuclear data covariances came from SCALE6.1 [88]. Due to the large computational cost of estimating the sensitivity coefficients needed for GLLS, only 41 isotopes were considered. These isotopes were determined to be most relevant to the uncertainty in $\Delta\rho_{rel}$ coming from nuclear data [89]. The following nuclear data were considered for fissile and fertile nuclides: elastic scattering (σ_e), inelastic scattering (σ_{in}), (n, 2n) reaction, fission (σ_f), capture (σ_c), the average number of neutrons (prompt and delayed, or MT452) per fission ($\bar{\nu}$), and the average fission spectrum (χ) for fission from thermal neutrons. For low Z nuclides, only total scattering was considered, not distinguishing between σ_e and σ_{in}.

The sensitivity coefficients used in GLLS were calculated by SHARK-X with Equivalent Generalized Perturbation Theory (EGPT) [90]. SHARK-X perturbs an input nuclear datum, σ_0, individually and independently to become a perturbed nuclear datum, σ_i. CASMO-5M is then run with both σ_0 and σ_i to create two k_{eff} values: k_0 and k_i. These values are used together in Eq. (4.3) to calculate the relative sensitivity coefficient of k_{eff} to that nuclear datum, $S_{k,\sigma}$.

$$S_{k,\sigma} = \frac{\sigma_0}{k_0} \frac{k_i - k_0}{\sigma_i - \sigma_0} \tag{4.3}$$

With EGPT, the sensitivity coefficient of $\Delta\rho_{rel}$ is a function of the $S_{k,\sigma}$ of a reference and of two perturbed states, as seen in Eq. (4.4). Here, $S_{k_{ref},\sigma}$, $S_{k_1,\sigma}$, and $S_{k_2,\sigma}$ are the sensitivity coefficients of k_{eff} for the reference state and perturbed states 1 and 2. The variables λ_{ref}, λ_1, and λ_2 are the lambda eigenvalues ($1/k_{\text{eff}}$) as calculated by CASMO-5M. For $\Delta\rho_{rel}$, state 1 is U_i, state 2 is U_{nat}, and the reference state is U_{ref}.

$$S_{\Delta\rho_{rel},\sigma} = -\frac{\lambda_{ref}(\lambda_1 - \lambda_2)}{(\lambda_{ref} - \lambda_1)(\lambda_{ref} - \lambda_2)} S_{k_{ref},\sigma} + \frac{\lambda_1}{\lambda_{ref} - \lambda_1} S_{k_1,\sigma} - \frac{\lambda_2}{\lambda_{ref} - \lambda_2} S_{k_2,\sigma} \tag{4.4}$$

SHARK-X calculates $S_{k,\sigma}$ with direct perturbation. The perturbations to σ_0 are chosen to be small enough for the linearity of k_{eff} to be guaranteed, but also for a change k_{eff} to still be observable. SHARK-X uses a 3-point-adaptive perturbation scheme in direct perturbation. The first point is the nominal or unperturbed CASMO-5M run common to all nuclide-reaction pair perturbations. The second point is a scoping calculation using a default perturbation size of 50% the nominal nuclear-datum value. The third simulation is chosen to generate a 0.1% change in the response, assuming a linear trend between the unperturbed case (first point) and the scoping calculation (second point).

For stochastic DA, SHARK-X made 1,000 random samples of the nuclear data. The data were sampled from multi-variate Gaussian distributions. The nuclear data sample set was then given to the CASMO-5 models to make 1,000 samples of the 32 $\Delta\rho_{rel}$. There were three moderating conditions, each with eleven k_{eff} calculations for the U_i and two more for U_{ref} and U_{nat}. That means 38,000 CASMO-5M simulations were done in total. For the direct perturbation calculations at 41 isotopes, approximately three nuclear data per isotope, 19 energy groups, and 32 relative reactivity values meant that approximately 90,000 CASMO-5 simulations were done.

4.3 Relative Reactivity Adjustments

In this section, the results from applying DA to the 32 relative reactivity values ($\Delta\rho_{rel}$) are analyzed. In particular, we consider how the biases may have arisen from nuclear data or from other sources such as modeling approximations, CASMO-5M methodologies, or the quality of

the experiments. This analysis is done with the $\Delta\chi^2$ parameter detailed in Section 4.3.1 and the nuclear data adjustments. Only GLLS and MOCABA were used for this analysis. Weight degeneracy occurred for BMC and BFMC because of the large prior χ^2 values of the integral data set. The weight degeneracy would have required many samples to have a statistically accurate posterior. Unfortunately, already the 128,000 CASMO-5 runs were computationally expensive and having more was not technically feasible. Because of this, BMC and BFMC were not applied. The nuclear data adjustments are applicable only to these specific models, for the SHARK-X code system, and for the given nuclear data. They are not intended to be recommendations to nuclear data evaluators.

4.3.1 Pre-adjustment Inconsistency Evaluation

Before DA, it was important to ensure consistency of the integral parameters to avoid spurious and non-physical adjustments.[2] For this data set, the CASMO-5 models and SHARK-X principally created the inconsistency. SHARK-X did not fully account for resonance self-shielding when it perturbed nuclear data. Additionally, neutron leakage effects in the 2D reflected assembly models may have been inaccurate and have biased the posteriors.

We used the $\Delta\chi^2$ metric (Section 2.3.3) to filter out inconsistent benchmarks. The filter removed any $\Delta\rho_{rel}$ where **E** and **C** were highly inconsistent. The inconsistent integral datum could not then influence the adjustment and erroneously skew the posteriors. The $\Delta\chi^2$-filter was chosen because it accounts for correlations between integral parameters, which for this application are important. The Adjustment Margin (Section 2.3.2) does not take into account correlations. At the point temporally when this work was done in the thesis, MLO (Section 2.3.4) had not yet been fully described for neutronics problems. Because of this, it was not used in this study, but certainly could have been and would be very useful.

To understand the importance of correlations, consider Fig. 4.3 which shows the biases of the 32 $\Delta\rho_{rel}$ values. The first analysis of this plot could say that parameters whose error bars do not cover a C/E - 1 = 0 are inconsistent and should be removed from influencing the adjustment. This is the Adjustment Margin approach. While this checks if the biases are consistent with their standard deviations, it cannot determine if they are consistent with their correlations.

Fig. 4.4 shows the correlations between the prior calculated $\Delta\rho_{rel}$, which range from 0.67 to 0.99. Consider the last two $\Delta\rho_{rel}$ of the H_2O data set (M3 and M4) in Fig. 4.3. Their **E** and **C** have correlation coefficients of 0.95 and 0.50, respectively. Without considering correlations, both integral parameters might be included in DA because both have uncertainty ranges that cover C/E - 1 = 0. This does not consider that these C/E - 1 values are not consistent given their high degree of correlation. While M4 has a bias of 1.2%, M3 has a bias of -3.2%. Two highly correlated integral parameters should have similar biases given identical inputs to their

---

[2]The importance of consistency of the integral data is described in detail in Section 2.3, along with the different techniques to account for it.
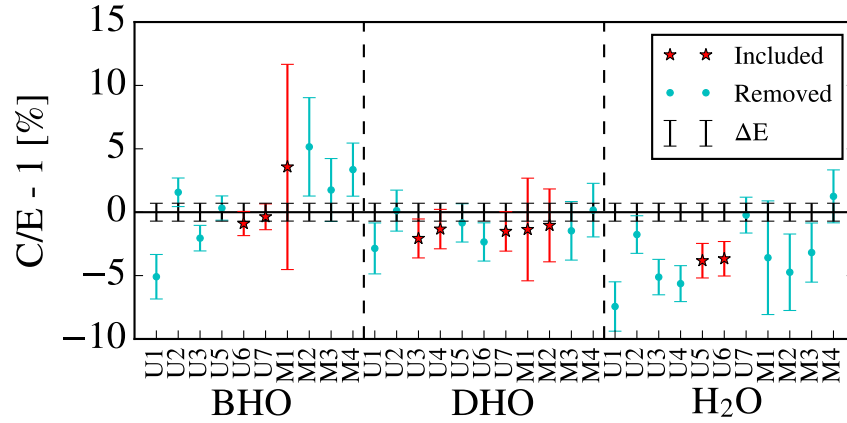
Figure 4.3 – Prior biases for all $\Delta\rho_{rel}$ with error bars as 1-relative-standard deviation. The $\Delta\rho_{rel}$ are categorized into those that are and are not removed with $\Delta\chi^2$-filtering.

calculation and identical experimental conditions. Something is amiss in the experiment or calculation and, therefore, the safest decision is to eliminate them from the DA. Their bias likely arises from sources other than nuclear data, like the modeling of the fuel burnup, the 2D model in CASMO, or from experimental methods.
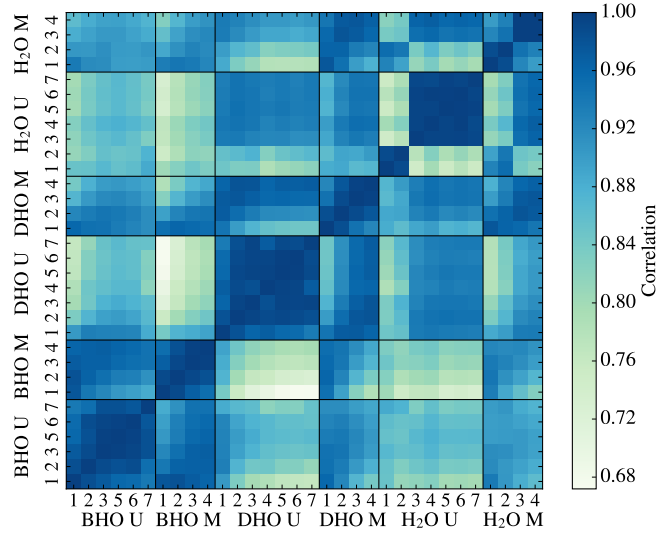
Figure 4.4 – Correlations between the 32 calculated $\Delta\rho_{rel}$.

When $\Delta\chi^2$-filtering was applied to the 32 $\Delta\rho_{rel}$, with a threshold of 1.25, 22 $\Delta\rho_{rel}$ are removed, leaving ten available for DA. The 1.25 threshold corresponds to one standard deviation above $\chi^2 = 1$ when there are 32 degrees of freedom. The inconsistency caused by incoherent biases and correlations is reflected in the prior χ^2 per degree of freedom for the data set, which was 12.1. With these $\Delta\rho_{rel}$ removed, the χ^2 per degree of freedom decreased to 2.1. These ten $\Delta\rho_{rel}$ were the integral parameters used in DA.

The importance of including the **E** covariances presented in Section 4.2.1 can be seen with $\Delta\chi^2$-filtering. If the covariances are excluded from $\mathbf{M_E}$, certain $\Delta\rho_{rel}$ (specifically BHO-U5, DHO-U1, DHO-M3, H2O-M1) are no longer removed from the adjustment. These parameters would then influence the DA, running the risk that they create unreliable posterior nuclear data and, consequently, unreliable posterior $\Delta\rho_{rel}$.

4.3.2 Posterior Calculated Values

The ten remaining $\Delta\rho_{rel}$ drove the adjustment. The 22 integral parameters that were filtered out were transformed into passive responses: they were still adjusted but did not actively contribute to the adjustment. For example with GLLS, they were not included in Eqs. (2.17) and (2.18), but their posteriors were computed with Eqs. (2.19) and (2.20). The passive responses were adjusted based on the correlations with the ten active $\Delta\rho_{rel}$ found in $\mathbf{M_C}$.
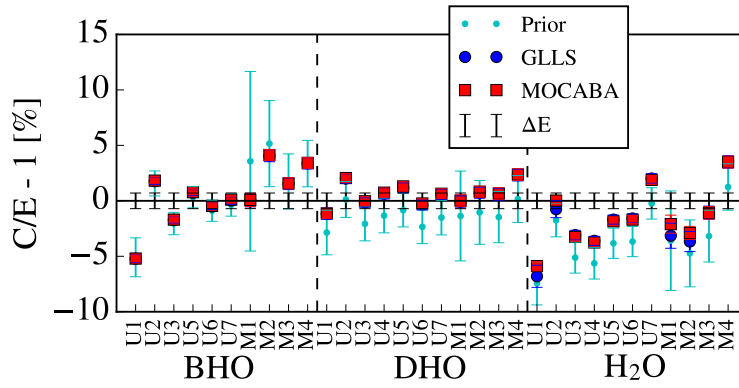
Figure 4.5 – Posterior biases for all LWR-PII fuel samples calculated with GLLS and MOCABA. Uncertainties are 1 standard deviation.

Fig. 4.5 presents the posterior biases calculated with GLLS and MOCABA. In general, the biases improved, especially for the DHO fuel samples. For all 32 $\Delta\rho_{rel}$, the χ^2 per degree of freedom (DoF) decreased from 12.1 to 11.7. For the ten $\Delta\rho_{rel}$ that actively influenced the adjustment, their χ^2 per DoF reduced from 2.1 to 0.96.

The $\mathbf{C}'$ between MOCABA and GLLS had a good agreement for 28 out of 32 $\Delta\rho_{rel}$. Four samples in the H2O data set showed large disagreements. Similarly for $\mathbf{C}'$ uncertainty, there were good agreements except for four H2O samples. The disagreement was caused by the limited numerical precision of CASMO-5M when it was used to calculate $\Delta\rho_{rel}$. A round-off error caused a spread of values that cannot be fully represented with the direct perturbation approach to compute sensitivity coefficients and thereby created differences between GLLS and MOCABA. Rounding effects when calculating a small difference in k_{eff} were simply more pronounced for these four samples, which was why they showed greater disagreement.

The BHO-M1 $\Delta\rho_{rel}$ showed the largest improvement, attributable to its large prior uncertainty and to being included as an active integral parameter. Certain biases degraded, *i.e.* C/E

- 1 moved farther from zero. Take DHO-M4 and H_2O-M4, which exemplify inconsistent integral parameters in terms of their correlations with other parameters. Both showed much different biases than other $\Delta\rho_{rel}$ in their moderator group, despite high inter-correlations. The adjustments sought to push the majority of biases to zero, and this minority of inconsistent $\Delta\rho_{rel}$ also were pushed in the same direction. Unfortunately, because they had prior biases that were inconsistent with the group and were also highly correlated to them, they were pushed in the same direction but away from C/E - 1 = 0. This effect is highlighted by the posterior χ^2 per DoF. For all 32 $\Delta\rho_{rel}$, it was still far from 1.0 at 11.7. For the ten active $\Delta\rho_{rel}$, it was reduced to 0.96. The overall adjustment for all 32 $\Delta\rho_{rel}$ was less effective because certain biases worsened.

The importance of the **E** covariances was seen when DA was performed again with them omitted from $\mathbf{M_E}$ in the DA equations. The average $\mathbf{C}'$ standard deviation of the 32 $\Delta\rho_{rel}$ was smaller without covariances at 0.384% vs. with at 0.372%. The average posterior bias was smaller as well at -0.373% vs. -0.811%. The **E** covariances constrained the adjustment, meaning that **C** standard deviations and the posterior biases were bigger. This result highlights the importance of properly quantifying $\mathbf{M_E}$ in DA.

4.3.3 Posterior Nuclear Data

The sensitivity coefficients used in GLLS allowed for a detailed analysis of the posteriors. We could show how C changes were created by adjustments of nuclear data and how reductions in C uncertainty came from changes to the nuclear data covariance matrix. In this way, we gain deeper insights into how biases in the CASMO-5M calculations might be caused by nuclear data. This breakdown was only possible with GLLS thanks to the sensitivity coefficients. With MOCABA, the information was lost because all the nuclear data are perturbed simultaneously. In order to capture the effect of each of MOCABA's posterior nuclear data, simulations would have needed to be re-done perturbing individually every single nuclear datum.

To calculate the effect of an adjustment, Eq. (4.5) can be used. Here, $\boldsymbol{\sigma}_i'$ is a nuclear data set that is identical to the prior ($\boldsymbol{\sigma}_0$) except that the ith nuclear datum is replaced by the posterior. For example, to calculate the change in C created by changes in $\boldsymbol{\sigma}$ associated to U-238, all the data in $\boldsymbol{\sigma}_0$ that correspond to U-238 would be replaced by the U-238 data in $\boldsymbol{\sigma}'$.

$$\mathbf{C}'(\boldsymbol{\sigma}_i') = \mathbf{C}(\boldsymbol{\sigma}_0) + \mathbf{S}(\boldsymbol{\sigma}_i' - \boldsymbol{\sigma}_0) \tag{4.5}$$

Tables 4.2 and 4.3 break down the C adjustments by their source, *i.e.* due to nuclear data adjustments. Table 4.2 shows how the nuclear data adjustments of each nuclide contribute to the change in C. Here, the C adjustment was averaged across all 32 $\Delta\rho_{rel}$. The nuclide contributing most to the C adjustment was U-238, followed by Pu-239 and U-235. At a smaller scale, Pu-241 and Pu-242 were important along with the moderator H-1, the clad Zr-92, and

Table 4.2 – Contribution of each nuclide to the GLLS adjustment of C.

Actinides		Fission Products and Others	
Isotope	(C'-C)/C (%)	Isotope	(C'-C)/C (%)
U-238	1.91	H-1	0.05
Pu-239	-1.06	Zr-92	-0.04
U-235	0.36	Rh-103	0.03
Pu-241	-0.09	Nd-143	0.01
Pu-242	0.08	Eu-154	-0.01

Table 4.3 – Contribution of the top nuclear data to the GLLS adjustment of C.

Actinides		Fission Products and Others	
Isotope/Data	(C'-C)/C (%)	Isotope/Data	(C'-C)/C (%)
U-238 σ_c	1.90	H-1 σ_c	0.05
Pu-239 $\bar{\nu}$	-0.93	Zr-92 σ_c	-0.04
U-235 σ_c	0.31	Rh-103 σ_c	0.02
Pu-239 σ_f	-0.11	Nd-143 σ_c	0.01
Pu-242 σ_c	0.08	Eu-154 σ_c	-0.01

fission products like Rh-103, Nd-143, and Eu-154. Importantly, the table shows that certain adjustments were positive and others were negative and that the total adjustment was an integral quantity that had canceling or compensating effects.

To further pinpoint which σ were most important, Table 4.3 must be examined. The influence of U-238 predominantly came from changes to its capture cross section, σ_c. U-235, Pu-242, and the fission products and structural materials were also all dominated by adjustments of σ_c. The importance of σ_c can be related to the large sensitivity of reactivity to capture, or parasitic neutron absorption. Pu-239 meanwhile had contributions from $\bar{\nu}$ and σ_f.

The breakdown can go one step deeper and examine how the adjustments at the energy group level contributed to the change in C. Fig. 4.6 presents the relative nuclear data adjustments created with GLLS and MOCABA and also the breakdown of how the GLLS adjustments at each energy group contributed to the average C adjustment.

First considering only the adjustments, GLLS and MOCABA agree well, which confirms results presented in Chp. 3. Continuing to how the individual nuclear data adjustments affect C, changes to U-238 σ_c at energies below 0.1 eV contributed most to the C adjustments. At these low energies, $\Delta\rho_{rel}$ was particularly sensitive to σ_c. Pu-239 $\bar{\nu}$ showed uniform adjustments from 0.01 eV to 10 keV, but below 1 eV it created very significant changes to C because, again, the sensitivity coefficients were highest there. The adjustment showed that changes to U-235 σ_c in energy group 5 (0.149 to 5.53 keV) of ~5.7% produced the largest C adjustment at 0.12%. Adjustments below 0.2 eV and above 5.53 keV were also important. Pu-242 σ_c saw its most important contribution at ~2.7 eV where there is a significant resonance of over 30,000 b.
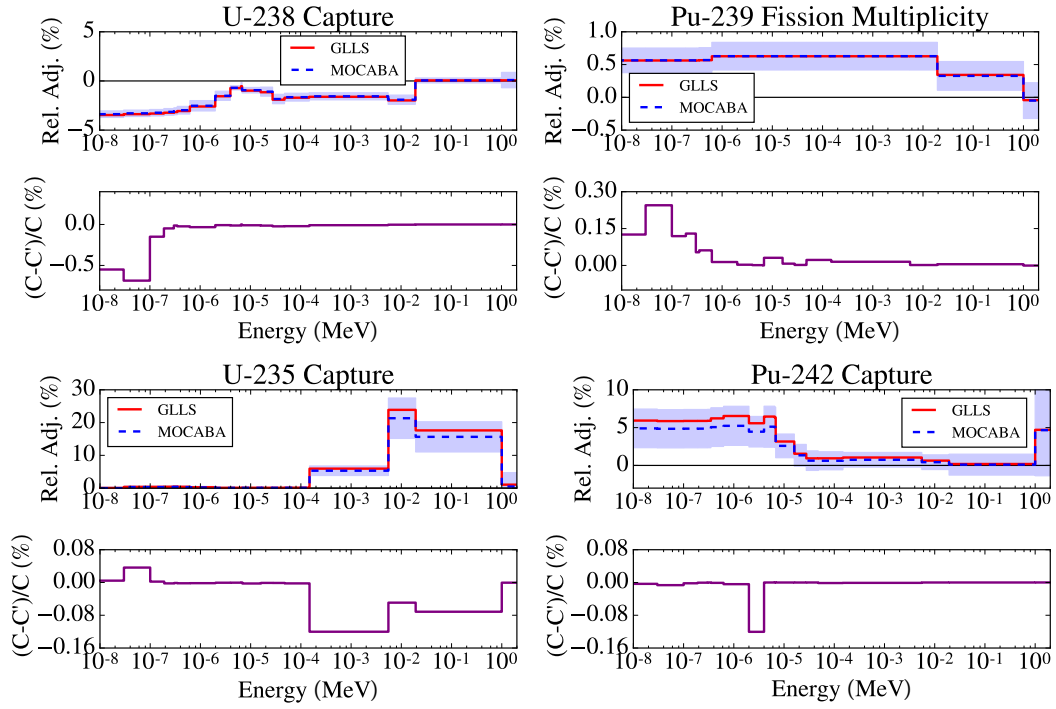
Figure 4.6 – Nuclear data adjustments, $(\boldsymbol{\sigma}' - \boldsymbol{\sigma}_0)/\boldsymbol{\sigma}_0$, with DA (above) and contribution of the adjustment of the average change in C. Blue shaded region is the bootstrap-estimated 95%-confidence interval (with 500 samples) of the MOCABA adjustments.

We can similarly break down from where the reduction in the C uncertainties ($\Delta_{\mathbf{C}'}$) originated in $\mathbf{M}'_{\sigma}$ when all nuclear data were simultaneously adjusted. Table 4.4 shows the top ten variance/covariance terms that contribute to $\Delta_{\mathbf{C}'}$. The variances are converted into standard deviations and the covariances are square rooted for consistency in units. The $\Delta_{\mathbf{C}'}$ was dominated by Pu-239 $\bar{\nu}$ uncertainties, which created a prior uncertainty of 1.34%. Through the adjustment, this uncertainty was reduced to 0.78%. The reduction is possible because of the reaction's high sensitivity and large uncertainty.

This result illustrates how DA can be useful to understand $\Delta_{\mathbf{C}'}$. Such a large reduction hints that the uncertainty of Pu-239 $\bar{\nu}$ was likely overestimated in the prior covariance matrix (from SCALE6.1). In fact, the new covariance matrix in SCALE6.2 has the $\bar{\nu}$ uncertainty reduced from ~1% to 0.2% [91]. These results for Pu-239 $\bar{\nu}$ motivate using the SCALE6.2 VCM in future SHARK-X problems. Most other isotope/reaction pairs saw modest reductions in their contributions to $\Delta_{\mathbf{C}'}$, except for U-238 σ_{c} where uncertainty decreased from 0.43% to 0.29%.

Another important component of the $\Delta_{\mathbf{C}'}$ reduction was the development of correlation terms that did not exist in the prior, both between the nuclear data of an isotope and between isotopes themselves [24]. Table 4.5 shows how these correlations served to reduce $\Delta_{\mathbf{C}'}$. Here, the uncertainties are presented as negative standard deviations. They are the square roots of the absolute values of the negative covariances with the -1 multiplied after the square root.

Table 4.4 – Decomposition of average $\Delta_{\mathbf{C'}}$ given as 1-relative-standard deviations (%).

Isotope/Data Pair	Prior	Posterior
Pu-239 $\bar{\nu}$ / Pu-239 $\bar{\nu}$	1.34	0.78
U-235 $\bar{\nu}$ / U-235 $\bar{\nu}$	0.51	0.47
Pu-239 σ_f / Pu-239 σ_f	0.51	0.47
U-238 σ_c / U-238 σ_c	0.43	0.29
Pu-239 σ_f / Pu-239 σ_c	0.40	0.35
Pu-239 σ_c / Pu-239 σ_c	0.36	0.34
U-235 σ_f / U-235 σ_f	0.29	0.27
U-235 σ_c / U-235 σ_c	0.25	0.24
Pu-239 σ_c / Pu-239 σ_c	0.23	0.22
U-235 σ_c / U-235 σ_f	0.23	0.21

Table 4.5 – Average $\Delta_{\mathbf{C'}}$ (%) created by new correlations not present in prior.

Isotope/Data Pair	Posterior
Pu-239 σ_f / Pu-239 $\bar{\nu}$	-0.62
U-235 $\bar{\nu}$ / Pu-239 $\bar{\nu}$	-0.54
Pu-239 σ_c / Pu-239 $\bar{\nu}$	-0.49
U-235 σ_f / Pu-239 $\bar{\nu}$	-0.33
U-235 σ_c / Pu-239 $\bar{\nu}$	-0.28
Pu-240 σ_c / Pu-239 $\bar{\nu}$	-0.26
Pu-239 σ_f / U-235 $\bar{\nu}$	-0.22
U-238 σ_c / U-235 $\bar{\nu}$	-0.22
U-235 σ_c / U-238 σ_c	-0.19
Pu-239 σ_c / U-235 $\bar{\nu}$	-0.18

This is done to ensure consistency in units with Table 4.4. Important reductions in uncertainty came from new correlations between Pu-239, specifically Pu-239 σ_f / Pu-239 $\bar{\nu}$ and Pu-239 σ_c / Pu-239 $\bar{\nu}$. Other important reductions arose from correlations between Pu-239 $\bar{\nu}$ and other isotopes' data such as U-235 $\bar{\nu}$, U-235 σ_f, or Pu-240 σ_c. New correlations with U-235 $\bar{\nu}$ were also significant to making $\Delta_{\mathbf{C'}}$ smaller relative to the prior.

Fig. 4.7 shows the prior and posterior correlations for Pu-239 nuclear data. Firstly, it illustrates the strong agreement between the GLLS and MOCABA posteriors. Secondly, it shows how correlations which were not in the prior appeared in the posterior. Large negative correlations appeared between σ_f and $\bar{\nu}$, which explains this pair's dominance in Table 4.5.

Due to the limits of the current DA scheme of the LWR-PII experiment, as evidenced by the large number of $\Delta\rho_{rel}$ values removed with $\Delta\chi^2$-filtering, we cannot definitively attribute the bias to any particular nuclear data. The adjustments of the nuclear data and of their covariance matrix show the importance of U-238 σ_c. This cross section heavily influences the C adjustment and was also a key source of uncertainty reduction due to changes in the covariance matrix. These results serve as a starting point for future bias evaluations.
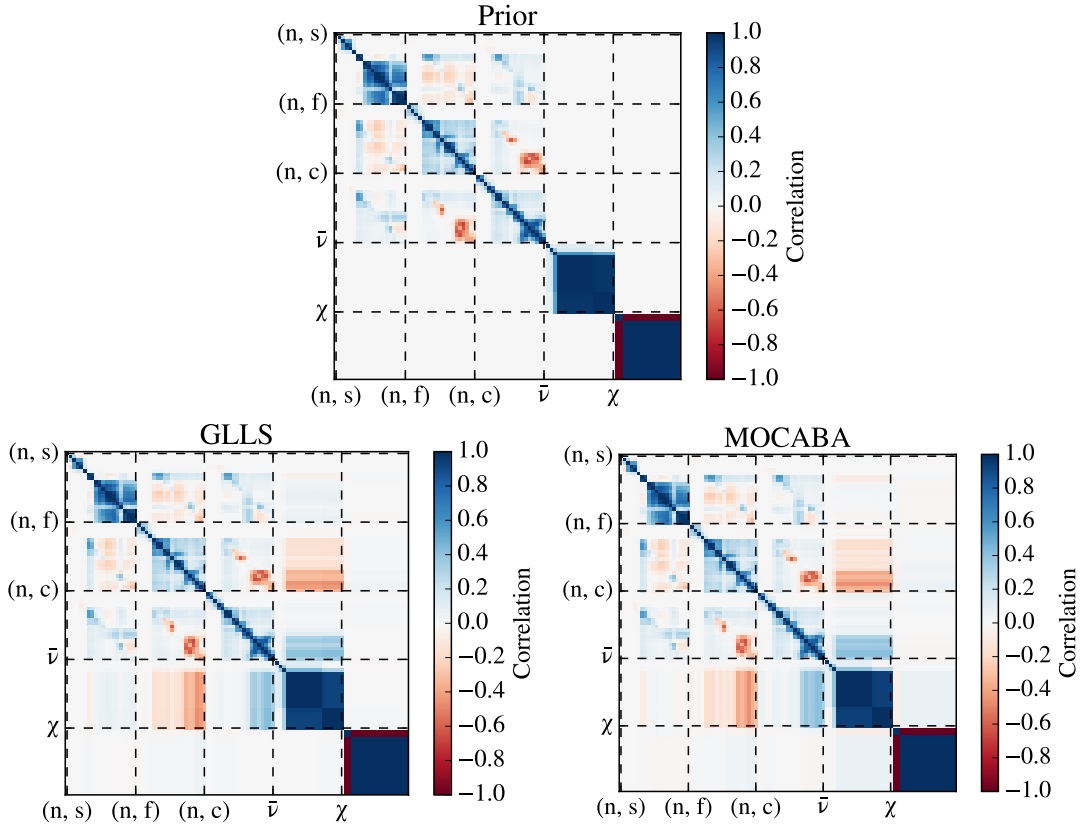
Figure 4.7 – Prior and posterior nuclear data correlation matrices for Pu-239. Correlations are given from high to low energy for each datum.

Perhaps the DA can be improved with higher fidelity in modeling the burnup history of the fuel samples. Other improvements could come from considering the effects of nuclear data, including fission yields, on the nuclide composition of the fuel samples used in the $\Delta\rho_{rel}$ calculations. Another option to improve the inconsistency would be to use the experimental compositions of the fuel samples that were measured in post-irradiation examination experiments instead of the compositions calculated by CASMO-5. Importantly left out from the DA equations used here was a modeling and methodology covariance matrix. This would have accounted for biases from modeling approximations and the neutron transport methodology. While this matrix is difficult to calculate for a deterministic neutron transport code like CASMO-5M, introducing it may help improve the adjustments. It could possibly be estimated in future projects with the MLO method, described in Section 2.3.4.

4.4   Conclusions

This study applied DA methods to the LWR-Phase II experiments using CASMO-5M and the SHARK-X tool. The methods were Generalized Linear Least Squares (GLLS) and Monte Carlo Bayesian Analysis (MOCABA). Analysis of the measured relative reactivity integral parameters

showed inconsistencies between biases as quantified with $\Delta\chi^2$-filtering. Highly correlated relative reactivities had very different bias behaviors. This indicated that their biases likely arose not from nuclear data but rather from the CASMO-5M models of the experiments, from inaccuracies in the irradiation histories of the fuel samples, or from the experimental data. Ten out of 32 relative reactivities were of sufficiently high quality to be used in DA, *i.e.* the origins of their biases could be attributed to nuclear data or experimental uncertainty. This unfortunate loss of experimental data showed a drawback related to the filtering methods. In the next chapter, the Marginal Likelihood Optimization technique is shown to help with inconsistent integral data without filtering.

The only differences between MOCABA and GLLS posteriors were caused by numerical round-off errors. Finally, analysis of the nuclear data adjustments showed that changes to the U-238 capture cross section were very important to improving the bias of the CASMO-5M simulations. The posterior nuclear data covariance matrices saw significant reductions in the variance terms of Pu-239 fission multiplicity data that led to reductions in the calculated $\Delta\rho_{rel}$ uncertainty. This supports previous conclusions that the Pu-239 fission multiplicity uncertainty may have been over-estimated in the SCALE6.1 covariance data.

4.5   Chapter's Key Points

- DA was done with the reactivity experiments of LWR-Proteus Phase II

- DA tools were implemented alongside PSI's code SHARK-X

- This experimental data set showed large degrees of inconsistency, particularly in terms of their correlations

- When $\Delta\chi^2$-filtering was done, only ten out of 32 integral parameters remained for the adjustment

- The large amount of lost data demonstrates the attractiveness of MLO for other studies

- MOCABA and GLLS were shown to give agreeing results for a different neutron transport code (CASMO-5), nuclear data covariances (SCALE6.1), and experimental data set

- The adjustments showed that Pu-239 fission multiplicity was likely over-estimated in the SCALE6.1 covariance data

5 Data Assimilation of Post-Irradiation Examination Experiments

> Our naive trust in models, and our
> failure to realize how fragile they were to
> our choice of assumptions, yielded
> disastrous results.
>
> –N. SILVER, *The Signal and the Noise* [39]

This chapter presents DA of post-irradiation examination data to adjust the model parameters of the GEF code. The fission yields (FYs) produced by GEF create large uncertainties in the calculated fission product concentrations in spent fuel. For the fuel in this study, the uncertainties are as large as 56% and average at 21%. Subgroup 26 of the OECD's WPEC [10] set target accuracies on nuclide inventories at a 1σ of 20% for fission products. The uncertainties here from GEF, on average and significantly at extremity, exceed this target accuracy and, therefore, point to the attraction of using DA in burnup. The goal of applying DA was to reduce the bias and uncertainties of calculated fission product concentrations in spent fuel. Additionally, the posterior FYs can be examined for trends, from a nuclear data standpoint.

DA was done with MOCABA and BFMC. This is because GEF can sample its model parameters and produce sample sets of FYs for use in neutron transport. The GEF FYs, and therefore the calculated nuclide concentrations using them, have non-normal distributions. As MOCABA assumes that the random variables have normal distributions and BFMC does not, this application was considered to be an interesting study of the DA methods. Additionally, the integral data set has a large degree of inconsistency, which also makes it interesting to apply the Marginal Likelihood Optimization technique. The study was structured around the original goals of the thesis: profit from experimental data from Proteus and build tools for PSI.

5.1 Introduction

Among nuclear data, FYs and their uncertainties are very important for burn-up [92, 93, 94, 95, 96], decay heat [97, 98], and nuclear waste management calculations [99]. These simulations need accurate predictions of the concentration of fission products (FPs) in spent fuel, which require reliable FY data with high quality covariances. Historically, nuclear data libraries did not consistently and completely provide covariances for FYs; they only gave nominal values and variances. A large amount of recent research has been devoted to proposing and testing methods to generate missing FY covariance data [100, 101, 102, 103]. One such method uses the code GEF [38]. GEF's covariance data create large uncertainties, up to 50%, of calculated FP concentrations. These large uncertainties make burnup calculations a strong target for DA. To do DA in this context, it is logical to use the experimental counterpart of calculated FP concentrations, or post-irradiation examination data. While in this chapter DA is done for GEF, it would also be feasible to do it for the FY uncertainty information given in Refs. [100, 101, 102, 103].

GEF produces covariance matrices for fission observables by Monte-Carlo sampling its model parameters. Fission observables consist of nuclear data like FYs, prompt fission neutron spectra, and prompt fission neutron multiplicities. These covariance matrices can then be used for uncertainty quantification and sensitivity analysis studies. A study presented in Ref. [104] used GEF to assimilate ENDF/B-VII.1 [68] FY data as the experimental evidence in DA. Herein, we propose using post-irradiation examination (PIE) data. PIE data have been used for nuclear data adjustments [105, 106], but never for FYs and only with sensitivity-based [27] approaches. It is important to consider FYs in DA with PIE data; the FPs are highly sensitive to the FYs and the FYs have large uncertainties.

We used GEF to create FYs and covariance data for thermal fission of U-235, Pu-239, and Pu-241 and fast fission of U-238. These FYs were then used in CASMO-5 simulations of spent fuel of the LWR-Phase II (LWR-PII) experimental campaign of Proteus. The integral data here are the concentrations of FPs in the spent fuel samples. The experiment and calculations were then used to perform a Bayesian update of the GEF model parameters. These posterior model parameters were given to GEF to create posterior FYs and covariance data. Finally, the posterior FYs were passed to the CASMO-5 simulations to evaluate their effect on the predicted FP concentrations.

MOCABA (Section 2.2.2) and BFMC (Section 2.2.3) were used to do the DA. BMC could not be used because the prior χ^2 values of the integral data set were so large as to cause immediate weight degeneracy. GLLS was not used because it would have required extensive code development to calculate sensitivity coefficients to FYs in CASMO-5. Additionally, burnup simulations are non-linear and would invalidate GLLS' linearity assumption. Chp. 3 showed that BFMC is not an unbiased estimate of the MAP distribution. The bias causes BFMC to return spurious posteriors for low χ^2 values due to a weight degeneracy. However for large χ^2 values, BFMC conservatively returns posteriors closer to the prior. In this way, BFMC can

be thought of as compensating for the inconsistency of the integral data set. Because this data set is in the regime of a large χ^2, it was determined that BFMC could be applied for this and in the worst case no adjustment from prior to posterior would occur.

This large degree of inconsistency between the experimental data and calculations, *i.e.* its large prior χ^2 is important to consider in the DA. In this work, the Marginal Likelihood Optimization technique (MLO), as presented in Section 2.3.4, was applied to account for the inconsistency. It was used instead of AM or $\Delta\chi^2$-filtering in order to keep all the integral points in the analysis. These techniques would have removed up to 75% of the integral data, which would have been an unfortunate loss of valuable information. Chp. 3.1.1 showed that applying MOCABA to inconsistent integral data sets can create dangerous adjustments, in terms of their basis in physics. Additionally, it was shown that BFMC will produce a small to possibly negligible adjustment when there is a large χ^2, and therefore the DA would not be as effective as it could be. This point makes this work interesting to study the effect of MLO. By adding an extra uncertainty term to account for the inconsistency, this helps to constrain the MOCABA adjustments. It will also lower the χ^2 and allow for BFMC to adjust to a larger extent as well.

This application is challenging for MOCABA because the FYs produced by GEF can be non-Gaussian. Their uncertainties propagate through calculations and create non-Gaussian distributions in integral parameters like k_∞ or nuclide compositions [107]. With non-Gaussian parameters, MOCABA may cause biases in the posteriors due to its Gaussian assumption, as shown in Section 3.1.2. In this study, we apply both methods to assess the effect of this non-Gaussianity.

In the following text, we present the adjustments of the GEF model parameters made with MOCABA and BFMC, with the LWR-PII PIE data, and CASMO-5 models. Section 5.2 outlines FYs and GEF. Here, we summarize the details that are most important for this work, but do not attempt to fully describe or explain the physics of the GEF model. If variables or phenomena are unclear to the reader, please refer to the GEF documentation cited herein, which certainly have more detailed and elegant explanations than could be achieved in this thesis.

Section 5.3 details the LWR-PII PIE data and the calculation scheme for DA (GEF input parameters, CASMO-5 models, and DA procedure). The results of the DA are presented in Section 5.4. The adjusted model parameters are given and discussed, along with the FYs generated with them. The prior and posterior GEF FY data are compared to those given in ENDF/B-VIII.0 [11] and JEFF3.3. The posterior FY data were re-used in the CASMO-5 simulations, both with the PIE data that were used to adjust the model parameters and with PIE data that were not part of the adjustment. We focus on the differences between the MOCABA and BFMC adjustments as well as the effect of applying MLO. The posterior FYs, FY correlation matrices, and nuclear data are all investigated.

5.2 GEF Background and Theory

Nuclear fission creates a large variety of phenomena. This process can certainly be modeled, and often is in very elaborate ways. These kinds of highly detailed models, using concepts like the Langevin equations [108], are often said to be *microscopic* or *optical*. TALYS [109] and EMPIRE [110] are examples of microscopic codes used for FYs. To date, only the pre-saddle and post-scission[1] phenomena are well mastered with optical models and statistical de-excitation codes [111]. These models also need significant computational resources. Microscopic modeling is, therefore, still challenging for the field.

Unfortunately, these limitations are highly consequential because FPs must be well estimated for nuclear technology applications. The fission fragments, after emitting prompt neutrons, are the starting points for decay chains. The decay chains then determine analyses for decay heat, the nuclear fuel cycle, nuclear safeguards, or the measurement of reactor anti-neutrinos.

To meet the demands of high quality FY evaluations, *empirical* and *semi-empirical* models are often employed. A foundational empirical model was made by Wahl and is often called *Wahl systematics* [112]. It has been developed since the early 1960s and is a standard in FY evaluations. For example, the FYs in the JEFF3.1.1 library [113], which was based on the UKFY3 evaluation [114], were evaluated with Wahl systematics, among other theories [115]. One model called GEF (**GE**neral description of **F**ission observables) [38, 116] is semi-empirical. In contrast to microscopic or empirical models, GEF models single aspects of the fission process by combining theoretical and empirical approaches.

GEF is designed to give a complete description of the fission process. It describes the excited compound nucleus formation and all intermediate processes until the formation of two separate nuclei at scission. The capture of the neutron and the competing processes of particle emission/gamma emission/fission are also considered. Additionally after scission, the excited fission fragments and how they decay are also considered. It defines two FPs for each fission event and can calculate the total excitation energy of the FPs.

The makers of GEF highlight that it is not intended to compete with microscopic models. Instead, GEF is tailored to get the best performance in nuclear technology. Empirical information is leveraged to globally describe fission quantities. It is able to describe in a general way, *i.e.* without adjusting to individual fission systems, all types of fission. GEF was originally fit to find the optimum model parameters for all available fission observables by minimizing the deviations from a large set of experimental data [117].

GEF is also used to estimate fission observables where experimental data are missing. This can be very useful in a nuclear data evaluation perspective to fill in holes in experimental data. For this purpose, work with GEF has been done with the computer code MATCH [118]. The code tunes calculated values to fit experimental data.

---

[1]Scission denotes the instant of rupture. Meanwhile, fission denotes the entire process including fission cross-sections, compound nucleus formation and the saddle.

5.2.1 Code System

Very detailed descriptions of the inner-workings GEF's coding are available in Refs. [38, 116]. Here, we summarize the details that are most important for this work and rely on abstractions of key features of the code. This inherently leaves some holes in the description, but must be done for the conciseness of this thesis.

GEF uses a Monte-Carlo approach to generate, event-by-event, the data for fission observables. An event starts with the model parameters and the user's input (*e.g.* the properties of the excited nucleus). Then GEF calculates the competing decays of the system, where the competition is between fission and neutron/photon/proton emission. If fission is initiated, the fission fragment properties at scission are calculated. Then the de-excitation of the fragments is calculated until they reach their ground or isomeric state. For radioactive FPs, GEF computes β^- decay and will calculate cumulative FYs.

There are three main computational sections in GEF that compose the code's core:

1. **Pre-fission process**: Input parameters are given to the code (Z, A, entrance channel). A Monte-Carlo routine starts with multi-chance fission.[2] It considers decay by particle emission from both pre-equilibrium processes[3] and emission from the compound nucleus. The output of this module is a list of excited nuclei *en route* to fission. It gives the Z, A, excitation energy, and angular momentum. It is Monte Carlo in nature because events are simulated to create a population of possible processes.

2. **Average fission-fragment properties**: This takes as an input the nucleus to fission, which is characterized by Z, A, excitation energy, and the root-mean-squared angular momentum. A Monte-Carlo sampling of the individual fragment properties is done based on key quantities that are calculated at this moment, like the central Z values of fragment shells or the curvature of macroscopic potential energy.

3. **Monte-Carlo sampling of fission events**: The distributions of fragment properties from the previous module are used in a Monte-Carlo sampling. This accounts for all correlations and respects conservation laws. Then arrays are built containing all calculated fission observables. There are statistical uncertainties of the resulting distributions that depend on the number of requested events.

---

[2]Multi-chance fission occurs when the excitation energy of the initial compound nucleus is so high that after de-excitation the remaining excitation energy is near or above the fission barrier of the daughter nucleus. This observed fission is then a mixture of fission of the mother (first-chance) and the daughter (second-chance). The de-excitation can occur from pre-fission γ-rays or nucleon emission.

[3]Pre-equilibrium reactions are those that occur during the decay of the excited nucleus before it reaches statistical equilibrium. They become very important for neutron energies of several tens of MeV [119].

5.2.2 Covariances between Fission Yields

A great advantage and innovation of GEF is its ability to generate covariances between fission observables, which were traditionally not available. To do so, GEF samples some of its model's parameters, which were decided by the code developers to be the most important. For each model parameter sample set, the core of the code system that was described previously is run to create a sample of FYs. From the population of FYs, a covariance matrix is constructed. GEF assumes that the parameters are normally distributed and independent. The independence assumption is based on the fact that an additional correlation is introduced when the whole FY distribution is normalized [120]. Because GEF was constructed to include sampling, it can be seamlessly integrated into MOCABA and BFMC.

In the covariance generation process, first the model parameters are sampled. These model parameters change the statistical distributions that GEF uses to describe the physics of fission. GEF then does its standard, core routine where it Monte Carlo samples the fission-physics distributions to create FYs. This FY data set is then the random sample that corresponds to the random sample of model parameters. In a way, this is similar to the TMC approach for UQ with a Monte Carlo neutron transport code. In TMC, the model parameters of TALYS are sampled to create perturbed cross sections that describe the physics of neutron transport. A code like MCNP then does Monte Carlo sampling of the neutron-transport physics (described by cross sections) to calculate a random sample of an integral parameter. From the population of random samples, a covariance matrix of the integral parameters is estimated.

GEF has the ability programmed into it to sample its model parameters and estimate covariances between FYs. Unfortunately, this option does not preserve FYs of each random sample, it only returns the mean FYs and their covariances. In other words, GEF does not automatically output the distribution of the FYs, only their first two moments. The distribution is interesting for this project because it is non-Gaussian. To gain access to the distribution, the GEF code was modified so that it would give the FYs for each sample. This is an important component of this study and is emphasized again: the FYs for CASMO-5 were not sampled from covariance matrices, rather they were generated directly from sampling of the GEF model parameters. Therefore, the covariance matrices were not used at any point in the assimilation; they were another output of GEF that was adjusted.

The prior and posterior FY covariances matrices will be compared in Section 5.4 as they are a form of nuclear data. To calculate the FY covariance matrices from GEF runs, the subsequent analysis should be followed. For the FYs of each fissioning nuclide, n Monte-Carlo fission events are used, which constitutes one GEF execution with one set of model parameters. The model parameters are sampled N times to have N GEF executions, each with n Monte-Carlo fission events. Returning to the TMC analogy, n would be the number of neutron histories used in MCNP, and N would be the number of random samples of the nuclear data used to do the UQ of the integral parameters.

Each sample i gives a set of FYs from which a population mean and covariance matrix are

calculated. The mean for the jth FY, or $\overline{FY_j}$, can be calculated with Eq. (5.1). The covariance between FY_j and FY_k can be calculated with Eq. (5.2), using Eq. (5.1) to calculate $\overline{FY_j}$ and $\overline{FY_k}$. Here, $\mathbf{M_{FY}}$ is the covariance matrix between FYs, and (j,k) is the index in the matrix that gives the covariance between FY_j and FY_k.

$$\overline{FY_j} = \frac{1}{N}\sum_{i=1}^{N} FY_{j,i} \tag{5.1}$$

$$\mathbf{M_{FY}}^{(j,k)} = \frac{1}{N-1}\sum_{i=1}^{N}\left(FY_{j,i} - \overline{FY_j}\right)\left(FY_{k,i} - \overline{FY_k}\right) \tag{5.2}$$

Ref. [120] discussed how $\mathbf{M_{FY}}$ is subjected to statistical uncertainties because a limited number of fission events, n, and of model perturbations N are used. From this formulation, n/N should be small in order to have a small statistical uncertainty. If it is too big, it will hide the sought-after correlations and the covariance matrices that are studied in this chapter will have too much statistical noise to be meaningful. In GEF, N is automatically chosen with the n supplied by the user. It does so with Eq. (5.3) and the n supplied by the user in order to have statistically converged results.

$$N = 1000(n^2 - 1/2) \tag{5.3}$$

In this study, n was chosen to be 2E5 events. Using Eq. (5.3) would give $N = 448$. For the prior, 10,000 samples were done. With $N = 10,000$, the FY covariance matrices were well converged according to GEF's internal rule. For the UQ of the posterior, 500 samples of the FYs were done, which is also adequate for convergence. Fewer samples were needed for the posterior because only forward UQ was done, not inverse UQ. The point of this discussion is to prove that any behavior observed in the prior and poster FY covariance matrices is linked to the GEF model and the DA, and not simply to statistical effects.

5.2.3 Model Parameters

The model parameters that are sampled in GEF and their means and standard deviations are shown in Table 5.1. These values are unique to the GEF2017/1.1 version of the code [121]. They are changed with different distributions of GEF as it is modified and improved. Importantly, these are not the only model parameters in GEF. There are over 100 parameters, including things like the curvature of the macroscopic potential energy. Those in Table 5.1 were deemed most important by the developers for the production of covariance data.

The model parameters associated with the fission channels are prominent in Table 5.1. These fission channels reproduce experimental mass and charge distributions of the FPs by super-

Table 5.1 – Means and standard deviations of GEF model parameters in GEF2017/1.1 [121].

Input Parameter	GEF Name	Mean	Std.	Units
Shell position for S_1 channel	P_DZ_Mean_S1	-0.18	0.1	Z
Shell position for S_2 channel	P_DZ_Mean_S2	-0.460	0.1	Z
Shell position for S_3 channel	P_DZ_Mean_S3	-0.37	0.1	Z
Shell position at $Z \approx 42$	P_DZ_Mean_S4	0.0	0.1	Z
Shell effect for S_1 channel	P_Shell_S1	-2.85	0.1	MeV
Shell effect for S_2 channel	P_Shell_S2	-4.4	0.1	MeV
Shell effect for S_3 channel	P_Shell_S3	-6.40	0.2	MeV
Shell effect at $Z \approx 42$	P_Shell_S4	-0.9	0.05	MeV
Rectangular contribution to S_2 channel width	P_A_Width_S2	12.5	5%	Mass
Shell effect at mass symmetry	Delta_S0	0	0.1	MeV
Shell curvature for S_1 channel	P_Z_Curv_S1	0.37	5%	Z^2/A
Shell curvature for S_2 channel	P_Z_Curv_S2	0.1850	5%	Z^2/A
Shell curvature for S_3 channel	P_Z_Curv_S3	0.156	5%	Z^2/A
Shell curvature at $Z \approx 42$	P_Z_Curv_SL	0.035	5%	Z^2/A
Weakening of the S_1 shell	T_low_SL	0.31	0.01	MeV
$(\hbar\omega)_{\text{eff}}$ for tunneling of S_1 channel	T_low_S1	0.32	0.01	MeV
$(\hbar\omega)_{\text{eff}}$ for tunneling of S_2 channel	T_low_S2	0.31	0.01	MeV
$(\hbar\omega)_{\text{eff}}$ for tunneling of S_3 channel	T_low_S3	0.31	0.01	MeV
$(\hbar\omega)_{\text{eff}}$ for tunneling at $Z \approx 42$	T_low_S4	0.31	0.01	MeV
Width of fragment distribution in N/Z	HOMPOL	1	10%	MeV
Charge Polarization	POLARadd	0.25	0.1	Z

imposing Gaussians. Many of the model parameters describe the width, shape, and central values of the fission channels. There are four principal fission channels: S_1, S_2, S_3, and the S_L, or super long channel. Fig. 5.1 shows the fission channels for Pu-239 thermal fission and how they overlap and combine to create the total, composite FY. There is a shell (S_4), not shown, at $Z \approx 42$ that enhances the yield of the S_1 channel in fissioning nuclei around Pu. The reader is directed to the GEF literature for more detailed descriptions [38, 116, 117].

Importantly, the model parameters were already fitted once to experimental data by the GEF code developers [122]. The fit was done with a wide variety of experimental data: independent fission-fragment yields, prompt-neutron spectra and multiplicities, prompt-gamma spectra and multiplicities, isomeric ratios, delayed-neutron yields, decay heat, *etc.* To perform the fit, each model parameter was varied until the agreement between the experimental and calculated fission observable significantly deteriorated. A significant deterioration was defined as an increase in the reduced χ^2 by 1.0. Correlations were investigated, but were determined by the developers to not be important.
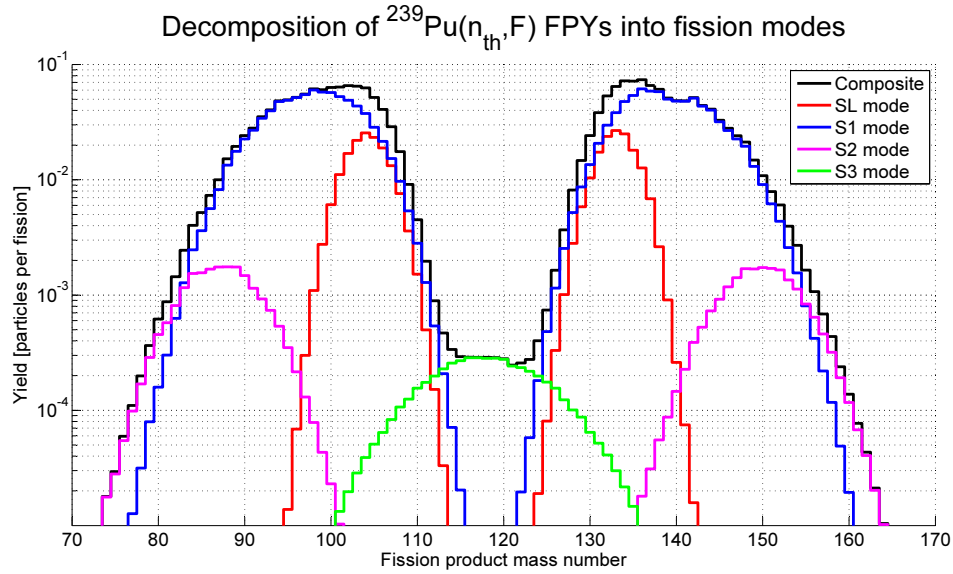
Figure 5.1 – FY distribution of thermal fission in Pu-239, decomposed into fission modes. This figure was made by K. Kern [120] using TALYS-1.4/GEF-2013/2.2 and is reused here.

5.3 Experimental Data and Computational Approach

5.3.1 LWR Proteus Phase II: PIE Data

The PIE data that function as the integral parameters in this DA study come from LWR-PII [75, 123], the same campaign outlined in Chp. 4. Chemical assays were done at the PSI hot laboratory to measure the composition of the irradiated fuel. This study used the measured FPs of a UO_2 sample with a burnup of ~38 MWd/kg. The fuel sample is called U1 in this document. The posterior GEF FYs were then used again in CASMO-5 to verify if there was improvement in predicted FP concentrations relative to the prior.

The posterior FYs were also tested on simulations of two separate fuel samples called U2 and M1, which are UO_2 and MOX fuels with burnups of ~58 and ~22 MWd/kg, respectively. Fuel samples U2 and M1 were used to test the performance of the posterior FYs for systems that were not included in the adjustment. The test assessed how the posterior FYs generalized to other systems and if they were over-fit to U1. Using U2 assessed how the posterior FYs performed on another UO_2 fuel with a higher burnup. By analyzing M1, we tested how the posterior FYs extrapolated to MOX fuel rather than UO_2 fuel.

The integral data were the concentrations of FPs in the spent fuel normalized to the total mass of uranium (all isotopes) in the fuel. In total, 33 nuclide concentrations were used in the adjustment. These FPs were composed of a variety of elements with varying mass numbers. Their mass numbers (A) are shown in Fig. 5.2 and are over-laid onto the independent FY spectrum of thermal fission in Pu-239 created by GEF.
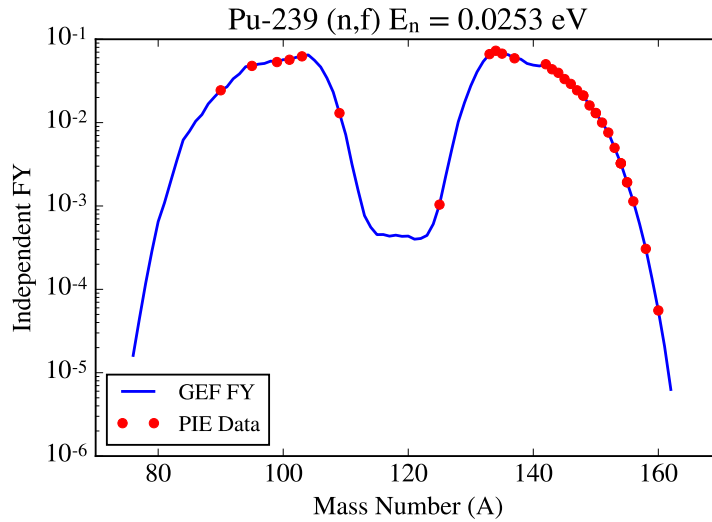
Figure 5.2 – Mass numbers of the PIE data on a FY distribution produced by GEF.

The nuclide concentrations were measured with liquid chromatography and mass spectrometry, and with γ-ray spectroscopy. The uncertainty associated with the experimental measurement depends on the analytic technique, with γ-ray spectroscopy giving the highest uncertainties. Through examination of the original experimental data from 2000–2004, we reconstructed the covariances between the measured nuclide concentrations that are not available in the official documentation. Fig. 5.3 gives the correlations for fuel sample U1. All of the measured concentrations have a degree of correlation induced by the normalization by the total uranium concentration. The nuclides of an element are also highly correlated by the use of a spiked reference sample during liquid chromatography and mass spectrometry, which creates a common source of uncertainty. A more detailed description of this covariance reconstruction process is presented in Appendix A.4.
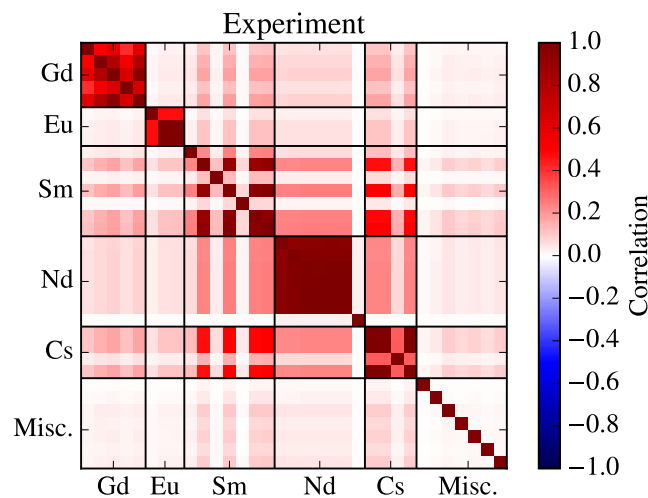
Figure 5.3 – Experimental correlations between the fission products in fuel sample U1.

The CASMO-5 depletion calculations used models that were created in Ref. [123] and also used in Ref. [107]. The U1 and U2 fuel samples were simulated in models that had a single fuel assembly with reflective boundary conditions. The M1 fuel sample was simulated in a MOX assembly that was surrounded by UO_2 assemblies in a 2×2 assembly model. The CASMO-5 models and the locations of the U1, U2, and M1 fuel pins are given in Fig. 5.4. The other fuel pins that were part of LWR-PII but not used in this study are also shown.
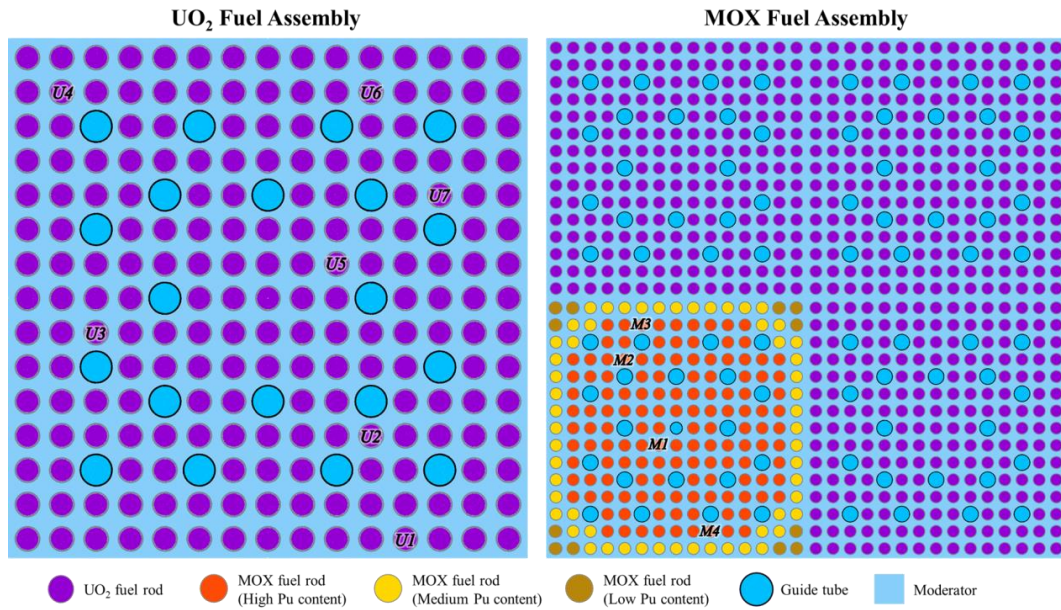
Figure 5.4 – CASMO-5 models for the depletion of the fuel samples. Taken from Ref. [107].

5.3.2 Computational Approach

CASMO-5M [87] modeled the LWR-PII fuel samples and predicted their FP concentrations after burnup. CASMO-5M employed a 586-energy-group structure and the ENDF-B/VII.1 nuclear data library [68]. The tool SHARK-X [78, 80, 79, 82] transferred the FY perturbations to CASMO-5M. The model parameters of GEF2017/1.1 were sampled 10,000 times from the distribution parameters outlined in Table 5.1. Then GEF was run 10,000 times with this set of model parameters. In each GEF run, 2E5 fission events were modeled. Subsequently, 10,000 CASMO-5M simulations were done to quantify the prior distribution of the calculated FP concentrations. With this prior distribution and population set of calculated values, the BFMC and MOCABA methods were applied to update the GEF model parameters. With the posterior model parameters, GEF was re-run 500 times, and then the CASMO-5M models were re-run 500 times with the posterior FY sample sets.

A PSI-developed script called `efficace` transferred the FYs in the ENDF files produced by GEF into a format that could be read by SHARK-X and fed into CASMO-5. CASMO-5 uses simplified decay chains that do not have the full detail contained in the ENDF files

made by GEF. `Efficace` also parsed the FYs in the ENDF files and simplified them to be compatible with CASMO-5. The flow structure and operations of `efficace` are shown in Fig. 5.5. Importantly, we had to modify the script for this project. This is because we desired for the true GEF FY values to be used in the simulation, not those from the CASMO-5 FY library. Previously, the script just put relative perturbations generated by GEF onto the CASMO-5 library. Now, the CASMO-5 FYs are fully replaced by the GEF FYs.
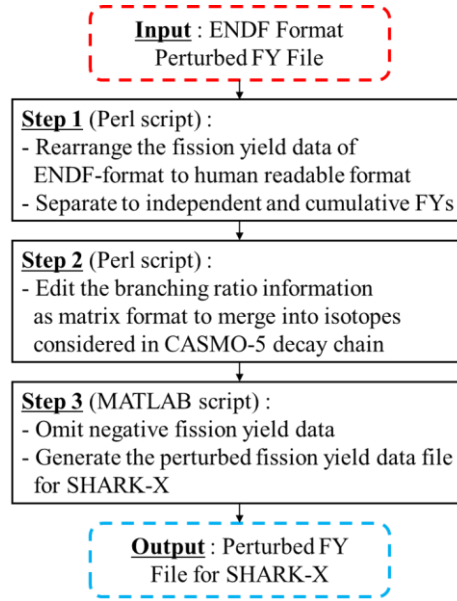
Figure 5.5 – Flow structure of the `efficace` script. Taken from Ref. [107].

The DA only considered uncertainties in the calculated FP concentrations that originated from the FY data. Certainly, there are many other uncertainties associated with the simulations. There are more nuclear data uncertainties that come from cross sections and other fission observables. There are also technological uncertainties associated with models. These include, but are not limited to, uncertainties in the enrichment, fuel temperature, cladding thickness, and moderator density. It was somewhat arbitrary to only include FY uncertainties, as SHARK-X could have certainly accounted for other sources of nuclear data uncertainty and uncertainties can be assigned to the technological parameters and they can be sampled. However, by defining the FYs as the only source of uncertainty, we isolated their effect and can focus solely on them. The PIE measurements also include data for minor actinides, but as they are not affected by FYs, they were not included.

The CASMO-5 simulations were also biased, or they have a *model inaccuracy*. For example, the irradiation history was approximated in a step-wise manner using a nodal core simulator with pin-power reconstruction. Furthermore, the models were 2D with reflective boundary conditions and did not account for the exact vertical location of the fuel sample on the fuel rod. Moreover, `efficace` and the reduced set of FYs in CASMO-5 were another possible source

of bias. Some of these biases could be mitigated by using a Monte-Carlo neutron transport code. This would allow a full representation of the geometry and to account for all FYs that GEF outputs. Monte-Carlo neutron transport, of course, would come with the disadvantage of increased computational cost. Because the stochastic-based DA methods can require many model runs, Monte-Carlo neutron transport codes were not pursued in this study.

For DA, the model biases and missing uncertainties manifest as inconsistent experimental and calculated integral data, quantified with χ^2. Not only may inconsistencies originate from the simulations, but also from missing covariances or underestimated uncertainties in the experimental data. The inconsistencies, if unaccounted for, can cause non-physically based adjustments to the model parameters. Because there are so many possible sources of bias and missing uncertainty, we chose to use the MLO method to approximate them and mitigate any effect of inconsistency on the adjustments.

To apply BFMC in the context of the current study, the process is summarized below,

1. Sample the GEF model parameters,

2. Run GEF with this model parameter sample set to produce a sample set of FYs,

3. Run `efficace` to transfer the GEF FY samples to a SHARK-X input for CASMO-5M,

4. Run the CASMO-5M model of fuel sample U1 with the FY sample set to create samples of calculated FP concentrations,

5. Use MLO to account for inconsistencies between the experiment and calculation,

6. Calculate the weights with Eq. (2.29) and the sample set of calculated FP concentrations, experimental mean values, and experimental covariance matrix,

7. Use the weights to update the model parameter distributions with Eqs. (2.27) and (2.28),

8. Re-sample the posterior GEF model parameters and rerun GEF to create posterior FYs,

9. Run the CASMO-5M models of fuel samples U1, U2, and M1 with the posterior FYs.

When the extra uncertainties were calculated with MLO, they were incorporated into the χ^2 values of each sample as shown in Eq. (5.4). These χ^2 for each sample are then used to calculate the weights with Eq. (2.29) and finally to update the GEF model parameters.

$$\chi_i^2 = \left(\mathbf{E} - \mathbf{C}(\boldsymbol{\sigma}_i)\right)^T \left(\mathbf{M_E} + \mathbf{M}_{\text{extra}}\right)^{-1} \left(\mathbf{E} - \mathbf{C}(\boldsymbol{\sigma}_i)\right) \tag{5.4}$$

To apply MOCABA, steps 1-5 are identical to BFMC with the following subsequent steps,

6. Estimate the the covariance matrices $\hat{\mathbf{M}}_{\mathbf{C}}$ and $\hat{\mathbf{M}}_{\sigma,\mathbf{C}}$, with Eqs. (2.21) and (2.22), from the sample set of model parameters and calculated FP concentrations,

7. Use $\hat{\mathbf{M}}_{\mathbf{C}}$ and $\hat{\mathbf{M}}_{\sigma,\mathbf{C}}$ to update the GEF model parameter distributions with Eqs. (2.12) and (2.13) including the $\mathbf{M}_{\text{extra}}$ calculated by MLO,

8. Re-sample the posterior GEF model parameters and rerun GEF to create posterior FYs,

9. Run the CASMO-5M models of fuel samples U1, U2, and M1 with the posterior FYs.

In this study, the posterior model parameters were re-sampled assuming that they remained normally distributed. In other words, they were re-sampled from multivariate normal distributions using $\boldsymbol{\sigma}'$ and $\mathbf{M}'_{\sigma}$, as calculated with either BFMC or MOCABA. Additionally, any correlation terms that arose in $\mathbf{M}'_{\sigma}$ were retained in the sampling. In the case of BFMC, it is possible to use the weights to create the posterior samples of the model parameters rather than to estimate a posterior mean and covariance matrix with Eqs. (2.27) and (2.28), respectively. In order to compare with MOCABA, we decided to re-sample from normal distributions. This does not take full advantage of BFMC's ability to account for non-normality, but it does simplify the comparison with MOCABA. It isolates the causes of potential differences to only the means and the covariance matrix of the model parameters.It also eliminates potential discrepancies caused by changes to shape of the distribution that BFMC might induce.

Section 2.3.4 showed that there are two formulations of the likelihood function used for MLO: Eqs. (2.42) and (2.44). In this study, both were tested and gave nearly equivalent outputs. For the results, Eq. (2.42) was technically used, but the other would have been equally valid.

5.4 Results and Discussion

In the following section, we present the prior and posterior distributions that were calculated with the previously detailed approach. First, Section 5.4.1 presents the prior distributions of the calculated FP concentrations and the results from applying MLO. Section 5.4.2 compares the MOCABA and BFMC adjustments, both of the model parameters and of the FY data that were produced with the adjusted model parameters. There, the GEF FYs are compared to the FY data of ENDF/B-VIII.0 and JEFF3.3. The posterior FP concentrations, calculated with the posterior FYs, are also presented. Section 5.4.3 discusses the effect of using MLO.

5.4.1 Prior and MLO

The first steps were to sample the GEF model parameters, to use GEF to generate a sample set of FYs, and to use the FY samples in the CASMO-5M simulations. The sample set of calculated FP concentrations was then extracted from the CASMO-5 outputs to estimate their prior distributions. Fig. 5.6 is the outcome of this procedure and presents the prior bias, or C/E - 1, of the CASMO-5 simulations along with the relative standard deviation of the C values.

It additionally gives the relative standard deviation of the E values. The sample mean and sample standard deviations of C are reported.
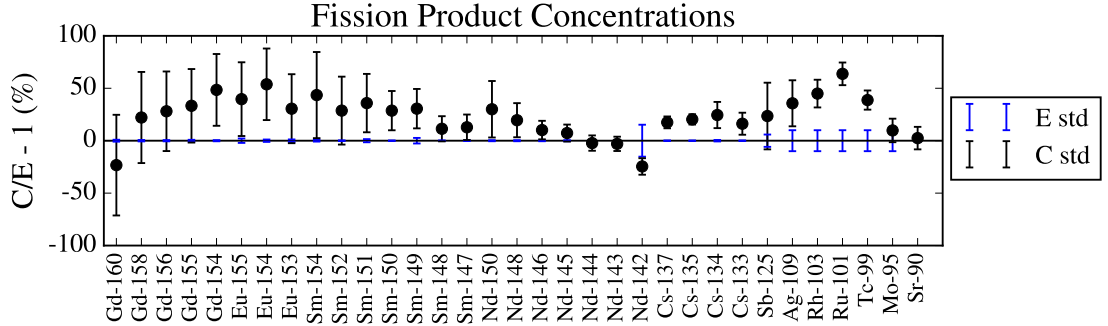
Figure 5.6 – Relative biases and uncertainties for fission products of fuel sample U1.

Fig. 5.6 demonstrates that some FP concentrations had large biases. The largest bias was 64% for Ru-101 and the average absolute value of all biases was 26%. The uncertainties created by the FY data were also large, with the largest being 56% for Gd-160 and the average being 21%. For reference, Subgroup 26 of the OECD's WPEC [10] set target accuracies on nuclide inventories (albeit for high temperature reactors) at a 1σ of 20% for FPs. The uncertainties here from GEF, on average and significantly at extremity, exceed this target accuracy and, therefore, point to the attraction of using DA in burnup. Importantly, some biases were very inconsistent, like for Rh-103, Ru-101, or Tc-99.

χ^2 can be used as a global measure of the consistency of the data set. When it is defined as in Eq. (5.5) and divided by the 33 degrees of freedom (DoF), or number of FP concentrations (N_E), its value is 38. A value of 38 is far from the 1.0 value expected, especially given that the standard deviation ($\sqrt{2N_E}$) per DoF of the χ^2 distribution is 0.3.

$$\chi^2 = \left(\mathbf{E} - \mathbf{C}\right)^T\left(\mathbf{M_E} + \mathbf{M_C}\right)^{-1}\left(\mathbf{E} - \mathbf{C}\right) \tag{5.5}$$

The distributions of C can also be examined to assess their degree of normality. Recall that MOCABA assumes C values are normally distributed. Any non-normality may cause biases in the adjustments. Fig. 5.7 shows normalized histograms of the calculated nuclide concentrations for various nuclide concentrations in fuel sample U1. Isotopes like Gd-160 and Sb-125 show a higher degree of non-normality than isotopes like Mo-95 or Nd-143.

The Shapiro-Wilks test [124] was used to test how likely it was that the C distributions were drawn from Gaussian PDFs. It gives a p-value that indicates how likely the null hypothesis is true, *i.e.* C is Gaussian. The p-value is compared to a threshold α level. Here, α was chosen to be 0.05. That means if the p-value ≤ 0.05, we reject the null hypothesis with 95% confidence. The Pearson skewness was used to assess the significance of the tail of each C distribution. For a normal distribution, whose left and right tails are symmetric, the skewness is 0. A positive or
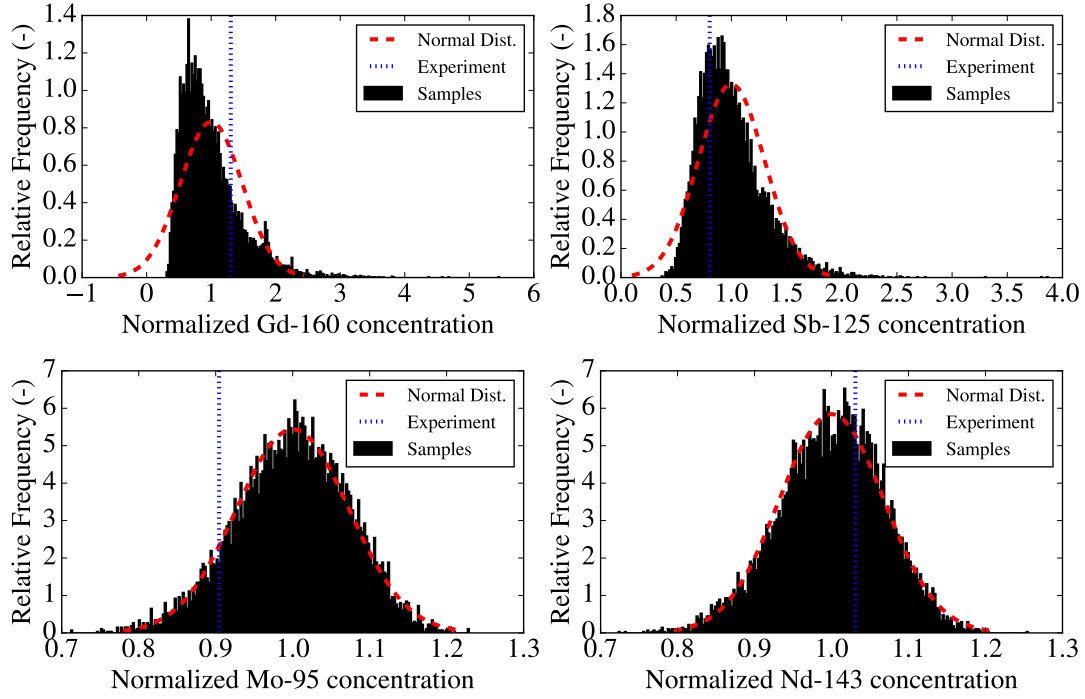
Figure 5.7 – Histograms of the prior calculated FP concentrations normalized to the mean.

negative skewness indicates asymmetry in the distribution. The skewness was calculated as shown in Eq. (5.6), where the number of samples N was 10,000.

$$\text{skew}(C) = \frac{\frac{1}{N}\sum_{i=1}^{N}\left(C_i - \bar{C}\right)^3}{\left(\sqrt{\frac{1}{N}\sum_{i=1}^{N}\left(C_i - \bar{C}\right)}\right)^3} \tag{5.6}$$

The p-values and skewness of each C are given in Fig. 5.8. Only three FPs pass the Shapiro-Wilks test: Nd-146, Nd-145, and Nd-144. That means that 30 of 33 FPs can be classified as non-normal with 95% confidence. The skewness helps to show which FPs are most non-Gaussian, and these are the Gd, Eu, and Sm isotopes along with Nd-150 and Sb-125. The effect that the non-normality and these degrees of skewness have on MOCABA will be discussed in the following sections.

Results from MLO

The χ^2 value of 38 per DoF indicated a large degree of inconsistency between the C and E data. This inconsistency may have been caused by ignoring sources of uncertainty or error in the simulations. As previously discussed, such inconsistency may induce unrealistic adjustments of the model parameters and FYs. The MLO method was applied to improve the consistency by adding extra uncertainty to integral parameters. The results from MLO are presented in Fig. 5.9.
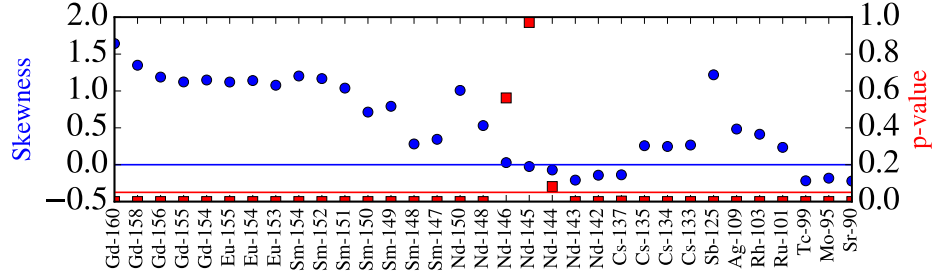
Figure 5.8 – Skewness values and p-values from a Shapiro-Wilks normality test for the calculated nuclide concentrations of fuel sample U1.

MLO added extra uncertainties to the isotopes that showed large degrees of inconsistency, *e.g.* Eu-154, Cs-134, Rh-103, Ru-101, or Tc-99. The χ^2, recalculated with $\mathbf{M}_{\text{extra}}$ as in Eq. (2.41), becomes 0.7 per DoF. This χ^2 is within the standard deviation of the χ^2 distribution for 33 DoF. The effect on the GEF model parameters, FYs, and C values of applying MLO is presented in Section 5.4.3.
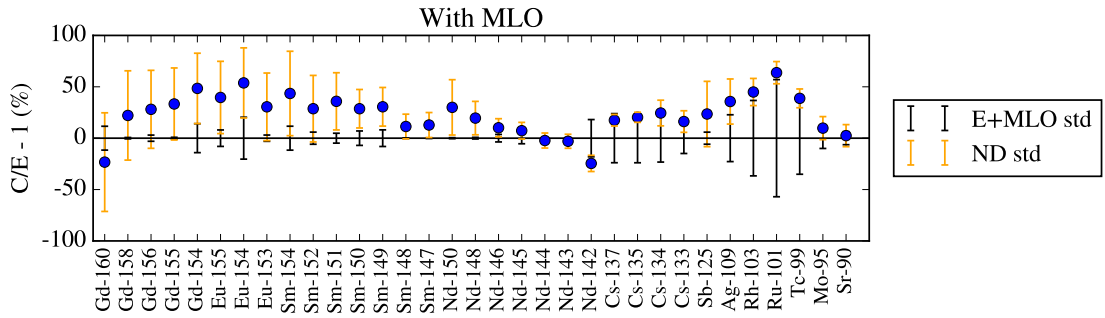
Figure 5.9 – Biases and uncertainties for the FP concentrations of U1 after applying MLO.

5.4.2 BFMC vs. MOCABA

This section presents all of the posteriors from BFMC and MOCABA. These include the posterior model parameters, independent FYs, and calculated FP concentrations. The posterior FYs are compared to ENDF/B-VIII.0 and JEFF3.3 data. Only the FYs of Pu-239 are presented to be concise. The posterior FYs of U-235, U-238, and Pu-241 are presented in Appendix A.5.

Model Parameter Adjustments

The adjustments of the 21 model parameters using BFMC and MOCABA are shown in Table 5.2. Their 95%-confidence-intervals with 500 bootstrap samples, see Section 3.2.1, are also shown. Many of the model parameters did not have adjustments from prior to posterior that were statistically significant. The parameters that were changed in a statistically significant way were those associated with the shell positions of the fission channels (P_DZ_Mean_S#), the shell curvatures (P_Z_Curv_S#), P_A_Width_S2, P_Shell_S3, and POLARadd. Among the

fission channels, the S_3 channel had its model parameters adjusted to the largest degree. Noticeably, the posterior BFMC model parameters have larger confidence intervals than those from MOCABA, which will be discussed further below. Only P_A_Width_S2 had statistically significant differences between MOCABA and BFMC.

Table 5.2 – Adjustments of the means and standard deviations of GEF's model parameters. 95%-confidence intervals are shown that were estimated with bootstrap sampling.

GEF Parameter	Mean			Standard Deviation		
	Prior	MOCABA	BFMC	Prior	MOCABA	BFMC
P_DZ_Mean_S1	-0.179	-0.138 ± 0.011	-0.150 ± 0.023	0.100	0.082 ± 0.003	0.086 ± 0.017
P_DZ_Mean_S2	-0.461	-0.477 ± 0.007	-0.476 ± 0.026	0.100	0.080 ± 0.002	0.076 ± 0.011
P_DZ_Mean_S3	-0.372	-0.315 ± 0.006	-0.295 ± 0.031	0.099	0.084 ± 0.001	0.084 ± 0.020
P_DZ_Mean_S4	0.002	-0.002 ± 0.005	-0.001 ± 0.027	0.100	0.100 ± 0.000	0.088 ± 0.014
P_Z_Curv_S1	0.370	0.368 ± 0.001	0.368 ± 0.007	0.018	0.017 ± 0.000	0.018 ± 0.004
P_Z_Curv_S2	0.185	0.185 ± 0.001	0.189 ± 0.003	0.009	0.009 ± 0.000	0.008 ± 0.002
P_A_Width_S2	12.491	11.908 ± 0.025	12.183 ± 0.174	0.628	0.433 ± 0.011	0.506 ± 0.095
P_Z_Curv_S3	0.156	0.155 ± 0.000	0.153 ± 0.002	0.008	0.007 ± 0.000	0.007 ± 0.001
P_Z_Curv_S4	0.035	0.035 ± 0.000	0.035 ± 0.000	0.002	0.002 ± 0.000	0.002 ± 0.000
P_Shell_S1	-2.849	-2.850 ± 0.004	-2.851 ± 0.025	0.099	0.076 ± 0.001	0.085 ± 0.023
P_Shell_S2	-4.401	-4.410 ± 0.005	-4.400 ± 0.031	0.100	0.072 ± 0.002	0.091 ± 0.030
P_Shell_S3	-6.400	-6.286 ± 0.009	-6.326 ± 0.045	0.199	0.124 ± 0.005	0.132 ± 0.035
P_Shell_S4	-0.900	-0.901 ± 0.003	-0.920 ± 0.030	0.050	0.050 ± 0.000	0.059 ± 0.019
T_low_S1	0.320	0.319 ± 0.001	0.318 ± 0.002	0.010	0.010 ± 0.000	0.009 ± 0.001
T_low_S2	0.310	0.310 ± 0.001	0.311 ± 0.003	0.010	0.010 ± 0.000	0.010 ± 0.002
T_low_S3	0.310	0.312 ± 0.001	0.310 ± 0.003	0.010	0.010 ± 0.000	0.011 ± 0.002
T_low_S4	0.310	0.310 ± 0.001	0.308 ± 0.004	0.010	0.010 ± 0.000	0.011 ± 0.002
T_low_SL	0.310	0.311 ± 0.001	0.308 ± 0.003	0.010	0.010 ± 0.000	0.009 ± 0.001
Delta_S0	-0.001	0.000 ± 0.005	-0.018 ± 0.029	0.099	0.099 ± 0.000	0.103 ± 0.018
HOMPOL	1.001	1.011 ± 0.005	0.994 ± 0.041	0.101	0.100 ± 0.000	0.096 ± 0.023
POLARadd	0.253	0.284 ± 0.004	0.269 ± 0.014	0.101	0.054 ± 0.003	0.049 ± 0.010

The update also produced correlations between the model parameters. Fig. 5.10 shows the correlation matrices between the posterior model parameters produced by MOCABA and BFMC. The prior matrix is not shown because it is diagonal as the prior model parameters are defined to be independent by the GEF developers. The 95%-confidence intervals from bootstrapping are also given for each correlation coefficient.

The first feature from Fig. 5.10 that captures the eye is the differences between the MOCABA and BFMC matrices. BFMC shows a much larger degree of inter-correlations than MOCABA. However, the 95%-confidence-intervals show that the BFMC correlations also have a much larger degree of uncertainty. Many of them cannot be declared to be statistically significant. The MOCABA correlations have much smaller confidence intervals, allowing them to be considered to be statistically significant. MOCABA shows that some model parameters do develop correlations, especially the P_Shell parameters and POLARadd.

Chp. 3 showed that the combined effects of weight degeneracy and too low sample size can create large uncertainties in the $\mathbf{M}'_\sigma$ calculated with BFMC. The degree of weight degeneracy
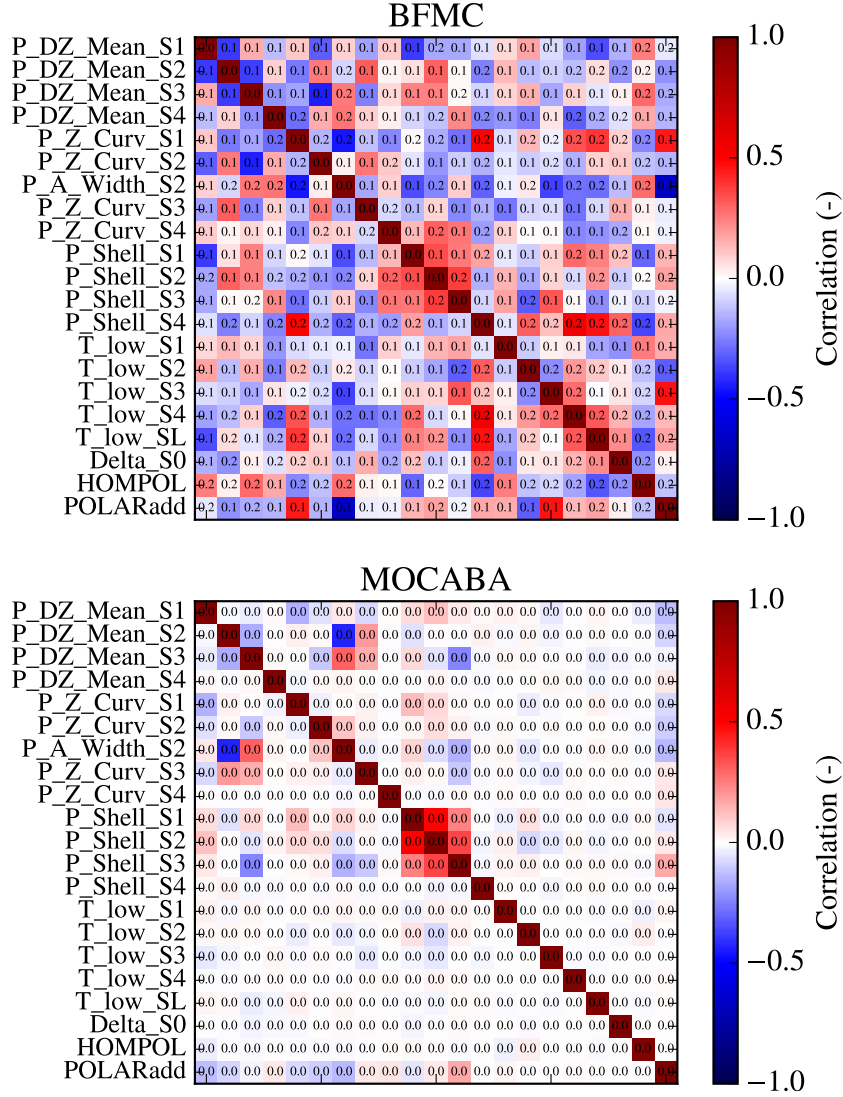
Figure 5.10 – Correlation matrices of the 21 posterior GEF-model parameters. Each correlation coefficient has its 95%-bootstrap-confidence interval over-laid on it.

can be qualified by examining the weight distribution of the sample set. Fig. 5.11 gives the weights that were calculated with the 10,000 samples and Eq. (2.29). The figure shows that many of the weights were, in a practical sense, zero-valued. The CDF of the weight distribution, shown in Fig. 5.11, shows that only ~1% of the weights, or 100 out of 10,000 samples, were significantly greater than 0. While this does not display a total weight degeneracy, it caused an insufficiently converged $\mathbf{M}'_\sigma$ with BFMC and thereby explains the large confidence intervals seen in the BFMC correlations. In Section 5.4.3, we find that BFMC without MLO had more significant weights and its posterior weighted averages were more highly converged. The off-diagonal correlations in $\mathbf{M}'_\sigma$ then disappeared.
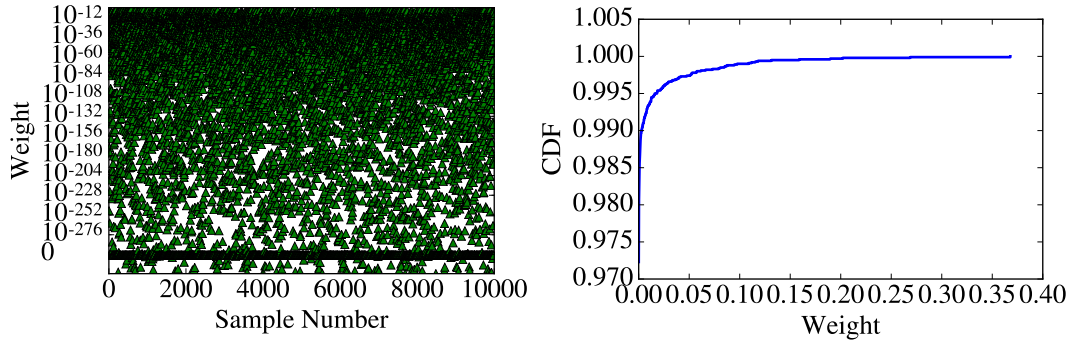
Figure 5.11 – Weights calculated with the BFMC weight definition and the corresponding CDF of the weight distribution.

FY Adjustments

In Fig. 5.12 we see the prior and posterior independent FYs for thermal fission of Pu-239. These were produced by running GEF with the model parameters given in Section 5.4.2. In general, it is difficult to discern differences between the prior and posterior with the logarithmic y-axis. For that reason, the posteriors are plotted again in Fig. 5.13 as the relative difference between the prior and posterior for the mean and standard deviation of the independent FYs.
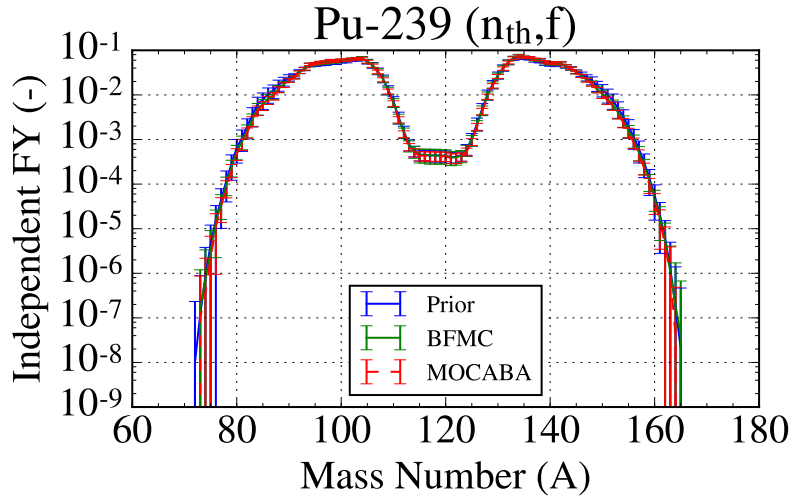
Figure 5.12 – Prior and posterior Pu-239 (n_{th}, f) independent FYs.

First examining the relative differences of the means, the adjustments from prior to posterior were largest at A = 135–160 and symmetrically at A = 80–105. The areas of large adjustment correspond to regions where experimental data were densest. Fig. 5.2 showed that most of the FP concentrations were isotopes of Nd, Eu, Sm, and Gd, all of which have A > 140. There was strong agreement between the FYs of MOCABA and BFMC for A = 90–150. There were stronger disagreements at A < 80 and A > 160, but these are rare yields with poor statistics in the Monte Carlo process of GEF. Given their large uncertainties, which are seen in the error

bars in Fig. 5.12, we can expect larger disagreements in the posteriors. Returning to the yields associated with A = 80–160, in general, MOCABA created larger adjustments than BFMC with peaks at A ≈ 115 and A ≈ 125. These adjustments were significantly affected by the posterior model parameters associated with the S_3 channel, as it is dominant for FYs at these A. Table 5.2 showed adjustments of the shell position for the S_3 channel (P_DZ_Mean_S3) of 21% with MOCABA and and 15% with BFMC. The shell effect of the S_3 channel (P_Z_Shell_S3) also saw adjustments of -2% and -1% with MOCABA and BFMC, respectively.
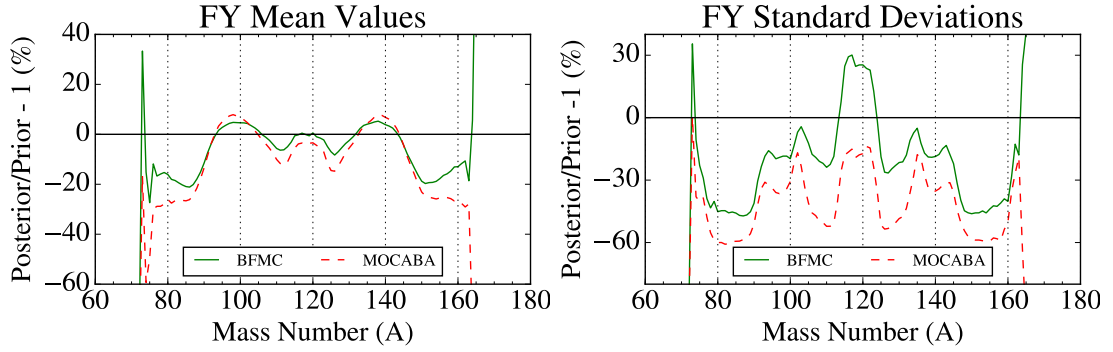
Figure 5.13 – Relative differences in the means and standard deviations of (n_{th}, f) Pu-239 independent FYs.

The adjusted standard deviations have similar trends. First, the reductions in uncertainty were largest at A = 135–160 and symmetrically at A = 80–100, where there were the most experimental integral data. For both the MOCABA and BFMC posteriors, at the A corresponding to the centers of the different fission channels, there were sharp reductions in the FY uncertainty. In the case of BFMC, the FYs in the region dominated by the S_3 and S_4 channels, at A ≈110–130, increased in uncertainty. The increase is explained in part by the increased uncertainty of P_Shell_S4, where the prior standard deviation was 0.05 MeV and the posterior was 0.07 MeV.

Additionally, the posterior covariance matrix of the model parameters (used to sample the posterior distributions) had significant correlation terms when BFMC was used (see Fig. 5.10). In particular, significant positive correlations appeared between P_Shell_S3 and P_Shell_S1, and P_Shell_S2. P_Shell_S2 also saw an increase in its standard deviation relative to the prior when BFMC was used, from 0.10 to 0.11. Through correlation with P_Shell_S3, this increase led to increased uncertainties in the FYs at 110 < A < 130. The FYs of U-235, U-238, and Pu-241 (see Appendix A.5) also showed an increase in uncertainty at this region. Again for very rare yields, at A < 80 and A > 160, there were more disagreements between MOCABA and BFMC and large changes to uncertainties. These adjustments were not reliable due to the limited statistics of GEF for these FYs.

Fig. 5.14 presents the prior and posterior correlation matrices for the independent FYs of thermal fission in Pu-239. These were calculated with the approach outlined in Section 5.2.2. The prior correlation matrix has large positive correlations (red) between FP pairs, which can be seen by following the lower-left to the upper-right of the matrix. The strong

correlations slightly off the main diagonal (upper-left to lower-right) come from FPs that are dominated by the same fission channel and are consequently highly correlated to the same model parameters.[4] For instance, the S_2 channel dominates at $70 < A < 90$ and $145 < A < 165$, and there are regions of strong correlation between FYs there. These correlations for FYs dominated by the same channel are present for S_1 at $91 < A < 100$ and $135 < A < 144$, for S_L at $101 < A < 112$ and $126 < A < 134$, and for S_2 at $113 < A < 125$. The within-channel correlations are also seen between the light and heavy humps of the FY spectrum.
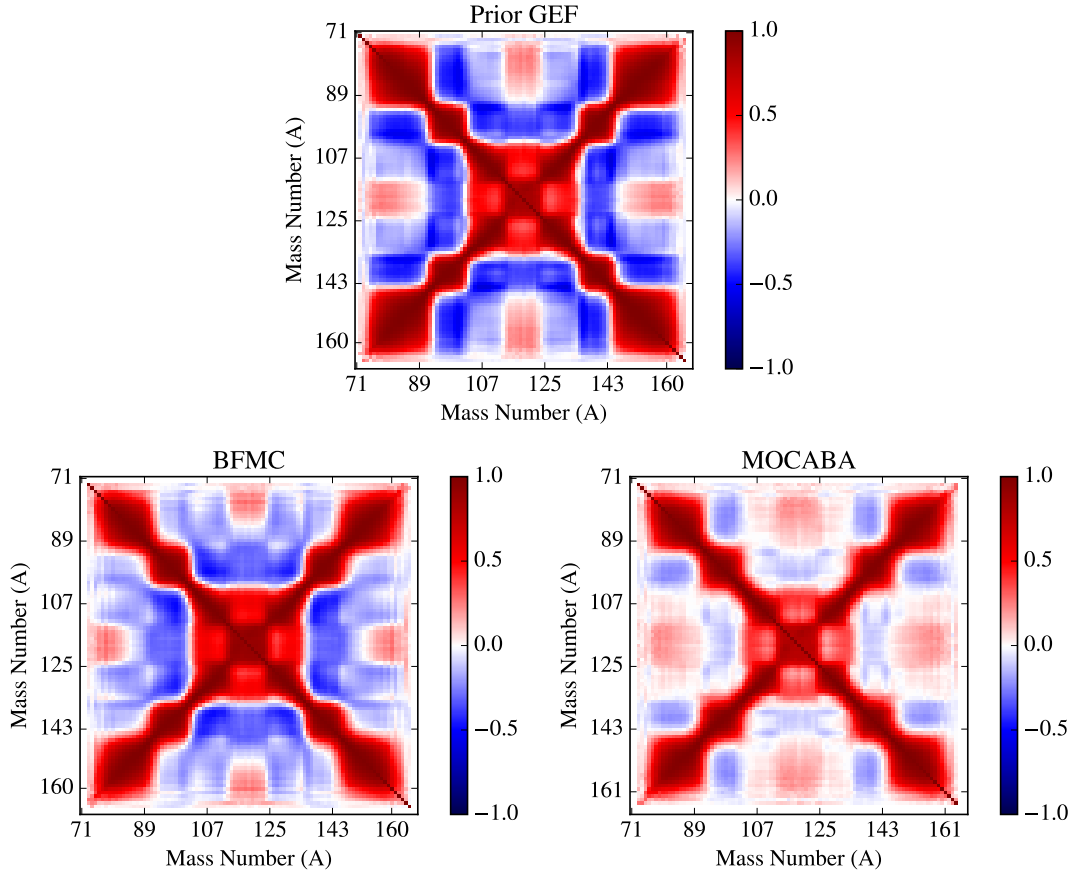
Figure 5.14 – Correlations for the (n_{th}, f) independent FYs of Pu-239.

The matrix also has large degrees of anti-correlation (blue) between fission channels. For example, the FYs between the S_2 and S_1, and between the S_1 and S_4 channels show anti-correlation. This is related to the fact that these channels overlap on the FY spectrum and compete to create the FYs. The S_2 and S_3 channels barely overlap and show a positive correlation. This positive correlation is likely induced by the more global model parameters in Table 5.1, like HOMPOL or POLARadd, or by the normalization of the FYs to 2.0 that affects all channels equally [120]. This could be confirmed with a global sensitivity analysis [1] in future work.

By incorporating experimental data, BFMC and MOCABA both reduced the degree of cor-

---

[4]Please refer to Fig. 5.1 for details on the influence of the channels on the FY spectrum.

relation between the FY data. In large part, the trends in the correlation matrices that were in the prior were retained, only the extent of correlation and anti-correlation were affected. Compared to BFMC, MOCABA created more significant reductions in correlation, particularly to the anti-correlation terms and especially between the S_1 and S_4 and S_3 and S_4 channels.

Fig. 5.15 provides the prior and posterior correlations between FYs of thermal fission in U-235 and Pu-239. As GEF was run with the same sets of model parameters to produce each nuclide's FYs, their data became correlated through the common inputs. Similar to the previously outlined behavior, large degrees of positive correlation appeared between the FYs of the two nuclides due to influences of the same fission channels. Similarly, competing fission channels created anti-correlations. From prior to posterior, the trends are similar: decreased degrees of correlation and anti-correlation, with MOCABA decreasing the correlation to a larger extent than BFMC.
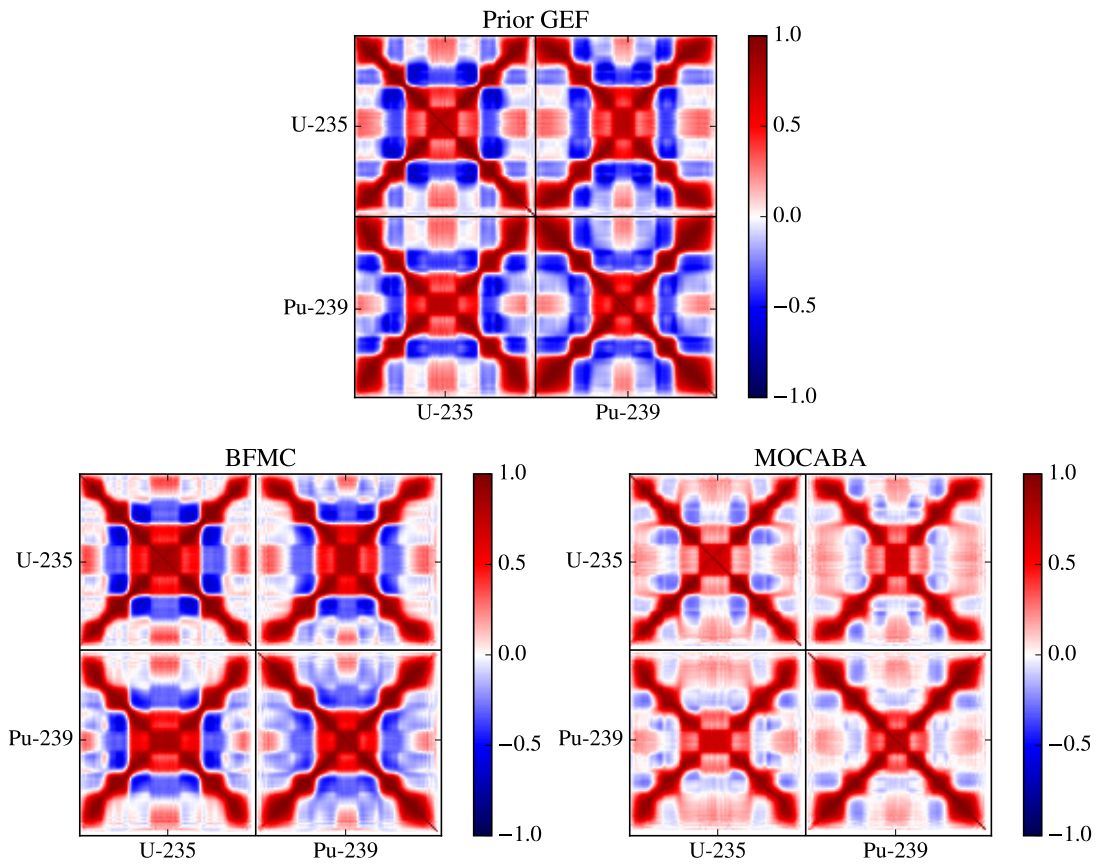
Figure 5.15 – Correlations between the (n_{th}, f) independent FYs of U-235 and Pu-239.

Fig. 5.16 compares the GEF FYs with those given in ENDF/B-VIII.0 and JEFF3.3. In general, it is difficult to discern differences between the FYs. To compare in more detail the posterior GEF FYs with ENDF and JEFF, the relative differences are plotted for the FY means in Fig. 5.17 and for the standard deviations in Fig. 5.18. In general, we observed relative differences of the

mean values at -40 to +40%. The biggest improvement from prior to posterior between the GEF FY data and those from JEFF3.3 and ENDF/B-VIII.0 occurred at 85 < A < 95 and 135 < A < 150. These improvements can be connected to where the experimental data were concentrated. Recalling Fig. 5.2, we see that approximately 70% of the integral data had A > 135. With a large concentration of evidence in this area, the adjustments were the most significant there.
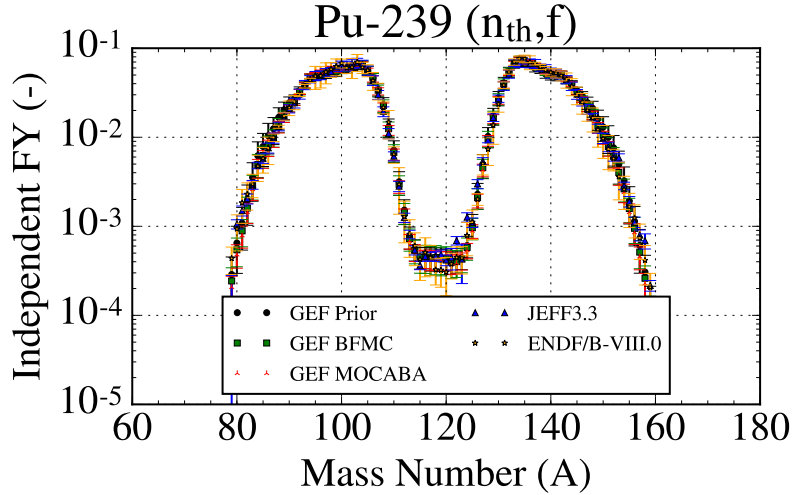
Figure 5.16 – Pu-239 FYs from ENDF/B-VIII.0, JEFF3.3, and prior/posterior GEF.

Fig. 5.18 shows that GEF's prior uncertainties tended to be larger compared to ENDF/B-VIII.0 and JEFF3.3. Similar to the means, the posteriors' reductions in uncertainty were largest at 85 < A < 95 and 135 < A < 150, where the integral data were densest. MOCABA produced smaller uncertainties than BFMC that were closer to those from ENDF/B-VIII.0 and JEFF3.3.
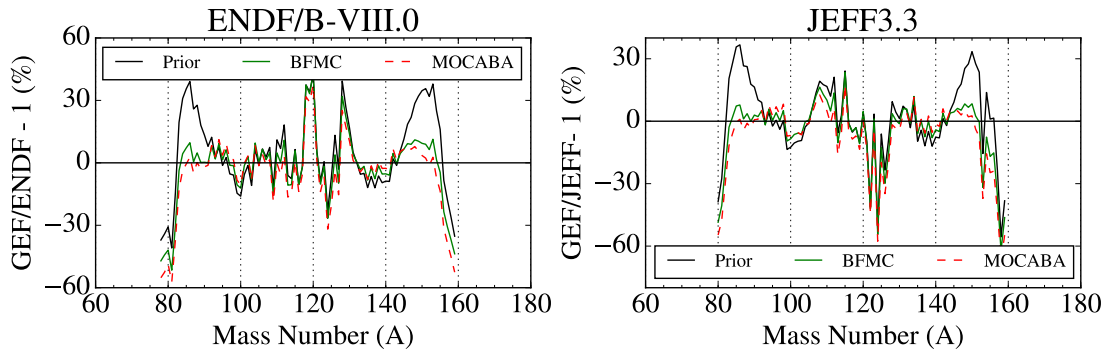
Figure 5.17 – Relative differences of the means of the independent FY data for Pu-239 between ENDF/B-VIII.0 and GEF and between JEFF3.3 and GEF.

Table 5.3 gives the comparison shown in Figs. 5.17 and 5.18 summarized over the whole independent FY data set for Pu-239, U-235, and Pu-241 thermal fission. U-238 is not shown because the FY data in JEFF3.3 and ENDF/B-VIII.0 are given for a neutron energy of 400 keV, while GEF was run for a neutron energy of 500 keV. This difference in neutron energy was significant enough to cause very large disagreements between GEF and the other nuclear data
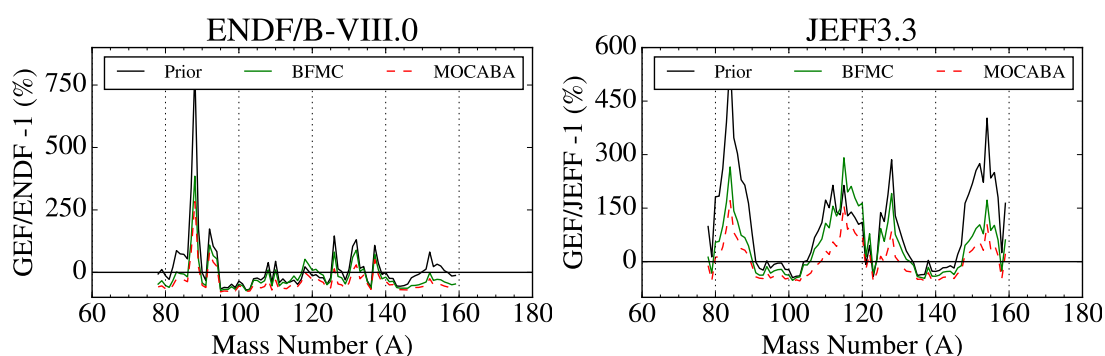
Figure 5.18 – Relative differences of the standard deviations of the independent FY data for thermal fission of Pu-239 between ENDF/B-VIII.0 and GEF and between JEFF3.3 and GEF

libraries, and unfortunately made comparisons between these data sets inconsistent.

For the relative difference of the mean FYs, the mean of the absolute value of the relative differences was taken. In the case of Pu-239 and Pu-241, there was improved agreement between the GEF FYs and ENDF/B-VIII.0 and JEFF3.3. For the means, there were not significant differences between the MOCABA and BFMC posteriors. MOCABA made larger uncertainty reductions than BFMC. For Pu-239 and Pu-241, the GEF posteriors had smaller uncertainties than ENDF/B-VIII.0, *i.e.* negative average relative differences in the standard deviations, both with MOCABA and BFMC. The agreement of GEF with ENDF/B-VIII.0 and JEFF3.3 deteriorated for U-235, although U-235 did still have its uncertainty reduced.

Table 5.3 – Comparing GEF independent FYs (prior & posterior) to JEFF3.3 and ENDF/B-VIII.0.

		Avg. Abs. Rel. Diff. (%)		Avg. Std. Rel. Diff. (%)	
		ENDF/B-VIII.0	JEFF3.3	ENDF/B-VIII.0	JEFF3.3
Pu-239	Prior	15.8	15.7	15.9	99.5
	BFMC	11.4	11.9	-15.5	45.7
	MOCABA	11.5	12.6	-37.5	4.3
U-235	Prior	12.9	11.6	176.8	157.4
	BFMC	15.0	13.2	100.6	92.6
	MOCABA	17.1	15.5	53.8	42.0
Pu-241	Prior	21.9	32.9	5.3	79.5
	BFMC	15.8	26.0	-27.7	18.4
	MOCABA	15.7	25.7	-46.5	-12.9

Noticeably, GEF produced 100% larger uncertainties for U-235, relative to ENDF/B-VIII.0 and JEFF3.3. This is due, in part, to GEF's design and, in another part, to the quality and abundance of U-235 experimental FYs. Section 5.2 detailed how GEF was designed to be as general as possible: one model and one set of model parameters predicts with good accuracy the fission observables of isotopes like U-235, or less commonly encountered isotopes like Bk-230 or Fm-256. For this generality, GEF sacrifices some accuracy for an isotope like U-235, which is very well characterized by experimental data. ENDF/B-VIII.0 and JEFF3.3 FYs, which profit

from this large quantity of quality U-235 experiments, have smaller reported uncertainties.

The degradation of agreement between the GEF FY for U-235 and those from ENDF/B-VIII.0 and JEFF3.3 has not yet bet completely explained. In part, this may be due to the fact that when the GEF model parameters were tuned by the developers the first time, *i.e.* the assessment of the prior model parameters, they used a large amount of high quality U-235 data. When we incorporated the experimental integral data here, we lost some of that tuning in order to improve the FY data of Pu-239, Pu-241, and U-238.

Alternatively, the observed degradation may just be a statistical effect. All of the FY data, on average, saw an improved agreement between GEF and the nuclear data libraries. While this is the case on average, some data may have worsened. Given that for U-235 the relative difference of ENDF/B-VIII.0 and JEFF3.3 from GEF increased only by +2.8% and +1.6%, respectively, these data could be the statistically unlucky ones that worsened. Given the complexity of the data set, it has not yet been possible to make a definitive conclusion about the U-235 FYs. Future studies with different fuel samples, possibly with lower burnups to further emphasize U-235 fission, could clarify this unresolved question.

Posterior FP Concentrations

In this section, we present how the posterior FYs performed in the CASMO-5M simulations of the LWR-PII fuel samples. We begin with fuel sample U1, which was the training data used to adjust the GEF model parameters. The prior and posterior biases of the FP concentrations are presented in Fig. 5.19. The average absolute value of the prior bias was 26.4% and the average uncertainty of the calculated FP concentrations was 20.6%. When BFMC adjusted the GEF FYs and then the FP concentrations were recalculated in CASMO-5 with these posterior FYs, the average absolute value of the bias was 15.4% and the uncertainty of the posterior calculated values was 14.1%. When MOCABA was used in the same manner, the average absolute value of the bias was 13.7% and the uncertainty of the posterior calculated values was 13.5%. Given the similarities between the posterior FYs of MOCABA and BFMC seen in Section 5.4.2, the agreement between the posterior biases is not surprising.
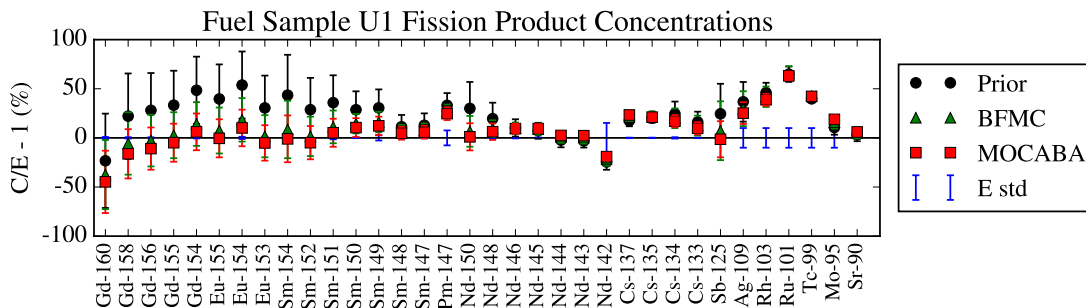
Figure 5.19 – Prior and posterior biases of the FP concentrations of fuel sample U1.

Next, we examine how the adjusted FYs performed to estimate FP concentrations that were not part of the training data. This tests for over-fitting of the model parameters to fuel sample U1. If they were indeed overfit, the posterior biases would be worse than the prior. Fig. 5.20 gives the prior and posterior biases of FP concentrations in fuel samples U2 and M1. The two fuel samples also showed improved biases and reduced uncertainties, along with agreement between BFMC and MOCABA.
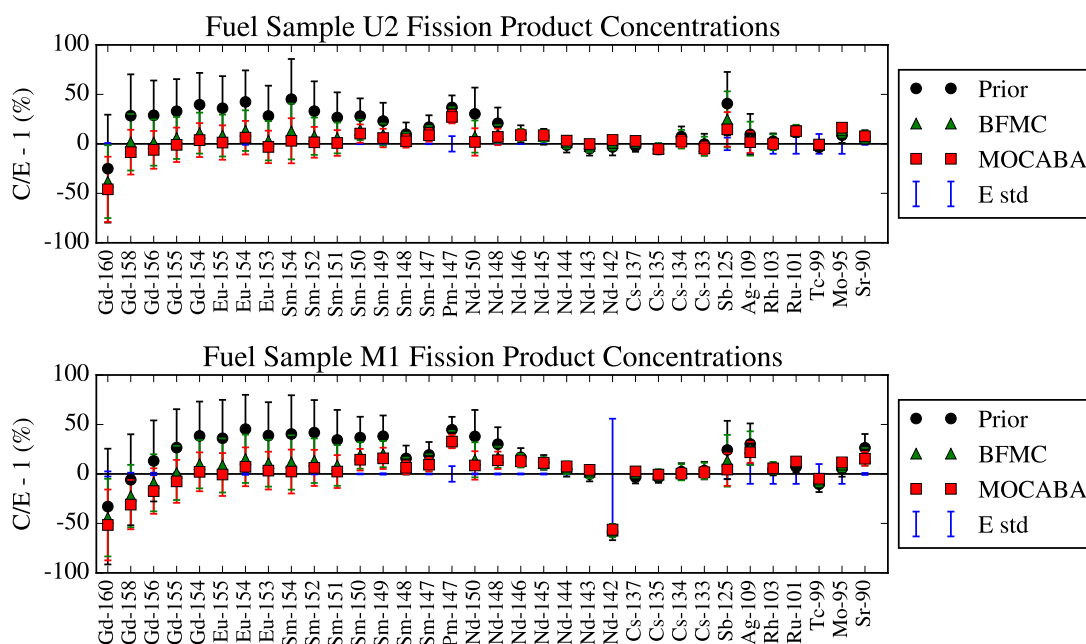
Figure 5.20 – Prior and posterior biases of the FP concentrations of fuel sample U2 and M1 when using BFMC and MOCABA. Calculated with the FYs trained with fuel sample U1.

The biases and uncertainties given in Figs. 5.19 and 5.20 are summarized in Table 5.4. Here, the absolute value of the biases and the relative standard deviations of the calculated vales are averaged across all FP concentrations. For all fuel samples, the bias improved from prior to posterior. Additionally, the MOCABA posterior FYs improved the bias to a larger extent than the BFMC FYs. Similarly, all three fuel samples had the uncertainty associated with their calculated values reduced from prior to posterior. MOCABA reduced the relative standard deviation to a larger extent than BFMC. From these results, we can conclude the adjustment was not over-fit to the U1 data because there was a similar performance for U2 and M1.

5.4.3 Effect of MLO

In this section, we present the adjusted model parameters, posterior FYs, and posterior calculated FP concentrations when they were calculated with and without MLO extra uncertainties, using both BFMC and MOCABA. The posteriors are compared to assess the effect that MLO had on the adjustments and to investigate the importance of accounting for the inconsisten-

Table 5.4 – Analysis of the bias and uncertainty of posterior calculated nuclide concentrations.

		Avg. Abs. Bias (%)	Avg. Rel. Std. (%)
	Prior	26.4	20.6
U1	BFMC	15.4	14.1
	MOCABA	13.7	13.5
	Prior	19.4	19.3
U2	BFMC	8.72	13.4
	MOCABA	7.04	10.5
	Prior	23.2	21.0
M1	BFMC	13.7	15.0
	MOCABA	11.9	11.6

cies of integral data. First in Section 5.4.3, the posterior model parameters are presented. Then Section 5.4.3 presents and discusses the posterior FYs obtained when GEF used these posterior model parameters. Finally, Section 5.4.3 has the posterior biases of the FP concentrations of the LWR-PII fuel samples that were calculated with these posterior FYs.

Posterior Model Parameters

Table 5.5 gives the posterior model parameters when BFMC was used with and without applying MLO. The table shows some clear differences in the posteriors that are statistically significant in terms of the bootstrap-estimated 95%-confidence intervals. For the mean values, the differences are prominent for P_DZ_Mean_S1, P_DZ_Mean_S3, P_A_Width_S2, P_Shell_S3, P_Shell_S4, and POLARadd. For the standard deviations of the model parameters, there were large differences for P_DZ_Mean parameters, P_A_Width_S2, P_Shell_S2, and POLARadd. Only for the parameters P_DZ_Mean_S1 and POLARadd can these differences, both for the means and standard deviations, be considered statistically significant within the 95%-confidence intervals. How these differences affected the FY data is shown in Section 5.4.3. The confidence intervals were smaller when MLO was not used, which will be discussed later.

Table 5.6 gives the same posterior model parameters but when MOCABA was applied with and without using MLO. MOCABA displayed more significant differences between the parameters when MLO was and was not applied than did BFMC. For instance, P_DZ_Mean_S1, P_DZ_Mean_S2, P_A_Width_S2, P_Z_Curv_S3, P_Shell_S3, T_low_S3, HOMPOL, and PO-LARadd all showed large differences between the two posterior sets. The posterior standard deviations of the model parameters also showed significant differences. When MLO was not used, the posterior standard deviations tended to be smaller than when MLO was used, for instance for P_DZ_Mean_S1, P_DZ_Mean_S2, P_A_Width_S2, P_Shell_S3, and POLARadd. That shows how MLO helped to constrain the model parameters' uncertainty reductions in the presence of inconsistent integral data. The FY data created by GEF with these model parameters are also shown in Section 5.4.3.

Table 5.5 – Adjustments to the means and standard deviations of GEF model parameters using BFMC with and without MLO. 95%-confidence intervals are given for the posteriors that were estimated with bootstrap sampling.

GEF Parameter	Mean			Standard Deviation		
	Prior	With MLO	No MLO	Prior	With MLO	No MLO
P_DZ_Mean_S1	-0.179	-0.150 ± 0.023	-0.209 ± 0.009	0.100	0.086 ± 0.017	0.087 ± 0.008
P_DZ_Mean_S2	-0.461	-0.476 ± 0.026	-0.476 ± 0.009	0.100	0.076 ± 0.011	0.104 ± 0.006
P_DZ_Mean_S3	-0.372	-0.295 ± 0.031	-0.338 ± 0.011	0.099	0.084 ± 0.020	0.095 ± 0.007
P_DZ_Mean_S4	0.002	-0.001 ± 0.027	0.010 ± 0.010	0.100	0.088 ± 0.014	0.100 ± 0.008
P_Z_Curv_S1	0.370	0.368 ± 0.007	0.370 ± 0.002	0.018	0.018 ± 0.004	0.018 ± 0.001
P_Z_Curv_S2	0.185	0.189 ± 0.003	0.185 ± 0.001	0.009	0.009 ± 0.002	0.008 ± 0.001
P_A_Width_S2	12.491	12.183 ± 0.174	12.283 ± 0.068	0.628	0.506 ± 0.095	0.624 ± 0.042
P_Z_Curv_S3	0.156	0.153 ± 0.002	0.155 ± 0.001	0.008	0.007 ± 0.001	0.008 ± 0.001
P_Z_Curv_S4	0.035	0.035 ± 0.000	0.035 ± 0.000	0.002	0.002 ± 0.000	0.002 ± 0.000
P_Shell_S1	-2.849	-2.851 ± 0.025	-2.868 ± 0.008	0.099	0.085 ± 0.023	0.077 ± 0.007
P_Shell_S2	-4.401	-4.400 ± 0.031	-4.413 ± 0.008	0.100	0.091 ± 0.030	0.073 ± 0.010
P_Shell_S3	-6.400	-6.326 ± 0.045	-6.299 ± 0.015	0.199	0.132 ± 0.035	0.155 ± 0.010
P_Shell_S4	-0.900	-0.920 ± 0.030	-0.902 ± 0.005	0.050	0.059 ± 0.019	0.054 ± 0.004
T_low_S1	0.320	0.318 ± 0.002	0.319 ± 0.001	0.010	0.009 ± 0.001	0.010 ± 0.001
T_low_S2	0.310	0.311 ± 0.003	0.311 ± 0.001	0.010	0.010 ± 0.002	0.010 ± 0.001
T_low_S3	0.310	0.310 ± 0.003	0.310 ± 0.001	0.010	0.011 ± 0.002	0.010 ± 0.001
T_low_S4	0.310	0.308 ± 0.004	0.309 ± 0.001	0.010	0.011 ± 0.002	0.010 ± 0.001
T_low_SL	0.310	0.308 ± 0.003	0.310 ± 0.001	0.010	0.009 ± 0.001	0.010 ± 0.001
Delta_S0	-0.001	-0.018 ± 0.029	-0.004 ± 0.010	0.099	0.103 ± 0.018	0.104 ± 0.007
HOMPOL	1.001	0.994 ± 0.041	1.001 ± 0.011	0.101	0.096 ± 0.023	0.105 ± 0.009
POLARadd	0.253	0.269 ± 0.014	0.182 ± 0.009	0.101	0.049 ± 0.010	0.081 ± 0.006

Fig. 5.21 gives the posterior correlation matrices of the model parameters when MOCABA and BFMC were applied without using MLO. These matrices should be compared to those previously presented in Fig. 5.10. For MOCABA, there are not large differences between the posterior matrices when MLO was and was not applied. The most significant differences appeared as larger correlations between P_DZ_Mean parameters when MLO was not used. The BFMC model-parameter correlation matrices do show large differences. The large degrees of correlation and anti-correlation seen in Fig. 5.10 are not present in Fig. 5.21. Without using MLO, the BFMC correlation matrix is more similar to that created by MOCABA. The 95%-confidence intervals were also smaller when MLO was not applied. Still, BFMC's confidence intervals are larger, indicating a less highly converged result.

This difference between BFMC's posterior correlations with and without MLO requires examining the weight distributions of the two data sets. Fig. 5.22 gives the CDFs of the weight distributions for the two BFMC executions. Where previously only ~1% of the weights from BFMC with MLO were significantly greater than 0, when MLO was not applied ~10% of the weights were significantly greater than 0.

The different weight distributions are linked to how $\mathbf{M}_{extra}$ affected BFMC. Section 3.1.1 described how the size of χ^2 affects the weight distribution in BFMC. When χ^2 is large the weight

Table 5.6 – Adjustments to the means and standard deviations of GEF model parameters using MOCABA with and without MLO. 95%-confidence intervals are given for the posteriors that were estimated with bootstrap sampling.

GEF Parameter	Mean			Standard Deviation		
	Prior	With MLO	No MLO	Prior	With MLO	No MLO
P_DZ_Mean_S1	-0.179	-0.138 ± 0.011	-0.425 ± 0.046	0.100	0.082 ± 0.003	0.059 ± 0.002
P_DZ_Mean_S2	-0.461	-0.477 ± 0.007	0.024 ± 0.063	0.100	0.080 ± 0.002	0.068 ± 0.002
P_DZ_Mean_S3	-0.372	-0.315 ± 0.006	0.013 ± 0.059	0.099	0.084 ± 0.001	0.082 ± 0.001
P_DZ_Mean_S4	0.002	-0.002 ± 0.005	-0.017 ± 0.062	0.100	0.100 ± 0.000	0.100 ± 0.000
P_Z_Curv_S1	0.370	0.368 ± 0.001	0.380 ± 0.010	0.018	0.017 ± 0.000	0.015 ± 0.000
P_Z_Curv_S2	0.185	0.185 ± 0.001	0.146 ± 0.006	0.009	0.009 ± 0.000	0.008 ± 0.000
P_A_Width_S2	12.491	11.908 ± 0.025	9.586 ± 0.294	0.628	0.433 ± 0.011	0.406 ± 0.013
P_Z_Curv_S3	0.156	0.155 ± 0.000	0.189 ± 0.006	0.008	0.007 ± 0.000	0.006 ± 0.000
P_Z_Curv_S4	0.035	0.035 ± 0.000	0.035 ± 0.001	0.002	0.002 ± 0.000	0.002 ± 0.000
P_Shell_S1	-2.849	-2.850 ± 0.004	-2.836 ± 0.048	0.099	0.076 ± 0.001	0.075 ± 0.002
P_Shell_S2	-4.401	-4.410 ± 0.005	-4.447 ± 0.044	0.100	0.072 ± 0.002	0.069 ± 0.002
P_Shell_S3	-6.400	-6.286 ± 0.009	-6.828 ± 0.127	0.199	0.124 ± 0.005	0.115 ± 0.005
P_Shell_S4	-0.900	-0.901 ± 0.003	-0.899 ± 0.031	0.050	0.050 ± 0.000	0.050 ± 0.000
T_low_S1	0.320	0.319 ± 0.001	0.310 ± 0.006	0.010	0.010 ± 0.000	0.010 ± 0.000
T_low_S2	0.310	0.310 ± 0.001	0.312 ± 0.006	0.010	0.010 ± 0.000	0.010 ± 0.000
T_low_S3	0.310	0.312 ± 0.001	0.268 ± 0.006	0.010	0.010 ± 0.000	0.009 ± 0.000
T_low_S4	0.310	0.310 ± 0.001	0.308 ± 0.006	0.010	0.010 ± 0.000	0.010 ± 0.000
T_low_SL	0.310	0.311 ± 0.001	0.311 ± 0.006	0.010	0.010 ± 0.000	0.010 ± 0.000
Delta_S0	-0.001	0.000 ± 0.005	-0.002 ± 0.063	0.099	0.099 ± 0.000	0.099 ± 0.000
HOMPOL	1.001	1.011 ± 0.005	1.164 ± 0.060	0.101	0.100 ± 0.000	0.099 ± 0.000
POLARadd	0.253	0.284 ± 0.004	0.364 ± 0.029	0.101	0.054 ± 0.003	0.049 ± 0.003

distribution is flatter than when χ^2 is small. In other words, a large χ^2 means that there are more weights significantly above zero and that the posterior weighted average is more accurate (more converged). Inversely, when χ^2 is small, fewer weights are significantly above 0 and the weighted average is less accurate (less converged).

MLO added extra uncertainties that made all χ_i^2 smaller. With 10,000 random samples, the population mean of χ_i^2 per DoF calculated without MLO, or with Eq. (5.7), is 1.1E5. With MLO, or using Eq. (5.8), it is 4.8E3, showing that indeed MLO helps to lower the χ_i^2 values. First, we see why BMC did not work for this data set: both with and without MLO, the χ_i^2 values were much higher than the absolute weight degeneracy threshold, or $\chi^2 = 745$. Secondly, it shows that MLO lowered the χ_i^2, which then lead to a greater degree of weight degeneracy (as evidenced by the CDFs). Subsequently, less precise posterior weighted averages were obtained for the posterior model parameter correlation matrices. As discussed in Section 3.1.1, the posterior covariance matrices are more affected by weight degeneracy than the means.

$$\chi_i^2 = \left(\mathbf{E} - \mathbf{C}_i(\boldsymbol{\sigma}_i)\right)^T (\mathbf{M_E})^{-1} \left(\mathbf{E} - \mathbf{C}_i(\boldsymbol{\sigma}_i)\right) \tag{5.7}$$
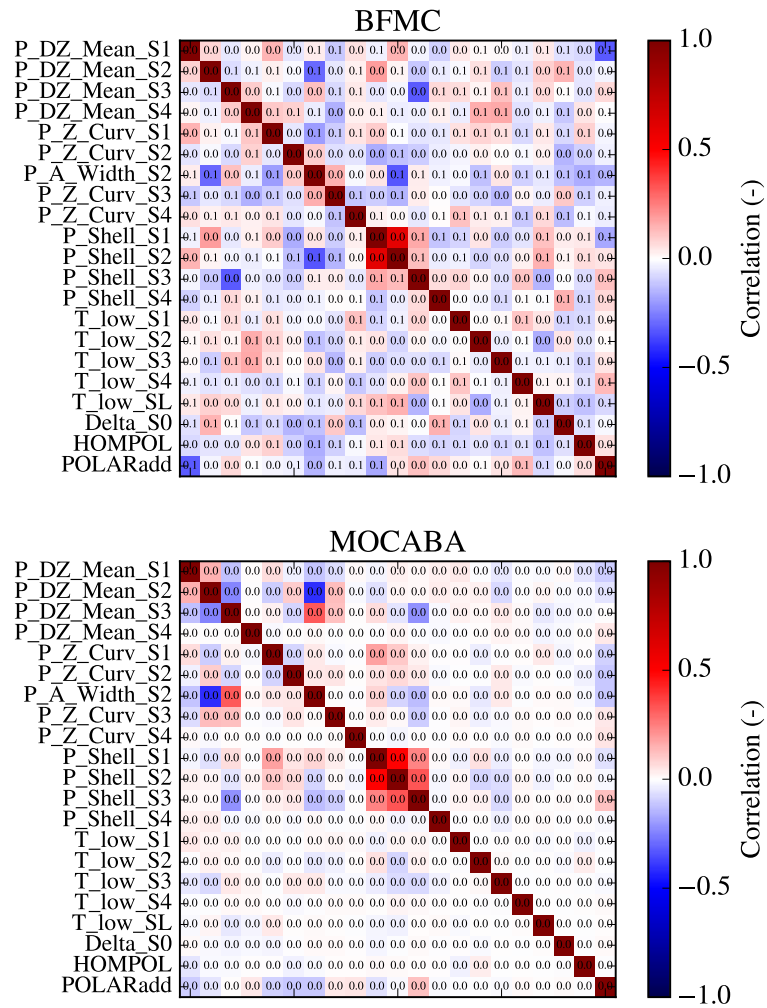
Figure 5.21 – Correlations between the model parameters when MLO is not used. Each correlation coefficient has its 95%-bootstrap-confidence interval over-laid on it.
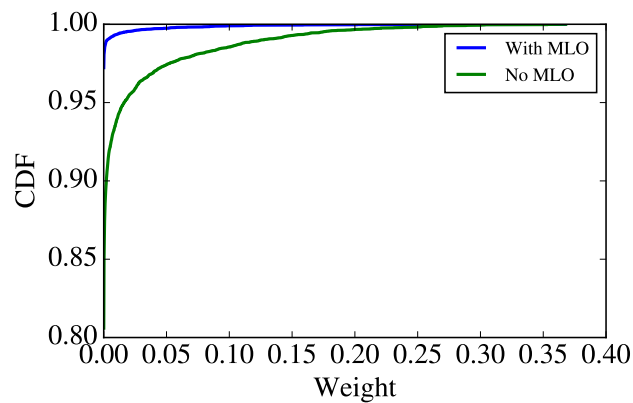
Figure 5.22 – CDFs of BFMC's weight distributions when MLO was and was not applied.

$$\chi_i^2 = \left(\mathbf{E} - \mathbf{C}_i(\boldsymbol{\sigma}_i)\right)^T (\mathbf{M_E} + \mathbf{M}_{\text{extra}})^{-1} \left(\mathbf{E} - \mathbf{C}_i(\boldsymbol{\sigma}_i)\right) \tag{5.8}$$

BFMC's weight definition, *i.e.* each χ_i^2 is normalized by $\chi_{\min}^2$, changed the weight distribution. The minimum χ^2 per DoF without MLO, or with Eq. (5.7), was 2.6E3. With MLO, or Eq. (5.8), it was 1.4E1. Without using MLO, $\chi_{\min}^2$ was bigger and, therefore, the normalization term was bigger. This shifted all the weights in the distributions to bigger values when $\chi_i^2/\chi_{\min}^2$ was then multiplied by -1 and put in an exponential. By consequence, more weights had higher values, leading to a more highly converged posterior weighted average.

Posterior FYs

Fig. 5.23 examines, in more detail, the differences between the FYs when MLO was and was not applied. It shows the relative differences between the mean values of the prior and posterior independent FYs of Pu-239. These plots for other isotopes are given in Appendix A.5. The MLO uncertainty that was added is shown in red on the figures. The size of the red dots is proportional to the skewness of the calculated FP concentration corresponding to that mass number. These skewness values were previously presented in Fig. 5.8.
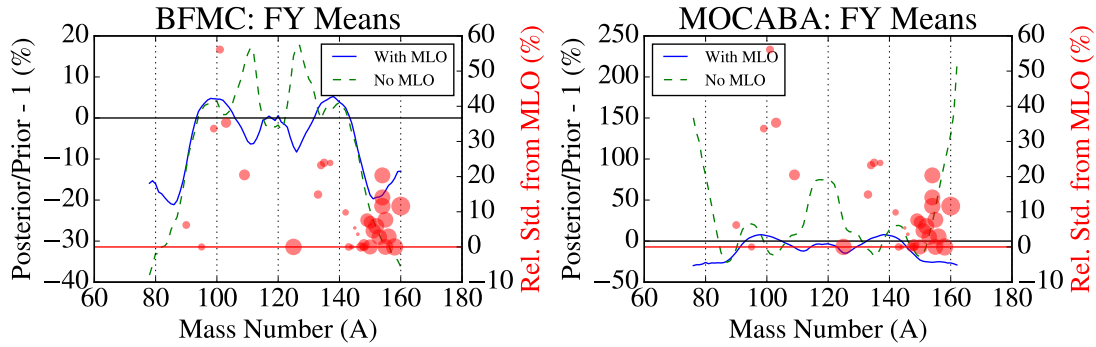
Figure 5.23 – Relative differences between the prior and posterior means FYs for (n_{th}, f) of Pu-239. Calculated with posteriors found when MLO was and was not used.

First consider the BFMC FYs, ignoring, for the moment, the possible effect that the skewness and not accounting for the integral data set's inconsistency had on the MOCABA posteriors. There are two regions where the posterior with and without MLO disagreed significantly: at 150 < A < 160 (and this region's opposite side of FY distribution at 80 < A < 90), and at 100 < A < 140. The majority of the experimental data was for A between 140 and 160, *i.e.* the isotopes of Gd, Eu, Sm, and Nd. When MLO was applied, many of these data had large increases in uncertainty, up to standard deviations of 20%. With increased uncertainty, they influenced less the adjustment. This is evidenced by the relative differences in Fig. 5.23 at 150 < A < 160 being smaller (in an absolute sense) when MLO was used.

These discrepancies are reflected in the model parameters. At these mass numbers, the S_1

and S_2 fission channels are most prominent in GEF. Table 5.5 presented statistically signifi-
cant differences for P_DZ_Mean_S1. BFMC, when done with MLO, adjusted the parameter's
mean from -0.179 Z to -0.150 ± 0.023 Z. When BFMC was applied with MLO, it adjusted
P_DZ_Mean_S1 to a larger extent to -0.209 ± 0.009 Z. P_A_Width_S2 also showed disagreeing
adjustments when MLO was and was not applied, which also influenced these posterior FYs.

Similarly, MLO gave integral data with A between 100 and 140 large uncertainty increases, up
to ~60% for Ru-101. These integral data then influenced the model-parameter adjustments
to a lesser degree. At these A, the S_1, S_3, and SL modes are important. Table 5.5 showed
disagreement between the adjusted model parameters for these fission modes, for instance
for P_DZ_Mean_S1, P_DZ_Mean_S3, P_DZ_Mean_S4, P_Shell_S1, P_Shell_S3, and P_Shell_S4.

Continuing to the MOCABA posterior FY data, there are much larger disagreements between
the posteriors when they were calculated with and without MLO extra uncertainties. The
disagreements are particularly large at As of 80–90, 110–130, and 150–160. In these regions, the
adjustments where MLO was not applied are much larger. As most of the FY data were affected,
this result should be able traceable to the model parameters of all the fission modes in GEF.
Table 5.6 showed that the posterior model parameters were quite different when MOCABA
was used with and without applying MLO. These differences are particularly prominent for
P_DZ_Mean_S1, P_DZ_Mean_S1, P_DZ_Mean_S1, P_A_Width_S2, POLARadd, and HOMPOL.

The same plots can be repeated for the relative difference between the standard deviations of
the prior and posterior GEF FYs, as shown in Fig. 5.24. Beginning with BFMC, the posterior
standard deviations tended to be smaller when MLO was applied. This agrees with our
understanding of how BFMC behaves: when χ^2 is larger, it gives posterior uncertainties closer
to the prior. When MLO was applied, it helped to lower χ^2 and allowed for larger reductions
in uncertainty to occur. BFMC showed previously an increase in uncertainty at 110 < A <
130 when MLO was used. This increase was hypothesized to be caused by increases in the
uncertainty of the P_Shell_S4 parameter and by large positive correlations between P_Shell_S3
and other parameters.

When MLO was applied, there was still a slight increase in the standard deviation of P_Shell_S4,
from a prior of 0.050 MeV to a posterior of 0.053 MeV. The increase was not as large as when
MLO was used, where the posterior standard deviation was 0.070 MeV. Additionally, the
posterior correlation matrices given in Figs. 5.10 and 5.21 showed that the correlations are
weaker when MLO was not used, likely due to better convergence, which may have helped
to lead to the decrease in uncertainty. Again, with the experimental data points over-laid on
the adjustments, we observe that the reduction in the uncertainties was largest in the densest
regions of experimental data.

Examine, next, the relative differences between the prior and MOCABA's posterior standard
deviations. Oppositely to BFMC, applying MOCABA with MLO helped to produce smaller
standard deviations, relative to the prior, than not applying it. At A > 150 and between 115
and 120, there was an increase in uncertainty. In general, these results demonstrate the effect
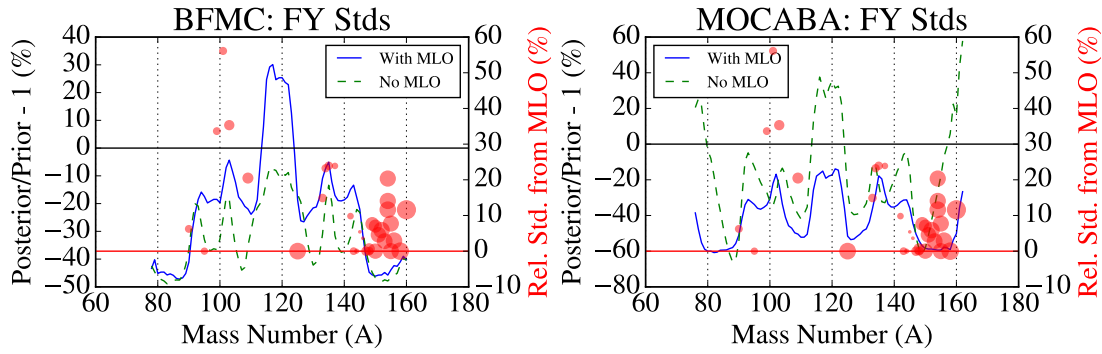
Figure 5.24 – Relative difference from prior to posterior of the standard deviations of FY for (n_{th}, f) of Pu-239. Calculated with posteriors found when MLO was and was not used.

that increasing and decreasing the importance of experimental data points, through adding uncertainties with MLO, can have on the posterior FYs.

Interestingly, these increases in uncertainty cannot be clearly linked to any changes in the standard deviations of the model parameters, which were given in Table 5.6. The only significant difference in the standard deviations, when comparing MOCABA with and without MLO, is that without MLO there were slightly larger correlations between the parameters. This may have helped to create the observed increases in uncertainties. Another possible explanation is that the changes in the means of the model parameters, combined with the non-linear nature of the GEF model, changed the interaction effects between the uncertain model parameters. Interactions, in sensitivity analysis literature [1], refer to effects on a model output caused by inputs that cannot be described as the sum of the single, independent effects of the model inputs. This hypothesis could be tested in a future study by applying global sensitivity analysis techniques to the GEF code.

MOCABA was affected to a larger extent than BFMC by the application of MLO. This is linked to two characteristics of the data set: the large degree of inconsistency and the skewness of the FP concentrations. In Chp. 3, we saw that MOCABA will adjust $\boldsymbol{\sigma}$ no matter the degree of consistency of the integral data. Large inconsistencies (*i.e.* large χ^2) cause large adjustments of $\boldsymbol{\sigma}$ to fit $\mathbf{C}$ and $\mathbf{E}$, even if the differences between the two are not caused by input uncertainty but by something else, like model inaccuracies. When MLO was not applied, the inconsistency may have caused large adjustments to the GEF parameters that were not based on physics, in effect over-fitting the model parameters to $\mathbf{E}$. Meanwhile BFMC, in contrast, has an auto-correction mechanism where large inconsistencies dampen the size of the adjustment. Because of this, MLO had less of an effect on BFMC.

At the same time, there was the effect of the skewness on MOCABA's normality assumption. Section 3.1.2 demonstrated that a log-normality, similar to the distribution of $\mathbf{C}$ and the FYs here, made MOCABA a biased estimate of the MAP distribution. Here when MLO was applied, it added uncertainties to many of data with large skewness, like Gd-160, and changed
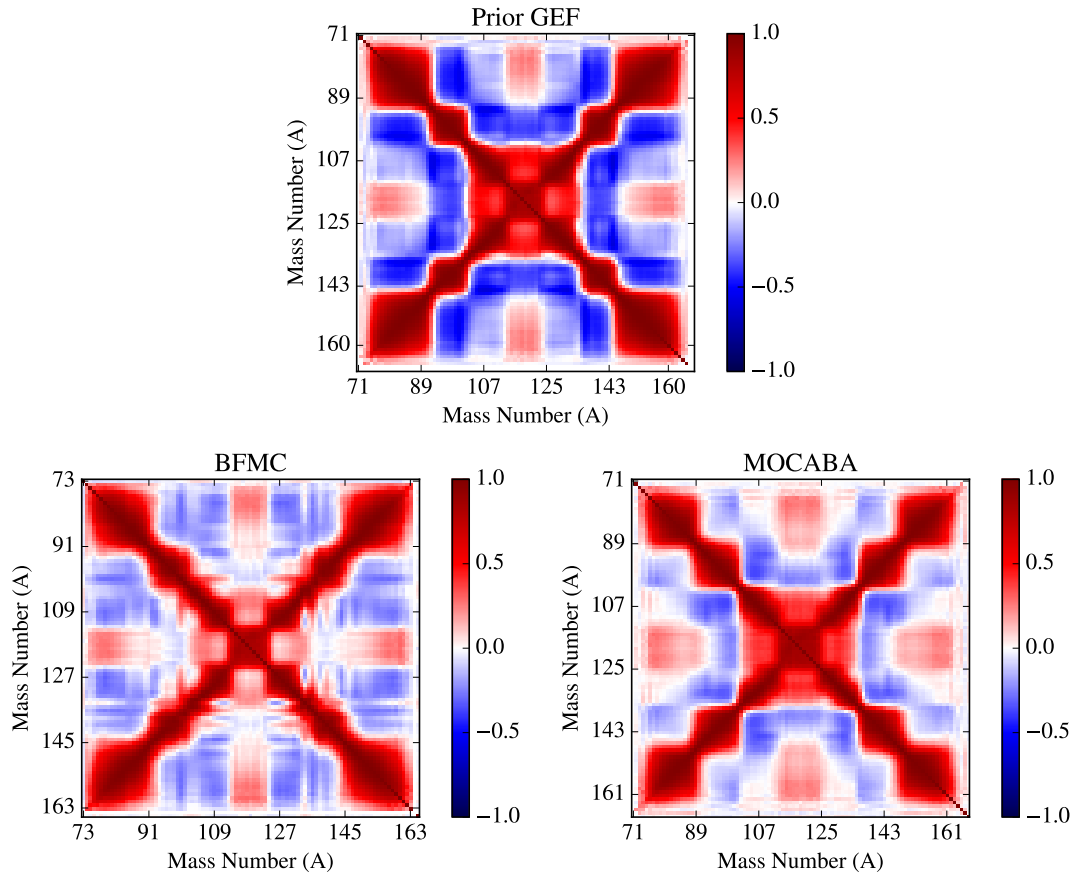
Figure 5.25 – Prior and posterior correlations for the independent FYs for (n_{th}, f) of Pu-239 without applying MLO.

the importance of these data to the adjustment. By decreasing the importance of these FP concentrations with large skewness, MLO may have limited the bias that MOCABA's normality assumption introduced. BFMC can account for the non-normality. The altered importance of the highly skewed data would not matter to BFMC.

With this data set, it is hard to separate the overlapping effects of the inconsistency and non-normality of the integral parameters. Both should affect MOCABA, but to an unknown degree. Future studies should be constructed that can separate the two effects. A highly inconsistent and Gaussian data set would allow determining if it was MLO that caused the observed behavior. Another data set that is non-Gaussian but consistent could be used to determine if it was the skewness that caused the observed behavior. This same data set would allow BMC to be applied, thereby removing any worry of BFMC biasing the posteriors.

Finally, Figs. 5.25 and 5.26 give the posterior correlation matrices of Pu-239 FYs and of the U-235/Pu-239 FYs. The matrices were calculated without MLO. Compared to those calculated with MLO in Figs. 5.14 and 5.15, some slight differences appear. Without MLO, the BFMC correlation matrix shows strong reductions in correlation and anti-correlation terms. MOCABA,
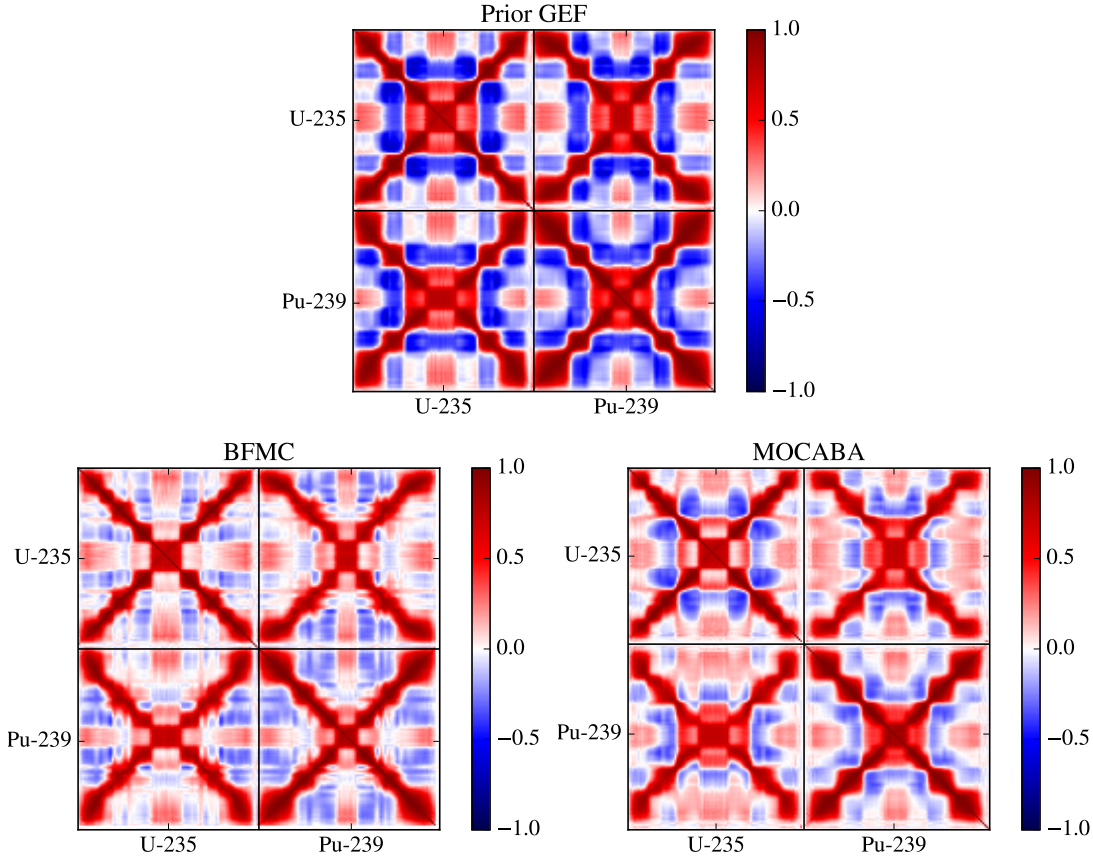
Figure 5.26 – Prior and posterior correlations between the independent FYs for (n_{th}, f) of U-235 and Pu-239 without applying MLO.

in contrast, shows slightly stronger correlations when MLO was not applied.

Posterior Nuclide Concentrations

The FYs from when MLO was not applied were also used in CASMO-5M simulations. Fig. 5.27 compares their posterior biases and uncertainties. Section 5.4.3 showed few significant differences between the BFMC posterior FYs when MLO was or was not applied. The only significant differences were around $A \approx 115$ and $A \approx 125$, and at $A > 150$, which are reflected in the posterior biases. Two isotopes are determined by FYs at $A \approx 115$ and $A \approx 125$: Sb-125 and Ag-109. When MLO was applied with BFMC, the biases improved from 23.5% to 7.3% for Sb-125, and from 35.7% to 29.7% for Ag-109. In contrast without applying MLO, the biases worsened to 34.2% and 49.7% for Sb-125 and Ag-109, respectively. Fig. 5.27 demonstrates that MLO also helped to create smaller biases for the Gd and Eu isotopes. This result is also shown in the posterior FYs, where at $A > 150$ they had more significant differences. Section 5.4.3 also showed that there were large differences between the posterior MOCABA FY data when MLO was and was not applied. These differences are reflected Fig. 5.27 as well. The posterior biases

of Sm, Nd, and Cs isotopes were particularly affected by these differences in the FY data.
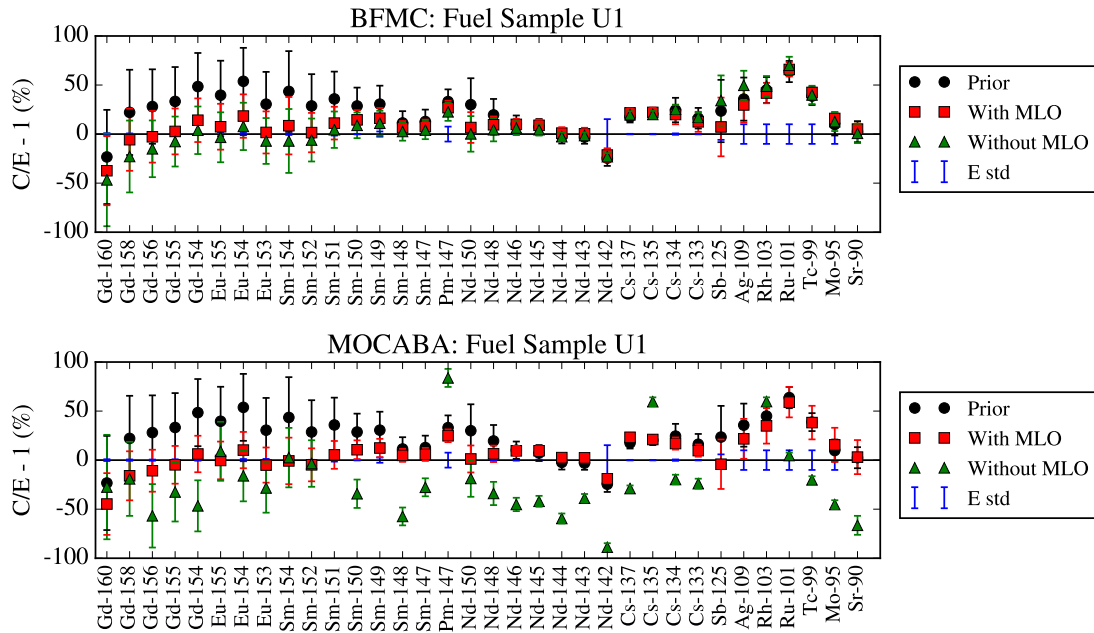
Figure 5.27 – Posterior biases and uncertainties of the FP concentrations obtained when MLO was and was not applied. Samples U2 and M1 are given in Appendix A.5.

In Table 5.7, the posterior biases and uncertainties are summarized for all FP concentrations, and for the fuel samples U1, U2, and M1. Again, the CASMO-5M models of U2 and M1 were re-run with the posterior FYs to test the performance and degree of over-fitting of the posteriors. The absolute bias of the FP concentrations, averaged across all 33 data, and the relative standard deviation of the calculated values, also averaged, are presented.

Beginning with the average absolute biases and fuel sample U1, we see that posterior biases of BFMC are only slightly affected by applying MLO. When MLO was applied, a 1.1% reduction in the bias occurred. This highlights an advantage of applying MLO with BFMC: it counteracts BFMC's push back towards the prior with inconsistent data sets, allowing for better improvement in the bias and a larger reduction in the uncertainty. The posterior biases from MOCABA, however, were extremely affected. Without applying MLO, the bias worsened from 26% for the prior to 56% for the posterior. MOCABA with MLO created a posterior bias of 14%. Fuel samples U2 and M2 also showed similar behavior: small differences between the BFMC average absolute biases, and much larger biases when MOCABA was used without MLO. M1 also had a posterior bias when MOCABA was used without MLO that was larger than the prior. In general, the results reflect what was observed for the FY data: MLO significantly affected the MOCABA adjustments, and noticeably but to a lesser extent the BFMC adjustments.

Concerning the average relative standard deviation of the posterior calculated values, for every fuel sample and for both BFMC and MOCABA, applying MLO produced smaller uncertainties. For BFMC, MLO helped to lower the χ^2 and allowed for larger adjustments occur, and thereby

reduce the uncertainties to a larger extent. The MOCABA average relative standard deviations in Table 5.7 show that MLO made the uncertainties smaller. This contradicts the expected behavior of MLO when used with MOCABA: the extra uncertainties, in theory, should have constrained the adjustment and limited the extent to which the uncertainties were reduced.

The difference from theory is related to the high degree of over-fitting of the model parameters, which severely effected the physics of GEF's model. The changes to the model parameters using MOCABA without MLO are very significant, especially to the means. P_DZ_Mean_S2, for example, changed from a prior of -0.461 to a posterior of 0.024, a 95% difference, which is much larger than the prior standard deviation of 22%. P_DZ_Mean_S3 also saw a 104% change in its mean compared to the prior standard deviation of 27%. These changes significantly altered the effect that the model parameters have on the FY means and standard deviations, as shown in Figs 5.23 and 5.24. Some FYs saw 100% increases in their means and even had their standard deviations increase relative to the prior. These larger standard deviations, especially for Sb-125, and the Gd, Sm, and Eu isotopes then propagated to the posterior FP concentrations. This then created the larger posterior uncertainties observed for MOCABA without MLO. In general, this result shows how over-fitting can create dangerous effects in posteriors, in some cases even increasing the uncertainty relativity to the prior.

Table 5.7 – Analysis of bias and uncertainty of posterior calculated nuclide concentrations.

		Avg. Abs. Bias (%)		Avg. Rel. Std. (%)	
		With MLO	No MLO	With MLO	No MLO
U1	Prior	26.4		20.6	
	BFMC	15.4	16.5	14.1	15.3
	MOCABA	13.7	55.9	13.5	15.4
U2	Prior	19.4		19.3	
	BFMC	8.72	8.60	13.4	13.5
	MOCABA	7.04	18.9	10.5	11.0
M1	Prior	23.2		21.0	
	BFMC	13.7	13.8	15.0	15.4
	MOCABA	11.9	28.1	11.6	12.5

5.5 Conclusions

This study presented a methodology to adjust the parameters of the GEF model with post-irradiation examination data. The goal was to improve the bias and uncertainty of the calculated concentration of fission products in spent fuel. The integral parameters were nuclide concentrations that were part of the LWR-Proteus Phase II experiment at PSI. The experiment was modeled with CASMO-5M. Two methods were applied to perform DA: MOCABA and BFMC. The application proved interesting because the FYs, and therefore the calculated nuclide concentrations, had non-normal distributions. MOCABA assumes that the data are normally distributed and BFMC does not. The integral data set also had a large degree of

inconsistency and proved to be interesting to test Marginal Likelihood Optimization (MLO).

After DA, the adjusted model parameters, FYs, and calculated nuclide concentrations were examined. The posterior model parameters, and subsequently FYs and calculations, showed good agreement between MOCABA and BFMC when MLO was employed, despite the non-normality of the calculated responses. The posterior GEF FYs showed stronger agreement with the FYs from ENDF/B-VIII.0 and JEFF3.3 than the prior. The posterior FYs also created lower biases and uncertainties in fission product concentrations. For the training data, the average absolute bias of prior was 26.4%. The posterior biases with MOCABA and BFMC were 13.7% and 15.4%, respectively. The uncertainty of the calculations dropped from 20.3% for the prior, to 13.5% and 14.1% with MOCABA and BFMC, respectively. When the posterior FYs were used with fuel samples that were not part of the training data, they also improved the biases and reduced uncertainties.

The BFMC posteriors exhibited slight differences when MLO was and was not applied. MO-CABA, in contrast, showed very significant differences when MLO was and was not used. The trends of the adjusted FYs were significantly changed, which had a deleterious effect on the posterior biases of the calculated FP concentrations. For the training data, the average absolute bias deteriorated from a prior of 26.4% to a posterior of 55.9%. This result is a combination of the increased degree of inconsistency of the integral data without using MLO, and from the increased importance of the skewness of the calculated values. These problems did not occur with BFMC because it accounts for the inconsistency with its weight normalization and because it can handle non-normality. Applying MLO did worsen the weight distribution, and therefore the statistical accuracy, of the BFMC posteriors. However, it also helped to create lower biases and lower uncertainties.

Important future work could focus on expanding the set of experimental data to be used in the adjustment. The strongest adjustments in the FYs were in areas with the highest density of experimental data. The Pu-239 and Pu-241 FYs were predominantly improved, through comparison with JEFF3.3 and ENDF/B-VIII.0, while U-235 was marginally adjusted. With a different experimental data set, the FYs of U-235 could be more precisely targeted. The SFCOMPO database [125, 126, 127] could be used to find more experimental data. Mapping the calculated FP concentrations onto normal distributions, as described in Section 2.2.2, and then using them in MOCABA could also be an interesting project. It may allow for MOCABA to account for the skewness induced by GEF.

5.6 Chapter's Key Points

- DA methods were applied for the first time to adjust fission yields with PIE data

- The adjustment was done by using PIE data from LWR-Proteus Phase II and with the GEF code

- GEF produces non-normal fission yields which then induce non-normal calculated

fission product concentrations

- PIE data have a large degree of inconsistency which was accounted for with MLO

- When BFMC and MOCABA were used in combination with MLO, good agreement was observed between their posterior GEF model parameters, fission yields, and calculated fission product concentrations

- The posterior fission yields saw improved agreement with the fission yields of ENDF/B-VIII.0 and JEFF3.3, relative to the prior

- The posterior covariance matrices saw a decreased degree of anti-correlation between competing fission channels in the GEF model

- The posterior calculated fission products had their biases and uncertainties reduced relative to the prior

- When MLO was not applied, important effects were seen for both MOCABA and BFMC

  - **MOCABA**: the agreement of the FYs with ENDF/B-VIII.0 and JEFF3.3 worsened, and the biases of the calculated fission product concentrations worsened. This is likely the combined effect of the integral data's inconsistency causing an overfit and the increased influence of the skewed calculated values on the adjustment
  - **BFMC**: no large differences were observed, but MLO helped to account for local inconsistencies of integral data, like for Sb-125

6 eXtended Generalized Linear Least Squares

The comparison between the DA methods presented in Chp. 3 extensively used sensitivity coefficients from the Monte-Carlo neutron transport code Serpent. Codes like Serpent are interesting for DA because they continuously treat the energy, space, and angle variables in neutron transport. Monte Carlo codes have their own methodology uncertainty coming from the stochasticity of the calculated responses and of the sensitivity coefficients. This chapter presents an extended version of the Generalized Linear Least Squares equations, called xGLLS, that accounts for the uncertainty of the sensitivities in the adjustment theory. xGLLS is studied with Serpent and a DA benchmark of the Nuclear Energy Agency.

6.1   Introduction

Recent advancements in Monte Carlo neutron transport codes allow calculating the sensitivity coefficients to nuclear data of integral parameters like k_{eff}, spectral indices, and reactivity coefficients [70, 128, 129]. These sensitivities are being used in data assimilation (DA) and have certain advantages: they continuously treat the energy, space, and angle variables in neutron transport and can explicitly model the geometry of a system. Such features are an asset for nuclear data adjustments because they make methodology and modeling biases, or differences between calculation and experiment caused by approximations in the neutron transport code or modeling, easier to account for. This then reduces inconsistencies between calculated and experimental integral parameters and thereby reduces the risk of over-fitting and having spurious nuclear data adjustments.

When DA is used with a deterministic code, inconsistencies can exist because the code discretizes the energy, space, and angular variables. Furthermore, the code often requires modeling approximations such as reflective boundary conditions or limiting to a 2D representation of the system. These biases can be accounted for as uncertainties in the DA equations [28]. Unfortunately, how to statistically represent the bias coming from the deterministic nature of the code is difficult, especially given that the errors may be correlated. Their modeling and methodology uncertainty is often estimated with parametric analysis and expert judgment or

with a data-driven approach like Marginal Likelihood Optimization. If Monte Carlo neutron transport codes are used, the modeling bias can be very limited and the methodology bias is primarily statistical uncertainty. Ideally, inconsistencies are limited from the outset and the need for expert judgment or Marginal Likelihood optimization is reduced.

Despite their advantages, using Monte Carlo estimates in DA come with challenges associated with the statistical uncertainties and the computational cost of the simulations. There can be thousands of sensitivity coefficients for each integral parameter and dozens of integral parameters in an adjustment. Individual examination of the uncertainty of each sensitivity coefficient becomes a difficult and nearly intractable task. These challenges lead to several questions: what effect does the statistical nature of the sensitivities have on the posteriors? Can the sensitivity uncertainties be theoretically accounted for in DA theory? Do sensitivity uncertainties have significant effects on the adjustments? How many particles should be simulated to have accurate posteriors?

The current chapter addresses these questions. To theoretically account for the sensitivity uncertainties, we propose and test an extension of the traditional DA method called Generalized Linear Least Squares (GLLS). The modified GLLS method is called eXtended Generalized Linear Least Squares (xGLLS). The study is done with Serpent version 2.1.29 [69] and a benchmark DA problem proposed by Subgroup 33 of the OECD/NEA's Working Party on International Nuclear Data Evaluation Co-operation (WPEC) [9]. The adjustments from GLLS and xGLLS of this benchmark are compared to assess the effect of sensitivity uncertainties. The convergence of the posteriors as more neutrons are used in the Serpent simulation is also investigated.

To find a balance between the cost and statistics of sensitivity calculations, a convergence criterion (building off work first presented in Ref. [71]) is proposed so that once a simulation's sensitivities are acceptable, the simulation can be stopped and computer time can be saved. Previously, simulations were run until some arbitrary criterion specified by the user was met, often leading to gross overuse of computational resources. Such a criterion must be simple and integral because there can be hundreds to thousands of sensitivity coefficients in a DA problem, making an individual inspection of the coefficients unreasonable.

6.2 Theory

With Monte Carlo codes, the nuclear data $\boldsymbol{\sigma}$ are no longer the only random variable, the sensitivity coefficients, $\mathbf{S}$, are as well. The linear approximation of $\mathbf{C}$, or Eq. (6.1), used in GLLS then has an uncertainty caused by $\boldsymbol{\sigma}$ and by $\mathbf{S}$. Additionally, where usually there are only correlations between $\boldsymbol{\sigma}$, there can also be correlations between $\mathbf{S}$ terms and between $\mathbf{S}$ and $\boldsymbol{\sigma}$.

$$
\begin{aligned}
\mathbf{C}(\boldsymbol{\sigma}) &= \mathbf{C}(\boldsymbol{\sigma}_0) + \left.\frac{\partial \mathbf{C}}{\partial \boldsymbol{\sigma}}\right|_{\boldsymbol{\sigma}=\boldsymbol{\sigma}_0} (\boldsymbol{\sigma} - \boldsymbol{\sigma}_0) + \cdots \\
&\approx \mathbf{C}(\boldsymbol{\sigma}_0) + \mathbf{S}(\boldsymbol{\sigma} - \boldsymbol{\sigma}_0)
\end{aligned}
\tag{6.1}
$$

In this situation, the variance of a single, scalar C value is given as Eq. (6.2). The equation is derived with a first-order propagation of moments on Eq. (6.1), considering that both $\boldsymbol{\sigma}$ and **S** are random variables. This requires taking the derivative of Eq. (6.1) with respect to **S**, or $\partial\mathbf{C}/\partial\mathbf{S}$, which is seen to be $\Delta\boldsymbol{\sigma}$.

$$\text{var}(C) = \sum_i^{N_\sigma} S_i^2 \text{var}(\sigma_i) + \sum_i^{N_\sigma} \Delta\sigma_i^2 \text{var}(S_i) + 2\sum_{i\neq j}^{N_\sigma} S_i \text{cov}(\sigma_i, \sigma_j) S_j +$$
$$2\sum_{i\neq j}^{N_\sigma} \Delta\sigma_i \text{cov}(S_i, S_j)\Delta\sigma_j + 2\sum_{i\neq j}^{N_\sigma} S_i \text{cov}(S_i, \sigma_j)\Delta\sigma_j \tag{6.2}$$

For multiple integral parameters, Eq. (6.2) can be written with linear algebra. The traditional vectors and matrices are extended from $\mathbf{M}_\sigma$ and **S** to $\widetilde{\mathbf{M}}_\sigma$ and $\widetilde{\mathbf{S}}$. $\widetilde{\mathbf{M}}_\sigma$ is the covariance matrix of all random variables and contains the variance and covariances between all $\boldsymbol{\sigma}$ and **S** values. It is formed by combining the standard $\mathbf{M}_\sigma$, the covariance matrix of the sensitivity coefficients $\mathbf{M_S}$ (whose size is $N_E * N_\sigma \times N_E * N_\sigma$), and the covariance matrix of $\boldsymbol{\sigma}$ and **S**, or $\mathbf{M}_{\sigma,\mathbf{S}}$, whose size is $N_\sigma \times N_E * N_\sigma$. The total size of $\widetilde{\mathbf{M}}_\sigma$ is then $(N_\sigma + N_E * N_\sigma) \times (N_\sigma + N_E * N_\sigma)$.

$$\widetilde{\mathbf{M}}_\sigma = \begin{bmatrix} \mathbf{M}_\sigma & \mathbf{M}_{\sigma,\mathbf{S}} \\ \mathbf{M}_{\sigma,\mathbf{S}}{}^T & \mathbf{M_S} \end{bmatrix} \tag{6.3}$$

$\widetilde{\mathbf{S}}$ is the extended matrix of first-order derivatives in Eq. (6.1) and contains the standard **S**, *i.e.* the derivative of **C** with respect to $\boldsymbol{\sigma}$, and the derivatives of **C** with respect to **S**, or $\Delta\boldsymbol{\sigma}$. The $\widetilde{\mathbf{S}}$ matrix can then be constructed as shown in Eq. (6.4) where $\widetilde{\mathbf{S}}$ has the dimensions $N_E \times (N_\sigma + N_E * N_\sigma)$. The matrix $\Delta\boldsymbol{\Sigma}$ contains $\Delta\boldsymbol{\sigma}$ repeated N_E times to create a matrix of size $N_E \times N_E * N_\sigma$. The **0** terms are zero vectors of size $1 \times N_\sigma$.

$$\widetilde{\mathbf{S}} = \begin{bmatrix} \mathbf{S} & \Delta\boldsymbol{\Sigma} \end{bmatrix}, \quad \Delta\boldsymbol{\Sigma} = \begin{bmatrix} \Delta\boldsymbol{\sigma}^T & \mathbf{0} & \dots & \mathbf{0} \\ \mathbf{0} & \Delta\boldsymbol{\sigma}^T & \mathbf{0} & \vdots \\ \mathbf{0} & \mathbf{0} & \ddots & \mathbf{0} \\ \mathbf{0} & \dots & \mathbf{0} & \Delta\boldsymbol{\sigma}^T \end{bmatrix} \tag{6.4}$$

Eq. (6.2) can be written in vector/matrix form as shown in Eq. (6.5). A major issue with this formulation is that one term, $\Delta\boldsymbol{\sigma}$, is not known *a priori*. A value can be assumed, but this formulation works best coincidentally with DA, which by its nature provides a $\Delta\boldsymbol{\sigma}$.

$$\mathbf{M_C} = \widetilde{\mathbf{S}}\widetilde{\mathbf{M}}_\sigma\widetilde{\mathbf{S}}^T \tag{6.5}$$

Chapter 6. eXtended Generalized Linear Least Squares

To complete the GLLS equations that account for **S** uncertainty, an additional extended vector must be defined. This vector, $\Delta\widetilde{\sigma}$, contains $\Delta\sigma$ and adjustments to the **S** of each integral parameter i, or $\Delta\mathbf{S}_i$. Its size is $(N_\sigma + N_E * N_\sigma) \times 1$.

$$\Delta\widetilde{\sigma} = \begin{bmatrix} \Delta\sigma \\ \Delta\mathbf{S}_1 \\ \vdots \\ \Delta\mathbf{S}_{N_E} \end{bmatrix} \tag{6.6}$$

The extended GLLS equations (xGLLS) for the nuclear data adjustments can be written as Eqs. (6.7) and (6.8). $\widetilde{\mathbf{M}}'_\sigma$ contains $\mathbf{M}'_\sigma$, the posterior sensitivity covariance matrix $\mathbf{M}'_\mathbf{S}$, and covariances between σ and **S**. $\Delta\widetilde{\sigma}$ contains $\Delta\sigma$ and adjusted sensitivities, $\mathbf{S}'$, where $\mathbf{S}' = \Delta\mathbf{S} + \mathbf{S}$.

$$\Delta\widetilde{\sigma} = \widetilde{\mathbf{M}}_\sigma \widetilde{\mathbf{S}}^T \left[\widetilde{\mathbf{S}}\widetilde{\mathbf{M}}_\sigma \widetilde{\mathbf{S}}^T + \mathbf{M_E} + \mathbf{M_M} \right]^{-1} \left[\mathbf{E} - \mathbf{C}(\sigma_0) \right] \tag{6.7}$$

$$\widetilde{\mathbf{M}}'_\sigma = \widetilde{\mathbf{M}}_\sigma - \widetilde{\mathbf{M}}_\sigma \widetilde{\mathbf{S}}^T \left[\widetilde{\mathbf{S}}\widetilde{\mathbf{M}}_\sigma \widetilde{\mathbf{S}}^T + \mathbf{M_E} + \mathbf{M_M} \right]^{-1} \widetilde{\mathbf{S}}\widetilde{\mathbf{M}}_\sigma \tag{6.8}$$

The posterior calculated values and their covariance matrix can be calculated with Eqs. (6.9) and (6.10). Importantly, $\mathbf{M}'_\mathbf{C}$ contains uncertainty of $\mathbf{C}'$ from $\mathbf{M}'_\sigma$, $\mathbf{M}'_\mathbf{S}$, and $\mathbf{M}'_{\sigma,\mathbf{S}}$.

$$\mathbf{C}' = \mathbf{C}(\sigma_0) + \mathbf{S}'\Delta\sigma \tag{6.9}$$

$$\mathbf{M}'_\mathbf{C} = \widetilde{\mathbf{S}}\widetilde{\mathbf{M}}'_\sigma \widetilde{\mathbf{S}}^T \tag{6.10}$$

xGLLS induces correlations between **E** and σ', and between **E** and $\mathbf{S}'$. In Chp. 2 GLLS was shown to induce correlations between **E** and σ' with Eq. (2.14). Now, these correlations can be represented in extended form with Eq. (6.11). The matrices $\widetilde{\mathbf{M}}_{\sigma,\mathbf{S},\mathbf{E}}$ and $\widetilde{\mathbf{M}}'_{\sigma,\mathbf{S},\mathbf{E}}$ are the prior and posterior covariance matrices that give the covariances between **E** and σ, and between **E** and **S**. Their size is $(N_\sigma + N_E * N_\sigma) \times N_E$. Again, in this study we assume that the prior has no correlations between **E** and σ, or between **E** and **S**, thus making $\widetilde{\mathbf{M}}_{\sigma,\mathbf{S},\mathbf{E}} = \mathbf{0}$.

$$\widetilde{\mathbf{M}}'_{\sigma,\mathbf{S},\mathbf{E}} = \widetilde{\mathbf{M}}_{\sigma,\mathbf{S},\mathbf{E}} - \left(\widetilde{\mathbf{M}}_{\sigma,\mathbf{S},\mathbf{E}} - \widetilde{\mathbf{M}}_\sigma \widetilde{\mathbf{S}}^T \right) \left[\widetilde{\mathbf{S}}\widetilde{\mathbf{M}}_\sigma \widetilde{\mathbf{S}}^T + \mathbf{M_E} + \mathbf{M_M} \right]^{-1} \left(\mathbf{M_E} - \widetilde{\mathbf{S}}\widetilde{\mathbf{M}}_{\sigma,\mathbf{E}} \right) \tag{6.11}$$

This study assumes that the terms in **S** are neither correlated with themselves nor with those in σ. $\mathbf{M_S}$ becomes a diagonal matrix that contains only the **S** variances and $\mathbf{M}_{\sigma,\mathbf{S}}$ becomes

a zero matrix. The extended matrix $\widetilde{\mathbf{M}}_\sigma$ is then Eq. (6.12). At this point in time, the author has not extensively investigated the correlations between these parameters and are unaware of any studies available in the literature. Theoretically, there is some degree of correlation because 1) the scores used to calculate **S** can come from the same neutron histories and 2) **S** is proportional to $\boldsymbol{\sigma}$, especially for the direct effect terms of spectral indices. Although the correlations are outside the scope of study, they could be an important area of future research.

$$\widetilde{\mathbf{M}}_\sigma = \begin{bmatrix} \mathbf{M}_\sigma & \mathbf{0} \\ \mathbf{0} & \mathbf{M_S} \end{bmatrix} \tag{6.12}$$

By assuming that **S** is uncorrelated and that **S** and $\boldsymbol{\sigma}$ are uncorrelated, the xGLLS equations can be split up as shown in Eqs. (6.13) to (6.16). Eqs. (6.13) and (6.14) are used to adjust $\boldsymbol{\sigma}$. They are very similar to Eqs. (2.17) and (2.18) except for the addition of the additional uncertainty term in **C**, $\Delta\boldsymbol{\Sigma}\mathbf{M_S}\Delta\boldsymbol{\Sigma}$, that comes from **S** uncertainties. Eqs. (6.15) and (6.16) show that the **S** themselves can also be updated with DA. Posterior sensitivities, $\mathbf{S}'$ can be calculated with Eq. (6.15) and their posterior covariances with Eq. (6.16).

$$\Delta\boldsymbol{\sigma} = \mathbf{M}_\sigma\mathbf{S}^T\left[\mathbf{SM}_\sigma\mathbf{S}^T + \Delta\boldsymbol{\Sigma}\mathbf{M_S}\Delta\boldsymbol{\Sigma} + \mathbf{M_E} + \mathbf{M_M}\right]^{-1}\left[\mathbf{E} - \mathbf{C}(\boldsymbol{\sigma}_0)\right] \tag{6.13}$$

$$\mathbf{M}'_\sigma = \mathbf{M}_\sigma - \mathbf{M}_\sigma\mathbf{S}^T\left[\mathbf{SM}_\sigma\mathbf{S}^T + \Delta\boldsymbol{\Sigma}\mathbf{M_S}\Delta\boldsymbol{\Sigma} + \mathbf{M_E} + \mathbf{M_M}\right]^{-1}\mathbf{SM}_\sigma \tag{6.14}$$

$$\mathbf{S}' = \mathbf{S} + \mathbf{M_S}\Delta\boldsymbol{\Sigma}\left[\mathbf{SM}_\sigma\mathbf{S}^T + \Delta\boldsymbol{\Sigma}\mathbf{M_S}\Delta\boldsymbol{\Sigma} + \mathbf{M_E} + \mathbf{M_M}\right]^{-1}\left[\mathbf{E} - \mathbf{C}(\boldsymbol{\sigma}_0)\right] \tag{6.15}$$

$$\mathbf{M}'_\mathbf{S} = \mathbf{M_S} - \mathbf{M_S}\Delta\boldsymbol{\Sigma}\left[\mathbf{SM}_\sigma\mathbf{S}^T + \Delta\boldsymbol{\Sigma}\mathbf{M_S}\Delta\boldsymbol{\Sigma} + \mathbf{M_E} + \mathbf{M_M}\right]^{-1}\Delta\boldsymbol{\Sigma}\mathbf{M_S} \tag{6.16}$$

With this formulation, $\Delta\boldsymbol{\sigma}$ is both a solution and an unknown. To solve the equations, the adjustment process needs to be run iteratively with $\Delta\widetilde{\boldsymbol{\sigma}}$ and $\widetilde{\mathbf{S}}$ updated until convergence. To start the iterations, the Ansatz is that $\Delta\boldsymbol{\sigma}$ is the standard GLLS solution, or Eq. (2.17). This $\Delta\boldsymbol{\sigma}$ is used in the first iteration of xGLLS and is then taken from Eq. (6.7) for the ensuing iterations. Similarly, the $\Delta\mathbf{S}$ terms in $\Delta\widetilde{\boldsymbol{\sigma}}$ are not known before the first iteration. For a first guess, we set $\Delta\mathbf{S} = 0$. Then after the first iteration, $\Delta\mathbf{S}$ becomes the true $\Delta\mathbf{S}$ taken from $\Delta\widetilde{\boldsymbol{\sigma}}$. The iterative loop continues until the difference in $\Delta\boldsymbol{\sigma}$ from one iteration to the next is below a numerical threshold. In this work, the threshold is set to 1×10^{-5} which is the numerical precision of the prior $\boldsymbol{\sigma}$. Well-posed problems typically converge within three iterations. We observed that with larger sensitivity uncertainties more iterations are needed for convergence.

6.3 The Benchmark Exercise

The Subgroup 33 benchmark of the NEA's WPEC [9] was used to test and characterize xGLLS. The benchmark has integral experiments that cover a wide range of fast-neutron energy spectra. Their integral responses include k_{eff}, spectral indices, and Na-void reactivity coefficients. In this document, spectral indices are referred to as Fij or Cij which represent the fission or capture rate of isotope 23j of element 9i (*i.e.* i = 2,3,4 for U, Np, and Pu, respectively). F37, for example, is the Np-237 fission rate. The experiments and 20 integral parameters are given in Table A.1 in Appendix A.6.

The nuclear data of ten isotopes were considered: B-10, O-16, Na-23, Fe-56, Cr-52, Ni-58, U-235, U-238, Pu-239, Pu-240, and Pu-241. The following nuclear data were explicitly adjusted: elastic scattering cross section, total inelastic scattering cross section, capture cross section, fission cross section, average prompt fission neutron multiplicity ($\bar{\nu}$), and the normalized prompt fission neutron spectrum. The benchmarks used a 33-energy-group structure (see Table A.2) and the COMMARA-2.0 covariance data [130]. This study used the older ENDF/B-VII.0 for the nuclear data [131] in Serpent to have consistency with the benchmark.

The benchmark used a correction factor approach to create simplified models of the critical systems. For the Serpent reproduction of the benchmark, the simple models for ZPPR-9, JOYO, and ZPR6-7 were kept so that the sensitivities were consistent with the benchmark. For JEZEBEL and FLATTOP, their full system geometries were modeled. This means that the correction factors were not applied to JEZEBEL and FLATTOP for the Serpent simulations. While using the simplified models did not take full advantage of the explicit modeling capabilities of Serpent, they were necessary to ensure consistency with the benchmark. The modeling/methodology covariance matrix should be different with Serpent, as it comes from the statistical uncertainties of the **C** values. However for consistency, the benchmark's modeling/methodology covariance matrix was retained.

6.3.1 Sensitivity Analysis Results

The sensitivities from Serpent are compared to those of Idaho National Laboratory (INL) from the benchmark. The comparison verifies the models developed in Serpent for the benchmark. INL did neutron transport and sensitivity analysis with the ERANOS code [132]. For k_{eff} sensitivity analysis, INL used Standard Perturbation-Theory (SPT) techniques with transport-theory. Generalized Perturbation Theory (GPT) [133] was used for the sensitivity analysis of the spectral indices. Equivalent Generalized Perturbation Theory (EGPT) [90] was employed for the sensitivity analysis of the Na-density reactivity coefficients. Serpent uses GPT for the sensitivity analysis of k_{eff} and spectral indices. Serpent can calculate Na-void reactivity sensitivities with GPT. Unfortunately, this option cannot be used because the ZPPR-9 benchmark model has a homogenized core. The homogenization links perturbations to the Na density to perturbations in the other material densities, leading to inaccurate sensitivities. Because of this, EGPT was used for the Na-void sensitivities with Serpent.
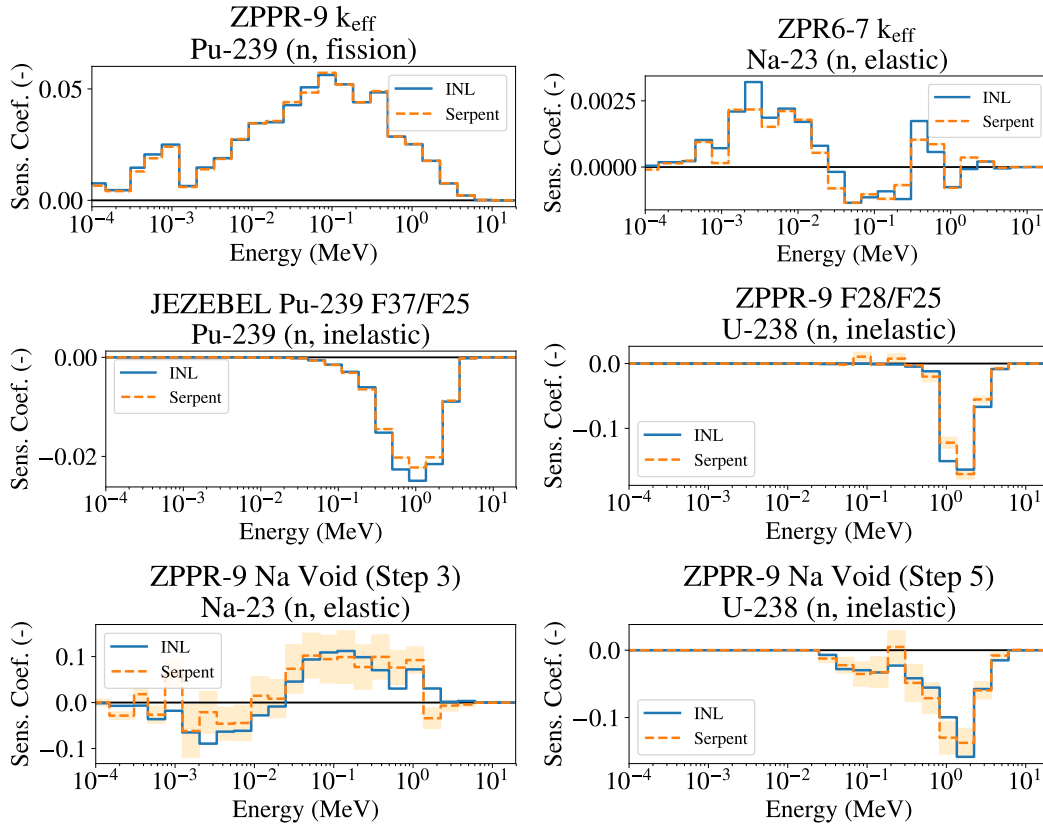
Figure 6.1 – Sensitivity profiles from INL (using ERANOS) and Serpent.

The Serpent simulations were done with 20 billion neutron histories and 15 latent generations. Sensitivities for several integral parameters are shown in Fig. 6.1. Good agreement is observed between Serpent and INL. However at certain energy ranges, the uncertainties in the Serpent sensitivities are large, especially for the Na-void reactivity coefficients. The ZPPR-9 Na-void Step 3 and Step 5 sensitivity profiles confirm conclusions drawn in the original benchmark exercise: Monte Carlo codes have difficulties in getting low sensitivity uncertainties for small reactivity variations with EGPT. This is linked to the fact that even though the Monte Carlo k_{eff} statistical uncertainty can be less than 5 pcm, the Δk_{eff} itself is inherently small at around 100 pcm. Consequently, the uncertainties are unavoidably important and need significant computational resources to be reduced.

For the prompt fission neutron spectrum, which is not shown here, Serpent2.1.29 gives constrained sensitivity coefficients while the benchmark participants return unconstrained sensitivities. Ref. [134] showed that using unconstrained or constrained sensitivities does not cause a difference in results when the sensitivities are folded with covariance matrices if a condition is met. Specifically, the covariance matrix must meet the zero-sum constraint, *i.e.* the sum of rows/columns of the absolute covariance matrix must be zero. For the COMMARA2.0 data used in this study, the constraint is met and, therefore, the differences in the sensitivities for the prompt neutron fission spectrum were not considered to be a possible source of error.

6.4 Adjustment Results

The xGLLS equations demonstrate how the statistically uncertain sensitivities can be incorporated into GLLS. The remainder of this text demonstrates how they perform relative to GLLS in different scenarios. First, we present a test of xGLLS where the sensitivity uncertainties are set to an artificially and unrealistically large size. This allows to test the xGLLS implementation and characterize how it is different from GLLS. Next in Section 6.4.2, xGLLS is studied using the real, nominal case where the sensitivity uncertainties have their true values after 20 billion neutron histories. Finally in Section 6.4.3, the adjustments are shown at different stages in the Serpent simulations from when the number of neutron histories is very low, and when the sensitivity uncertainties are large, to the end point of 20 billion neutron histories.

6.4.1 Large Sensitivity Uncertainty

First, we compare xGLLS and GLLS with the sensitivity uncertainties artificially increased to exaggerate their effect. The posteriors highlight xGLLS and how its adjustments are different from GLLS. The sensitivity uncertainties were set to 300% when xGLLS was used, while GLLS was ignorant of the sensitivity uncertainties.

Fig. 6.2 shows the adjustments of several nuclear data for this case. Consider first the relative adjustments ($\Delta\boldsymbol{\sigma}/\boldsymbol{\sigma}_0$) where significant differences appear between GLLS and xGLLS. Depending on the reaction, $\Delta\boldsymbol{\sigma}/\boldsymbol{\sigma}_0$ differed by several percents, especially for Pu-239 inelastic scattering. Importantly, however, the general trends of the adjustments did not change, just the magnitude. Concerning the posterior uncertainties, for certain reactions like Pu-239 elastic and inelastic, the posterior uncertainty from xGLLS was larger than that from GLLS. This indicates that xGLLS constrained the nuclear data's uncertainty reduction in the presence of large sensitivity uncertainties.

Fig. 6.3 gives the posterior biases ($\mathbf{C}'/\mathbf{E}$ - 1) and posterior uncertainties of $\mathbf{C}'$. The figure shows that the differences in $\boldsymbol{\sigma}'$ between GLLS and xGLLS were significant enough to cause disagreements between the biases. The posterior uncertainties from xGLLS were larger than those from GLLS. This demonstrates the effect of the constrained uncertainty reduction in $\mathbf{M}'_\sigma$ in the presence of large sensitivity uncertainty when using xGLLS.

The prior and posterior $\widetilde{\mathbf{M}}_\sigma$ correlation matrices are shown in Fig. 6.4. The plot is limited to only Pu-239 nuclear data and to the $\mathbf{S}$ of two integral parameters (k_{eff} and F28/F25 of JEZEBEL Pu-239). This is done to limit the size of the matrix, otherwise it would be so large that no discernible features would appear. In order to plot the small correlations in the posterior, a log axis is used. This choice does not allow negative correlations to be plotted, but they do exist. In the posterior, new correlations appeared between $\mathbf{S}'$ and between $\mathbf{S}'$ and $\boldsymbol{\sigma}'$. Certain correlations can be on the same order of magnitude as those in $\mathbf{M}_\sigma$.

Fig. 6.5 plots the prior and posterior sensitivity profiles of several integral parameters to
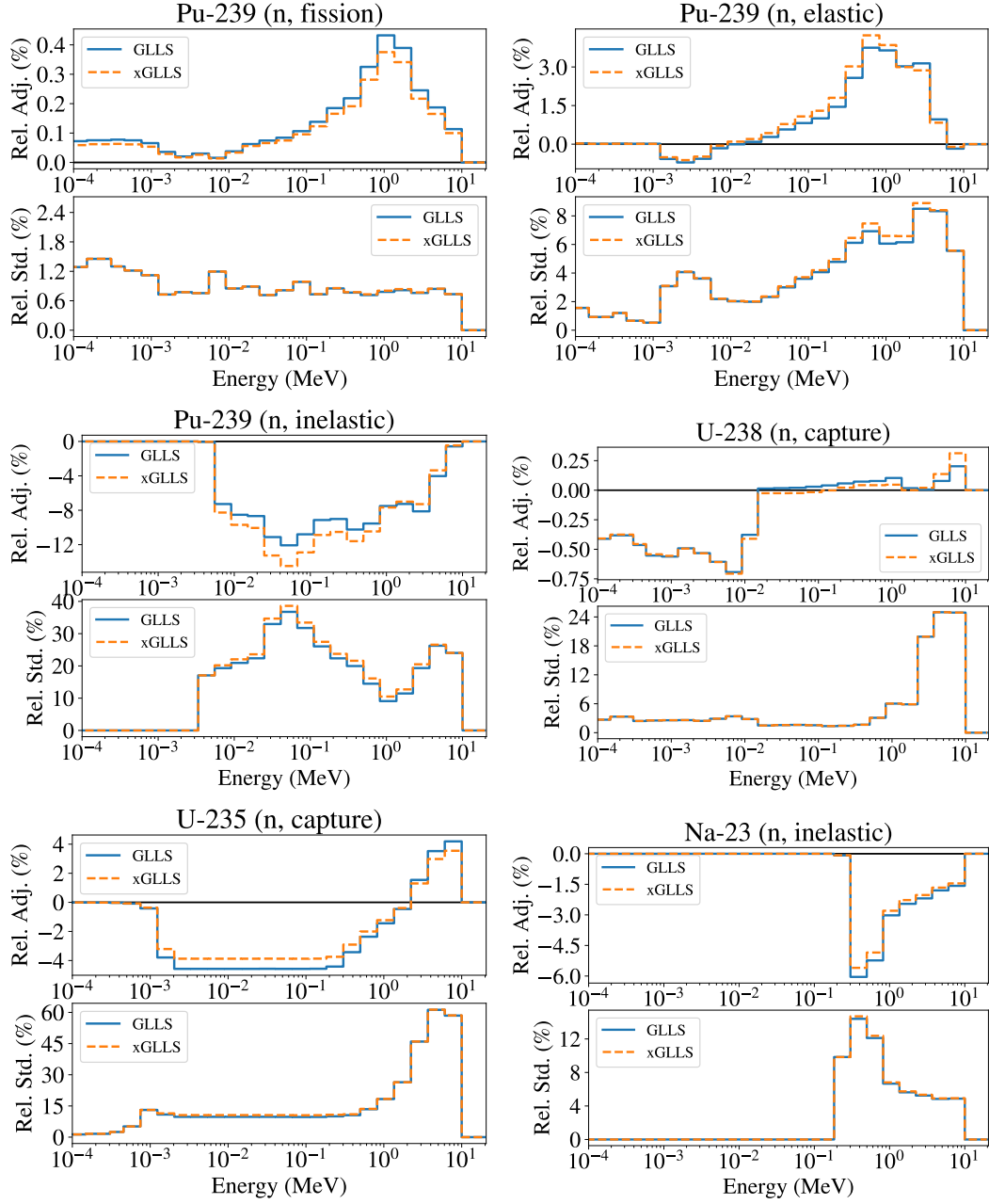
Figure 6.2 – Nuclear data adjustments using xGLLS and GLLS with sensitivity uncertainties set to 300%. In each subfigure, the top plot is the relative adjustment, $\Delta\boldsymbol{\sigma}/\boldsymbol{\sigma}_0$, and the bottom plot is the posterior relative standard deviation.

different nuclear data. The posterior sensitivities were created by the xGLLS method. Small adjustments can be seen for the mean values and uncertainties. For every integral parameter, sensitivities of inelastic scattering cross sections had the largest adjustments, especially for Pu-239 and U-238.
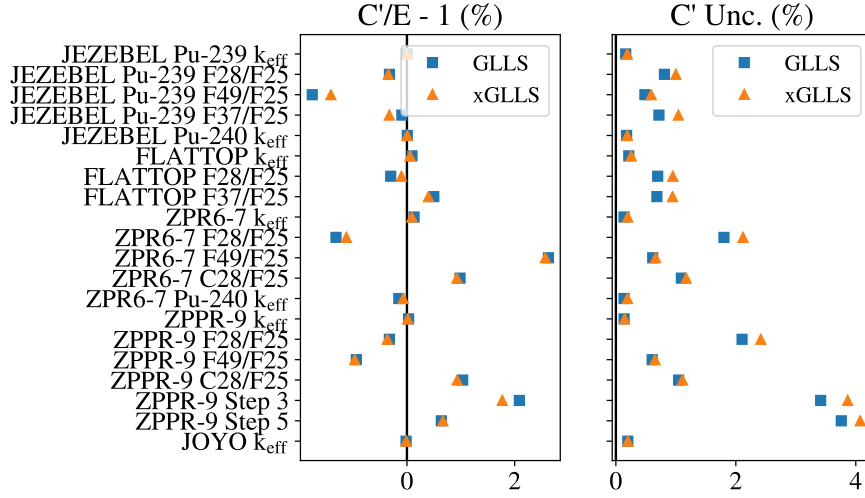
Figure 6.3 – Posterior biases and $\mathbf{C}'$ uncertainty with GLLS and xGLLS when sensitivity uncertainties are set to 300%.

Breakdown of the Source of xGLLS Adjustments

The results have demonstrated that the posterior nuclear data, $\boldsymbol{\sigma}'$, of GLLS and xGLLS are different. Additionally, the xGLLS posterior sensitivities, $\mathbf{S}'$, have been significantly adjusted. It is interesting to separate the effects of these two posteriors and see how they individually influence the bias. In this section, the biases are calculated with different combinations of $\boldsymbol{\sigma}'$ and $\mathbf{S}'$ to analyze the effects of the individual posteriors.

First, consider the bias obtained with GLLS posteriors. It is calculated with the $\boldsymbol{\sigma}'$ found with GLLS, which is called $\boldsymbol{\sigma}'_{\mathrm{GLLS}}$ here, and with the unadjusted $\mathbf{S}$. The xGLLS biases are calculated with its $\boldsymbol{\sigma}'$, or $\boldsymbol{\sigma}'_{\mathrm{xGLLS}}$, and the adjusted sensitivities, $\mathbf{S}'$. If we use $\boldsymbol{\sigma}'_{\mathrm{xGLLS}}$ and $\mathbf{S}$, we remove the effect that $\mathbf{S}$ adjustments have on the xGLLS bias and isolate the effect of $\boldsymbol{\sigma}'_{\mathrm{xGLLS}}$. Similarly, to assess the effect of $\mathbf{S}'$, the biases are calculated with $\mathbf{S}'$ and $\boldsymbol{\sigma}'_{\mathrm{GLLS}}$, removing how xGLLS affected the $\boldsymbol{\sigma}'$ when it took into account $\mathbf{S}$ uncertainties. By splitting the adjustments in this way, we can highlight and separate the effect of the $\mathbf{S}'$ and $\boldsymbol{\sigma}'_{\mathrm{xGLLS}}$.

Fig. 6.6 presents the posterior biases of the stress test broken down in this manner. The data are shown as the difference between the absolute value of the xGLLS biases and the absolute value of the GLLS bias. If there are no differences, the color is white. If the xGLLS bias is larger, or farther from zero in a positive or negative direction, the color is red. Conversely, if the xGLLS bias is smaller, the color is blue.

Examine first the differences between the GLLS biases (with $\boldsymbol{\sigma}'_{\mathrm{GLLS}}$ and $\mathbf{S}$) and the biases calculated with $\boldsymbol{\sigma}'_{\mathrm{xGLLS}}$ and $\mathbf{S}$ in the first column of Fig. 6.6. These data show how the differences between the $\boldsymbol{\sigma}'_{\mathrm{GLLS}}$ and $\boldsymbol{\sigma}'_{\mathrm{xGLLS}}$ affect the posterior biases, ignoring the $\mathbf{S}'$ of xGLLS. We see that the xGLLS nuclear data tend to create larger posterior biases (redder) than GLLS. The average of the bias differences is -0.031%. This indicates that $\boldsymbol{\sigma}'_{\mathrm{xGLLS}}$ was constrained to limit
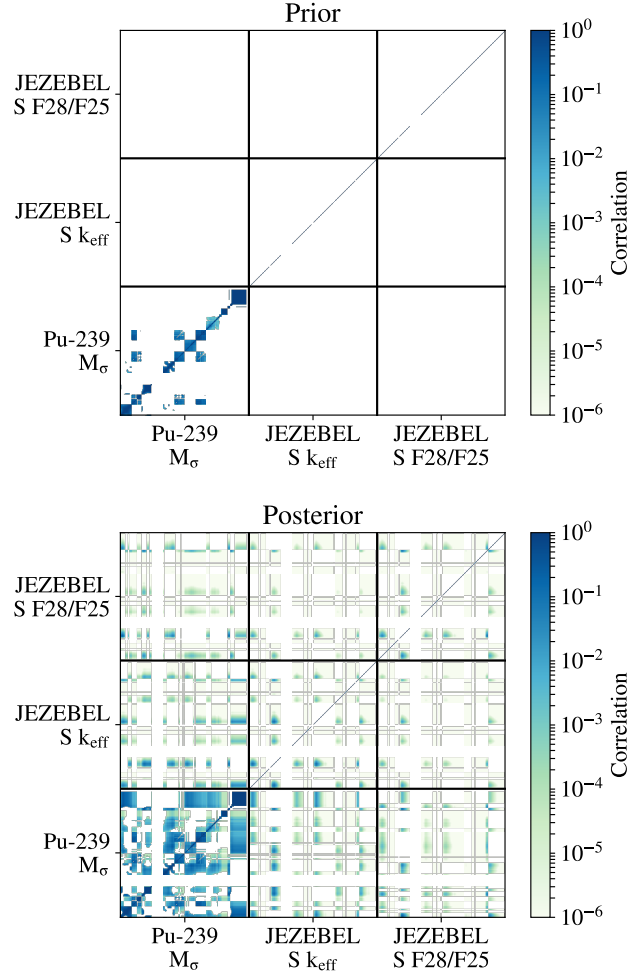
Figure 6.4 – Prior and posterior $\widetilde{\mathbf{M}}_\sigma$ correlation matrices from xGLLS when sensitivity uncertainties are set to 300%.

the improvement of the biases in the presence of large sensitivity uncertainty.

Continuing to the biases calculated with $\mathbf{S}'$ from xGLLS and $\boldsymbol{\sigma}'_{\text{GLLS}}$ to assess the affect of sensitivity adjustments, we see that these biases are smaller than those from GLLS for many integral parameters. This is shown by the blue shift in column two of Fig. 6.6 and the average absolute bias difference of 0.098%. The data show that the $\mathbf{S}'$ can lead to improved biases relative to the same $\boldsymbol{\sigma}'$ with unadjusted sensitivities. JEZEBEL F49/F25, FLATTOP F28/F25, ZPR6-7 F28/F25, and the two Na-void reactivity coefficients are the integral parameters that show the largest improvements in their posterior biases. Only JEZEBEL F37/F25 shows a degradation in its bias, increasing by 0.255%.

When considering the full xGLLS biases, or with $\mathbf{S}'$ and $\boldsymbol{\sigma}'_{\text{xGLLS}}$, the $\mathbf{S}'$ keep their important effect on the bias. The third column of Fig. 6.6 shows that the xGLLS biases are, in general, smaller than those from GLLS. This is supported by the average difference being 0.063%.
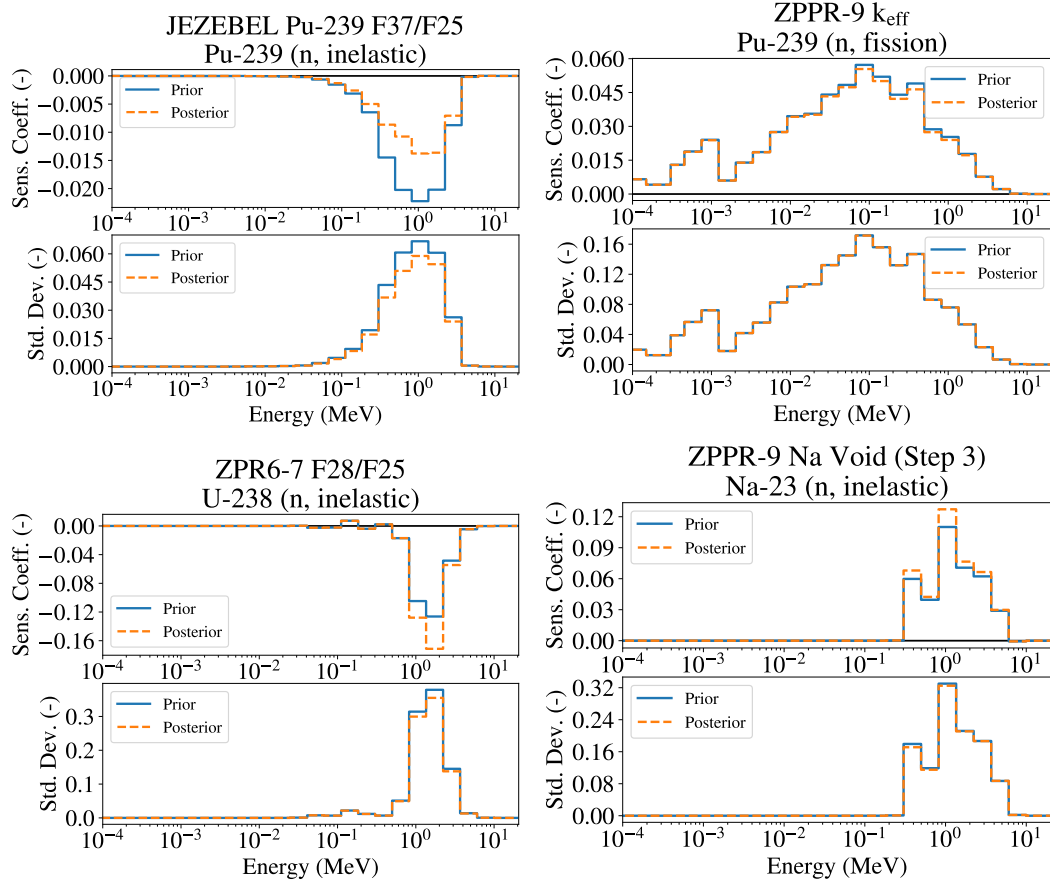
Figure 6.5 – Prior and posterior sensitivity coefficients, with the posteriors given by xGLLS. The bottom plot of each subfigure shows the standard deviations of the sensitivities, whose relative values are 300%.

We can also note the competing effects between $\boldsymbol{\sigma}'_{\text{xGLLS}}$ and $\mathbf{S}'$. For Na-void Step 5, the two adjustments have compensating and cancelling effects that make the GLLS and xGLLS biases different only by 0.010%. Whereas with $\boldsymbol{\sigma}'_{\text{xGLLS}}$ and $\mathbf{S}$, and with $\boldsymbol{\sigma}'_{\text{GLLS}}$ and $\mathbf{S}'$, the differences were -0.236% and 0.221%, respectively.

The $\mathbf{C}'$ uncertainties, or $\Delta_{\mathbf{C}'}$, from xGLLS can also be subdivided to isolate the effects of the posteriors. Recall that the uncertainty reduction is created by changes to $\mathbf{M}_{\sigma}$, by $\mathbf{S}$ adjustments, and by the possible creation of covariance terms between $\mathbf{S}$ terms and between $\mathbf{S}$ and $\boldsymbol{\sigma}$ in the extended posterior matrix $\widetilde{\mathbf{M}}'_{\sigma}$. Similar to the process presented for the posterior biases, the $\Delta_{\mathbf{C}'}$ are also broken down to examine the individual effects of the posteriors. The $\mathbf{M}'_{\sigma}$ of GLLS and xGLLS are differentiated as $\mathbf{M}'_{\sigma,\text{GLLS}}$ and $\mathbf{M}'_{\sigma,\text{xGLLS}}$. Fig. 6.7 analyzes the $\Delta_{\mathbf{C}'}$ as the difference between the GLLS $\Delta_{\mathbf{C}'}$ and the given xGLLS $\Delta_{\mathbf{C}'}$. Red values indicate that the $\Delta_{\mathbf{C}'}$ with GLLS is larger than with xGLLS, blue that it is smaller, and white that they are equal.

Begin with the first column of Fig. 6.7, which shows the differences in $\Delta_{\mathbf{C}'}$ when it was calculated with the $\mathbf{M}'_{\sigma}$ of both methods and the unadjusted $\mathbf{S}$. These data isolate the differences
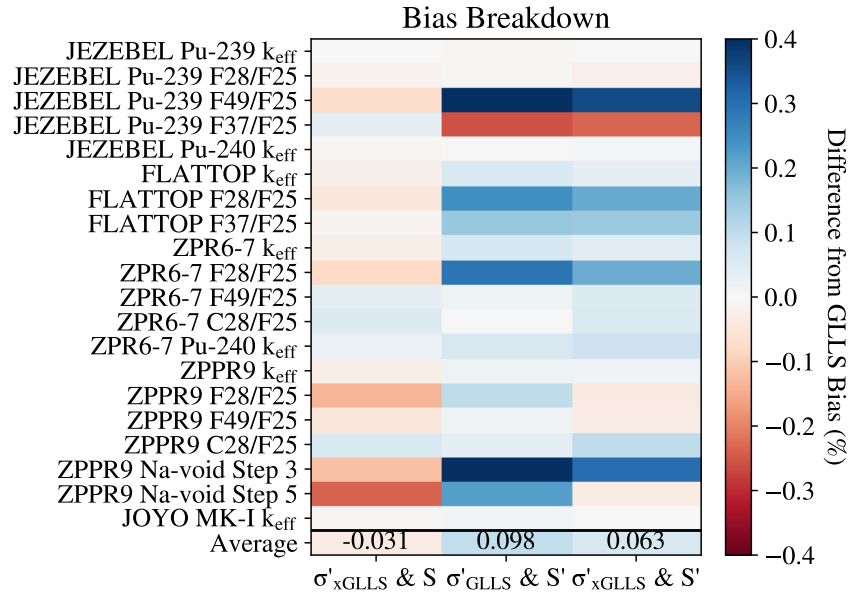
Figure 6.6 – Analysis of the different sources of bias adjustment.
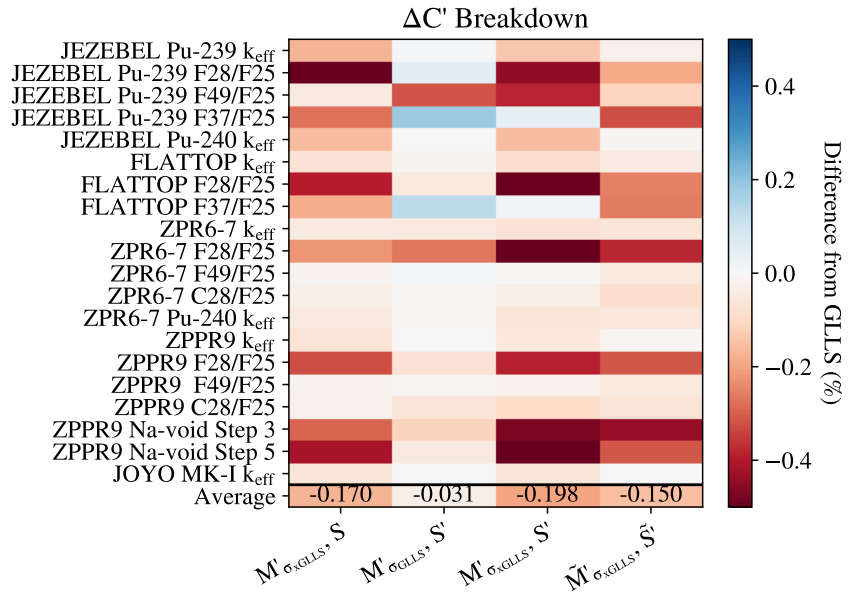
Figure 6.7 – Breakdown of the xGLLS $\Delta_{\mathbf{C'}}$, shown as difference from GLLS $\Delta_{\mathbf{C'}}$.

between $\mathbf{M}'_{\sigma,\text{GLLS}}$ and $\mathbf{M}'_{\sigma,\text{xGLLS}}$ and their effect on $\Delta_{\mathbf{C'}}$. For all integral parameters, the $\Delta_{\mathbf{C'}}$ were larger with $\mathbf{M}'_{\sigma,\text{xGLLS}}$ than with $\mathbf{M}'_{\sigma,\text{GLLS}}$, *i.e.* the differences are all negative (red). This indicates that xGLLS, in the presence of the large $\mathbf{S}$ uncertainty, restrained the reduction of the uncertainties and the generation of covariances in $\mathbf{M}'_{\sigma}$.

Examining when $\mathbf{S}'$ was used with $\mathbf{M}'_{\sigma,\text{GLLS}}$ to highlight the effect of $\mathbf{S}$ adjustments, the differences from GLLS $\Delta_{\mathbf{C'}}$ were small for most integral parameters. For F37/F25 of JEZEBEL

Pu-239 and F37/F25 of FLATTOP, the **S** adjustments were significant enough to create smaller $\Delta_{\mathbf{C}'}$ than if unadjusted **S** were used. The $\Delta_{\mathbf{C}'}$ of JEZEBEL F49/F25 increases by 0.316% with **S**′. In general, the **S**′ had a smaller effect than $\mathbf{M}'_{\sigma,\text{xGLLS}}$ on $\Delta_{\mathbf{C}'}$. Using **S**′ with $\mathbf{M}'_{\sigma,\text{GLLS}}$ gave an average difference from GLLS and **S** of -0.31%. Meanwhile, with **S** and $\mathbf{M}'_{\sigma,\text{xGLLS}}$ the average difference was -0.170%.

Folding $\mathbf{M}'_{\sigma,\text{xGLLS}}$ and **S**′ shows their combined effect on $\Delta_{\mathbf{C}'}$. The difference with the GLLS $\Delta_{\mathbf{C}'}$ shows that $\Delta_{\mathbf{C}'}$ is larger with xGLLS, with an average difference of -0.198%. The two posteriors compound to limit the uncertainty reduction in $\Delta_{\mathbf{C}'}$ with the very large **S** uncertainties present in the stress test. Finally, the full xGLLS $\Delta_{\mathbf{C}'}$ with $\widetilde{\mathbf{S}}'$ and $\widetilde{\mathbf{M}}'_\sigma$ can be examined, which includes the correlations between **S**′ and between **S**′ and $\boldsymbol{\sigma}'$ that exist in $\widetilde{\mathbf{M}}'_\sigma$. $\widetilde{\mathbf{M}}'_\sigma$ with correlations gave lower $\Delta_{\mathbf{C}'}$ than without correlations. The correlations grew to have a significant effect that reduced $\Delta_{\mathbf{C}'}$ so that it was more similar to that from GLLS.

When considered as a whole, the xGLLS adjustments performed better than the GLLS adjustments, *i.e.* their biases are closer to 0. When the absolute values of the biases are averaged across all 20 integral parameters, the GLLS bias is 0.665%. With xGLLS, or $\boldsymbol{\sigma}'_{\text{xGLLS}}$ and **S**′, the average is 0.602%. Considering only $\boldsymbol{\sigma}'_{\text{xGLLS}}$ and **S**, the average is the worst at 0.696%. This shows that the xGLLS equations restrained the $\boldsymbol{\sigma}$ adjustments, in the sense of limiting their movement that can effect improved biases. The average absolute bias is the best at 0.567% for **S**′ with $\boldsymbol{\sigma}'_{\text{GLLS}}$, showing how important the **S** adjustments are.

This result can also be confirmed through a different analysis using the χ^2 parameter as defined in Eq. (6.17). Lower χ^2 indicate better agreement between **C** and **E**. GLLS gives a χ^2 of 9.7 and xGLLS gives 6.5. Using $\boldsymbol{\sigma}'_{\text{xGLLS}}$ and **S** gives 10.39, and $\boldsymbol{\sigma}'_{\text{GLLS}}$ and **S**′ gives 5.94.

$$\chi^2 = \left(\mathbf{E} - \mathbf{C}'(\boldsymbol{\sigma}')\right)^T (\mathbf{M_E})^{-1}\left(\mathbf{E} - \mathbf{C}'(\boldsymbol{\sigma}')\right) \tag{6.17}$$

6.4.2 Nominal Case

This section presents the adjustments with xGLLS when the true uncertainties of the sensitivity coefficients, after 20 billion neutron histories, were used. These adjustments show what the effect of xGLLS would be in a realistic application scenario. The adjustments of several nuclear data are presented in Fig. 6.8. The figure shows no discernible differences between GLLS and xGLLS adjustments for any of the nuclear data. For these levels of sensitivity uncertainty, the xGLLS equations do not produce adjustments different from GLLS. Fig. 6.9 presents the posterior biases and calculated value uncertainties computed with the adjusted nuclear data. As there are no significant differences in $\Delta\boldsymbol{\sigma}$, by consequence, the figure shows that there are no differences in the posterior biases or $\Delta_{\mathbf{C}'}$.

Fig. 6.10 gives the posterior $\widetilde{\mathbf{M}}_\sigma$ from xGLLS transformed into a correlation matrix. Concerning the results, small correlations are created in the posterior $\widetilde{\mathbf{M}}_\sigma$. These correlations exist between $\boldsymbol{\sigma}'$ and **S**′, and between **S**′ themselves. The correlations are much smaller than those presented
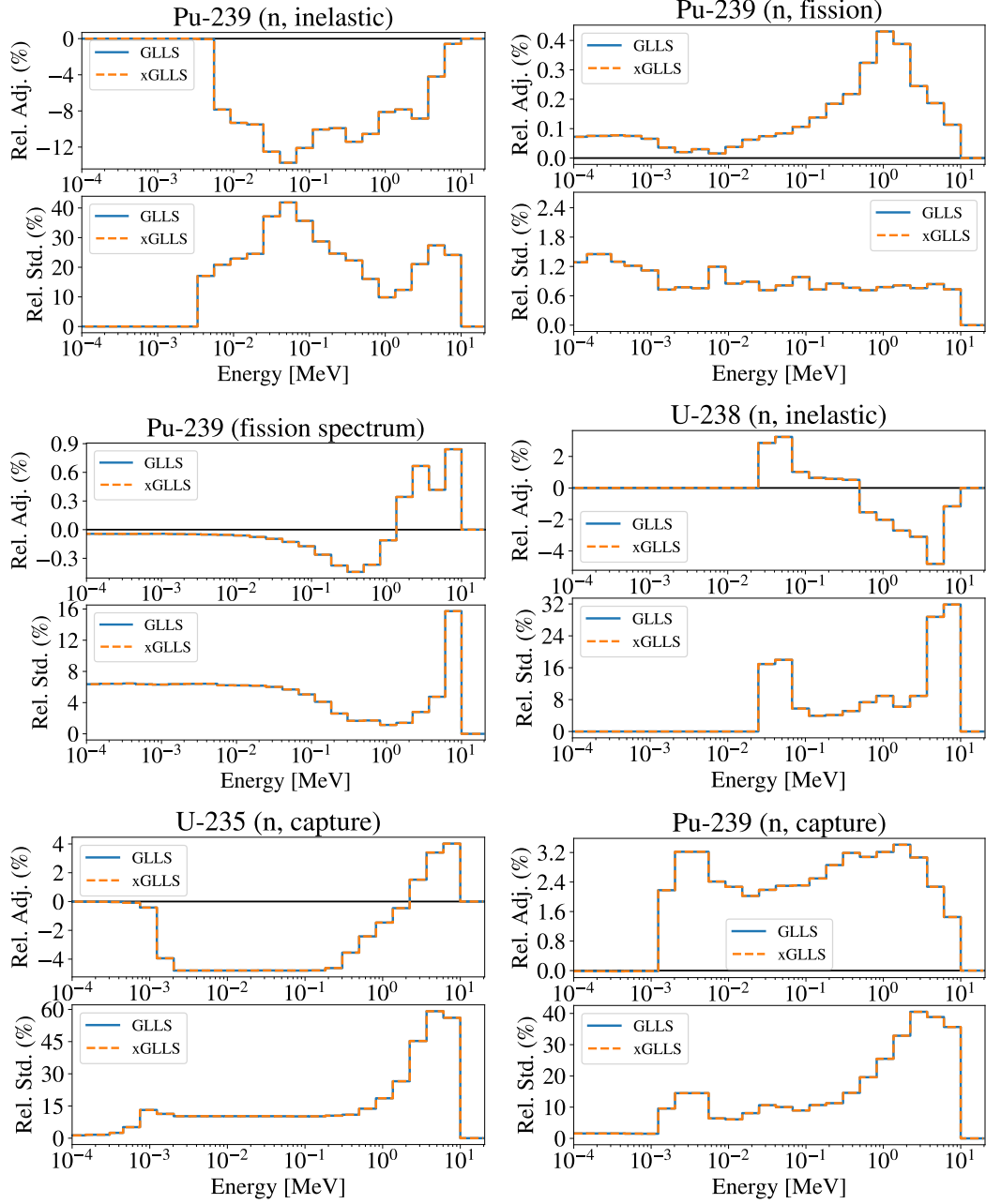
Figure 6.8 – Nuclear data adjustments made with sensitivities calculated using 20 billion neutron histories. In each subfigure, the top plot is the relative adjustment, $\Delta\boldsymbol{\sigma}/\boldsymbol{\sigma}_0$, and the bottom plot is the posterior relative standard deviation.

previously in Fig. 6.4 and show that for more realistic levels of sensitivity uncertainty, new correlation terms in the posterior extended matrices are not significant.

In summary, for the magnitude of sensitivity uncertainty encountered after 20 billion neutron histories for all 20 integral parameters, their effect when accounted for in xGLLS is negligible.
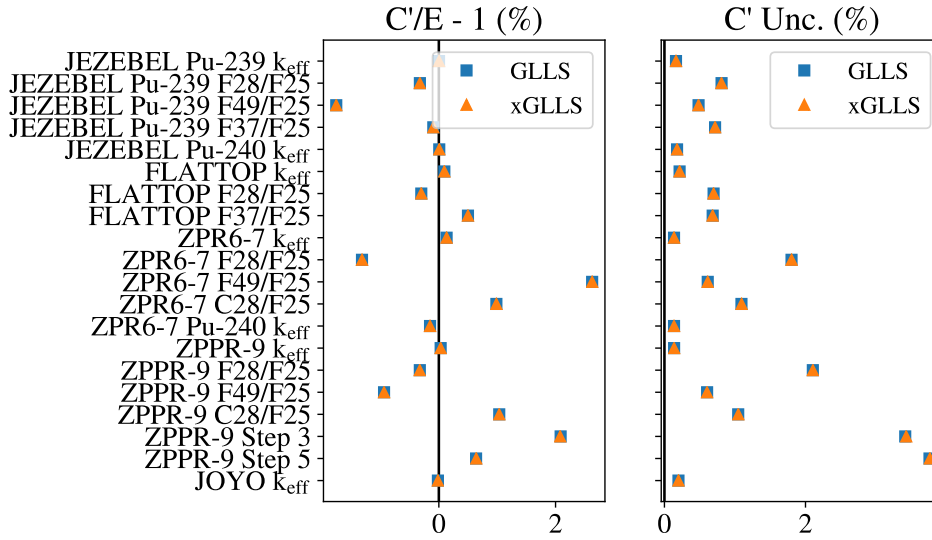
Figure 6.9 – Posterior biases and C' uncertainties with GLLS and xGLLS when the sensitivity uncertainties after 20 billion neutron histories are used.
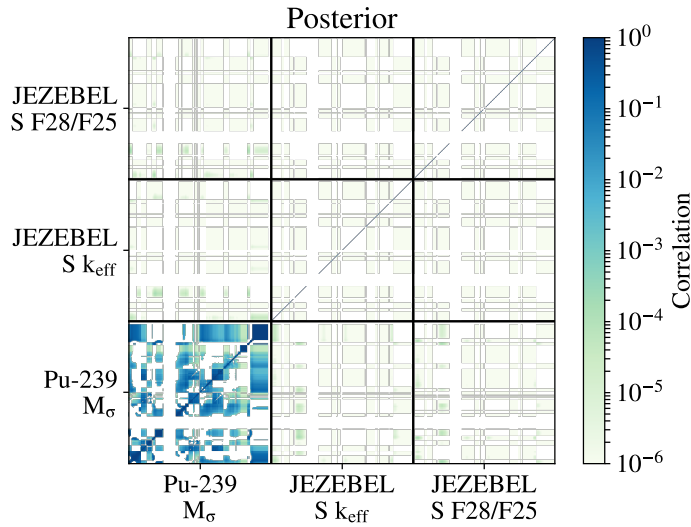
Figure 6.10 – $\widetilde{\mathbf{M}}'_\sigma$ for Pu-239 nuclear data and JEZEBEL Pu-239 k_{eff} and F28/F25.

No significant differences appeared for the posterior nuclear data and, therefore, neither in the posterior calculated values. The adjusted sensitivity coefficients, which are not shown, also did not show any significant adjustments from prior to posterior.

6.4.3 Adjustment Convergence

The previous section demonstrated the performance of xGLLS for a nominal case when the sensitivity coefficients are well converged and have low uncertainties. In reality, uncertainties

could be larger at earlier stages in the Serpent simulation, or when few neutron histories are used. Not only are the sensitivity uncertainties larger, but also their mean values fluctuate during the simulation before they eventually converge. The following section presents the posteriors of GLLS and xGLLS when they were calculated at increasing neutron histories, from 20 million to 20 billion, to see if xGLLS has a significant effect earlier in the simulation. The calculated values of the integral parameters, $\mathbf{C}$, and the modeling and methodology uncertainties, $\mathbf{M_M}$, are kept constant when calculating the posteriors; only the sensitivity means and their uncertainties are changed in the GLLS and xGLLS equations.

The results show the maximum realistic effect that the sensitivity uncertainties can have in xGLLS because the uncertainties will be at their maximum early in the simulation. The study also captures the effect of the sensitivity mean-value oscillations, which are not accounted for in xGLLS. Because too few neutron histories can easily be used in a simulation and because we do not know *a priori* how converged sensitivities must be for DA, these results are important to understand the question of how many neutron histories are needed in DA.
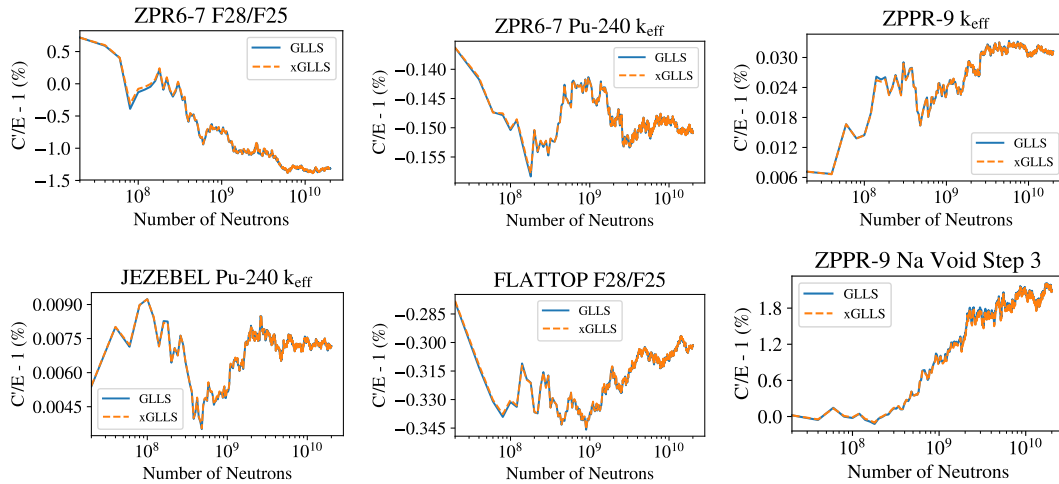
Figure 6.11 – Posterior bias, $\mathbf{C'}/\mathbf{E}$ - 1, from 20 million to 20 billion neutron histories in the sensitivity calculations.

Fig. 6.11 presents the posterior biases, $\mathbf{C'}/\mathbf{E}$ - 1, of several integral parameters. The biases can greatly vary as the number of neutron histories increases, which is caused by fluctuations in the $\mathbf{S}$ mean values. Spectral indices show larger fluctuations and converge later than k_{eff} as their $\mathbf{S}$ uncertainties were bigger. For large cores like ZPR6-7 and ZPPR-9, their $\mathbf{S}$ had bigger uncertainties and their biases varied more significantly and had later convergence. The Na-void Step 3 bias, with its $\mathbf{S}$ being highly uncertain with EGPT, also showed large fluctuations. Even at low numbers of neutrons where $\mathbf{S}$ uncertainties were largest, there were no significant differences between the GLLS and xGLLS posterior biases. Fig. 6.12 gives the GLLS and xGLLS $\mathbf{C'}$ uncertainties due to $\mathbf{M'_\sigma}$ with increasing neutron histories. The $\mathbf{C'}$ uncertainties also varied as $\mathbf{S}$ converged. They tended to converge faster than the posterior biases. Certain k_{eff}, like for JOYO, showed very small fluctuations at less than 1 pcm.
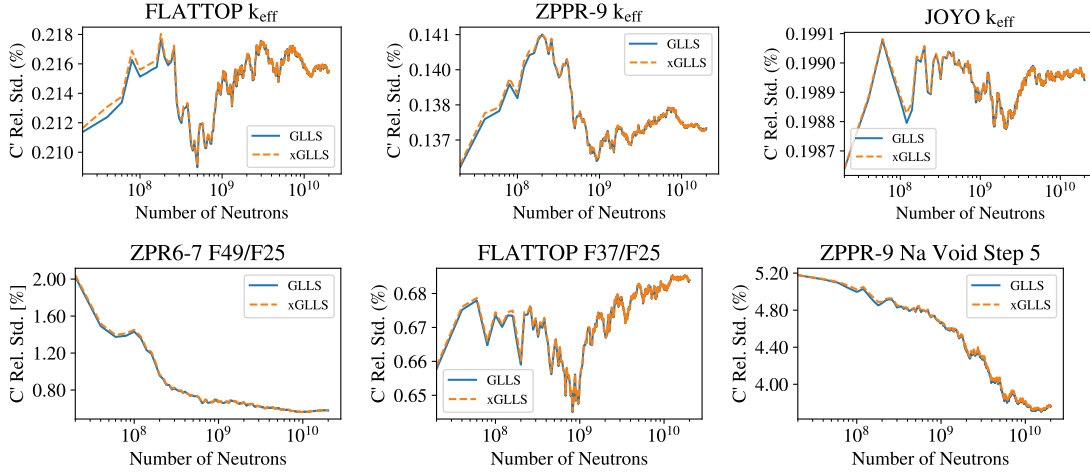
Figure 6.12 – Uncertainty associated with $\mathbf{C}'$ resulting from $\mathbf{S}$ uncertainty.

Fig. 6.13 shows the relative adjustments of different $\boldsymbol{\sigma}$ at specific energy groups as the number of neutron histories increases. There are no discernible differences between GLLS and xGLLS, even at low numbers of histories where $\mathbf{S}$ uncertainties are largest. The variations in adjustments can be quite large before convergence. The inelastic scattering cross section of Pu-239 stands out again as having very large fluctuations and very late convergence. Fig. 6.14 gives the convergence behavior of the $\boldsymbol{\sigma}'$ relative standard deviations. They have large fluctuations of up to several percents and no meaningful differences between GLLS and xGLLS.
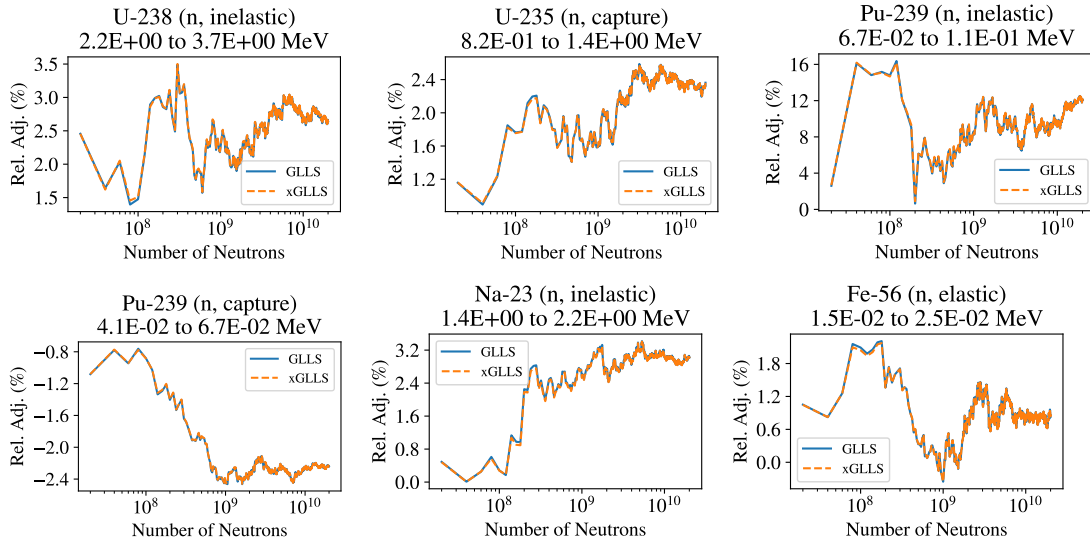
Figure 6.13 – $\boldsymbol{\sigma}'$ relative adjustments ($\Delta\boldsymbol{\sigma}/\boldsymbol{\sigma}_0$) as the number of neutron histories used in the Serpent simulations increases.

Why did the $\mathbf{S}$ uncertainties have such a limited effect in xGLLS? The answer is that, in comparison to other uncertainty terms in the adjustment equations ($\mathbf{M_E}$, $\mathbf{SM}_\sigma\mathbf{S}^T$, and $\mathbf{M_M}$), the
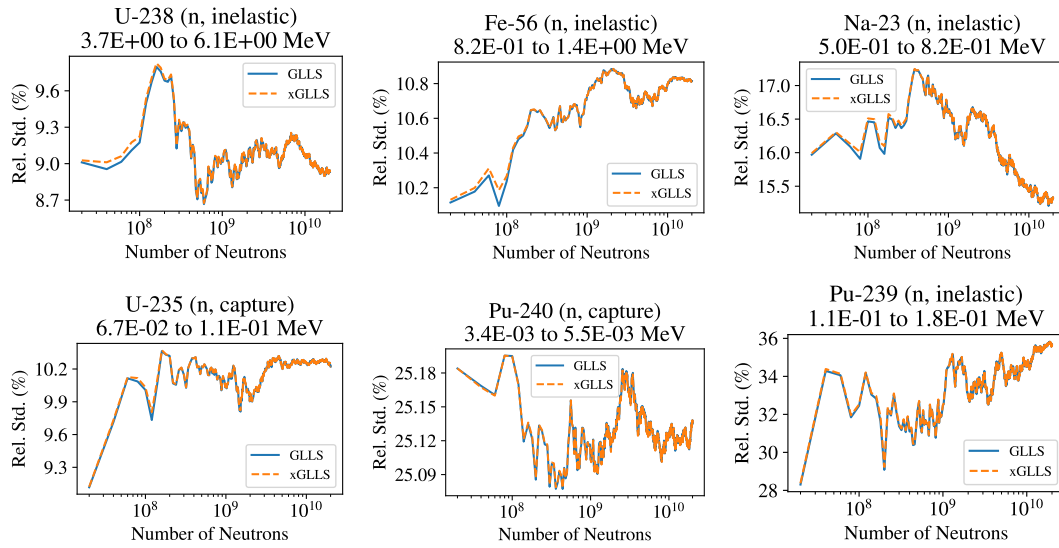
Figure 6.14 – $\boldsymbol{\sigma}'$ relative standard deviations as the number of neutron histories used in the Serpent simulations increases.

uncertainty of **C** caused by sensitivity uncertainties was small. The new term in xGLLS that accounts for the sensitivity uncertainties then had a negligible effect; it was diluted by the traditional terms in GLLS. This idea is demonstrated in Fig. 6.15 where the uncertainties in **C** that come from nuclear data uncertainty ($\mathbf{SM}_\sigma\mathbf{S}^T$), methodology ($\mathbf{M_M}$), sensitivity uncertainty ($\Delta\Sigma\mathbf{M_S}\Delta\Sigma$), and the experimental uncertainty ($\mathbf{M_E}$) are plotted. Here the true $\mathbf{M_M}$ from Serpent is plotted, not that used in the benchmark. The nuclear data uncertainty is calculated with the prior $\mathbf{M}_\sigma$. The uncertainty from sensitivities is calculated using first order error propagation like in Eq. (6.2) isolating only the sensitivity uncertainty terms. This gives the expression $\Delta\Sigma\mathbf{M_S}\Delta\Sigma$ to calculate the uncertainty of **C** from sensitivity uncertainties. $\Delta\Sigma$ is the same as in Eq. (6.4), and the $\Delta\boldsymbol{\sigma}$ in this formulation is taken from xGLLS.

Fig. 6.15 shows several interesting results. First, and most important for this study, is that even at few neutron histories, the uncertainty of **C** from sensitivities is small compared to the nuclear data and methodology uncertainties and to the experimental uncertainty. This explains why xGLLS does not create adjustments significantly different from GLLS, even at few neutron histories when the sensitivity uncertainties are at their maximum. Second, we see that for a spectral index in a large core like ZPR6-7 F49/F25 or for the ZPPR-9 Na-void Step 3, the methodology uncertainties can be quite large and many neutron histories may be needed for them to be reduced. Third, we see that the Na-void uncertainty is highly overestimated at few neutron histories, showing how difficult it is to estimate the sensitivities of this integral parameter with EGPT and Monte Carlo neutron transport.

Interestingly, the nuclear data uncertainties of ZPR6-7 F49/F25 and ZPPR-9 Na Void Step 3 monotonically decrease. They do not show up and down statistical fluctuations that might be expected from converging random variables. The decrease is related to sensitivities that have
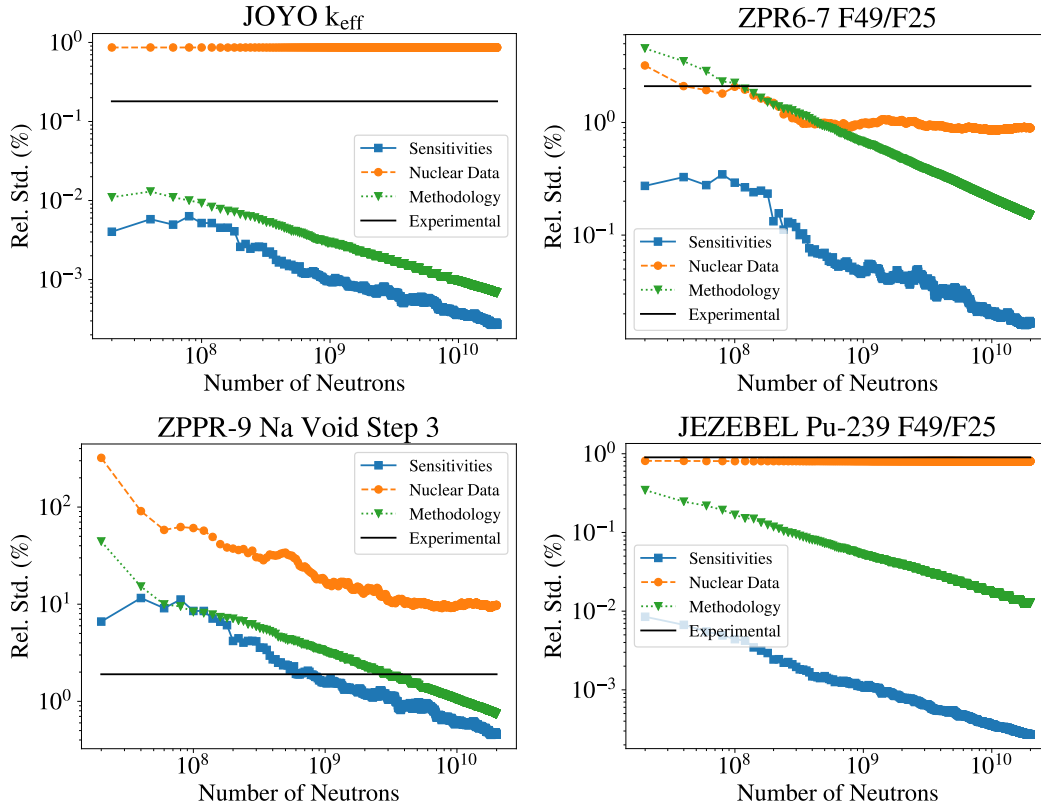
Figure 6.15 – Uncertainties of **C** from sensitivities, nuclear data, and modeling/methodology plotted with increasing numbers of neutron histories.

zero values or near zero values when they are fully converged or estimated with deterministic codes. When they are not fully converged, the sensitivities can be very large, up to several orders of magnitude larger than the converged results. When these sensitivities are used in $\mathbf{SM}_\sigma \mathbf{S}^T$, they produce an over-estimation of the nuclear data uncertainty. As they converge to zero or near zero, their contribution to the total uncertainty decreases. This over-estimation then decreases until the uncertainty from nuclear data is created only by sensitivity coefficients that are much greater than zero. This effect was more prominent for these two integral parameters because these integral parameters had more difficult convergence than k_{eff} in general and they were from larger systems than JEZEBEL-Pu239 and therefore needed more neutrons for similar precision.

Fig. 6.16 shows several sensitivity profiles corresponding to the integral parameters of Fig. 6.15 that exhibit this behavior. The INL deterministic sensitivity profile is also shown for comparison to indicate what a non-stochastic result would be. For each integral parameter, the sensitivity profile is shown for increasing numbers of neutron histories. JOYO k_{eff} and JEZEBEL-Pu239 F49/F25 both show well converged sensitivity profiles even at 2E6 neutron histories. ZPPR-9 Na Void Step 3 and ZPR6-7 F49/F25 show large over-estimations of the fully converged result at low neutron histories. These over-estimations were important for the Pu-240 capture

cross section, especially around 3E-3 MeV where the uncertainty is 25%. The over-estimated sensitivity for highly uncertain nuclear data caused an over-estimation of the nuclear data uncertainty in **C**. This over-estimation decreased as the sensitivity profiles converged to their smaller values.
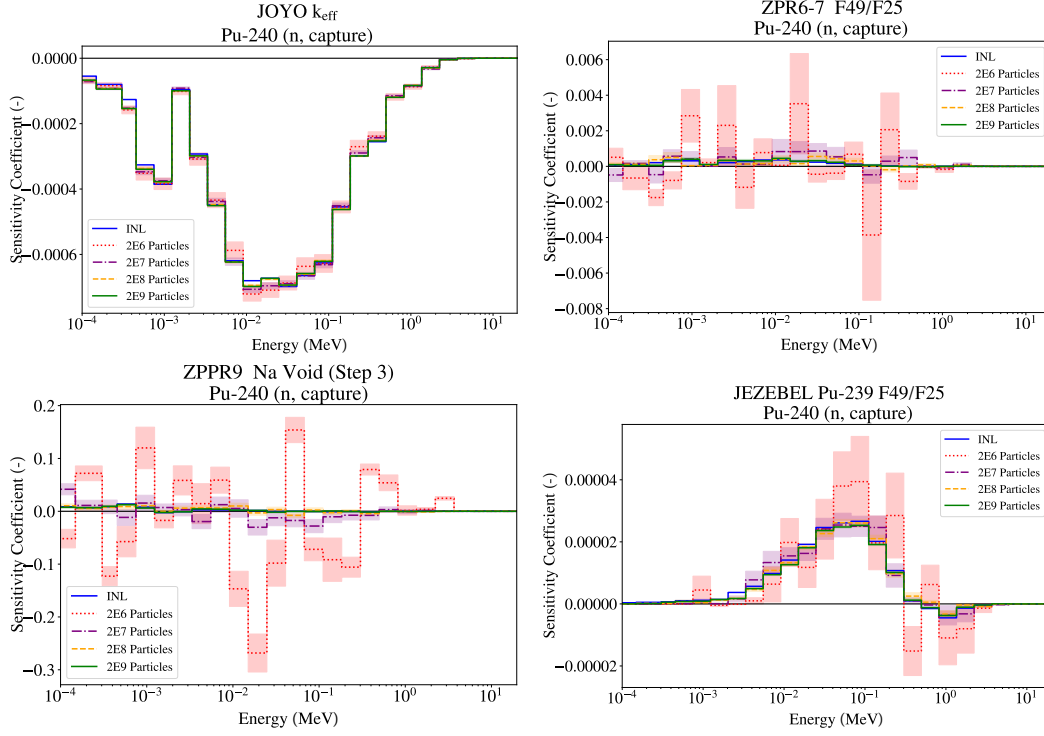
Figure 6.16 – Sensitivity profiles with varying neutron histories for the Pu-240 capture cross section. the INL profiles were calculated with ERANOS during the Subgroup 33 benchmark.

We can build on work presented in [71] to provide a guideline for using sensitivity coefficients from Monte Carlo neutron transport codes. This can help to avoid the over-estimation of the nuclear data uncertainties and to limit the uncertainty in **C** caused by sensitivity profiles while simultaneously minimizing the invested computational resources. Comparing the convergence plots presented in Figs. 6.11, 6.12, 6.13, and 6.14 to Fig. 6.15, the posteriors are approximately converged once the combined uncertainties in **C** from methodology and sensitivities are much smaller than that from nuclear data, or $(\mathbf{M_M} + \Delta\Sigma\mathbf{M_S}\Delta\Sigma) << \mathbf{SM}_\sigma\mathbf{S}^T$. As a convergence guideline, we propose to stop a simulation once this criterion is met.

The criterion's advantage can be seen by examining the **C** uncertainties of JOYO k_{eff} in Fig. 6.15. For this integral parameter, even at 20 million neutron histories, the uncertainty of **C** from methodology and sensitivities is much smaller than that from nuclear data. Now examining the **C**′ uncertainty of this integral parameter in Fig. 6.12, we see that it had very small fluctuations, even at few neutron histories, of less than 1 pcm. This indicates that this simulation could have been stopped much earlier, and have significantly saved computational cost, without severely affecting the accuracy of the posterior. Contrast this with ZPR6-7 F49/F25 in Fig. 6.15, where

only after more than 10 billion neutron histories is $(\mathbf{M_M} + \Delta\Sigma\mathbf{M_S}\Delta\Sigma) << \mathbf{SM}_\sigma\mathbf{S}^T$. This is also reflected in the $\mathbf{C}'$ uncertainty from nuclear data of this integral parameter in Fig. 6.12, where significant numbers of neutrons are needed before the posterior converges. This shows that the additional neutron histories, and computational resources, committed to the simulation of ZPR6-7 F49/F25 were necessary for convergence.

6.5   Conclusions

Sensitivities from continuous-energy Monte Carlo codes have many advantages in data assimilation. This chapter discussed the impact of their statistical uncertainties on the adjustments of calculated integral parameters and nuclear data. To account for the sensitivity uncertainties, the traditional Generalized Linear Least Squares (GLLS) equations were adapted to create the eXtended Generalized Linear Least Squares (xGLLS) method. This new xGLLS approach was tested by simulating an NEA data assimilation benchmark with Serpent2.

The xGLLS method was tested first with large and exaggerated sensitivity uncertainties of 300%. For this artificial case, xGLLS posteriors showed significant differences from GLLS. xGLLS' nuclear data adjustments were restrained in a way that the posterior χ^2 was larger than that from GLLS. In other words, when compared to GLLS, xGLLS created larger biases and larger posterior calculated value uncertainties with its posterior nuclear data. The adjusted sensitivities created by xGLLS were shown to have an important role, helping to produce a lower χ^2 than GLLS. The posterior correlation terms created between sensitivities and between sensitivities and nuclear data were also seen to be important. They created smaller posterior calculated uncertainties for the integral parameters than if they were ignored.

For a realistic range of sensitivity uncertainties, xGLLS did not show any significant differences from GLLS. This conclusion is even valid at 20 million neutron histories when the sensitivity uncertainties were largest. The sensitivity uncertainties did not have a large effect because they were small compared to nuclear data, modeling/methodology, and experimental uncertainties.

Convergence analysis of the posteriors with increasing neutron histories showed that fluctuations of sensitivity mean values were an important factor for having converged posteriors. Posterior calculated integral parameters from large cores like ZPPR-9 and ZPR6-7 and the spectral indices converged later because of their larger sensitivity uncertainties. We proposed a guideline for economizing simulations with Monte Carlo neutron transport codes for data assimilation: the posteriors are approximately converged once the combined uncertainty of the calculated value of an integral parameter from methodology and sensitivities is much smaller than that from nuclear data. This guideline can be used in future DA studies to help economize the expensive Monte-Carlo neutron transport simulations. It could also be used in uncertainty quantification studies, with an assumption for $\Delta\boldsymbol{\sigma}$, or the nuclear data adjustment term.

In this work, xGLLS was applied assuming that the sensitivity coefficients were independent of each other and from the nuclear data. In reality, these correlations exist, especially for the sensitivities of spectral indices. Important future work could be focused on calculating these correlations and evaluating their effect on the adjustments with xGLLS.

6.6 Chapter's Key Points

- The sensitivity coefficients from Monte Carlo neutron transport codes have statistical uncertainties

- The uncertainties of sensitivities are not taken into account in GLLS

- We proposed the xGLLS method to account for the sensitivity uncertainties in DA

- We tested xGLLS with an NEA benchmark that has 20 integral parameters

- xGLLS was proven to constrain the adjustments of nuclear data and calculated integral parameters in the presence of large sensitivity uncertainty

- For the range of sensitivity uncertainties encountered in practice, they were not influential on the adjustment and xGLLS did not give posteriors different from GLLS

- To optimize the run time of sensitivity calculations, they can be stopped once the combined uncertainty of the calculated value of an integral parameter from methodology and sensitivities is much smaller than that from nuclear data

7 Conclusions

> All models are wrong, but some models are useful.
>
> ─────────────────────────────
>
> G.E.P. BOX [135]

This thesis began with two well defined goals and one ambiguous goal. A clear target was to use experimental data from the Proteus research campaigns in data assimilation (DA). Another was to develop DA tools for use at PSI and EPFL. The undefined goal was scientific and sought to advance DA knowledge, theory, and application range in the field of neutronics. The start of the thesis coincided with two developments: 1) the adaptation of DA methods based on stochastic sampling to neutronics problems, and 2) sensitivity analysis tools being implemented in continuous-energy Monte Carlo neutron transport codes. It was around these two advancements that the research aspects of the thesis were constructed. Excluding the introduction and conclusion, a chapter-wise summary of the thesis is given below.

7.1 Chapter-wise Summary

Chapter 2 – Overview of Data Assimilation Theory

The first stage of the thesis required understanding the theoretical bases of DA in neutronics. Chp. 2 summarized the state-of-the-art of DA in the field. First an introduction to Bayes' theorem was given, which was then expanded to the case of nuclear data and integral experiments. Then, the three principal DA methods of the field were described: Generalized Linear Least Squares (GLLS), Monte Carlo Bayesian Analysis (MOCABA), and Bayesian Monte Carlo (BMC). A second flavor of BMC, called Backward Forward Monte Carlo (BFMC).

This chapter is, to the author's knowledge, the first time in literature that these methods were all shown to derive from the same theoretical bases. The theory was also described in a more detailed fashion than usually encountered. For one, the posterior covariances between

nuclear data and experimental data were described in their mathematical form. Secondly, a united description of the state-of-the-art ways to handle inconsistencies between calculated and experimental integral data was provided. This included the filtering techniques with the Adjustment Margin and $\Delta\chi^2$ parameters, and with a data-driven approach called Marginal Likelihood Optimization (MLO).

Chapter 3 – Comparison of Data Assimilation Methods

For the first time, the three DA methods GLLS, MOCABA, and BMC/BFMC were compared. First, the comparison was done with simplified toy models to specifically target linear and non-Gaussian systems. Then, the methods were applied to the JEZEBEL-Pu239 benchmark as a complex, real-world case study. The code Serpent2 simulated neutron transport and calculated sensitivity coefficients, and NUSS randomly sampled nuclear data.

The principle conclusion was that the DA methods' results agree within the stochastic uncertainties of MOCABA and BMC. The toy problems demonstrated some interesting behavior in terms of the performance of the DA methods as algorithms. The BMC and BFMC methods proved to be highly sensitive to the sample size and to the magnitude of the data set's χ^2. With BMC, as the χ^2 gets larger the degree of degeneracy increases in the weight distributions, leading to less statistically accurate posteriors. This will continue in BMC up until a maximum, threshold χ^2 at which all weights become zero and no posterior can be calculated. BFMC, oppositely, counteracts this behavior with a weight normalization, but no longer gives an unbiased estimate of the maximum *a posteriori* distribution.

The JEZEBEL-Pu239 study importantly showed that, for a more complex DA problem, the methods' results all agree. Additionally, it served to develop the DA tool DAN (**D**ata **A**ssimilatio**N**), completing an original goal of the thesis. DAN will serve as a computational tool for future studies at PSI and EPFL. For JEZEBEL, a more complex system, the BFMC posteriors agreed to a better extent with the other DA methods, which improved the confidence in this method and allowed it to be used in other studies in the thesis.

Chapter 4 – Data Assimilation of the LWR-Proteus Phase II Reactivity Experiments

The LWR-Proteus Phase II (LWR-PII) experiments from PSI were targeted for use in DA. They provide a rich amount of experimental data that is topical for the current state of the nuclear industry in Switzerland. Nowadays, the focus is on the optimization of LWRs and their nuclear waste management. This chapter presented a DA of reactivity measurements that were conducted at the Proteus reactor. Fuel samples from real Swiss PWRs were put into Proteus to evaluate the effect that burnup has on reactivity. The experiment serves as a basis to validate reactivity simulations, and now to perform DA.

The GLLS, MOCABA, BMC, and BFMC DA techniques that were used in Chp. 3 were implemented into the tool SHARK-X that is maintained at PSI to do sensitivity analysis and

uncertainty quantification. First, the consistency of the experimental and calculated values of these integral parameters was evaluated. To do so, we used the $\Delta\chi^2$-filtering technique. This test showed how taking into account the correlations between integral data is very important for consistency evaluation. Only ten out of 32 relative reactivities were sufficiently consistent to be used in DA. MOCABA and GLLS were used to adjust the calculated relative reactivity values and the chosen nuclear data. BMC and BFMC were not used because the required sample sizes to have statistically accurate posteriors were too prohibitive.

Small but statistically significant differences appeared between the posterior relative reactivities given by MOCABA and GLLS. These differences were attributed to round-off errors in SHARK-X and not to any theoretical difference between the DA methods. Finally, analysis of the nuclear data adjustments showed large changes to the U-238 capture cross section. These changes were very important in improving the bias of the CASMO-5M simulations. The posterior nuclear data covariance matrices gained significant negative correlation terms between Pu-239 fission multiplicity data that led to reductions in calculated value uncertainty. This supported previous conclusions that the Pu-239 fission multiplicity uncertainty may have been overestimated in the SCALE6.1 covariance data.

Chapter 5 – Data Assimilation of Post-Irradiation Examination Experiments

Chp. 5 was devoted to using post-irradiation examination experiments to adjust the model parameters of the code GEF. The purpose was to improve the bias and to reduce the uncertainties of calculated fission product concentrations in spent fuel. The post-irradiation examination (PIE) experiments were also part of the LWR-PII experimental campaign. They involved analytical chemistry to determine the composition of nuclear fuel after exposure in a reactor. In this thesis, the experiments were used with BFMC and MOCABA to adjust the fission yields of GEF. This project was a stimulating theoretical challenge from a scientific point of view because GEF's fission yields can have non-normal distributions. Because BFMC can account for this non-normality and MOCABA cannot, this served as an interesting case study to highlight the strengths and weaknesses of the different DA methods.

The PIE experiments were simulated in CASMO-5 after sampling the GEF model parameters 10,000 times to create 10,000 sets of fission yields. One fuel sample from LWR-PII was then used to adjust the model parameters of GEF. Before the adjustment, the MLO technique was applied to account for the large degree of inconsistency in the PIE integral data set. Applying DA gave posterior model parameters of GEF which were then used to create posterior fission yields and their covariance matrices. The posterior fission yields were then used again in CASMO-5 simulations to assess their performance.

The posterior model parameters, and subsequently fission yields and their covariance data, and subsequently again the simulations of the fuel sample compositions, showed good agreement between MOCABA and BFMC when MLO was applied. This occurred despite the non-normality of the fission yields and calculated responses. The posterior GEF fission yields

showed stronger agreement with the fission yields from ENDF/B-VIII.0 and JEFF3.3 than the prior. The posterior fission yields also created lower biases and uncertainties in nuclide concentrations. For the fuel sample used in the DA, the prior average absolute bias was 26.4%. The posterior biases with MOCABA and BFMC were 13.7% and 15.4%, respectively. The uncertainty of the calculations dropped from a prior of 20.3%, to a posterior of 13.5% and 14.1% with MOCABA and BFMC, respectively. When the posterior fission yields were used with fuel samples that were not part of the training data, they also improved the biases and reduced uncertainties.

The BFMC posteriors exhibited slight differences when MLO was and was not used. MOCABA, in contrast, showed very significant differences. The trends of the adjusted fission yields were significantly changed, which had a deleterious effect on the posterior biases of the calculated nuclide concentrations. For the training data, the average absolute bias deteriorated from a prior of 26.4% to a posterior of 55.9%. We hypothesize that better posteriors were obtained when MLO was applied with MOCABA for two reasons: 1) MLO decreased the inconsistency of the integral data set and 2) it de-emphasized the influence of integral data with large skewness. With the integral data's full inconsistency, MOCABA over-fit the model parameters to the integral data. With the full degree skewness included in the adjustment, MOCABA's incorrect normality assumption biased the posteriors. This did not occur with BFMC because it compensates for inconsistent integral data and accounts for non-normality.

Chapter 6 – eXtended Generalized Linear Least Squares

Over the course of using Serpent to calculate sensitivity coefficients for GLLS in Chp. 3, several questions arose. They pertained to the effect of the uncertainties of the sensitivities that are inherent to Monte Carlo neutron-transport codes. The GLLS methodology was adapted to xGLLS (eXtended GLLS) to address these questions. xGLLS can account for the sensitivity uncertainties in the adjustment equations in a statistically consistent way. Now, the sensitivity coefficients are treated as random variables that can also be adjusted through DA.

xGLLS was investigated with a benchmark DA problem proposed by a working group at the Nuclear Energy Agency. With very large sensitivity uncertainties, xGLLS acted to constrain the adjustment. This means that the changes to the nuclear data and the reductions to their uncertainties were weaker when xGLLS accounted for the sensitivity uncertainties. These weaker adjustments then propagated to create smaller adjustments to the calculated integral parameters. Importantly, however, the range of sensitivity uncertainties commonly encountered in applications did not have a significant effect on the posteriors. The study showed that once the calculated integral parameters were converged, their sensitivities had enough statistical accuracy to have converged posteriors. The convergence of the calculated integral parameters can then be used a convergence criterion to stop Monte Carlo neutron transport simulations, and thereby significantly economize computational resources.

7.2 Future Work

The thesis unveiled several avenues for future projects. Firstly, it showed that BMC and BFMC have room for improvement in terms of their efficiency as algorithms. While they are applicable to any problem because they make no linearity or normality assumption, their parsimony also makes them less efficient and they require much more computational resources than MOCABA or GLLS. For instance in Chp. 6, only 100 out of 10,000 samples in BFMC had weights that were significantly greater than 0. Approximately 9,900 CASMO runs did not contribute to calculating the posterior and were effectively a waste of computational resources. New sampling techniques could be investigated, like importance sampling [136] from the prior, or using Markov Chain Monte Carlo approaches [137].

Concerning xGLLS, the study presented here never accounted for the correlations between sensitivities and between sensitivities and nuclear data. The sensitivities are correlated, in theory, because the same neutron histories are used to calculate them. The sensitivities and nuclear data are correlated because nuclear data directly impact the sensitivities. Important future work could focus on calculating these sensitivities and implementing them into continuous-energy Monte Carlo neutron transport codes. Once they are implemented, xGLLS must be re-evaluated to see if the conclusions made in this thesis are still valid.

The DA of the reactivity measurements of LWR-PII has much room for improvement. Higher fidelity in modeling the burnup history of the fuel samples should be used to improve the neutronics model's accuracy. A modeling and methodology covariance matrix needs to be estimated with the MLO approach. Other improvements will come from considering the effects of nuclear data, including fission yields, on the nuclide composition of the fuel samples used in the relative reactivity calculations.

Using DA with GEF has a lot of potential for future work. Different kinds of integral data should be used, like reactivity or decay heat experiments. When more PIE data are to be used, the SFCOMPO data base should be exploited. Fuel samples with lower burnup or higher enrichment could be assimilated, possibly allowing for better performance of U-235 fission yield data. PIE experiments that were done in more controlled environments, like a high flux research reactor rather than an operating nuclear power plant, could be very useful. This would allow for a more accurate irradiation history to be modeled and to lessen the inconsistency of the integral data that arises from model inaccuracy. If the BMC method advances and becomes more efficient, Monte Carlo neutron transport calculations could be used to model the fuel burnup, thereby alleviating some model inaccuracies. Other future work should try to separate the effects of model inconsistency and non-normality on the posteriors from MOCABA.

Time-dependent DA problems can also be pursued in future research. Ideally, the research can start from simple case studies in zero-power research reactors. This would limit the physics to purely neutronics effects. Once the DA methods are characterized for these simple problems, they could be expanded to include thermal-hydraulic feed-backs with higher-power research

reactors. Finally, they could be expanded to real nuclear power plants. The CROCUS reactor at EPFL would be a good starting point for zero-power research reactor applications. Serpent and PARCS models of the reactor [138, 139, 140, 141, 142] could be used with DA methods similar to those outlined in this thesis. Methods like the Extended Kalman Filter, the Ensemble Kalman Filter, and the Particle Filter could be applied to transients in CROCUS.

Bibliography

[1] A. Saltelli et al. *Global Sensitivity Analysis. The Primer*. John Wiley & Sons Ltd, Chichester, West Sussex UK, 1st edition, 2008.

[2] G. Evenson. *Data Assimilation : The Ensemble Kalman Filter*. Springer, 2007.

[3] G.E. Wilson. Historical insights in the development of best estimate plus uncertainty safety analysis. *Annals of Nuclear Energy*, 52, 2013.

[4] G. Palmiotti and M. Salvatores. The role of experiments and of sensitivity analysis in simulation validation strategies with emphasis on reactor physics. *Annals of Nuclear Energy*, 52, 2013.

[5] R. Pericas et al. Comparison of best-estimate plus uncertainty and conservative methodologies for a PWR MSLB analysis using a coupled 3-d neutron-kinetics/thermal-hydraulic code. *Nuclear Technology*, 198, 2017.

[6] AIAA. Guide for the verification and validation of computational fluid dynamics simulations. *American Institute of Aeronautics and Astronautics*, AIAA-G-077-1998, 1998.

[7] ASME. Guide for verification and validation in computational solid mechanics. *American Society of Mechanical Engineers*, PTC 60/V&V 10, 2006.

[8] American national standard for validation of neutron transport methods for nuclear criticality safety calculations. *American Nuclear Society*, ANSI/ANS-8.24-2007, 2007.

[9] M. Salvatores et al. Methods and issues for the combined use of integral experiments and covariance data: Results of a NEA international collaborative study. *Nuclear Data Sheets*, 118, 2014.

[10] M. Salvatores et al. Uncertainty and target accuracy assessment for innovative systems using recent covariance data evaluations. Technical report, NEA/NSC/WPEC/-DOC(2008)6410, 2008.

[11] D.A. Brown et al. ENDF/B-VIII.0: The 8th major release of the nuclear reaction data library with CIELO-project cross sections, new standards and thermal scattering data. *Nuclear Data Sheets*, 148, 2018. Special Issue on Nuclear Reaction Data.

[12] G. Arbanas et al. Advancing inverse sensitivity/uncertainty methods for nuclear fuel cycle applications. *Nuclear Data Sheets*, 123, 2015.

[13] G. Palmiotti et al. Applications of integral benchmark data. *Nuclear Science and Engineering*, 178, 2014.

[14] G. Palmiotti and M. Salvatores. Use of integral experiments in the assessment of large liquid-metal fast breeder reactor basic design parameters. *Nuclear Science and Engineering*, 87, 1984.

[15] T. Sano and T. Takeda. Generalized bias factor method for accurate prediction of neutronics characteristics. *Journal of Nuclear Science and Technology*, 43(12), 2006.

[16] E. Alhassan et al. Combining Total Monte Carlo and benchmarks for nuclear data uncertainty propagation on a lead fast reactor's safety parameters. *Nuclear Data Sheets*, 118, 2014.

[17] H. Mitani and H. Kuroi. Adjustment of group cross sections by means of integral data, (I), (II). *Journal of Nuclear Science and Technology*, 9, 1972.

[18] J.B. Dragt et al. Methods of adjustment and error evaluation of neutron capture cross sections; application to fission product nuclides. *Nuclear Science and Engineering*, 62, 1977.

[19] A. Pazy et al. The role of integral data in neutron cross-section evaluation. *Nuclear Science and Engineering*, 55, 1974.

[20] R.N. Hwang. Topics in data adjustment theory and applications. *Argonne National Laboratory Report CONF-88091–28*, 1988.

[21] A. Gandini and Petilli. AMARA: A code using the Lagrange multipliers method for nuclear data adjustment. *CNEN-RI/FI(73)39, Comitato Nazionale Energia Nucleare*, 1973.

[22] H. Häggblom. Adjustment of neutron cross section data by a lest square fit of calculated quantities to experimental results. Part I theory. Technical report, Studsvik, 1971.

[23] V. Lamirand et al. Design of separated element reflector experiments in CROCUS: PETALE. In *Proceedings of the Sixteenth International Symposium on Reactor Dosimetry, Santa Fe, New Mexico, USA*, 2017.

[24] G. Palmiotti, M. Salvatores, and G. Aliberti. A-priori and a-posteriori covariance data in nuclear cross section adjustments. *Nuclear Data Sheets*, 123, 2015.

[25] E. Bauge and D. Rochman. Cross-observables and cross-isotopes correlations in nuclear data from integral constraints. *EPJ Nuclear Science and Technology*, 4, 2018.

[26] D. Rochman et al. Nuclear data correlation between different isotopes via integral information. *EPJ Nuclear Science and Technology*, 4, 2018.

[27] G. Palmiotti, M. Salvatores, and G. Aliberti. A-priori and a-posteriori covariance data in nuclear cross section adjustments: Issues and challenges. *Nuclear Data Sheets*, 123, 2015.

[28] M. Salvatores et al. Methods and issues for the combined use of integral experiments and covariance data. Technical report, NEA/NSC/WPEC/DOC(2013)445, 2013.

[29] B.L. Broadhead et al. Sensitivity and uncertainty analysis applied to criticality safety validation. Technical report, NUREG/CR-6655, Vol 1; ORNL/TM-13692/V1, 1999.

[30] A.J. Koning and D. Rochman. Towards sustainable nuclear energy: putting nuclear physics to work. *Annals of Nuclear Energy*, 35, 2008.

[31] D. Rochman et al. Propagation of nuclear data uncertainty: Exact or with covariances. *EPJ Web of Conferences*, 8, 2010.

[32] T. Watanabe et al. Cross section adjustment method based on random sampling technique. *Journal of Nuclear Science and Technology*, 51, 2014.

[33] A. Hoefer et al. MOCABA: A general Monte Carlo-Bayes procedure for improved predictions of integral functions of nuclear data. *Annals of Nuclear Energy*, 77, 2015.

[34] E. Castro et al. Improving PWR core simulations by Monte Carlo uncertainty analysis and Bayesian inference. *Annals of Nuclear Energy*, 95, 2016.

[35] E. Alhassan et al. On the use of integral experiments for uncertainty reduction of reactor macroscopic parameters within the TMC methodology. *Progress in Nuclear Energy*, 88, 2016.

[36] D. Rochman et al. How inelastic scattering stimulates nonlinear reactor core parameter behaviour. *Annals of Nuclear Energy*, 112, 2018.

[37] O. Leray et al. Methodology for core analyses with nuclear data uncertainty quantification and application to Swiss PWR operated cycles. *Annals of Nuclear Energy*, 110, 2017.

[38] K.-H. Schmidt et al. General Description of Fission Observables: GEF Model Code. *Nuclear Data Sheets*, 131, 2016.

[39] N. Silver. *The Signal and the Noise: Why So Many Predictions Fail-but Some Don't.* Penguin Publishing Group, 2012.

[40] D. Cacuci and M. Ionescu-Bujor. Best-estimate model calibration and prediction through experimental data assimilation – 1: Mathematical framework. *Nuclear Science and Engineering*, 165, 2010.

[41] S. Pelloni and D. Rochman. Cross-section adjustment in the fast energy range on the basis of an Asymptotic Progressing nuclear data Incremental Adjustment (APIA) methodology. *Annals of Nuclear Energy*, 115, 2018.

Bibliography

[42] A. Hoefer, O. Buss, and J. C. Neuber. How confident can we be in confidence intervals for the computational bias obtained with the generalized linear least squares methodology? - a toy model analysis. In *Proc. International Conference on Nuclear Criticality*, 2011.

[43] A. Hoefer et al. Applications of multivariate normal bayesian models in nuclear engineering. In *ANS Best Estimate Plus Uncertainty International Conference (BEPU 2018)*, 2018.

[44] Roberto Capote et al. A new formulation of the unified monte carlo approach (umc-b) and cross-section evaluation for the dosimetry reaction 55 mn(n,) 56 mn. *Journal of ASTM International*, 9, 2012.

[45] D. Rochman et al. Monte Carlo nuclear data adjustment via integral information. *EPJ Plus*, 133, 2018.

[46] E. Bauge, S. Hilaire, and P. Dossantos-Uzarralde. Evaluation of the covariance matrix of neutronic cross sections with the Backward-Forward Monte Carlo method. *International Conference on Nuclear Data for Science and Technology 2007*, 2007.

[47] A.J. Koning and D. Rochman. Modern nuclear data evaluation with the TALYS code system. *Nuclear Data Sheets*, 113, 2012.

[48] G. Welch, G. Bishop, et al. An introduction to the Kalman filter. 1995.

[49] M.S. Arulampalam et al. A tutorial on particle filters for online nonlinear/non-Gaussian Bayesian tracking. *IEEE Transactions on signal processing*, 50, 2002.

[50] International handbook of evaluated criticality safety benchmark experiments NEA-1486/16. 2019.

[51] International handbook of evaluated reactor physics benchmark experiments NEA/N-SC/DOC(2006)1. 2017.

[52] M. Salvatores. Nuclear and covariance data adjustment for nuclear data files improvement: new methods and approaches. In *Proceedings of ND2019, Beijing, China*, 2019.

[53] M. L. Williams et al. 6.6 TSURFER: An adjustment code to determine biases and uncertainties in nuclear system responses by consolidating differential data and benchmark integral experiments. *SCALE: A Comprehensive Modeling and Simulation Suite for Nuclear Safety Analysis and Design, ORNL/TM-2005/39, Version 6.1*, 2011.

[54] H. Sjöstrand, G. Schnabel, and P. Helgesson. Monte carlo integral adjustment of nuclear data libraries – experimental covariances and inconsistent data. In *Proceedings of WONDER2018, 2018, Aix–en–Provence, France*, 2018.

[55] P. Helgesson. *Approaching well-founded comprehensive nuclear data uncertainties : Fitting imperfect models to imperfect data*. PhD thesis, Uppsala University, Applied Nuclear Physics, 2018.

152

[56] G. Schnabel. Fitting and analysis technique for inconsistent data. In *Proceedings of M&C 2017, Jeju, South Korea*, 2017.

[57] O. Schwerer. EXFOR formats description for users (EXFOR basics). *Nuclear Data Section, IAEA*, 2008.

[58] A. Carlson et al. International evaluation of neutron cross section standards. *Nuclear Data Sheets*, 110, 2009.

[59] N. Larson. User's guide for sammy: Multilevel r-matrix fits to neutron data using bayes' equations. *ORNL*, 2008.

[60] M. Moxon, T. Ware, and C. Dean. REFIT-2009: A least-square fitting program for resonance analysis of neutron transmission, capture, fission and scattering data. 2010.

[61] ENDF-6 formats manual. *Brookhaven National Laboratory*, Technical Report, BNL-990365-2009, 2011.

[62] R.E. MacFarlane and A.C. Kahler. Methods for processing ENDF/B-VII with NJOY. *Nuclear Data Sheets*, 111, 2010.

[63] PREPRO 2017: 2017 ENDF/B pre-processing codes. Technical Report, IAEA-NDS-39 Rev. 17, 2017.

[64] D. Rochman et al. Nuclear data uncertainty propagation: Perturbation vs. Monte Carlo. *Annals of Nuclear Energy*, 38, 2011.

[65] A. Doucet and A. Johansen. A tutorial on particle filtering and smoothing: Fifteen years later. *Handbook of Nonlinear Filtering*, 12, 2011.

[66] S.C. Surace, A. Kutschireiter, and J.P. Pfister. How to avoid the curse of dimensionality: scalability of particle filters with and without importance weights. *arXiv preprint*, 1703.07879, 2017.

[67] D. Siefman et al. Sensitivity vs. stochastic data assimilation for nuclear data. *European Physics Journal Plus*, 130, 2018.

[68] M.B. Chadwick et al. ENDF/B-VII.1 nuclear data for science and technology: cross sections, covariances, fission product yields and decay data. *Nuclear Data Sheets*, 112, 2011.

[69] J. Leppänen et al. The Serpent Monte Carlo code: Status, development and applications in 2013. *Annals of Nuclear Energy*, 82, 2015.

[70] M. Aufiero et al. A collision history-based approach to sensitivity/perturbation calculations in the continuous energy Monte Carlo code SERPENT. *Annals of Nuclear Energy*, 85, 2015.

[71] D. Siefman et al. Convergence analysis and criterion for parameters estimated with sensitivities from Monte Carlo neutron transport codes. In *Proceedings of PHYSOR2018, Cancun, Mexico*, 2018.

[72] T. Zhu, A. Vasiliev, H. Ferroukhi, and A. Pautz. NUSS: A tool for propagating multigroup nuclear data covariances in pointwise ACE-formatted nuclear data using stochastic sampling method. *Annals of Nuclear Energy*, 75, 2015.

[73] B. Efron and R. Tibshirani. Bootstrap methods for standard errors, confidence intervals, and other measures of statistical accuracy. *Statistical Science*, 1, 1986.

[74] E. Lehmann and G. Casella. *Theory of Point Estimation*, volume 2. Springer-Verlag New York, 1998.

[75] M.F. Murphy et al. Reactivity and neutron emission measurements of highly burnt PWR fuel rod samples. *Annals of Nuclear Energy*, 33, 2006.

[76] P. Grimm et al. Analysis of reactivity worths of burnt PWR fuel samples measured in LWR-PROTEUS Phase II using a CASMO-5 reflected-assembly model. *Progress in Nuclear Energy*, 101, 2017.

[77] P. Grimm et al. CASMO-5 analysis of reactivity worths of burnt PWR fuel samples measured in LWR-PROTEUS Phase II. In *Proceedings of PHYSOR2016*, 2016.

[78] W. Wieselquist et al. PSI methodologies for nuclear data uncertainty propagation with CASMO-5M and MCNPX: Results for OECD/NEA UAM benchmark phase I. *Science and Technology of Nuclear Installations*, 2013.

[79] A. Aures et al. Benchmarking and application of the state-of-the-art uncertainty analysis methods XSUSA and SHARK-X. *Annals of Nuclear Energy*, 101, 2017.

[80] M. Hursin et al. Verification of the new implementations in SHARK-X for reactivity coefficients and relative reactivity worth UQ. In *Proceedings of PHYSOR2016*, 2016.

[81] M. Hursin et al. Representativity analysis of the LWR-PROTEUS Phase II experiments using SHARK-X stochastic sampling method. In *ANS Best Estimate Plus Uncertainty International Conference (BEPU 2018)*, 2018.

[82] M. Hursin et al. Determination of Sobol sensitivity indices for correlated inputs with SHARK-X. In *Proceedings of PHYSOR2018, Cancun, Mexico*, 2018.

[83] O. Leray et al. Nuclear data uncertainty propagation on spent fuel nuclide compositions. *Annals of Nuclear Energy*, 94, 2016.

[84] D. Siefman et al. Case study of data assimilation methods with the LWR-Proteus Phase II experimental campaign. In *Proceedings of M&C 2017, Jeju, South Korea*, 2017.

[85] D. Siefman et al. Uncertainty quantification of the LWR experiments at the PROTEUS research reactor using stochastic sampling. In *Proceedings of ANS Student Conference 2015, Texas, USA*, 2015.

[86] Proteus facility. https://www.psi.ch/en/erp/proteus. Accessed: 2019-06-05.

[87] J. Rhodes et al. CASMO-5, a Fuel Assembly Burnup Program: User's Manual Rev. 5. SSP-07/431, 2012.

[88] M. L. Williams and B. T. Rearden. SCALE-6 sensitivity/uncertainty methods and covariance data. *Nuclear Data Sheets*, 109, 2008.

[89] D. Siefman. Uncertainty quantification and representativity analysis of the LWR-PROTEUS Phase II experimental campaign. *EPFL*, Master's Thesis, 2015.

[90] A. Gandini, G. Palmiotti, and M. Salvatores. Equivalent generalized perturbation theory (EGPT). *Annals of Nuclear Energy*, 13, 1986.

[91] B. Rearden. Sensitivity and uncertainty enhancements in SCALE6.2. In *SG39 meeting of OECD/NEA's WPEC*, May 11, 2016.

[92] O. Leray et al. Nuclear data uncertainty propagation on spent fuel nuclide compositions. *Annals of Nuclear Energy*, 94, 2016.

[93] J. S. Martinez et al. Propagation of neutron cross section, fission yield, and decay data uncertainties in depletion calculations. *Nuclear Data Sheets*, 118, 2014.

[94] R. Macian, M.A. Zimmermann, and R. Chawla. Statistical uncertainty analysis applied to fuel depletion calculations. *Journal of Nuclear Science and Technology*, 44, 2007.

[95] R.W. Mills. Uncertainty propagation of fission product yield data in spent fuel inventory calculations. *Nuclear Data Sheets*, 118, 2014.

[96] H. Sjöstrand et al. Propagation of nuclear data uncertainties for ELECTRA burn-up calculations. *Nuclear Data Sheets*, 118, 2014.

[97] O. Leray et al. Uncertainty propagation of fission product yields to nuclide composition and decay heat for a PWR UO$_2$ fuel assembly. *Progress in Nuclear Energy*, 101, 2017.

[98] G. Ilas and H. Liljenfeldt. Decay heat uncertainty for BWR used fuel due to modeling and nuclear data uncertainties. *Nuclear Engineering and Design*, 319, 2017.

[99] J.J. Herrero et al. Impact of nuclear data uncertainty on safety calculations for spent nuclear fuel geological disposal. *EPJ Web Conf.*, 146, 2017.

[100] L. Fiorito et al. Generation of fission yield covariances to correct discrepancies in the nuclear data libraries. *Annals of Nuclear Energy*, 88, 2016.

Bibliography

[101] M.T. Pigni, M.W. Francis, and I.C. Gauld. Investigation of inconsistent ENDF/B-VII.1 independent and cumulative fission product yields with proposed revisions. *Nuclear Data Sheets*, 123, 2015.

[102] N. Terranova et al. Covariance generation and uncertainty propagation for thermal and fast neutron induced fission yields. *EPJ Web Conf.*, 146, 2017.

[103] N. Terranova et al. Fission yield covariance matrices for the main neutron-induced fissioning systems contained in the JEFF-3.1.1 library. *Annals of Nuclear Energy*, 109, 2017.

[104] D. Rochman et al. A Bayesian Monte Carlo method for fission yield covariance information. *Annals of Nuclear Energy*, 95, 2016.

[105] T. Frosio, T. Bonaccorsi, and P. Blaise. Extension of Bayesian inference for multi-experimental and coupled problem in neutronics - a revisit of the theoretical approach. *EPJ Nuclear Science Technology*, 4, 2018.

[106] A. Rizzo et al. Nuclear data adjustment based on the interpretation of post-irradiation experiments with the DARWIN2.3 package. *EPJ Nuclear Science Technology*, 4, 2018.

[107] J. Park et al. Uncertainty quantification of LWR-PROTEUS phase II experiments using CASMO-5. *Annals of Nuclear Energy*, 131, 2019.

[108] D. Boilley, E Suraud, Y. Abe, and S. Ayik. Nuclear fission with a Langevin equation. *Nuclear Physics A*, 556, 1993.

[109] A.J. Koning and D. Rochman. Modern nuclear data evaluation with the talys code system. *Nuclear Data Sheets*, 113(12), 2012. Special Issue on Nuclear Reaction Data.

[110] M. Herman et al. EMPIRE: Nuclear reaction model code system for data evaluation. *Nuclear Data Sheets*, 108, 2007. Special Issue on Evaluations of Neutron Cross Sections.

[111] K.-H. Schmidt and B. Jurado. Review on the progress in nuclear fission - experimental methods and theoretical descriptions. *Rep. Progr. Phys.*, 81, 2018.

[112] A. C. Wahl. Systematics of fission-product yields. *LANL Report*, LA-13928, 2002.

[113] R. W. Mills. M. A. Kellett, O. Bersillon. JEFF-3.1.1 radioactive decay data and fission yields sub-library. *JEFF Report 20, OECD NEA, Paris, France*, 2009.

[114] R.W. Mills. *Fission product yield evaluation.* PhD thesis, 1995.

[115] U. Brosa, S. Grossmann, and A. Muller. Nuclear scission. *Physics Reports*, 197(4), 1990.

[116] K.-H. Schmidt, B. Jurado, and C. Amouroux. General description of fission observables, JEFF-Report 24. *Nuclear Energy Agency Data Bank*, NEA/DB/DOC(2014)1, 2014.

[117] C. Schmitt, K.-H. Schmidt, and B. Jurado. Benchmark of the GEF code for fission-fragment yields over an enlarged range in fissioning nucleus mass, excitation energy, and angular momentum. *Phys. Rev. C*, 98, 2018.

[118] K.-H. Schmidt. MATCH: A computer code for matching the information from incomplete experimental data and a model calculation. http://www.khs-erzhausen.de/Work_space.html#MATCH. Accessed: 2019-05-30.

[119] E. Gadioli and P. E. Hodgson. *Pre-Equilibrium Nuclear Reactions*. Oxford University Press, Oxford, UK, 1992.

[120] K. Kern. *Advanced Treatment of Fission Yield Effects and Method Development for Improved Reactor Depletion Calculations*. PhD thesis, Karlsruher Institut fur Technologie (KIT), 2018.

[121] K.-H. Schmidt. GEF2017/1.1: General description of fission observables. released September 24, 2017. http://www.khs-erzhausen.de/GEF-2017-1-1.html. Accessed: 2019-05-30.

[122] K.-H. Schmidt. Personal Communication. 2019-28-05.

[123] P. Grimm et al. Analysis of reactivity worths of burnt PWR fuel samples measured in LWR-PROTEUS Phase II using a CASMO-5 reflected-assembly model. *Progress in Nuclear Energy*, 101, 2017.

[124] S.S. Shapiro and M.B. Wilk. An analysis of variance test for normality (complete samples). *Biometrika*, 52, 1965.

[125] F. Michel-Sendis et al. A new OECD/NEA database of nuclide compositions of spent nuclear fuel. In *Proceedings of the PHYSOR 2014 International Conference, Kyoto, Japan*, 2014.

[126] F. Michel-Sendis et al. SFCOMPO-2.0: An OECD NEA database of spent nuclear fuel isotopic assays, reactor design specifications, and operating data. *Annals of Nuclear Energy*, 110, 2017.

[127] I.C. Gauld et al. Integral nuclear data validation using experimental spent nuclear fuel compositions. *Nuclear Engineering and Technology*, 49, 2017.

[128] B.C. Kiedrowski and F.B. Brown. Adjoint-based k-eigenvalue sensitivity coefficients to nuclear data using continuous-energy Monte Carlo. *Nuclear Science and Engineering*, 174, 2013.

[129] C.M. Perfetti and B.T. Rearden. Development of a Generalized Perturbation Theory Method for Sensitivity Analysis using continuous-energy Monte Carlo methods. *Nuclear Science and Engineering*, 182, 2016.

Bibliography

[130] M. Herman et al. COMMARA-2.0 neutron cross section covariance library. *U.S. Department of Energy*, BNL-94830-2011, 2011.

[131] M.B. Chadwick et al. ENDF/B-VII.0: Next generation evaluated nuclear data library for nuclear science and technology. *Nuclear Data Sheets*, 107, 2006.

[132] G. Rimpault et al. The ERANOS data and code system for fast reactor neutronic analyses. In *Proceedings of PHYSOR 2002, Seoul, South Korea*, 2002.

[133] A. Gandini. A generalized perturbation method for bi-linear functionals of the real and adjoint neutron fluxes. *Journal of Nuclear Energy*, 21, 1967.

[134] Y. Nagaya et al. Evaluation of sensitivity coefficients of effective multiplication factor with respect to prompt fission neutron spectrum. *Nuclear Instruments and Methods in Physics Research A*, 603, 2009.

[135] G.E.P. Box. Robustness in the strategy of scientific model building. In *Robustness in Statistics*. Academic Press, 1979.

[136] R. Liesenfeld and J.F. Richard. Monte Carlo methods and Bayesian computation: Importance sampling. In *International Encyclopedia of the Social Behavioral Sciences (Second Edition)*. Elsevier, Oxford, second edition, 2015.

[137] S. Brooks et al. *Handbook of Markov Chain Monte Carlo.* Chapman & Hall/CRC Handbooks of Modern Statistical Methods. CRC Press, 2011.

[138] D. Siefman et al. Full core modeling techniques for research reactors with irregular geometries using Serpent and PARCS applied to the CROCUS reactor. *Annals of Nuclear Energy*, 85, 2015.

[139] A. Rais et al. Methods and models for the coupled neutronics and thermal-hydraulics analysis of the CROCUS Reactor at EFPL. *Science and Technology of Nuclear Installations*, 2015, 2015.

[140] A. Rais et al. Neutronics modeling of the CROCUS reactor with SERPENT and PARCS codes. In *Proceedings of M&C 2017, Jeju, South Korea*, 2017.

[141] M. Hursin et al. Verification of a reactor physics calculation scheme for the Crocus reactor. In *Proceedings of 3rd International Technical Meeting on Small Reactors, Ottawa, Canada*, 2014.

[142] A. Rais et al. PARCS Few-group Homogenized Parameters Generation using Serpent Monte Carlo code at the CROCUS Reactor. In *IGORR 2014: International Group on Research Reactors, Argentina*, 2014.

A Supplementary Information

A.1 Derivation of Generalized Linear Least Squares

This derivation is adapted from Refs. [40, 29]. The notation has been adapted and clarifications have been added that are meant to make the derivation easier to follow. In Ref. [40] the equations are derived with Bayes' theorem and in Ref. [29] they are derived with linear regression theory. Both derivations yield the same set of equations. The Bayesian approach is used here to allow it to be easily compared to other DA methods.

There are benchmark integral parameters, $\mathbf{E}$, that are represented as a vector, $\mathbf{E} = \{E_i | i = 1, \cdots, N_E\}$, where N_E is the number of integral parameters. The vector has a corresponding covariance matrix, $\mathbf{M_E} = \langle \Delta\mathbf{E}\Delta\mathbf{E}^T \rangle$[1] whose size is $N_E \times N_E$. These same integral parameters have calculated values represented by the vector $\mathbf{C} = \{C_i | i = 1, \cdots, N_E\}$, which is a function of $\boldsymbol{\sigma}$. The vector has the corresponding covariance matrix $\mathbf{M_C} = \langle \Delta\mathbf{C}\Delta\mathbf{C}^T \rangle$. There is also a vector of nuclear data $\boldsymbol{\sigma} = \{\sigma_i | i = 1, \cdots, N_\sigma\}$, where N_σ is the number of nuclear data. It has the covariance matrix $\mathbf{M}_\sigma = \langle \Delta\boldsymbol{\sigma}\Delta\boldsymbol{\sigma}^T \rangle$ whose size is $N_\sigma \times N_\sigma$.

With these terminology, we can construct Bayes' theorem for updating $\boldsymbol{\sigma}$ with $\mathbf{E}$ in Eq. (A.1). The prior is $p(\boldsymbol{\sigma}, \text{model})$ and is assumed to be a multivariate normal distribution as in Eq. (A.2). The prior and the neutronics model together lead to the likelihood function, $\mathscr{L}(\mathbf{E}|\boldsymbol{\sigma}, \text{model})$, which is also assumed to be a multivariate normal distribution as in Eq. (A.3). It conceptually describes the likelihood of obtaining $\mathbf{E}$ given $\boldsymbol{\sigma}$ and the neutron transport code. Finally, the posterior is the PDF $p(\boldsymbol{\sigma}'|\mathbf{E}, \text{model})$.

$$p(\boldsymbol{\sigma}'|\mathbf{E},\text{model}) \propto \mathscr{L}(\mathbf{E}|\boldsymbol{\sigma},\text{model})\,p(\boldsymbol{\sigma}) \tag{A.1}$$

---

[1] The symbol $\langle \cdot \rangle$ denotes the expected value of some random variable. The mean of random variable x would be $\langle x \rangle = \int_\infty p(x)x\,dx$, where $p(x)$ is the PDF of x. The symbol Δ represents possible deviations from the mean value, or $x - \langle x \rangle$. Therefore, $\langle \Delta x \Delta x \rangle = \int_\infty (x - \langle x \rangle)(x - \langle x \rangle)p(x)\,dx$.

$$p(\boldsymbol{\sigma}|\boldsymbol{\sigma}_0, \mathbf{M}_\sigma) = (2\pi)^{-N_\sigma/2} \det(\mathbf{M}_\sigma)^{-1/2} \cdot \exp\left[-\frac{1}{2} \Delta\boldsymbol{\sigma}^T \mathbf{M}_\sigma^{-1} \Delta\boldsymbol{\sigma} \right] \tag{A.2}$$

$$\mathscr{L}(\mathbf{E}|\boldsymbol{\sigma}, \text{model}) = (2\pi)^{-N_E/2} \det(\mathbf{M_E})^{-1/2} \cdot \exp\left[-\frac{1}{2} \big(\mathbf{E} - \mathbf{C}(\boldsymbol{\sigma})\big)^T \mathbf{M_E}^{-1} \big(\mathbf{E} - \mathbf{C}(\boldsymbol{\sigma})\big) \right] \tag{A.3}$$

The posterior can then be written as Eq. (A.4), which after taking the negative logarithm of both sides becomes Eq. (A.5). From here, we can apply MAP and calculate the moments of the posterior distribution. We will not do this yet, because we want to take the derivation a step further. We want to take into account possible correlations between $\mathbf{E}$ and $\boldsymbol{\sigma}$

$$p(\boldsymbol{\sigma}'|\mathbf{E}) \propto \exp\left[-\frac{1}{2} \big(\mathbf{E} - \mathbf{C}(\boldsymbol{\sigma})\big)^T \mathbf{M_E}^{-1} \big(\mathbf{E} - \mathbf{C}(\boldsymbol{\sigma})\big) \right] \cdot \exp\left[-\frac{1}{2} (\boldsymbol{\sigma} - \boldsymbol{\sigma}_0)^T \mathbf{M}_\sigma^{-1} (\boldsymbol{\sigma} - \boldsymbol{\sigma}_0) \right] \tag{A.4}$$

$$(\boldsymbol{\sigma}' - \boldsymbol{\sigma}_0')^T \mathbf{M}_\sigma'^{-1} (\boldsymbol{\sigma}' - \boldsymbol{\sigma}_0') \propto \big(\mathbf{E} - \mathbf{C}(\boldsymbol{\sigma})\big)^T \mathbf{M_E}^{-1} \big(\mathbf{E} - \mathbf{C}(\boldsymbol{\sigma})\big) + (\boldsymbol{\sigma} - \boldsymbol{\sigma}_0)^T \mathbf{M}_\sigma^{-1} (\boldsymbol{\sigma} - \boldsymbol{\sigma}_0) \tag{A.5}$$

Indeed, it is possible for the integral data to be correlated to the nuclear data, although this is often ignored in practical applications of DA. The nuclear data evaluators may have, in an *ad hoc* way, already tuned the performance of a nuclear data library to common integral benchmarks like JEZEBEL or FLATTOP. The correlation may also be induced inversely where the evaluated nuclear data were somehow used in the experimental procedure, for example as a normalization coefficient. In this text, we assume that this is the case in order to have the most complete derivation as possible.

The covariances between $\boldsymbol{\sigma}$ and $\mathbf{E}$ are given by the $N_\sigma \times N_E$ sized matrix $\mathbf{M}_{\sigma,\mathbf{E}} = \langle \Delta\boldsymbol{\sigma}\Delta\mathbf{E}^T \rangle$ and by the $N_E \times N_\sigma$ sized matrix $\mathbf{M}_{\mathbf{E},\sigma} = \langle \Delta\mathbf{E}\Delta\boldsymbol{\sigma}^T \rangle$. Here, $\mathbf{M}_{\sigma,\mathbf{E}} = \mathbf{M}_{\mathbf{E},\sigma}{}^T$. It should be noted that these are not true variance-covariance matrices as they are not square and the main diagonals do not contain variance terms, but rather covariance terms.

We perform a first-order linear approximation $\mathbf{C}(\boldsymbol{\sigma})$ with sensitivity coefficients, $\mathbf{S}$, are the first derivatives of $\mathbf{C}(\boldsymbol{\sigma})$, $\partial\mathbf{C}/\partial\boldsymbol{\sigma}$, evaluated at $\boldsymbol{\sigma}_0$ or the nominal nuclear data mean values. $\mathbf{S}$ is a matrix of dimensions $N_E \times N_\sigma$. This then allows to approximate $\mathbf{M_C}$ with Eq. (A.7). This reflects the propagation of $\mathbf{M}_\sigma$ through $\mathbf{C}(\boldsymbol{\sigma})$.

$$\mathbf{C}(\boldsymbol{\sigma}) \approx \mathbf{C}(\boldsymbol{\sigma}_0) + \mathbf{S}\Delta\boldsymbol{\sigma} \tag{A.6}$$

$$\mathbf{M_C} = \mathbf{S}\mathbf{M}_\sigma \mathbf{S}^T \tag{A.7}$$

We can then define a discrepancy vector as $\mathbf{d}$ and its covariance matrix, $\mathbf{M_d}$, that will help to simplify later equations.

$$\mathbf{d} = \mathbf{C}(\boldsymbol{\sigma}) - \mathbf{E} = \mathbf{C}(\boldsymbol{\sigma}_0) + \mathbf{S}\Delta\boldsymbol{\sigma} - \mathbf{E} \tag{A.8}$$

$$
\begin{aligned}
\mathbf{M_d} &= \left\langle \Delta(\mathbf{C}-\mathbf{E}) - \Delta(\mathbf{C}-\mathbf{E})^T \right\rangle \\
&= \left\langle \Delta\mathbf{C}\Delta\mathbf{C}^T \right\rangle + \left\langle \Delta\mathbf{E}\Delta\mathbf{E}^T \right\rangle - \left\langle \Delta\mathbf{C}\Delta\mathbf{E}^T \right\rangle - \left\langle \Delta\mathbf{E}\Delta\mathbf{C}^T \right\rangle \\
&= \mathbf{M_C} + \mathbf{M_E} - \mathbf{M_{C,E}} - \mathbf{M_{E,C}} \\
&= \mathbf{S}\mathbf{M}_\sigma\mathbf{S}^T + \mathbf{M_E} - \mathbf{S}\mathbf{M}_{\sigma,\mathbf{E}} - \mathbf{M}_{\mathbf{E},\sigma}{}^T\mathbf{S}
\end{aligned}
\tag{A.9}
$$

Where $\left\langle \Delta\mathbf{C}\Delta\mathbf{E}^T \right\rangle = \mathbf{S}\mathbf{M}_{\sigma,\mathbf{E}}$ through the math outlined in Eq. (A.54).

$$
\begin{aligned}
\left\langle \Delta\mathbf{C}\Delta\mathbf{E}^T \right\rangle &= \left\langle \left(\mathbf{C}(\boldsymbol{\sigma}) - \mathbf{C}(\boldsymbol{\sigma}_0) \right)(\mathbf{E}-\mathbf{E}_0)^T \right\rangle \\
&= \left\langle \left(\mathbf{C}(\boldsymbol{\sigma}_0) + \mathbf{S}(\boldsymbol{\sigma}-\boldsymbol{\sigma}_0) - \mathbf{C}(\boldsymbol{\sigma}_0) \right)(\mathbf{E}-\mathbf{E}_0)^T \right\rangle \\
&= \left\langle \mathbf{S}(\boldsymbol{\sigma}-\boldsymbol{\sigma}_0)(\mathbf{E}-\mathbf{E}_0)^T \right\rangle = \mathbf{S}\left\langle (\boldsymbol{\sigma}-\boldsymbol{\sigma}_0)(\mathbf{E}-\mathbf{E}_0)^T \right\rangle \\
&= \mathbf{S}\left\langle \Delta\boldsymbol{\sigma} - \Delta\mathbf{E}^T \right\rangle = \mathbf{S}\mathbf{M}_{\sigma,\mathbf{E}}
\end{aligned}
\tag{A.10}
$$

With Bayes' formula defined and all possible correlations taken in to account, we can maximize the *a posteriori* distribution. This maximization is classically done with Lagrangian multipliers as the mathematical objective can be interpreted as a constrained optimization problem. The constraint that we impose is that $\mathbf{E} = \mathbf{C}'(\boldsymbol{\sigma}')$, or $\mathbf{C}'(\boldsymbol{\sigma}') - \mathbf{E} = 0$. This is equivalent to forcing $\boldsymbol{\sigma}'$ to be consistent with $\mathbf{E}$ within the constraints of linearity. For simplicity, the adjustments will be defined as $\mathbf{x} = \boldsymbol{\sigma}' - \boldsymbol{\sigma}$ and $\mathbf{y} = \mathbf{C}' - \mathbf{E}$. With the linear constraint, $\mathbf{y}$ can then be rewritten,

$$
\begin{aligned}
\mathbf{C}'(\boldsymbol{\sigma}') &= \mathbf{C}(\boldsymbol{\sigma}_0) + \mathbf{S}\mathbf{x} \\
\mathbf{C}'(\boldsymbol{\sigma}') - \mathbf{E} &= \mathbf{C}(\boldsymbol{\sigma}_0) - \mathbf{E} + \mathbf{S}\mathbf{x} = 0 \\
\mathbf{y} &= \mathbf{d} + \mathbf{S}\mathbf{x} = 0
\end{aligned}
\tag{A.11}
$$

Now, the function that is to be maximized can be defined as

$$p\left(\begin{bmatrix} \mathbf{y} \\ \mathbf{x} \end{bmatrix} \middle| \mathbf{M} \right) = (2\pi)^{-(N_E+N_\sigma)/2}\det(\mathbf{M})^{-1/2} \cdot \exp\left[-\frac{1}{2}\mathbf{Q} \right] \tag{A.12}$$

Appendix A. Supplementary Information

Where,

$$\mathbf{M} = \begin{bmatrix} \mathbf{M_E} & \mathbf{M_{E,\sigma}} \\ \mathbf{M_{\sigma,E}} & \mathbf{M_\sigma} \end{bmatrix} \tag{A.13}$$

$$\mathbf{Q} = \begin{bmatrix} \mathbf{y} \\ \mathbf{x} \end{bmatrix}^T \mathbf{M}^{-1} \begin{bmatrix} \mathbf{y} \\ \mathbf{x} \end{bmatrix} \tag{A.14}$$

Eq. (A.14) can be reformulated using Lagrangian multipliers, $\boldsymbol{\lambda}$, in Eq. (A.15) so that $\mathbf{x}$ and $\mathbf{y}$ satisfy Eq. (A.16), where ∇ denotes the gradient. This is effectively taking the derivative of $\mathbf{R}(\mathbf{x}, \mathbf{y})$ with respect to $\mathbf{x}$ and $\mathbf{y}$ and setting it equal to zero.

$$\mathbf{R}(\mathbf{x}, \mathbf{y}) = \mathbf{Q} + 2\boldsymbol{\lambda}^T \mathbf{Sx} - \mathbf{y} \tag{A.15}$$

$$\nabla_{\mathbf{x}} \mathbf{R}(\mathbf{x}, \mathbf{y}) = \nabla_{\mathbf{y}} \mathbf{R}(\mathbf{x}, \mathbf{y}) = \mathbf{0} \tag{A.16}$$

The matrix $\mathbf{M}$ can be inverted with the following relation, where $\mathbf{A} = \mathbf{M_\sigma} - \mathbf{M_{\sigma,E}} \mathbf{M_E}^{-1} \mathbf{M_{E,\sigma}}$.

$$\mathbf{M}^{-1} = \begin{bmatrix} \mathbf{M_E} & \mathbf{M_{E,\sigma}} \\ \mathbf{M_{\sigma,E}} & \mathbf{M_\sigma} \end{bmatrix}^{-1} = \begin{bmatrix} \mathbf{M_E}^{-1} + \mathbf{M_E}^{-1} \mathbf{M_{E,\sigma}} \mathbf{A}^{-1} \mathbf{M_{\sigma,E}} \mathbf{M_E}^{-1} & -\mathbf{M_E}^{-1} \mathbf{M_{E,\sigma}} \mathbf{A}^{-1} \\ -\mathbf{A}^{-1} \mathbf{M_{\sigma,E}} \mathbf{M_E}^{-1} & \mathbf{A}^{-1} \end{bmatrix} \tag{A.17}$$

Eq. (A.15) then becomes,

$$\begin{aligned} \mathbf{R}(\mathbf{x}, \mathbf{y}) = &\mathbf{y}^T \left[\mathbf{M_E}^{-1} + \mathbf{M_E}^{-1} \mathbf{M_{E,\sigma}} \mathbf{A}^{-1} \mathbf{M_{\sigma,E}} \mathbf{M_E}^{-1} \right] \mathbf{y} - \mathbf{y}^T \left[\mathbf{A}^{-1} \mathbf{M_{\sigma,E}} \mathbf{M_E}^{-1} \right] \mathbf{y} \\ &- \mathbf{y}^T \left[\mathbf{M_E}^{-1} \mathbf{M_{E,\sigma}} \mathbf{A}^{-1} \right] \mathbf{x} + \mathbf{x}^T \mathbf{A}^{-1} \mathbf{x} + 2\boldsymbol{\lambda}^T (\mathbf{Sx} - \mathbf{y}) \end{aligned} \tag{A.18}$$

Eq. (A.16) can then be re-written as Eq. (A.19) and Eq. (A.20). The unit and zero vectors $\mathbf{1}$ and $\mathbf{0}$ and have dimensions of $N_\sigma \times 1$ in Eq. (A.19) and $N_E \times 1$ in Eq. (A.20).

$$\begin{aligned} \nabla_{\mathbf{x}} \mathbf{R}(\mathbf{x}, \mathbf{y}) &= \mathbf{0} \\ &= -\mathbf{1}^T \left[\mathbf{A}^{-1} \mathbf{M_{\sigma,E}} \mathbf{M_E}^{-1} \right] \mathbf{y} - \mathbf{y}^T \left[\mathbf{M_E}^{-1} \mathbf{M_{E,\sigma}} \mathbf{A}^{-1} \right] \mathbf{1} \\ &\quad + \mathbf{1}^T \mathbf{A}^{-1} \mathbf{x} + \mathbf{x} \mathbf{A}^{-1} \mathbf{1} + 2\boldsymbol{\lambda}^T \mathbf{S1} \end{aligned} \tag{A.19}$$

$$\nabla_{\mathbf{y}}\mathbf{R}(\mathbf{x},\mathbf{y}) = \mathbf{0}$$
$$= \mathbf{1}^{T}\left[\mathbf{M_E}^{-1} + \mathbf{M_E}^{-1}\mathbf{M}_{\mathbf{E},\sigma}\mathbf{A}^{-1}\mathbf{M}_{\sigma,\mathbf{E}}\mathbf{M_E}^{-1}\right]\mathbf{y}$$
$$+ \mathbf{x}\left[\mathbf{M_E}^{-1} + \mathbf{M_E}^{-1}\mathbf{M}_{\mathbf{E},\sigma}\mathbf{A}^{-1}\mathbf{M}_{\sigma,\mathbf{E}}\mathbf{M_E}^{-1}\right]\mathbf{1}$$
$$- \mathbf{x}^{T}\left[\mathbf{A}^{-1}\mathbf{M}_{\sigma,\mathbf{E}}\mathbf{M_E}^{-1}\right]\mathbf{1} - \mathbf{1}^{T}\left[\mathbf{M_E}^{-1}\mathbf{M}_{\mathbf{E},\sigma}\mathbf{A}^{-1}\right]\mathbf{x} - 2\boldsymbol{\lambda}^{T}\mathbf{S}\mathbf{1} \tag{A.20}$$

With some linear algebra, the equations can be simplified further by knowing that the term $\mathbf{A}^{-1}$ is symmetric and the transpose of a scalar and a scalar are equal. The terms then add together, and after dividing by 2 gives,

$$\mathbf{S}^{T}\boldsymbol{\lambda} + \mathbf{A}^{-1}\mathbf{x} - \mathbf{A}^{-1}\mathbf{M}_{\sigma,\mathbf{E}}\mathbf{M_E}^{-1}\mathbf{y} = 0 \tag{A.21}$$

$$-\boldsymbol{\lambda} + \left[\mathbf{M_E}^{-1} + \mathbf{M_E}^{-1}\mathbf{M}_{\mathbf{E},\sigma}\mathbf{A}^{-1}\mathbf{M}_{\sigma,\mathbf{E}}\mathbf{M_E}^{-1}\right]\mathbf{y} + \left[\mathbf{M_E}^{-1}\mathbf{M}_{\mathbf{E},\sigma}\mathbf{A}^{-1}\right]\mathbf{x} = \mathbf{0} \tag{A.22}$$

Solving for $\mathbf{x}$ and $\mathbf{y}$ gives

$$\mathbf{x} = \left[\mathbf{M}_{\sigma,\mathbf{E}} - \mathbf{M}_{\sigma}\mathbf{S}^{T}\right]\boldsymbol{\lambda} \tag{A.23}$$

$$\mathbf{y} = \left[\mathbf{M_E} - \mathbf{M}_{\mathbf{E},\sigma}\mathbf{S^T}\right]\boldsymbol{\lambda} \tag{A.24}$$

Taking these values of $\mathbf{x}$ and $\mathbf{y}$ and substituting them into Eq. (A.11) gives the Lagrangian multipliers and their covariance matrix, $\mathbf{M}_{\lambda}$.

$$\boldsymbol{\lambda} = \mathbf{M_d}^{-1}\mathbf{d} \tag{A.25}$$

$$\mathbf{M}_{\lambda} = \left\langle\Delta\boldsymbol{\lambda}\Delta\boldsymbol{\lambda}^{T}\right\rangle = \mathbf{M_d}^{-1}\left\langle\Delta\mathbf{d}\Delta\mathbf{d}^{T}\right\rangle\mathbf{M_d}^{-1} = \mathbf{M_d}^{-1} \tag{A.26}$$

Eq. (A.25) can then be put into the definition of $\mathbf{x}$ in Eq. (A.23) to find the posterior nuclear data, $\boldsymbol{\sigma}'$, as shown in Eq. (A.27). When ignoring $\mathbf{M}_{\sigma,\mathbf{E}}$, this simplifies down to Eq. (A.28). This is slightly different than Eq. (2.17). The difference is the $\mathbf{C} - \mathbf{E}$ term, which causes a minus

instead of a plus to appear before the $\mathbf{M}_\sigma \mathbf{S}^T$ term.

$$\boldsymbol{\sigma}' = \boldsymbol{\sigma} + \left[\mathbf{M}_{\sigma,\mathbf{E}} - \mathbf{M}_\sigma \mathbf{S}^T\right]\mathbf{M_d}^{-1}\mathbf{d} \tag{A.27}$$

$$\boldsymbol{\sigma}' = \boldsymbol{\sigma} - \mathbf{M}_\sigma \mathbf{S}^T\left[\mathbf{S}\mathbf{M}_\sigma \mathbf{S}^T + \mathbf{M_E}\right]^{-1}\left[\mathbf{C} - \mathbf{E}\right] \tag{A.28}$$

We now have a best-estimate for the true value of the integral parameter, $\mathbf{T}$, that takes into account the information contained in $\mathbf{E}$ and $\mathbf{C}$. Practically, $\mathbf{T}$ is not used and we are more interested in what effect $\boldsymbol{\sigma}'$ has on $\mathbf{C}$. This preserves the role of the computational model.

$$\mathbf{T}(\boldsymbol{\sigma}') = \mathbf{E} + \left[\mathbf{M_E} - \mathbf{M}_{\mathbf{E},\sigma}\mathbf{S^T}\right]\mathbf{M_d}^{-1}\mathbf{d} \tag{A.29}$$

A posterior set of calculated values, $\mathbf{C}'$, can be calculated using the linearization of Eq. (A.6), which is the most often used formulation. It is evident that $\mathbf{C}'(\boldsymbol{\sigma}') \neq \mathbf{T}(\boldsymbol{\sigma}')$ because when $\mathbf{S}$ is calculated with $\boldsymbol{\sigma}'$ is not equal to $\mathbf{S}$ when calculated with $\boldsymbol{\sigma}$, unless the model is perfectly linear and free of numerical errors.

$$\mathbf{C}'(\boldsymbol{\sigma}') = \mathbf{C}(\boldsymbol{\sigma}_0) + \mathbf{Sx} = \mathbf{C}(\boldsymbol{\sigma}_0) + \mathbf{S}(\boldsymbol{\sigma}' - \boldsymbol{\sigma}_0) \tag{A.30}$$

The posterior covariance matrix of the adjusted nuclear data, $\mathbf{M}'_\sigma$, is found from

$$\begin{aligned}\mathbf{M}'_\sigma &= \left\langle \Delta\boldsymbol{\sigma}'\Delta\boldsymbol{\sigma}'^T \right\rangle \\ &= \mathbf{M}_\sigma + \left[\mathbf{M}_{\sigma,\mathbf{E}} - \mathbf{M}_\sigma \mathbf{S}^T\right]\mathbf{M_d}^{-1}\left\langle \Delta\mathbf{d}\Delta\mathbf{d}^T \right\rangle\mathbf{M_d}^{-1}\left[\mathbf{M}_{\mathbf{E},\sigma} - \mathbf{S}\mathbf{M}_\sigma\right] \\ &\quad + \left[\mathbf{M}_{\sigma,\mathbf{E}} - \mathbf{M}_\sigma \mathbf{S}^T\right]\mathbf{M_d}^{-1}\left\langle \Delta\mathbf{d}\Delta\boldsymbol{\sigma}^T \right\rangle + \left\langle \Delta\boldsymbol{\sigma}\Delta\mathbf{d}^T \right\rangle\mathbf{M_d}^{-1}\left[\mathbf{M}_{\sigma,\mathbf{E}} - \mathbf{M}_\sigma \mathbf{S}^T\right]\end{aligned} \tag{A.31}$$

Given the following relation for $\left\langle \Delta\mathbf{d}\Delta\boldsymbol{\sigma}'^T \right\rangle$

$$\left\langle \Delta\mathbf{d}\Delta\boldsymbol{\sigma}'^T \right\rangle = \left\langle \Delta(\mathbf{C} - \mathbf{E})\Delta\boldsymbol{\sigma}^T \right\rangle = \mathbf{S}\left\langle \Delta\boldsymbol{\sigma}\Delta\boldsymbol{\sigma}^T \right\rangle - \left\langle \Delta\mathbf{E}\Delta\boldsymbol{\sigma}^T \right\rangle = \mathbf{S}\mathbf{M}_\sigma - \mathbf{M}_{\mathbf{E},\sigma} \tag{A.32}$$

$\mathbf{M}'_\sigma$ can then be found to be

$$\begin{aligned}\mathbf{M}'_\sigma &= \mathbf{M}_\sigma + \left[\mathbf{M}_{\sigma,\mathbf{E}} - \mathbf{M}_\sigma \mathbf{S}^T\right]\mathbf{M_d}^{-1}\left[\mathbf{M}_{\mathbf{E},\sigma} - \mathbf{S}\mathbf{M}_\sigma\right] - 2\left[\mathbf{M}_{\sigma,\mathbf{E}} - \mathbf{M}_\sigma \mathbf{S}^T\right]\mathbf{M_d}^{-1}\left[\mathbf{M}_{\sigma,\mathbf{E}} - \mathbf{M}_\sigma \mathbf{S}^T\right] \\ &= \mathbf{M}_\sigma - \left[\mathbf{M}_{\sigma,\mathbf{E}} - \mathbf{M}_\sigma \mathbf{S}^T\right]\mathbf{M_d}^{-1}\left[\mathbf{M}_{\mathbf{E},\sigma} - \mathbf{S}\mathbf{M}_\sigma\right]\end{aligned} \tag{A.33}$$

In the most common case where $\mathbf{M}_{\sigma,\mathbf{E}} = \mathbf{0}$ or it is ignored, $\mathbf{M}'_\sigma$ can be written as,

$$\mathbf{M}'_\sigma = \mathbf{M}_\sigma - \mathbf{M}_\sigma \mathbf{S}^T \left[\mathbf{S}\mathbf{M}_\sigma \mathbf{S}^T + \mathbf{M_E}\right]^{-1} \mathbf{S}\mathbf{M}_\sigma \tag{A.34}$$

The covariance matrix of $\mathbf{T}$, or $\mathbf{M_T}$, can also be estimated,

$$\begin{aligned}
\mathbf{M_T} &= \left\langle \Delta\mathbf{T}\Delta\mathbf{T}^T \right\rangle \\
&= \mathbf{M_E} + \left[\mathbf{M_E} - \mathbf{M}_{\mathbf{E},\sigma}\mathbf{S}^T\right]\mathbf{M_d}^{-1}\left\langle \Delta\mathbf{d}\Delta\mathbf{d}^T \right\rangle \mathbf{M_d}^{-1}\left[\mathbf{M_E} - \mathbf{S}\mathbf{M}_{\sigma,\mathbf{E}}\right] \\
&\quad + \left[\mathbf{M_E} - \mathbf{M}_{\mathbf{E},\sigma}\mathbf{S}^T\right]\mathbf{M_d}^{-1}\left\langle \Delta\mathbf{d}\Delta\mathbf{E}^T \right\rangle + \left\langle \Delta\mathbf{E}\Delta\mathbf{d}^T \right\rangle \mathbf{M_d}^{-1}\left[\mathbf{M_E} - \mathbf{S}\mathbf{M}_{\sigma,\mathbf{E}}\right]
\end{aligned} \tag{A.35}$$

Where

$$\left\langle \Delta\mathbf{d}\Delta\mathbf{E}^T \right\rangle = \left\langle \Delta(\mathbf{C} - \mathbf{E})\Delta\mathbf{E}^T \right\rangle = \mathbf{S}\left\langle \Delta\boldsymbol{\sigma}\Delta\mathbf{E}^T \right\rangle - \left\langle \Delta\mathbf{E}\Delta\mathbf{E}^T \right\rangle = \mathbf{S}\mathbf{M}_{\sigma,\mathbf{E}} - \mathbf{M_E} \tag{A.36}$$

And finally giving

$$\mathbf{M_T} = \mathbf{M_E} - \left[\mathbf{M_E} - \mathbf{M}_{\mathbf{E},\sigma}\mathbf{S}^T\right]\mathbf{M_d}^{-1}\left[\mathbf{M_E} - \mathbf{S}\mathbf{M}_{\sigma,\mathbf{E}}\right] \tag{A.37}$$

The covariances between the integral and nuclear data can be adjusted with

$$\begin{aligned}
\mathbf{M}'_{\sigma,\mathbf{E}} &= \left\langle \Delta\boldsymbol{\sigma}'\Delta\mathbf{E}'^T \right\rangle \\
&= \mathbf{M}_{\sigma,\mathbf{E}} - \left[\mathbf{M}_{\sigma,\mathbf{E}} - \mathbf{M}_\sigma\mathbf{S}^T\right]\mathbf{M_d}^{-1}\left\langle \Delta\mathbf{d}\Delta\mathbf{d}^T \right\rangle \mathbf{M_d}^{-1}\left[\mathbf{M_E} - \mathbf{S}\mathbf{M}_{\sigma,\mathbf{E}}\right] \\
&\quad + \left[\mathbf{M}_{\sigma,\mathbf{E}} - \mathbf{M}_\sigma\mathbf{S}^T\right]\mathbf{M_d}^{-1}\left\langle \Delta\mathbf{d}\Delta\mathbf{E}^T \right\rangle + \left\langle \Delta\boldsymbol{\sigma}\Delta\mathbf{d}^T \right\rangle \mathbf{M_d}^{-1}\left[\mathbf{M_E} - \mathbf{S}\mathbf{M}_{\sigma,\mathbf{E}}\right]
\end{aligned} \tag{A.38}$$

Giving,

$$\mathbf{M}'_{\sigma,\mathbf{E}} = \mathbf{M}_{\sigma,\mathbf{E}} - \left[\mathbf{M}_{\sigma,\mathbf{E}} - \mathbf{M}_\sigma\mathbf{S}^T\right]\mathbf{M_d}^{-1}\left[\mathbf{M_E} - \mathbf{S}\mathbf{M}_{\sigma,\mathbf{E}}\right] \tag{A.39}$$

It is important to note that even if there are not correlations between the integral and nuclear data in the prior, there are certainly correlations in the posterior. If any other adjustment or iterative technique is applied, these covariances should not be forgotten.

The covariance matrix of $\mathbf{C}'$, or $\mathbf{M}'_\mathbf{C}$, can then be calculated using $\mathbf{M}'_\sigma$ as

$$\mathbf{M}'_\mathbf{C} = \mathbf{S}\mathbf{M}'_\sigma\mathbf{S}^T \tag{A.40}$$

A.2 MOCABA Derivation

MOCABA is derived here using the GLLS equations, in a similar way to how the ensemble Kalman filter is derived in Ref. [2]. The author does not know of any full derivation of MOCABA being presented in the literature. From their understanding, this is the most direct way to reaching the MOCABA equations.

To derive the MOCABA equations requires recognizing that there are ways to estimate the important terms in the GLLS equations with random sampling. Take the posterior nuclear data, $\boldsymbol{\sigma}'$, as calculated with GLLS in Eq. (A.41). Here, there are two terms $\mathbf{M}_\sigma \mathbf{S}^T$ and $\mathbf{S}\mathbf{M}_\sigma \mathbf{S}^T$ that use sensitivity coefficients, *i.e.* that use first-order perturbation theory. The essence of MOCABA is to approximate these two terms with random sampling instead of first-order perturbation theory.

$$\boldsymbol{\sigma}' = \boldsymbol{\sigma}_0 - \mathbf{M}_\sigma \mathbf{S}^T \left[\mathbf{S}\mathbf{M}_\sigma \mathbf{S}^T + \mathbf{M_E} \right]^{-1} \left[\mathbf{C} - \mathbf{E} \right] \tag{A.41}$$

The $\mathbf{S}\mathbf{M}_\sigma \mathbf{S}^T$ term is easiest to start with. It represents $\mathbf{M_C} = \left\langle \Delta\mathbf{C}\Delta\mathbf{C}^T \right\rangle$, or the covariance matrix of $\mathbf{C}$ created by $\mathbf{M}_\sigma$. This can be shown below, by inserting the linearity approximation and the property of matrix transposes $\left(\mathbf{S}(\boldsymbol{\sigma} - \boldsymbol{\sigma}_0)\right)^T = (\boldsymbol{\sigma} - \boldsymbol{\sigma}_0)^T \mathbf{S}^T$.

$$\begin{aligned}
\left\langle \Delta\mathbf{C}\Delta\mathbf{C}^T \right\rangle &= \left\langle \left(\mathbf{C}(\boldsymbol{\sigma}) - \mathbf{C}(\boldsymbol{\sigma}_0)\right)\left(\mathbf{C}(\boldsymbol{\sigma}) - \mathbf{C}(\boldsymbol{\sigma}_0)\right)^T \right\rangle \\
&= \left\langle \left(\mathbf{C}(\boldsymbol{\sigma}_0) + \mathbf{S}(\boldsymbol{\sigma} - \boldsymbol{\sigma}_0) - \mathbf{C}(\boldsymbol{\sigma}_0)\right)\left(\mathbf{C}(\boldsymbol{\sigma}_0) + \mathbf{S}(\boldsymbol{\sigma} - \boldsymbol{\sigma}_0) - \mathbf{C}(\boldsymbol{\sigma}_0)\right)^T \right\rangle \\
&= \left\langle \mathbf{S}(\boldsymbol{\sigma} - \boldsymbol{\sigma}_0)\left(\mathbf{S}(\boldsymbol{\sigma} - \boldsymbol{\sigma}_0)\right)^T \right\rangle = \left\langle \mathbf{S}(\boldsymbol{\sigma} - \boldsymbol{\sigma}_0)(\boldsymbol{\sigma} - \boldsymbol{\sigma}_0)^T \mathbf{S}^T \right\rangle \\
&= \mathbf{S}\left\langle (\boldsymbol{\sigma} - \boldsymbol{\sigma}_0)(\boldsymbol{\sigma} - \boldsymbol{\sigma}_0)^T \right\rangle \mathbf{S}^T = \mathbf{S}\mathbf{M}_\sigma \mathbf{S}^T
\end{aligned} \tag{A.42}$$

Next, one simply has to define the population estimate of $\mathbf{M_C}$, where N is the population size, $\mathbf{C}_i$ is a random sample of $\mathbf{C}$, and $\bar{\mathbf{C}}$ is the population mean of $\mathbf{C}$.

$$\hat{\mathbf{M}}_\mathbf{C} = \frac{1}{N-1} \sum_{i=1}^{N} \left(\mathbf{C}_i - \bar{\mathbf{C}}\right)\left(\mathbf{C}_i - \bar{\mathbf{C}}\right)^T \tag{A.43}$$

The term $\mathbf{M}_\sigma \mathbf{S}^T$ is recognized to first-order estimate of $\mathbf{M}_{\sigma,\mathbf{C}} = \left\langle \Delta\boldsymbol{\sigma}\Delta\mathbf{C}^T \right\rangle$ as shown below,

$$\begin{aligned}
\left\langle \Delta\boldsymbol{\sigma}\Delta\mathbf{C}^T \right\rangle &= \left\langle (\boldsymbol{\sigma} - \boldsymbol{\sigma}_0)\left(\mathbf{C}(\boldsymbol{\sigma}) - \mathbf{C}(\boldsymbol{\sigma}_0)\right)^T \right\rangle \\
&= \left\langle (\boldsymbol{\sigma} - \boldsymbol{\sigma}_0)\left(\mathbf{C}(\boldsymbol{\sigma}_0) + \mathbf{S}(\boldsymbol{\sigma} - \boldsymbol{\sigma}_0) - \mathbf{C}(\boldsymbol{\sigma}_0)\right)^T \right\rangle \\
&= \left\langle (\boldsymbol{\sigma} - \boldsymbol{\sigma}_0)\left(\mathbf{S}(\boldsymbol{\sigma} - \boldsymbol{\sigma}_0)\right)^T \right\rangle = \left\langle (\boldsymbol{\sigma} - \boldsymbol{\sigma}_0)(\boldsymbol{\sigma} - \boldsymbol{\sigma}_0)^T \mathbf{S}^T \right\rangle \\
&= \left\langle (\boldsymbol{\sigma} - \boldsymbol{\sigma}_0)(\boldsymbol{\sigma} - \boldsymbol{\sigma}_0)^T \right\rangle \mathbf{S}^T = \mathbf{M}_\sigma \mathbf{S}^T
\end{aligned} \tag{A.44}$$

$\mathbf{M}_{\sigma,\mathbf{C}}$ can then also be estimated with a population set of N random sample of $\mathbf{C}$ and $\boldsymbol{\sigma}$,

$$\hat{\mathbf{M}}_{\sigma,\mathbf{C}} = \frac{1}{N-1} \sum_{i=1}^{N} (\boldsymbol{\sigma}_i - \bar{\boldsymbol{\sigma}})(\mathbf{C}_i - \bar{\mathbf{C}})^T \tag{A.45}$$

The MOCABA equation for $\boldsymbol{\sigma}'$ can then be rewritten as Eq. (A.46). $\mathbf{M}'_\sigma$ can also be written as Eq. (A.59) with the same logic.

$$\boldsymbol{\sigma}' = \boldsymbol{\sigma}_0 - \hat{\mathbf{M}}_{\sigma,\mathbf{C}}\big[\hat{\mathbf{M}}_\mathbf{C} + \mathbf{M_E}\big]^{-1}\big[\mathbf{C} - \mathbf{E}\big] \tag{A.46}$$

$$\mathbf{M}'_\sigma = \mathbf{M}_\sigma - \hat{\mathbf{M}}_{\sigma,\mathbf{C}}\big[\hat{\mathbf{M}}_\mathbf{C} + \mathbf{M_{EM}}\big]^{-1}\hat{\mathbf{M}}_{\mathbf{C},\sigma} \tag{A.47}$$

To find $\mathbf{C}'$ and $\mathbf{M}'_\mathbf{C}$, requires more manipulations of the GLLS equations. First, recall the GLLS equation for $\mathbf{C}'$,

$$\mathbf{C}'(\boldsymbol{\sigma}') = \mathbf{C}(\boldsymbol{\sigma}_0) + \mathbf{S}(\boldsymbol{\sigma}' - \boldsymbol{\sigma}_0) \tag{A.48}$$

Replacing $\boldsymbol{\sigma}'$, with Eq. (A.41) gives

$$\begin{aligned}
\mathbf{C}' &= \mathbf{C}(\boldsymbol{\sigma}_0) + \mathbf{S}\big(\boldsymbol{\sigma}_0 - \mathbf{M}_\sigma \mathbf{S}^T\big[\mathbf{S}\mathbf{M}_\sigma \mathbf{S}^T + \mathbf{M_E}\big]^{-1}\big[\mathbf{C}(\boldsymbol{\sigma}_0) - \mathbf{E}\big] - \boldsymbol{\sigma}_0\big) \\
&= \mathbf{C}(\boldsymbol{\sigma}_0) + \mathbf{S}\mathbf{M}_\sigma \mathbf{S}^T\big[\mathbf{S}\mathbf{M}_\sigma \mathbf{S}^T + \mathbf{M_E}\big]^{-1}\big[\mathbf{C}(\boldsymbol{\sigma}_0) - \mathbf{E}\big]
\end{aligned} \tag{A.49}$$

And finally remembering that $\mathbf{S}\mathbf{M}_\sigma \mathbf{S}^T \approx \hat{\mathbf{M}}_\mathbf{C}$ gives the formula for calculating $\mathbf{C}'$ with MOCABA,

$$\mathbf{C}' = \mathbf{C}(\boldsymbol{\sigma}_0) + \hat{\mathbf{M}}_\mathbf{C}\big[\hat{\mathbf{M}}_\mathbf{C} + \mathbf{M_E}\big]^{-1}\big[\mathbf{C}(\boldsymbol{\sigma}_0) - \mathbf{E}\big] \tag{A.50}$$

$\mathbf{M}'_\mathbf{C}$ can also be found in similar way. First start with the GLLS-defined $\mathbf{M}'_\mathbf{C}$, and substitute the full expression for $\mathbf{M}'_\sigma$, or Eq. (A.34), into it,

$$\begin{aligned}
\mathbf{M}'_\mathbf{C} &= \mathbf{S}\mathbf{M}'_\sigma \mathbf{S}^T \\
&= \mathbf{S}\Big(\mathbf{M}_\sigma - \mathbf{M}_\sigma \mathbf{S}^T\big[\mathbf{S}\mathbf{M}_\sigma \mathbf{S}^T + \mathbf{M_E}\big]^{-1}\mathbf{S}\mathbf{M}_\sigma\Big)\mathbf{S}^T \\
&= \mathbf{S}\mathbf{M}_\sigma \mathbf{S}^T - \mathbf{S}\mathbf{M}_\sigma \mathbf{S}^T\big[\mathbf{S}\mathbf{M}_\sigma \mathbf{S}^T + \mathbf{M_E}\big]^{-1}\mathbf{S}\mathbf{M}_\sigma \mathbf{S}^T
\end{aligned} \tag{A.51}$$

Again, it must be recognized that $\mathbf{SM}_\sigma \mathbf{S}^T \approx \hat{\mathbf{M}}_\mathbf{C}$ and then the MOCABA equation for $\mathbf{M}'_\mathbf{C}$ can be written as,

$$\mathbf{M}'_\mathbf{C} = \hat{\mathbf{M}}_\mathbf{C} - \hat{\mathbf{M}}_\mathbf{C} \left[\hat{\mathbf{M}}_\mathbf{C} + \mathbf{M}_\mathbf{E} \right]^{-1} \hat{\mathbf{M}}_\mathbf{C} \tag{A.52}$$

Where $\left\langle \Delta \mathbf{C} \Delta \mathbf{E}^T \right\rangle = \mathbf{SM}_{\sigma,\mathbf{E}}$ through the math outlined in Eq. (A.54).

The GLLS derivation also included posterior correlations between $\mathbf{E}$ and $\boldsymbol{\sigma}'$, or $\mathbf{M}'_{\sigma,\mathbf{E}}$, that can also be defined with MOCABA.

$$\mathbf{M}'_{\sigma,\mathbf{E}} = \mathbf{M}_{\sigma,\mathbf{E}} - \left[\mathbf{M}_{\sigma,\mathbf{E}} - \mathbf{M}_\sigma \mathbf{S}^T \right] \left[\mathbf{SM}_\sigma \mathbf{S}^T + \mathbf{M}_\mathbf{E} - \mathbf{SM}_{\sigma,\mathbf{E}} - \mathbf{M}_{\mathbf{E},\sigma}{}^T \mathbf{S} \right]^{-1} \left[\mathbf{M}_\mathbf{E} - \mathbf{SM}_{\sigma,\mathbf{E}} \right] \tag{A.53}$$

MOCABA needs an estimate for $\mathbf{SM}_{\sigma,\mathbf{E}}$ and $\mathbf{M}_{\mathbf{E},\sigma}{}^T \mathbf{S}$, which can be shown to be $\mathbf{M}_{\mathbf{C},\mathbf{E}} = \left\langle \Delta \mathbf{C} \Delta \mathbf{E}^T \right\rangle$,

$$\begin{aligned} \left\langle \Delta \mathbf{C} \Delta \mathbf{E}^T \right\rangle &= \left\langle \left(\mathbf{C}(\boldsymbol{\sigma}) - \mathbf{C}(\boldsymbol{\sigma}_0) \right) (\mathbf{E} - \mathbf{E}_0)^T \right\rangle \\ &= \left\langle \left(\mathbf{C}(\boldsymbol{\sigma}_0) \right) + \mathbf{S}(\boldsymbol{\sigma} - \boldsymbol{\sigma}_0) - \mathbf{C}(\boldsymbol{\sigma}_0) \right) (\mathbf{E} - \mathbf{E}_0)^T \right\rangle \\ &= \left\langle \mathbf{S}(\boldsymbol{\sigma} - \boldsymbol{\sigma}_0)(\mathbf{E} - \mathbf{E}_0)^T \right\rangle = \mathbf{S} \left\langle (\boldsymbol{\sigma} - \boldsymbol{\sigma}_0)(\mathbf{E} - \mathbf{E}_0)^T \right\rangle \\ &= \mathbf{S} \left\langle \Delta \boldsymbol{\sigma} - \Delta \mathbf{E}^T \right\rangle = \mathbf{SM}_{\sigma,\mathbf{E}} \end{aligned} \tag{A.54}$$

Now MOCABA must find a population estimate for $\mathbf{M}_{\mathbf{C},\mathbf{E}}$. The easiest implementation is to assume that $\mathbf{M}_{\mathbf{C},\mathbf{E}} = \mathbf{0}$ in the prior, *i.e.* $\mathbf{E}$ and $\mathbf{C}$ are not *a priori* correlated. If they are correlated, it would be induced by correlations between $\boldsymbol{\sigma}$ and $\mathbf{E}$, or by $\mathbf{M}_{\sigma,\mathbf{E}}$. To find $\mathbf{M}_{\mathbf{C},\mathbf{E}}$ would then require sampling from the joint distribution of $\boldsymbol{\sigma}$ and $\mathbf{E}$, which was shown in Eq. (A.12), N times and then calculating the population estimate of $\mathbf{M}_{\mathbf{C},\mathbf{E}}$ as,

$$\hat{\mathbf{M}}_{\mathbf{C},\mathbf{E}} = \frac{1}{N-1} \sum_{i=1}^{N} \left(\mathbf{C}_i - \bar{\mathbf{C}} \right) \left(\mathbf{E}_i - \bar{\mathbf{E}} \right)^T \tag{A.55}$$

$\hat{\mathbf{M}}_{\mathbf{C},\mathbf{E}}$ could then be used in MOCABA to calculate $\mathbf{M}'_{\sigma,\mathbf{E}}$ as,

$$\mathbf{M}'_{\sigma,\mathbf{E}} = \mathbf{M}_{\sigma,\mathbf{E}} - \left[\mathbf{M}_{\sigma,\mathbf{E}} - \hat{\mathbf{M}}_{\mathbf{C},\sigma} \right] \left[\hat{\mathbf{M}}_\mathbf{C} + \mathbf{M}_\mathbf{E} - \hat{\mathbf{M}}_{\mathbf{C},\mathbf{E}} - \hat{\mathbf{M}}_{\mathbf{E},\mathbf{C}} \right]^{-1} \left[\mathbf{M}_\mathbf{E} - \hat{\mathbf{M}}_{\mathbf{C},\mathbf{E}} \right] \tag{A.56}$$

In practical cases, $\mathbf{M}_{\sigma,\mathbf{E}} = \mathbf{0}$ and $\mathbf{M}'_{\sigma,\mathbf{E}}$ can be written as

$$\mathbf{M}'_{\sigma,\mathbf{E}} = -\hat{\mathbf{M}}_{\mathbf{C},\sigma} \left[\hat{\mathbf{M}}_\mathbf{C} + \mathbf{M}_\mathbf{E} \right]^{-1} \mathbf{M}_\mathbf{E} \tag{A.57}$$

For completeness, the MOCABA equations assuming that $\mathbf{M_{C,E}}$ exists through $\mathbf{M}_{\sigma,\mathbf{E}}$ are given below. Again, in practice $\mathbf{M}_{\sigma,\mathbf{E}}$ either does not exist or is not known. However, if MOCABA was used in an iterative way, these correlations would need to be taken into account.

$$\boldsymbol{\sigma}' = \boldsymbol{\sigma}_0 + \left[\mathbf{M}_{\sigma,\mathbf{E}} - \hat{\mathbf{M}}_{\mathbf{C},\sigma}\right]\left[\hat{\mathbf{M}}_\mathbf{C} + \mathbf{M}_\mathbf{E} - \hat{\mathbf{M}}_{\mathbf{C},\mathbf{E}} - \hat{\mathbf{M}}_{\mathbf{E},\mathbf{C}}\right]^{-1}\left[\mathbf{C}(\boldsymbol{\sigma}_0) - \mathbf{E}\right] \tag{A.58}$$

$$\mathbf{M}'_\sigma = \mathbf{M}_\sigma - \left[\mathbf{M}_{\sigma,\mathbf{E}} - \hat{\mathbf{M}}_{\sigma,\mathbf{C}}\right]\left[\hat{\mathbf{M}}_\mathbf{C} + \mathbf{M}_\mathbf{E} - \hat{\mathbf{M}}_{\mathbf{C},\mathbf{E}} - \hat{\mathbf{M}}_{\mathbf{E},\mathbf{C}}\right]^{-1}\left[\mathbf{M}_{\mathbf{E},\sigma} - \hat{\mathbf{M}}_{\mathbf{C},\sigma}\right] \tag{A.59}$$

$$\mathbf{C}' = \mathbf{C}(\boldsymbol{\sigma}_0) + \left[\hat{\mathbf{M}}_{\mathbf{C},\mathbf{E}} - \hat{\mathbf{M}}_\mathbf{C}\right]\left[\hat{\mathbf{M}}_\mathbf{C} + \mathbf{M}_\mathbf{E} - \hat{\mathbf{M}}_{\mathbf{C},\mathbf{E}} - \hat{\mathbf{M}}_{\mathbf{E},\mathbf{C}}\right]^{-1}\left[\mathbf{C}(\boldsymbol{\sigma}_0) - \mathbf{E}\right] \tag{A.60}$$

$$\mathbf{M}'_\mathbf{C} = \hat{\mathbf{M}}_\mathbf{C} - \left[\hat{\mathbf{M}}_{\mathbf{C},\mathbf{E}} - \hat{\mathbf{M}}_\mathbf{C}\right]\left[\hat{\mathbf{M}}_\mathbf{C} + \mathbf{M}_\mathbf{E} - \hat{\mathbf{M}}_{\mathbf{C},\mathbf{E}} - \hat{\mathbf{M}}_{\mathbf{E},\mathbf{C}}\right]^{-1}\left[\hat{\mathbf{M}}_{\mathbf{E},\mathbf{C}} - \hat{\mathbf{M}}_\mathbf{C}\right] \tag{A.61}$$

A.3 LWR-PII Relative Reactivity Supplementary Information

A.3.1 Experimental Covariance Matrix

The literature of LWR-PII details the experimental standard deviations, but gives no information about their correlations. Because $\Delta\rho_{rel}$ share a common denominator, they will be inherently correlated and this needs to be taken into account. For easy comprehension, the names of the following variables are changed in this section only: the $\Delta\rho_{rel}$ of the ith fuel sample is represented as z_i, its absolute reactivity worth, or $\Delta\rho(U_{\text{ref}} \rightarrow U_i)$, as x_i, and the absolute reactivity worth between the U_{nat} and U_{ref}, or $\Delta\rho(U_{\text{ref}} \rightarrow U_{\text{nat}})$, as x_{nat}. To derive the variances and covariances of z_i, linear error propagation is used.

The correlations are estimated by reviewing the LWR-PII experiment. The x values are obtained with a compensation method. It measured x in equivalent-autorod-units (eAUR) by quantifying the degree of reactivity compensation by an absorbing auto-rod (AR). A coefficient can be used to convert from eAUR to dollars ($) and was determined by the inverse kinetics method. Each x measurement was repeated several times at the same power and at three different powers. The first repetition improved statistics and the second removed the effect of the intrinsic neutron source of the spent fuel sample on reactivity. The three measurements were used to interpolate the reactivity worth to infinite power, where the neutron source from the fuel sample is negligible. The extrapolation to infinite power with the three measurements is not considered in the uncertainty quantification. Instead, conservatism to account for neglecting all of these factors is introduced by assuming that their uncertainties of the x values are 0.5% where in fact they are ~0.2-0.3%.

Corrections to the x values (see Eq. (A.62)) were introduced to account for small sample length differences and for neutron absorption in the cladding. The purpose of these corrections was to compare experimental results to the CASMO results where all samples are modeled with the same length. The sample length of U_{ref}, l_{ref}, and x of the clad measurements, x_{clad}, are sources of common uncertainty as well. A z value with length-corrected $\tilde{x}$ is then calculated using Eq. (A.63), where the ratio between the lengths of U_{nat} and U_i, $\frac{l_{ref}}{l_i}$, seen in Eq. (A.62) is represented as k_i for readability. For this study, uncertainties in z are taken into account starting with Eq. (A.63). This means that the coefficient to convert from eAUR to $ will cancel out and is not considered in the uncertainty propagation.

$$\tilde{x}_i = (x_i - x_{clad})\frac{l_{ref}}{l_i} + x_{clad} \tag{A.62}$$

$$\Delta\rho_{rel} = z = \frac{\tilde{x}_i}{\tilde{x}_{nat}} = \frac{(x_i - x_{clad})k_i + x_{clad}}{(x_{nat} - x_{clad})k_{nat} + x_{clad}} = \frac{k_i x_i + (1 - k_i)x_{clad}}{k_{nat}x_{nat} + (1 - k_{nat})x_{clad}} \tag{A.63}$$

Now uncertainties in the x_i, x_{clad}, l_{ref}, and l_i need to be taken into account. The uncertainty

of an l is approximately 0.5%. The terms x_i and l_i are independent as they are unique from sample to sample. The terms x_{clad} and l_{ref} are used identically in each calculation and are sources of correlation between $\widetilde{x}$ values. The uncertainties associated with l_i and l_{ref} are not included because they are negligible compared to the total uncertainty. This leaves only the uncertainties of x_i and x_{clad} to be considered to derive the correlation between z values.

With the sources of uncertainty in the $\widetilde{x}$ values defined, they can be used in Eq. (A.70) to calculate the variances and covariances of the z values. They are contained in the matrix $\mathbf{V_{out}}$, which is then used as $\mathbf{M_E}$ in DA. Eq. (A.70) is linear error propagation, where $\mathbf{J}$ is the Jacobian matrix of first-order partial derivatives of z and $\mathbf{V_{in}}$ is the covariance matrix of x values. $\mathbf{J}$ is shown in Eq. (A.71) and has a size of $[(n+2) \times n]$, where n is the number of z values considered. $\mathbf{V_{in}}$ has a size of $[(n+2) \times (n+2)]$ and is shown in Eq. (A.75), where $\Delta^2_{x_i}$ is the variance of x_i and $\Delta^2_{x_i x_j}$ is the correlation between x_i and x_j.

$$\mathbf{V_{out}} = \mathbf{J}^T \mathbf{V_{in}} \mathbf{J} \tag{A.64}$$

$$\mathbf{J} = \begin{bmatrix} \frac{\delta z_1}{\delta x_1} & \frac{\delta z_2}{\delta x_1} & \cdots & \frac{\delta z_n}{\delta x_1} \\ \vdots & \vdots & \ddots & \vdots \\ \frac{\delta z_1}{\delta x_n} & \frac{\delta z_2}{\delta x_n} & \cdots & \frac{\delta z_n}{\delta x_n} \\ \frac{\delta z_1}{\delta x_{nat}} & \frac{\delta z_2}{\delta x_{nat}} & \cdots & \frac{\delta z_n}{\delta x_{nat}} \\ \frac{\delta z_1}{\delta x_{clad}} & \frac{\delta z_2}{\delta x_{clad}} & \cdots & \frac{\delta z_n}{\delta x_{clad}} \end{bmatrix} \tag{A.65}$$

$$\mathbf{V_{in}} = \begin{bmatrix} \Delta^2_{x_1} & \cdots & \Delta^2_{x_1 x_n} & \Delta^2_{x_1 x_{nat}} & \Delta^2_{x_1 x_{clad}} \\ \vdots & \ddots & \vdots & \vdots & \vdots \\ \Delta^2_{x_n x_1} & \cdots & \Delta^2_{x_n} & \Delta^2_{x_n x_{nat}} & \Delta^2_{x_n x_{clad}} \\ \Delta^2_{x_{nat} x_1} & \cdots & \Delta^2_{x_{nat} x_n} & \Delta^2_{x_{nat}} & \Delta^2_{x_{nat}, x_{clad}} \\ \Delta^2_{x_{clad} x_1} & \cdots & \Delta^2_{x_{clad} x_n} & \Delta^2_{x_{clad} x_{nat}} & \Delta^2_{x_{clad}} \end{bmatrix} \tag{A.66}$$

Evaluating $\mathbf{J}$ and $\mathbf{V_{in}}$ gives Eq. (A.67) for the diagonal variance terms and Eq. (A.68) for the off-diagonal covariance terms in $\mathbf{V_{out}}$. The full $\mathbf{V_{out}}$ matrix becomes $\mathbf{M_E}$ in DA. Here, the equations are simplified by creating the following variables: $\widetilde{x}_i = k_i x_i + (1 - k_i) x_{clad}$, $\widetilde{x}_{i,f} = (1 - k_i) k_{nat} x_{nat} - (1 - k_{nat}) k_i x_i$, and $\widetilde{x}_{nat} = k_{nat} x_{nat} + (1 - k_{nat}) x_{clad}$.

$$\left[\mathbf{V_{out}} \right]_{i,i} = \frac{1}{\widetilde{x}^4_{nat}} \left[k_i^2 \widetilde{x}^2_{nat} \Delta^2_{x_i} + k_{nat}^2 \widetilde{x}_i^2 \Delta^2_{x_{nat}} + \widetilde{x}^2_{i,f} \Delta^2_{x_{clad}} \right] \tag{A.67}$$

$$\left[\mathbf{V_{out}} \right]_{i,j} = \frac{1}{\widetilde{x}^4_{nat}} \left[k_{nat}^2 \widetilde{x}_i \widetilde{x}_j \Delta^2_{x_{nat}} + \widetilde{x}_{i,f} \widetilde{x}_{j,f} \Delta^2_{x_{clad}} \right] \tag{A.68}$$
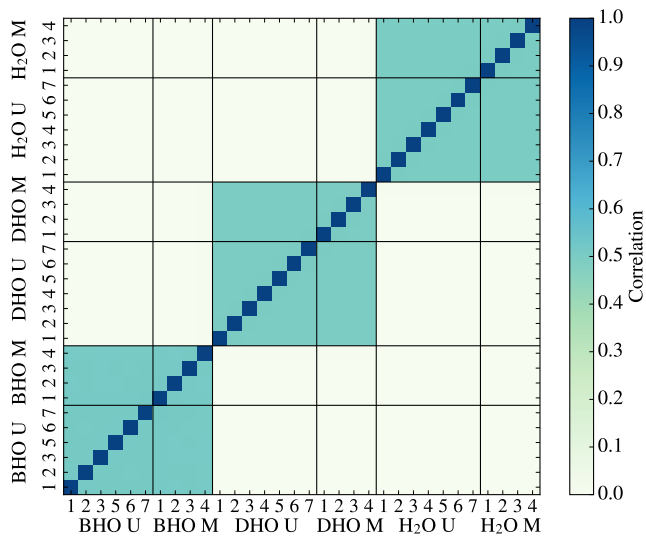
171

Figure A.1 – Correlations between the 32 experimental $\Delta\rho_{rel}$.

A.4 LWR-PII PIE Experimental Correlations

In this subsection, we detail the process that was used to estimate the covariances between the experimental nuclide concentrations. In order to understand the covariances requires a bit of digging into the hotlab measurements of LWR-PII. The PIE measured 17 actinides and 40 fission product nuclides. The measurements involved dissolving the fuel samples in HNO_3 at 150 C. The residue from the dissolution was further dissolved in a HCL/HNO_3 mixture at 180 C. The solutions were then used with a combination of high-performance liquid chromatography (HPLC) and a multicollector inductively-coupled plasma[2] mass spectrometer (MC-ICP-MS) to measure the nuclide concentrations. HPLC was used to separate chemical elements, and then mass spectrometry (MS) was used to measure the isotopic concentrations. The combination was needed because mass spectrometry cannot distinguish between isobars. For the metallic fission products Mo-95, Tc-99, Ru-101, Rh-103, and Ag-109 along with Np-237, only the mass spectrometer was used because these have no isobaric interference. The isotopes Ru-106, Sb-125, Ce-144, and Cm-243 were measured with gamma ray spectrometry because they were present in very small concentrations.

The MS needs to be calibrated in order to measure isotopic concentrations in spent nuclear fuel samples. The most commonly used technique, due to its accuracy, is isotope dilution analyses (IDA). It allows to acquire a precision better than 0.5% when used with multi-collection instruments. For calibration, it used the principle of isotope dilution. The fuel sample has an unknown amount of element with a measurable isotopic composition. A reference sample (a so-called "spike") with a certified element mass and known isotopic composition is added. Because these two samples are mixed, the isotopic composition of that element is changed. The new ratios of isotopes are measured in the mixture. Next, knowing the isotope concentrations in the fuel sample, the spike sample (which is certified), and the mixture, and knowing the mass of the spike sample and the amount of sample and spike mixed together (through weighing), the concentration of the element in the fuel sample can be calculated.

Concerning the uncertainties in this process, there is a random error in the measurements that arises from unpredictable or stochastic variations in quantities. Systematic errors remain constant or vary in a predictable way over the course of a number of analyses. For instance, all isotopes of an element used the same spike. Uncertainty in the spike is then common to all isotopes of an element. A list of other possible sources of error are given below,

- **Sampling, or cutting the fuel from the fuel rod:** The error in the cutting position was ±0.15 mm, or ~1.5%. This did not influence the experimental result. It only influences comparisons to calculations that are based on the theoretical cutting position.

- **Dissolution of the fuel:** When the fuel was heated in 8 M of HNO_3, errors may have

---

[2]The ionization source for mass spectroscopy was an inductively couple plamsa (ICP). The liquefied fuel sample was turned into an aerosol and then introduced to a plasma. This was done by applying an RF field around a quartz torch. The plasma has a temperature above 5,000 K. It vaporizes, desolvates, and atomizes the fuel sample, which causes the sample's atoms to be ionized.

arisen from the volatility of elements, adsorbtion on container walls, impurities introduced by reagents or equipment material. The sample dissolution error was assumed to be 0.05%.

- **Dissolution of fuel residues:** The error sources are the same as the fuel above, and are assumed to be 0.1%.

- **Sample Dilution:** The dilutions were prepared by weighing, and the weighing uncertainty was included in the reported results.

- **Sample preparation:** Uncertainties here were the amount of the added spike and the accuracy of spike solution. The amount of spike was controlled by weighing and the accuracy of the solution was given by a certificate. Gamma-ray measurements were also prepared by weighing and the dilution uncertainty was reported in the results.

The uncertainty of the measured elemental compositions was typically less than 0.1%, but can be larger for isotopes with low abundance. This uncertainty was calculated as the standard deviations of four repeated measurements of the unspiked samples. For the isotopic concentrations, the uncertainties ranged between 0.3% and 1%. The uncertainties came from the statistical errors of the unspiked and spiked samples, the weighing of the fuel and spike solutions, and the uncertainty of the compositions and concentrations of the spike materials. The uncertainty of the gamma-spectroscopy measurements is 5-10%. An uncertainty of 10% was assumed for the metallic fission products because of the large discrepancies observed between participants in the MALIBU program.

The final experimental value to be used in DA is the mass of the isotope relative to the total mass of uranium, in units of mg/g. This concentration, ϵ, of isotope i is given in Eq. (A.69). w_i is the measured weight percent of that isotope, U_{tot} is the mass of uranium per total mass of fuel (mg/g), and η_j is the mass of the element j (measured with IDA) that the given isotope belongs to per total mass of fuel (g/g). Through analysis of the experimental campaign, it can be reasonably assumed that w, U_{tot}, and η are all independent. The correlations between ϵ are then created by the common normalization U_{tot} used in all calculations, and by the common η used between isotopes of the same element.

$$\epsilon_i = w_i \frac{\eta_j}{U_{\text{tot}}} \tag{A.69}$$

With the sources of uncertainty in the ϵ values defined, they can be used in Eq. (A.70) to calculate the variances and covariances. They are contained in the covariance matrix $\mathbf{V_{out}}$, which is then used as the experimental covariance matrix in the DA methods. Eq. (A.70) is the linear error propagation formula with $\mathbf{J}$ being the Jacobian matrix of first-order partial derivatives of ϵ and $\mathbf{V_{in}}$ being the covariance matrix of the w, U_{tot}, and η values. $\mathbf{J}$ is shown in

Eq. (A.71).

$$\mathbf{V_{out}} = \mathbf{J}^T \mathbf{V_{in}} \mathbf{J} \tag{A.70}$$

$$\mathbf{J} = \begin{bmatrix} \frac{\delta\epsilon_1}{\delta U_{\text{tot}}} & \frac{\delta\epsilon_2}{\delta U_{\text{tot}}} & \cdots & \frac{\delta\epsilon_n}{\delta U_{\text{tot}}} \\ \frac{\delta\epsilon_1}{\delta\eta_1} & \frac{\delta\epsilon_2}{\delta\eta_1} & \cdots & \frac{\delta\epsilon_n}{\delta\eta_1} \\ \vdots & \vdots & \ddots & \vdots \\ \frac{\delta\epsilon_1}{\delta\eta_n} & \frac{\delta\epsilon_2}{\delta\eta_n} & \cdots & \frac{\delta\epsilon_n}{\delta\eta_n} \\ \frac{\delta\epsilon_1}{\delta w_1} & \frac{\delta\epsilon_2}{\delta w_1} & \cdots & \frac{\delta\epsilon_n}{\delta w_1} \\ \vdots & \vdots & \ddots & \vdots \\ \frac{\delta\epsilon_1}{\delta w_n} & \frac{\delta\epsilon_2}{\delta w_n} & \cdots & \frac{\delta\epsilon_n}{\delta w_n} \end{bmatrix} \tag{A.71}$$

The derivatives in the **J** matrix are given below,

$$\frac{\Delta\epsilon_i}{\Delta U_{\text{tot}}} = -\frac{\eta_j w_i}{U_{\text{tot}}^2} \tag{A.72}$$

$$\frac{\Delta\epsilon_i}{\Delta\eta_j} = \frac{w_i}{U_{\text{tot}}} \tag{A.73}$$

$$\frac{\Delta\epsilon_i}{\Delta w_i} = \frac{\eta_j}{U_{\text{tot}}} \tag{A.74}$$

The covariance matrix of w, U_{tot}, and η is given in Eq. (A.75). We assume that the measurement of w, U_{tot}, and η were all uncorrelated. This means that correlations between ϵ values are created only by the common terms U_{tot} and η between two different values. It is possible to define a correlation term for w, U_{tot}, and η and it theoretically they can be correlated because the same experimental setup (chemical process, mass spectrometer, gamma spectrometer)

were shared between the measurements.

$$
\mathbf{V_{in}} = \begin{bmatrix}
\Delta^2_{U_{\text{tot}}} & \Delta^2_{U_{\text{tot}}\eta_1} & \cdots & \Delta^2_{U_{\text{tot}}\eta_n} & \Delta^2_{U_{\text{tot}}w_1} & \cdots & \Delta^2_{U_{\text{tot}}w_n} \\
\Delta^2_{\eta_1 U_{\text{tot}}} & \Delta^2_{\eta_1} & \cdots & \Delta^2_{\eta_1\eta_n} & \Delta^2_{\eta_1 w_1} & \cdots & \Delta^2_{\eta_1 w_n} \\
\vdots & \vdots & \ddots & \vdots & \vdots & \vdots & \vdots \\
\Delta^2_{\eta_n U_{\text{tot}}} & \Delta^2_{\eta_1\eta_n} & \cdots & \Delta^2_{\eta_n} & \Delta^2_{\eta_n w_1} & \cdots & \Delta^2_{\eta_n w_n} \\
\Delta^2_{w_1 U_{\text{tot}}} & \Delta^2_{w_1\eta_1} & \cdots & \Delta^2_{w_1\eta_n} & \Delta^2_{w_1} & \cdots & \Delta^2_{w_1,w_n} \\
\vdots & \vdots & \vdots & \vdots & \cdots & \ddots & \vdots \\
\Delta^2_{w_n U_{\text{tot}}} & \Delta^2_{w_n\eta_1} & \cdots & \Delta^2_{w_n\eta_n} & \Delta^2_{w_n w_1} & \cdots & \Delta^2_{w_n}
\end{bmatrix}
\tag{A.75}
$$

After applying this formulation, the correlation matrix can be found, and is shown in Fig. 5.3. The variances are reproduced for all isotopes measured with HPLC-MC-ICP-MS or only MC-ICP-MS. The gamma ray variances are underestimated by an order of magnitude. However, this is because the uncertainties were artificially set to 10% by the experimenters to account for differences observed between other participants in the experimental campaign MALIBU.

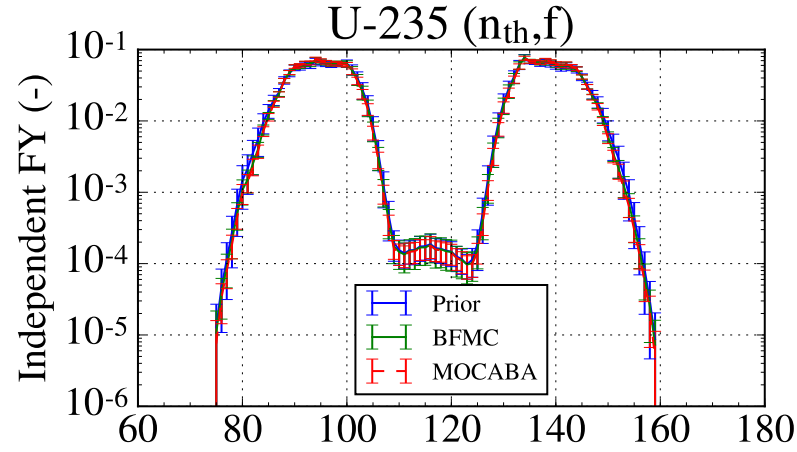## A.5 GEF DA Supplementary Figures

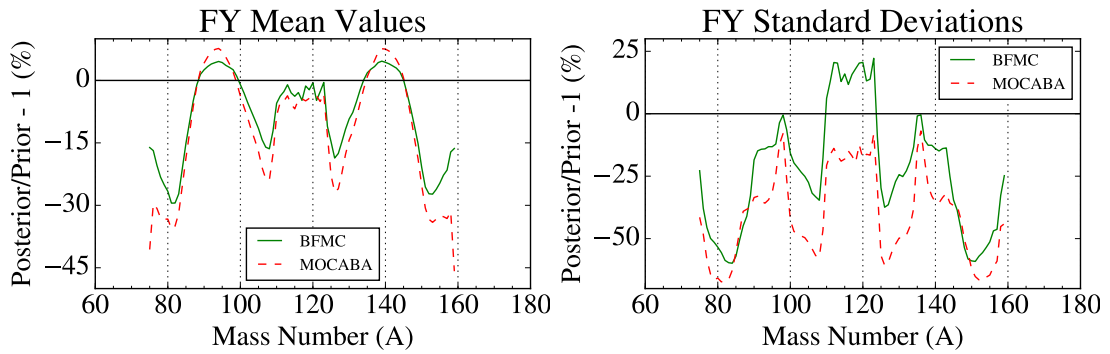Figure A.2 – Prior and posterior U-235 independent thermal fission yields

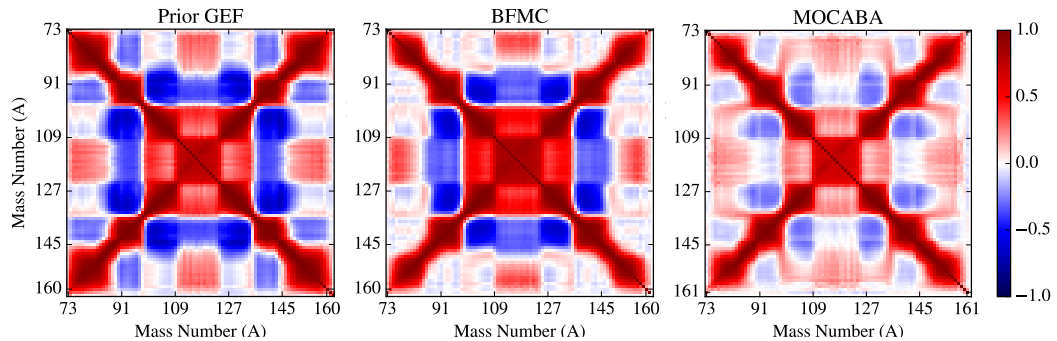Figure A.3 – Relative differences in the mean and relative standard deviations of the U-235 (n_{th}, f) yields.

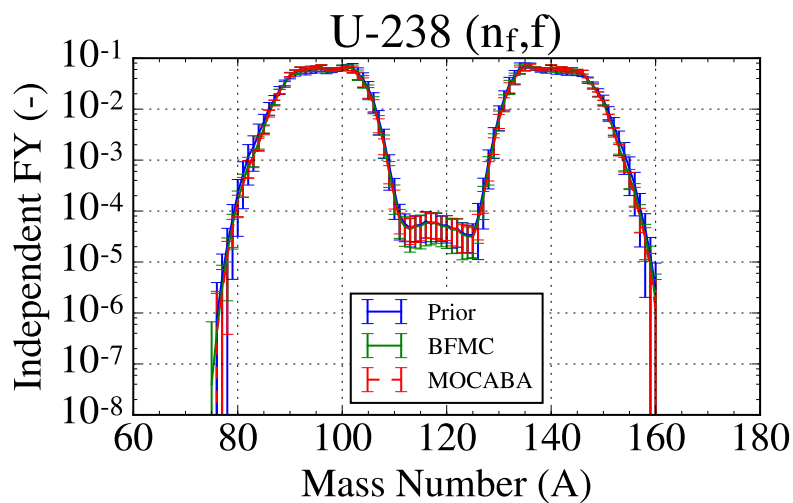Figure A.4 – Prior and posterior correlation matrices for the independent FYs of U-235 (n_{th}, f).

177

Figure A.5 – Prior and posterior U-238 fast fission independent FYs.

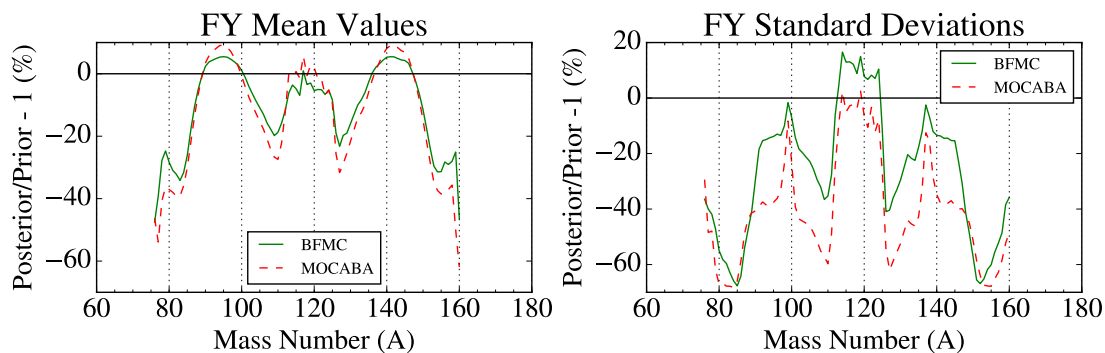

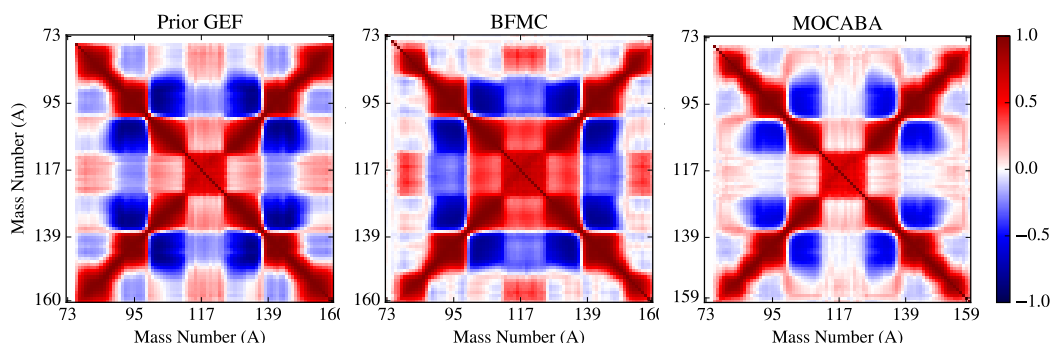Figure A.6 – Relative differences in the mean and relative standard deviations of U-238 (n_f, f) independent FYs.

Figure A.7 – Prior and posterior correlation matrices for the independent FYs of U-238 (n_f, f).
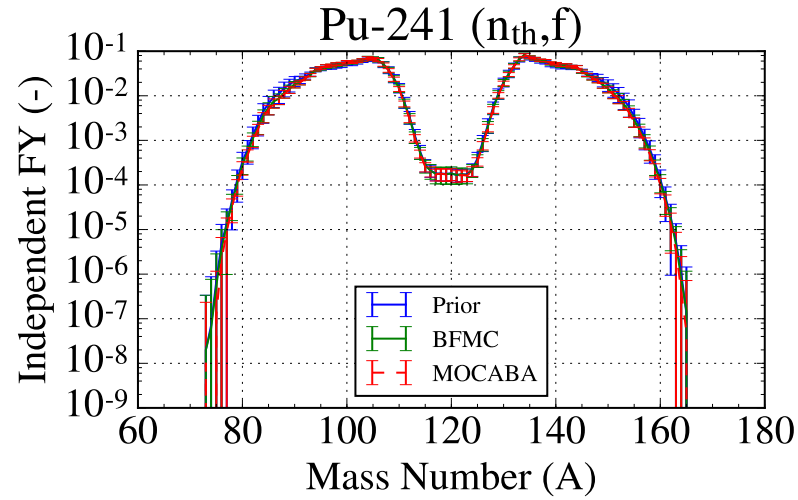
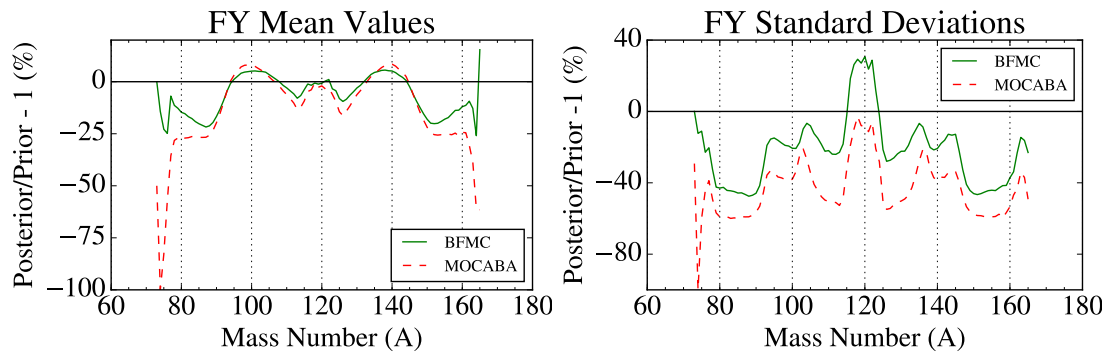Figure A.8 – Prior and posterior Pu-241 thermal fission yields

Figure A.9 – Relative differences in the mean and relative standard deviations of of the Pu-241 thermal fission yields.
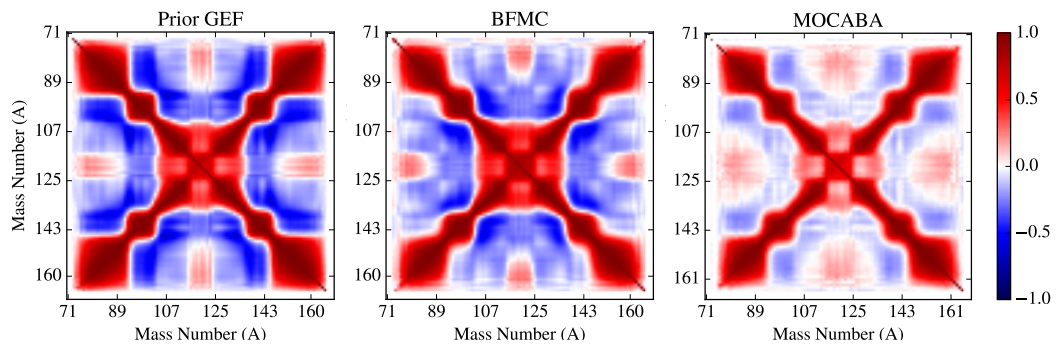

Figure A.10 – Prior and posterior correlation matrices for the independent FYs of thermal fission of Pu-241.

179

Figure A.11 – FY data for thermal fission of U-235 from ENDFB/VIII.0, JEFF3.3, and the prior and posterior GEF model parameters

Figure A.12 – Relative differences of the means of the independent FY data for thermal fission of U-235 between ENDFB/VIII.0 and GEF and between JEFF3.3 and GEF

Figure A.13 – Relative differences of the standard deviations of the independent FY data for thermal fission of U-235 between ENDFB/VIII.0 and GEF and between JEFF3.3 and GEF
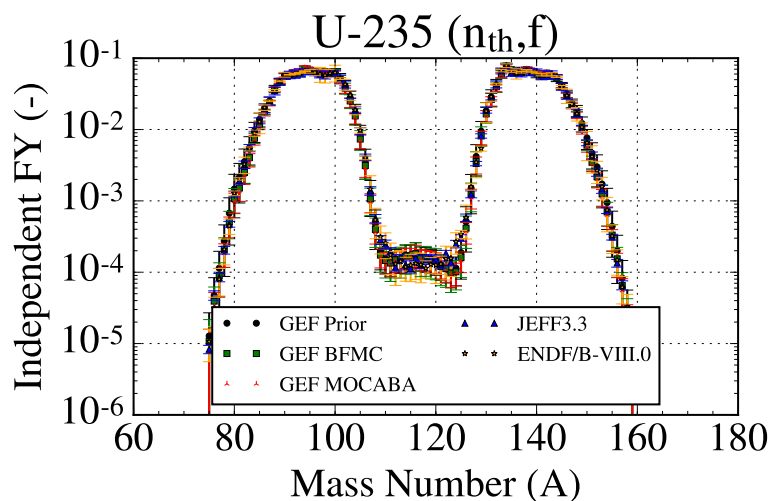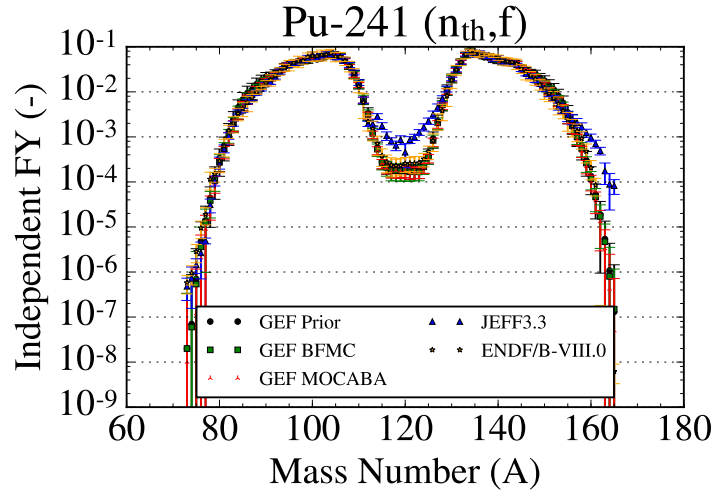
Figure A.14 – FY data for thermal fission of Pu-241 from ENDFB/VIII.0, JEFF3.3, and the prior and posterior GEF model parameters
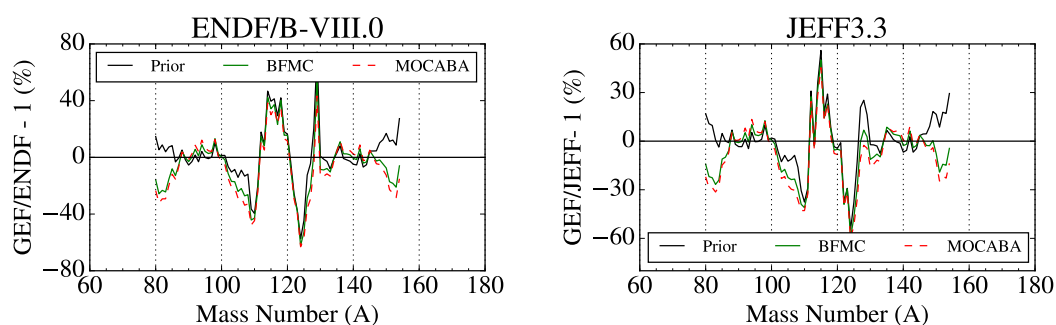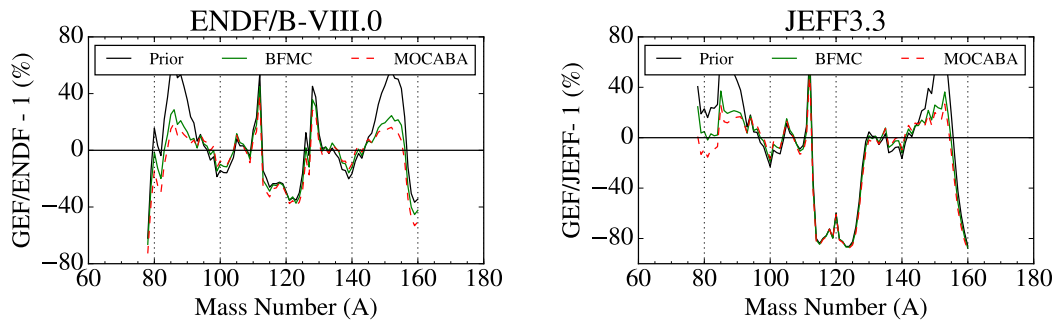

Figure A.15 – Relative differences of the means of the independent FY data for thermal fission of Pu-241 between ENDFB/VIII.0 and GEF and between JEFF3.3 and GEF
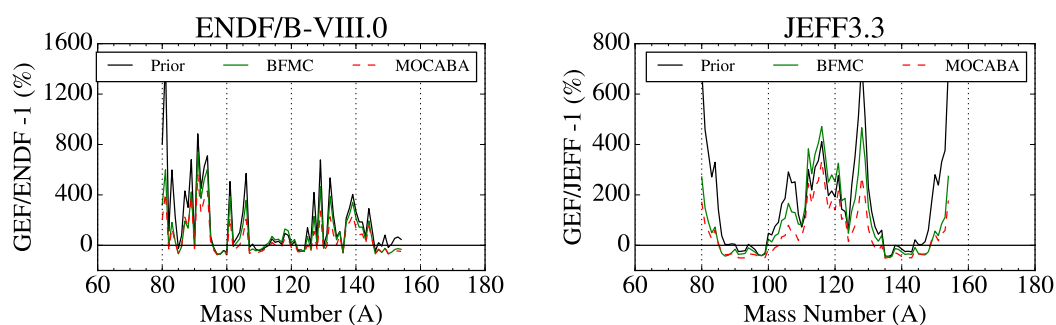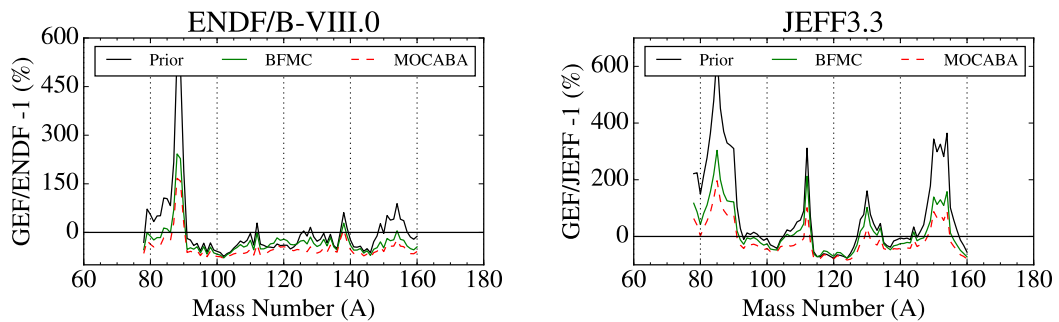

Figure A.16 – Relative differences of the standard deviations of the independent FY data for thermal fission of Pu-241 between ENDFB/VIII.0 and GEF and between JEFF3.3 and GEF
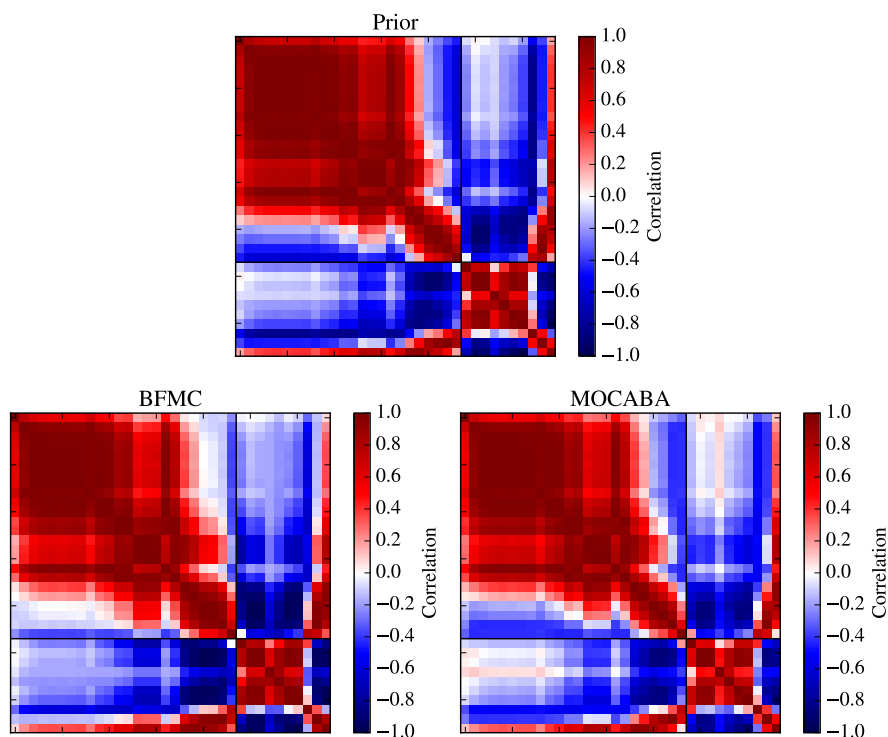
Figure A.17 – Correlation matrices of the calculated nuclide concentrations in fuel sample U2.
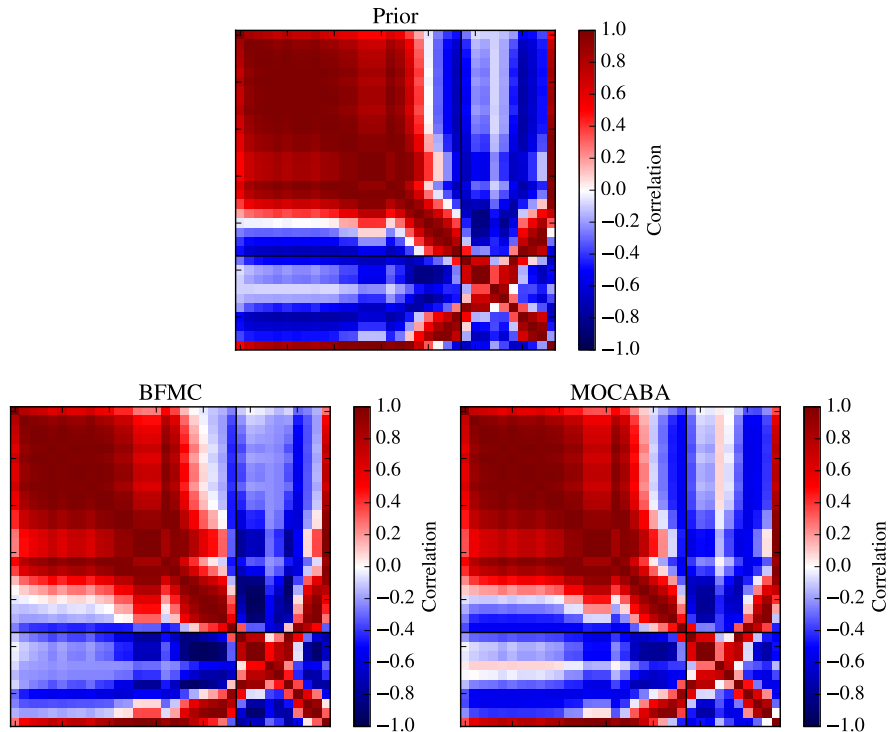
Figure A.18 – Correlation matrices of the calculated nuclide concentrations in fuel sample M1.
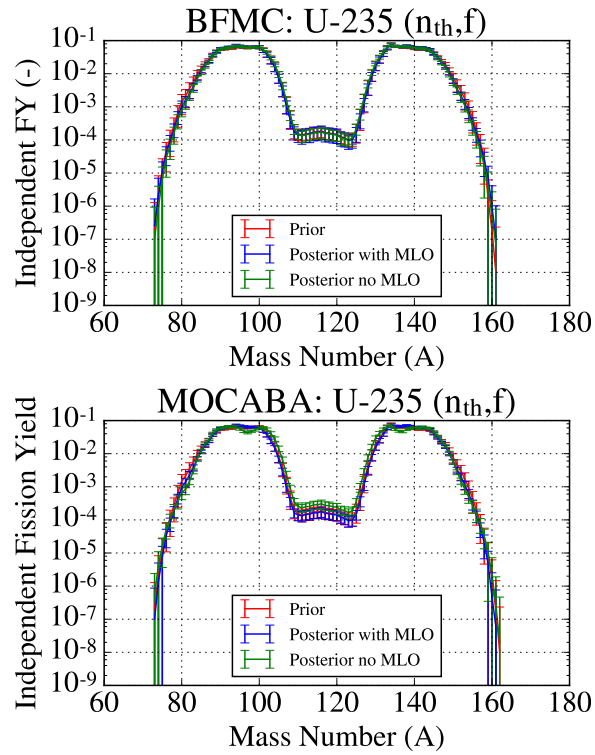
Figure A.19 – Prior and posterior U-235 thermal fission yields using BFMC and MOCABA, with and without MLO.
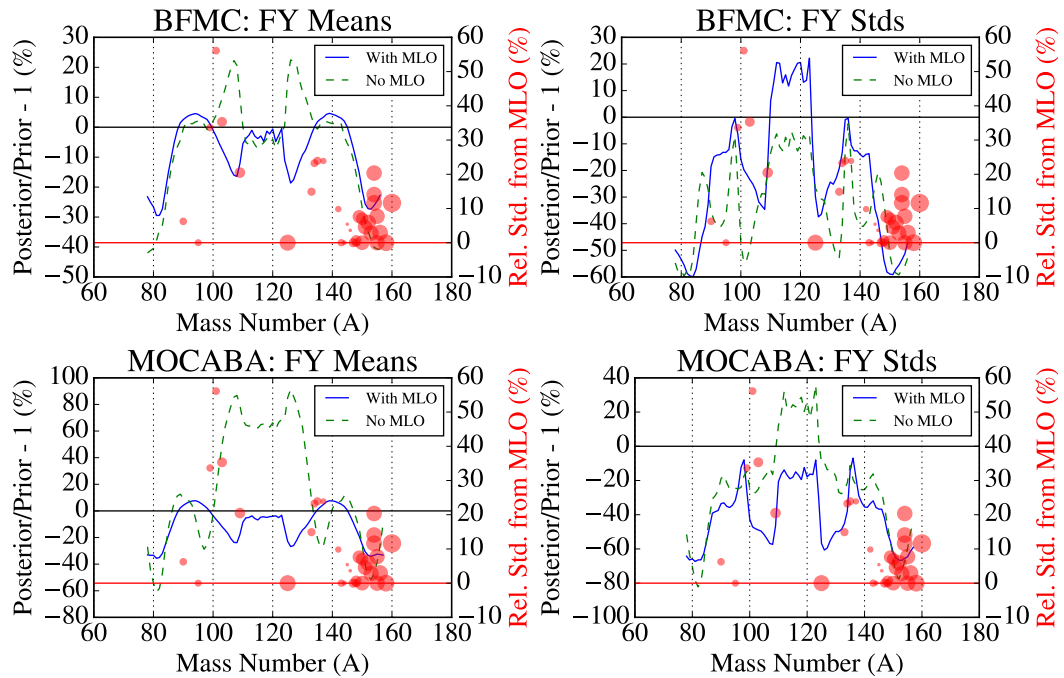
Figure A.20 – Relative differences in the mean and relative standard deviations of of the U-235 thermal fission yields.
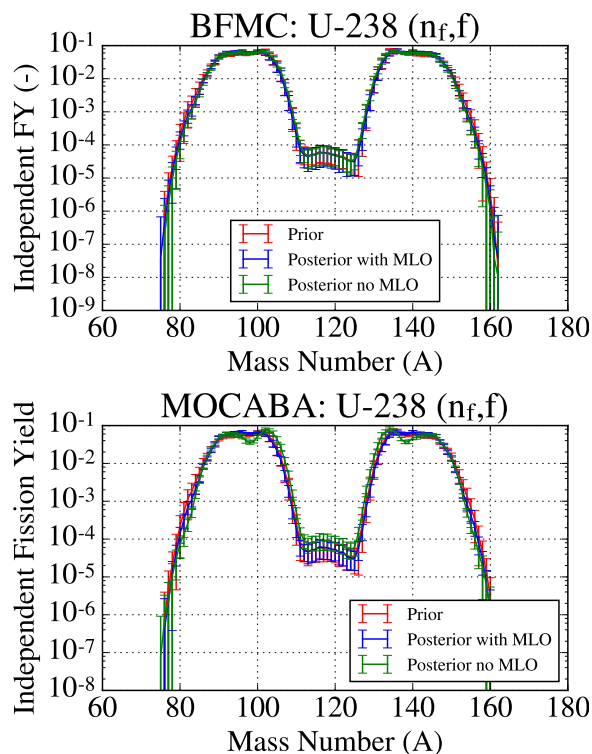
Figure A.21 – Prior and posterior U-238 independent fast fission yields using BFMC and MOCABA, with and without MLO.
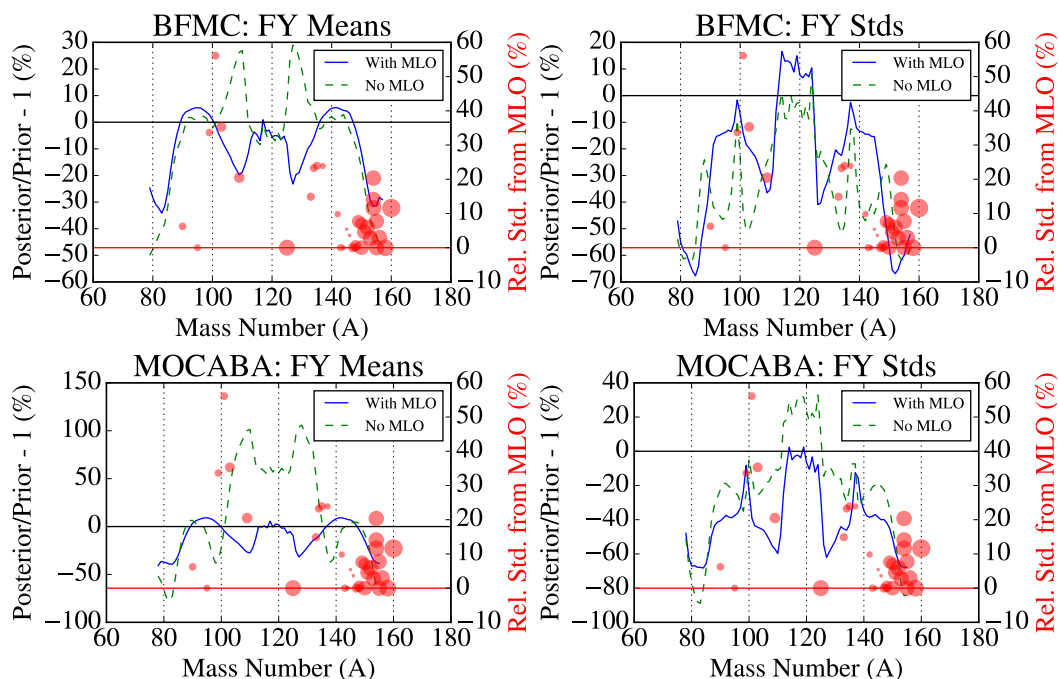
Figure A.22 – Relative differences in the mean and relative standard deviations of of the U-238 fast fission yields.
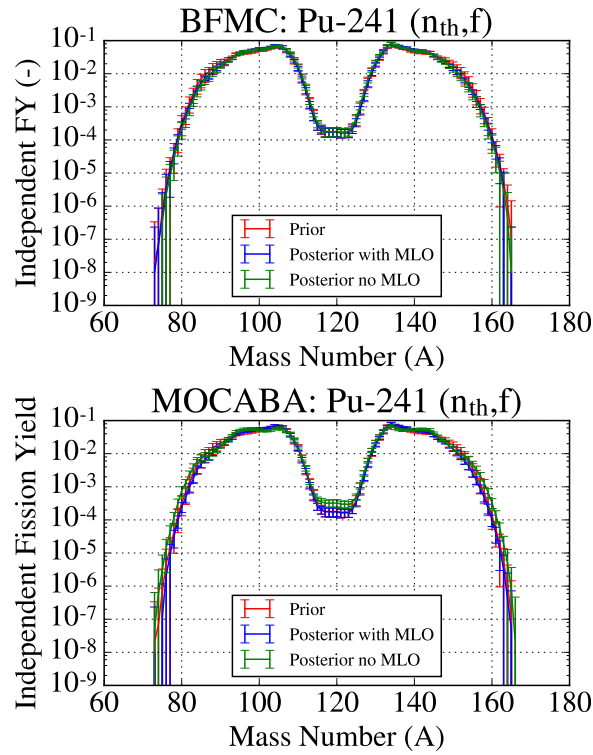
Figure A.23 – Prior and posterior Pu-241 thermal fission yields using BFMC and MOCABA, with and without MLO.
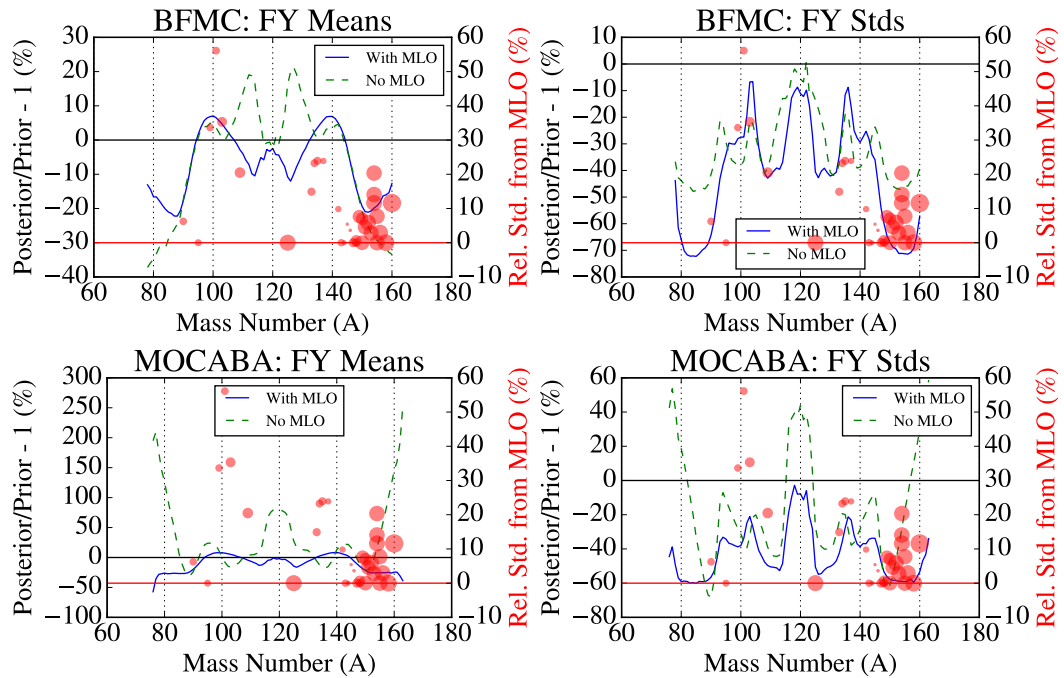
Figure A.24 – Relative differences in the mean and relative standard deviations of of the Pu-241 thermal fission yields.
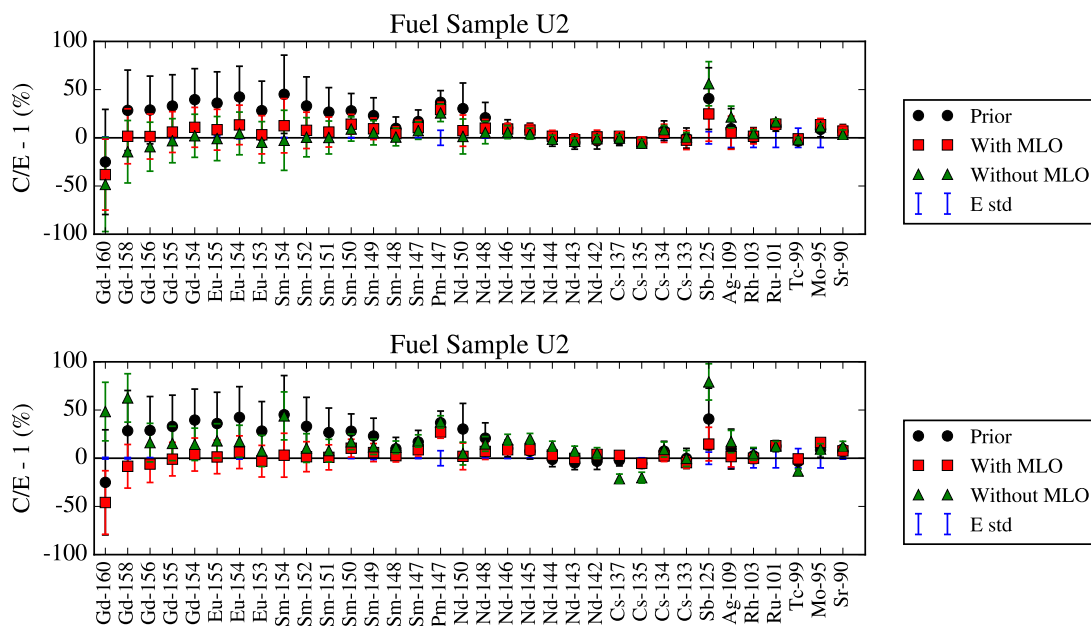
Figure A.25 – Posterior biases and uncertainties of the nuclide concentrations of fuel sample U2 obtained with BFMC and MOCABA FY data when MLO was and was not applied.
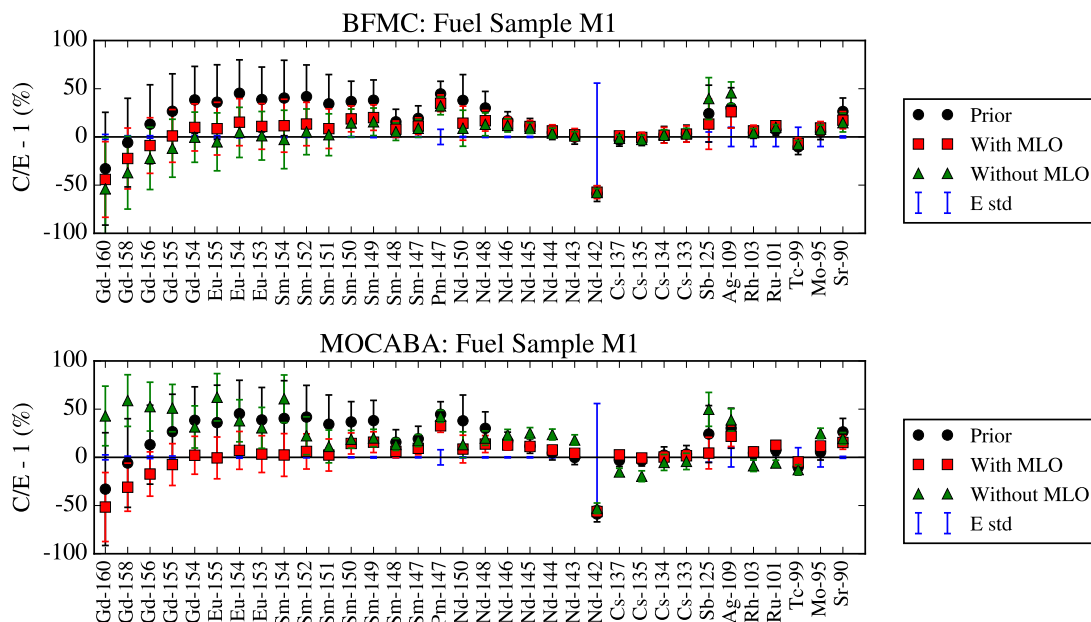
Figure A.26 – Posterior biases and uncertainties of the nuclide concentrations of fuel sample M1 obtained with BFMC and MOCABA FY data when MLO was and was not applied.
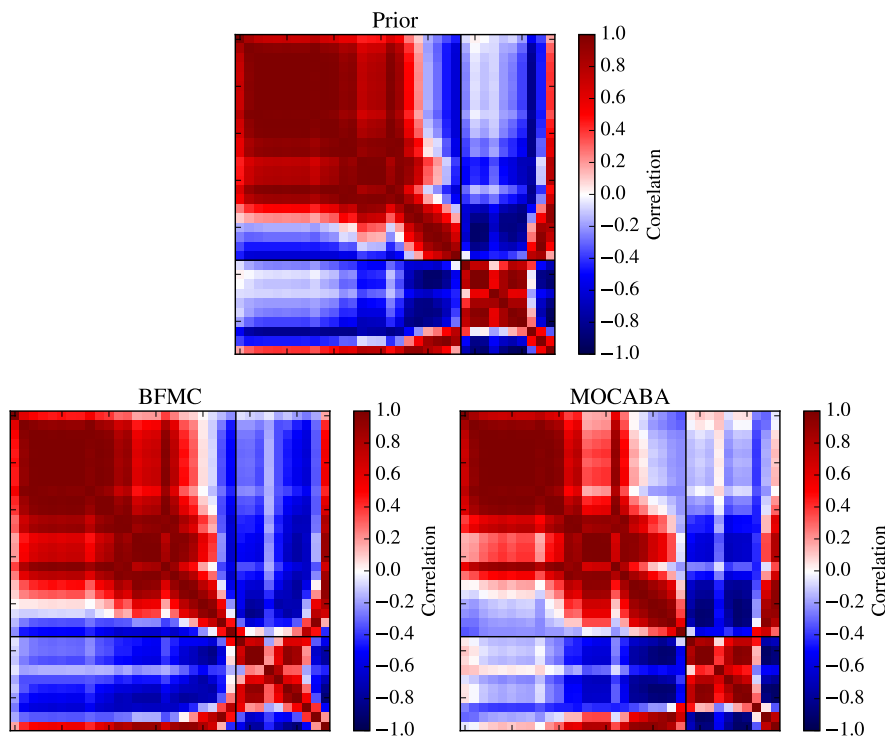
Figure A.27 – Correlation between **C** in fuel sample U2 without applying MLO.
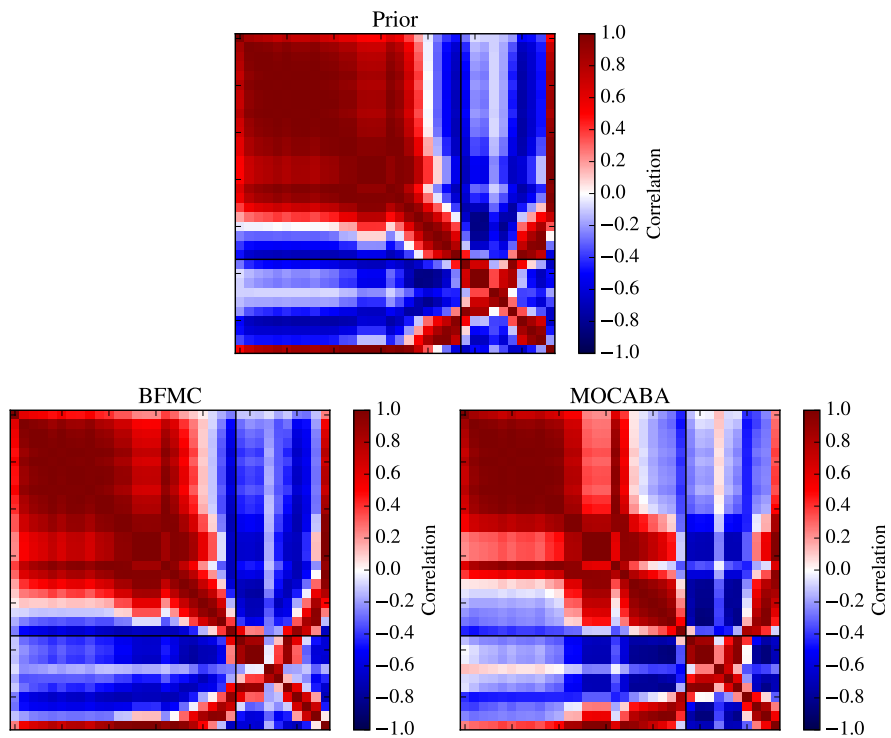
Figure A.28 – Correlation between **C** in fuel sample M1 without applying MLO.

A.6   xGLLS: Additional Information

Table A.1 – Integral parameters included in the Subgroup 33 benchmark exercise.

Core	Parameter
JEZEBEL Pu-239	k_{eff}
	F28/F25
	F49/F25
	F37/F25
JEZEBEL Pu-240	k_{eff}
FLATTOP	k_{eff}
	F28/F25
	F37/F25
ZPR6-7	k_{eff}
	F28/F25
	F49/F25
	C28/F25
ZPR6-7 Pu-240	k_{eff}
ZPPR-9	k_{eff}
	F28/F25
	F49/F25
	C28/F25
	Na Void Step 3
	Na Void Step 5
JOYO MK-I	k_{eff}

Table A.2 – ERANOS 33-energy-group structure (eV).

Group	Upper Energy	Group	Upper Energy	Group	Upper Energy
1	1.96×10^7	12	6.74×10^4	23	3.04×10^2
2	1.00×10^7	13	4.09×10^4	24	1.49×10^2
3	6.07×10^6	14	2.48×10^4	25	9.17×10^1
4	3.68×10^6	15	1.50×10^4	26	6.79×10^1
5	2.23×10^6	16	9.12×10^3	27	4.02×10^1
6	1.35×10^6	17	5.53×10^3	28	2.26×10^1
7	8.21×10^5	18	3.35×10^3	29	1.37×10^1
8	4.98×10^5	19	2.03×10^3	30	8.32×10^0
9	3.02×10^5	20	1.23×10^3	31	4.00×10^0
10	1.83×10^5	21	7.49×10^2	32	5.40×10^{-1}
11	1.11×10^5	22	4.54×10^2	33	1.00×10^{-1}

Table A.3 – Experimental variance-covariance matrix from the Subgroup 33 exercise. The diagonal values are 1-relative standard deviations and the non-diagonal values are correlation coefficients.

No.	Core	Parameter	1	2	3	4	5	6	7	8	9	10	11	12	13	14	15	16	17	18	19	20
1		k_{eff}	0.2																			
2	JEZEBEL Pu-239	F28/F25	0	1.1																		
3		F49/F25	0	0.23	0.9																	
4		F37/F25	0	0.23	0.32	1.4																
5	JEZEBEL Pu-240	k_{eff}	0	0	0	0	0.2															
6		k_{eff}	0	0	0	0	0	0.3														
7	FLATTOP	F28/F25	0	0	0	0	0	0	1.1													
8		F37/F25	0	0	0	0	0	0	0.23	1.4												
9		k_{eff}	0	0	0	0	0	0	0	0	0.23											
10	ZPR6-7	F28/F25	0	0	0	0	0	0	0	0	0	3.0										
11		F49/F25	0	0	0	0	0	0	0	0	0	0.23	2.1									
12		C28/F25	0	0	0	0	0	0	0	0	0	0.23	0.32	2.4								
13	ZPR6-7 240	k_{eff}	0	0	0	0	0	0	0	0	0.13	0	0	0	0.22							
14		k_{eff}	0	0	0	0	0	0	0	0	0.31	0	0	0	0	0.117						
15		F28/F25	0	0	0	0	0	0	0	0	0	0	0	0	0	0	2.7					
16	ZPPR-9	F49/F25	0	0	0	0	0	0	0	0	0	0	0	0	0	0	0.23	2.0				
17		C28/F25	0	0	0	0	0	0	0	0	0	0	0	0	0	0	0.23	0.32	1.9			
18		Na ρ #3	0	0	0	0	0	0	0	0	0	0	0	0	0	0	0	0	0	1.9		
19		Na ρ #5	0	0	0	0	0	0	0	0	0	0	0	0	0	0	0	0	0	0.41	1.9	
20	JOYO	k_{eff}	0	0	0	0	0	0	0	0	0	0	0	0	0	0	0	0	0	0	0	0.18

Table A.4 – Modeling variance-covariance matrix for the Subgroup 33 exercise. The diagonal values are 1-relative standard deviations and the non-diagonal values are correlation coefficients.

No.	Core	Parameter	1	2	3	4	5	6	7	8	9	10	11	12	13	14	15	16	17	18	19	20
1	JEZEBEL Pu-239	k_{eff}	5E-3																			
2		F28/F25	0	0.08																		
3		F49/F25	0	0.5	0.07																	
4		F37/F25	0	0.5	0.5	0.07																
5	JEZEBEL Pu-240	k_{eff}	0	0	0	0	3E-3															
6	FLATTOP	k_{eff}	0	0	0	0	0	4E-3														
7		F28/F25	0	0	0	0	0	0	0.7													
8		F37/F25	0	0	0	0	0	0	0.5	0.6												
9	ZPR6-7	k_{eff}	0	0	0	0	0	0	0	0	0.01											
10		F28/F25	0	0	0	0	0	0	0	0	0	3.3										
11		F49/F25	0	0	0	0	0	0	0	0	0	0.5	2.2									
12		C28/F25	0	0	0	0	0	0	0	0	0	0.5	0.5	2.6								
13	ZPR6-7 Pu-240	k_{eff}	0	0	0	0	0	0	0	0	0	0	0	0	0.01							
14		k_{eff}	0	0	0	0	0	0	0	0	0	0	0	0	0	0.01						
15		F28/F25	0	0	0	0	0	0	0	0	0	0	0	0	0	0	2.5					
16	ZPPR-9	F49/F25	0	0	0	0	0	0	0	0	0	0	0	0	0	0	0.5	1.4				
17		C28/F25	0	0	0	0	0	0	0	0	0	0	0	0	0	0	0.5	0.5	1.6			
18		Na ρ Step 3	0	0	0	0	0	0	0	0	0	0	0	0	0	0	0	0	0	4.5		
19		Na ρ Step 5	0	0	0	0	0	0	0	0	0	0	0	0	0	0	0	0	0	0	4.7	
20	JOYO	k_{eff}	0	0	0	0	0	0	0	0	0	0	0	0	0	0	0	0	0	0	0	0.01

Table A.5 – Prior and posterior parameters using INL (ERANOS) and Serpent2 (shown as SSS2). The xGLLS method is used for the Serpent2 sensitivities. All values are given in percent (%). $\Delta\mathbf{E}$, $\Delta\mathbf{M}$, and $\Delta\mathbf{C}$ are the experimental, modeling/methodology, and calculation due to nuclear data uncertainties, which are all expressed as relative standard deviations.

| Core	Parameter	$\Delta\mathbf{M}$	$\Delta\mathbf{E}$	$(\mathbf{E-C})/\mathbf{C}$ INL	SSS2	$\Delta\mathbf{C}$ INL	SSS2	$(\mathbf{E-C'})/\mathbf{C'}$ INL	GLLS	xGLLS	$\Delta\mathbf{C'}$ INL	GLLS	xGLLS
	k_{eff}	0.2	0.03	0.014	0.014	0.636	0.612	0.009	-0.003	-0.003	0.167	0.164	0.164
JEZEBEL Pu-239	F28/F25	1.1	0.9	2.354	2.221	3.696	3.506	0.739	0.326	0.326	0.983	0.810	0.809
	F49/F25	0.9	0.8	2.533	2.579	0.823	0.803	1.832	1.789	1.789	0.528	0.483	0.483
	F37/F25	1.4	0.8	1.317	1.284	2.354	2.222	0.259	0.095	0.095	0.815	0.721	0.718
JEZEBEL Pu-240	k_{eff}	0.2	0.03	0.019	0.014	0.656	0.650	-0.002	-0.007	-0.007	0.181	0.179	0.179
	k_{eff}	0.3	0.03	-0.097	-0.103	0.764	0.599	-0.070	-0.094	-0.094	0.230	0.215	0.215
FLATTOP	F28/F25	1.1	0.8	1.812	2.057	3.093	3.002	0.362	0.302	0.302	0.844	0.697	0.697
	F37/F25	1.4	0.7	0.442	0.633	2.034	1.980	-0.551	-0.497	-0.497	0.768	0.687	0.683
	k_{eff}	0.23	0.03	-0.043	-0.003	0.968	0.965	-0.080	-0.133	-0.133	0.123	0.136	0.136
ZPR6-7	F28/F25	3.0	2.2	-0.448	3.248	6.395	6.193	-1.482	1.334	1.333	1.719	1.823	1.803
	F49/F25	2.1	1.4	3.756	-2.132	0.836	0.892	3.251	-2.560	-2.560	0.589	0.616	0.614
	C28/F25	2.4	1.2	-0.970	-1.341	1.512	1.585	-0.724	-0.976	-0.976	0.963	1.092	1.094
ZPR6-7 Pu-240	k_{eff}	0.22	0.03	0.063	0.284	0.971	0.967	0.027	0.151	0.151	0.124	0.136	0.135
	k_{eff}	0.117	0.02	0.078	0.167	1.191	1.190	-0.017	-0.031	-0.031	0.114	0.137	0.137
ZPPR-9	F28/F25	2.7	2.1	2.987	2.343	7.896	7.322	1.847	0.328	0.327	1.944	2.130	2.105
	F49/F25	2.0	1.2	1.958	1.392	0.870	0.858	1.478	0.948	0.948	0.586	0.605	0.604
	C28/F25	1.9	1.4	-0.921	-1.186	1.545	1.627	-0.688	-1.024	-1.024	0.972	1.046	1.047
	Na Void Step 3	1.9	5.3	-1.884	-3.721	7.563	9.797	-2.467	-2.044	-2.037	3.000	3.368	3.428
	Na Void Step 5	1.9	5.0	2.754	-2.491	9.679	11.23	1.922	-0.634	-0.637	3.692	3.696	3.764
JOYO MK-I	k_{eff}	0.18	0.03	0.255	0.080	0.863	0.863	0.024	0.016	0.016	0.178	0.199	0.199
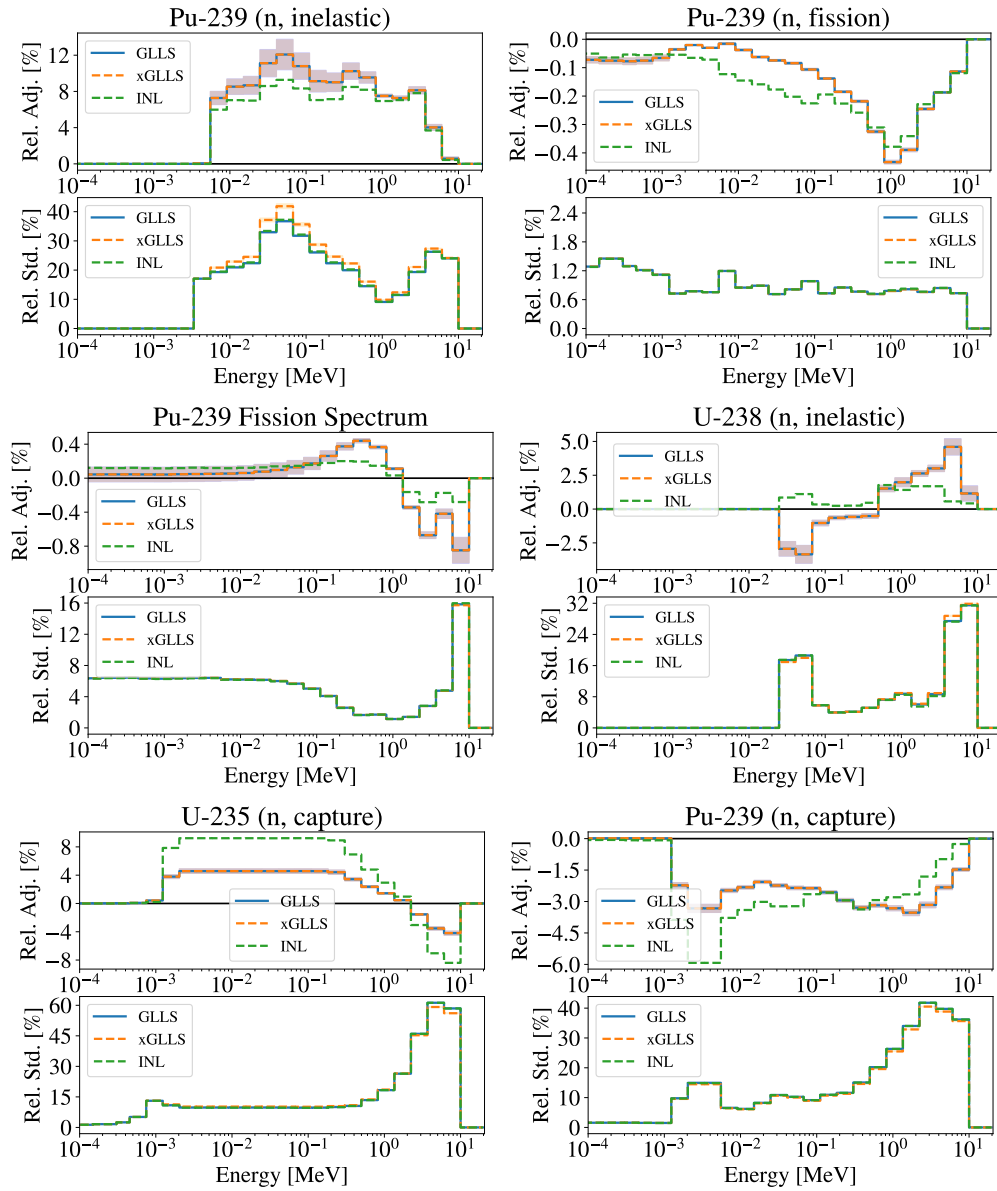
Figure A.29 – Nuclear data adjustments with Serpent sensitivities using xGLLS and GLLS. Compared to INL's adjustments using ERANOS. In each subfigure, the top plot is the relative adjustment, $(\sigma - \sigma')/\sigma$, and the bottom plot is the posterior relative standard deviation.

Daniel J. Siefman, PhD

Curriculum Vitae

PERSONAL DETAILS

Date of Birth	February 25th, 1991
Nationality	United States of America
Address	Chemin des Pâquis 6A
	CH-1025 Lausanne
Email	dsiefman@gmail.com
Phone	+41 78 966 37 23

EDUCATION

École Polytechnique Fédérale de Lausanne (EPFL)   **2019**
Energy - Nuclear Engineering, PhD

Eidgenössische Technische Hochschule Zürich (ETHZ)   **2015**
Nuclear Engineering, M.Sc.

École Polytechnique Fédérale de Lausanne (EPFL)   **2015**
Nuclear Engineering, M.Sc.

University of Florida Honors College   **2013**
Nuclear Engineering, B.Sc.
- Magna Cum Laude with a Minor in *Russian Language and Culture*

EMPLOYMENT HISTORY

Doctoral Candidate   **October 2015 - September 2019**

Reactor Physics, EPFL, CH

– Data assimilation, uncertainty quantification and sensitivity analysis to nuclear data using random sampling and sensitivity coefficients.
– Adjusting model parameters in the GEF code to better evaluate fission yield data.
– Development of data assimilation of spent nuclear fuel inventories.
– Licensed reactor operator and radiation protection expert for the Crocus reactor.

Engineering Internship   **July 2014 - October 2014**

National Cooperative for the Disposal of Radioactive Waste (Nagra), CH

– MCNP simulations for characterizing the activation of core internals, shielding, and structural materials in Swiss nuclear power plants for decommissioning planning.
– Applying classical and hybrid variance reduction methods to neutron streaming problems in Monte Carlo simulations.

    – Analyzing novel packaging techniques to optimize long-term spent fuel storage casks.

Research Assistant   **June 2013 - June 2014**

  Laboratory for Reactor Physics and Systems Behaviour, EPFL, Lausanne, CH

- Developing methods to model the research reactor Crocus by interfacing Monte Carlo and deterministic codes (Serpent and PARCS).
- Transient analyses of accidental reactivity insertions to estimate peak fuel temperature.
- Translation of the reactor's safety analysis report from French to English.

Reactor Core and Safety Analyst   **June 2012 - June 2013**

  University of Florida Training Reactor (UFTR), Gainesville, FL, USA

- Neutronics modeling using the Monte Carlo codes MCNP5/MCNPX and SCALE6.1.
- Coupled neutronics/thermal-hydraulics safety analyses of reactivity insertion accidents.
- Composing sections of the reactor's Safety Analysis Report for relicensing.

SKILLS

Languages
  English (native), French (B2), Russian (A2)

Software
  Python, Matlab, C++, Linux, MCNP, Serpent, SCALE6.1, NJOY, CASMO-5, PARCS

ACHIEVEMENTS/AWARDS

- EPFL Excellence Fellowship (2013-2015)
- Nuclear engineering student of the year finalist (University Florida) 2013
- Florida Bright Futures Scholarship (100% tuition) (2009-2013)
- Paul and Harriette Franklin Scholarship (2009)

References and academic transcripts available upon request
LinkedIn : https://www.linkedin.com/in/daniel-siefman-4466a364

PUBLICATIONS

On Data Assimilation with Monte-Carlo-Calculated and Statistically Uncertain Sensitivity Coefficients
Siefman, D, Hursin M, Aufiero M, Bidaud A, Pautz A
Annals of Nuclear Energy, 135 (2020)

Data Assimilation Applied to the LWR-PROTEUS Phase II Integral Experiments
Siefman, D, Hursin M, Perret G, Pautz A
In Preparation

Sensitivity vs. Stochastic Data Assimilation for Nuclear Data
Siefman, D, Hursin M, Rochman D, Pelloni S, Pautz A
European Physics Journal Plus, 133 (2018)

Analysis of reactivity worths of burnt PWR fuel samples measured in LWR-PROTEUS Phase II using a CASMO-5 reflected-assembly model
Grimm P, Hursin M, Perret G, **Siefman D**, Ferroukhi H
Progress in Nuclear Energy, 101 (2018)

Full Core modeling techniques for research reactors with irregular geometries using Serpent and PARCS applied to the CROCUS reactor
Siefman D, Girardin G, Rais A, Hursin M, Pautz A
Annals of Nuclear Energy, 85 (2015)

Methods and Models for the Coupled Neutronics and Thermal-Hydraulics Analysis of the CROCUS Reactor at EPFL
Rais A, **Siefman D**, Girardin G, Hursin M, Pautz A
Science and Technology of Nuclear Installations, 2015 (2015)

CONFERENCE PROCEEDINGS

Data Assimilation with Post Irradiation Examination Experiments
Siefman, D, Hursin M, Pautz A
ND2019, May 19-24, 2019. Beijing, China

Convergence Analysis and Criterion for Data Assimilation with Sensitivities from Monte Carlo Neutron Transport Codes
Siefman, D, Hursin M, Aufiero M, Bidaud A, Pautz A
PHYSOR 2018, April 22-26, 2018. Cancun, Mexico (2018)

Determination of Sobol Sensitivity Indices for Correlated Inputs with SHARK-X
Hursin M, **Siefman, D**, Perret G, Vasiliev A, Ferroukhi H
PHYSOR 2018, April 22-26, 2018. Cancun, Mexico (2018)

Representativity Analysis of the LWR-Proteus Phase II Experiments Using SHARK-X Stochastic Sampling Method
Hursin M, **Siefman, D**, Perret G, Pautz A
BEPU 2018, May 13-19, 2018. Lucca, Italy (2018)

Case Study of Data Assimilation Methods with the LWR-Proteus Phase II Experimental Campaign
Siefman D, Hursin M, Grimm P, Pautz A
M&C 2017, April 16-20, 2017. Jeju, South Korea. (2017)

Neutronics modeling of the CROCUS reactor with SERPENT and PARCS codes
Rais A, **Siefman D**, Hursin M, Ward A, Pautz A
M&C 2017, April 16-20, 2017. Jeju, South Korea. (2017)

Verification of the New Implementations in SHARK-X For Reactivity Coefficients and Relative Reactivity Worth UQ
Hursin M, **Siefman D**, Perret G, Grimm P, Pautz A
PHYSOR 2016, May 2016, Sun Valley ID, USA (2016)

Neutron Streaming Investigations with Classic and Hybrid Monte Carlo Variance Reduction Methods for the AGN-211-P Research Reactor in Basel (CH)
Vlassopolus S, Bykov V, **Siefman D**, Pantelas M, Volmert B
PHYSOR 2016, May 2016, Sun Valley ID, USA (2016)

CASMO-5 Analysis of Reactivity Worths of Burnt PWR Fuel Samples Measured in LWR-PROTEUS Phase II
Grimm P, Hursin M, Perret G, **Siefman D**, Ferroukhi H
PHYSOR 2016, May 2016, Sun Valley ID, USA (2016)

Uncertainty Quantifcation of the LWR Experiments at the PROTEUS Research Reactor Using Stochastic Sampling
Siefman D, Hursin M, Perret G, Pautz A
ANS Student Conference, April 2015, Texas AM, USA (2015)

Verification of a Reactor Physics Calculation Scheme for the CROCUS Reactor
Hursin M, **Siefman D**, Rais A, Girardin G, Pautz A
ITMSR-3: 3rd International Technical Meeting on Small Reactors, November 2014, Ottawa, Canda (2015)

PARCS Few-group Homgenized Parameters Generation using Serpent Monte Carlo code at the CROCUS Reactor
Rais A, **Siefman D**, Girardin G, Hursin M, Pautz A
IGORR: International Group on Research Reactor, November 2014, Bariloche, Argentina, (2014)

A Fully-reconstituted Safety Basis for the University of Florida Training Reactor
Jordan K, **Siefman D**, Cronin D
IGORR: International Group on Research Reactor, October 2013, Daejeon, Korea (2013)

The Quest for a Negligible-Risk Reactor: A Safety Analysis of the UFTR
Siefman D, Kowalczyk S
ANS Student Conference at MIT, April 2013, Boston, USA (2013)